UNIVERSITY OF BIRMINGHAM

High-field SANS studies of the vortex lattice in YBCO

by Stephen Phillip Brown

A thesis submitted
to the University of Birmingham
for the degree of
DOCTOR OF PHILOSOPHY

School of Physics and Astronomy
The University of Birmingham
September, 2005

Contents

List of figures

Synopsis

In this thesis is presented the first high-field structural study of the vortex lattice in $YBa_2Cu_3O_7$. Small-angle neutron scattering was used to deduce the configuration of vortices in a twinned sample of $YBa_2Cu_3O_7$ over the field range 1–11 T applied parallel to the crystal c-axis. The experiments revealed a field-induced continuous transition from a distorted London-like vortex lattice at 1 T, to an unconventional square vortex lattice with a slight rectangular distortion. It is clear from the data that some kind of unconventional intrinsic anisotropy is responsible for the high-field square lattice and the data are suggestive of two possible origins, Fermi surface anisotropy and d-wave effects, both of which may be described as non-local effects. However, from the present data it is not possible to determine which of these effects is more important.

The dependence of the vortex lattice structure upon temperature and angle of applied field was also studied. In accordance with expectation, it was found that the unconventional anisotropy responsible for the stability of the square vortex lattice is diminished with increasing temperature and the distorted triangular configuration eventually reappears via a continuous transition. Similarly, the square vortex lattice is suppressed by rotating the applied field away from the crystal c-axis. However, in this case the transition between the triangular and square vortex lattices becomes first-order. Moreover, the low-field triangular domains are very different to those observed with the field parallel to the c-axis.

Three other neutron studies in which this author was involved were also briefly presented. Of these, two were small-angle neutron scattering studies of the vortex lattice (in $Nd_{1.85}Ce_{0.15}CuO_4$ and detwinned $YBa_2Cu_3O_{7-\delta}$) and are thus intimately related to the main topic. In $Nd_{1.85}Ce_{0.15}CuO_4$, a square vortex lattice was observed, but at unprecedentedly low fields (20 mT). The detwinned $YBa_2Cu_3O_{7-\delta}$ samples have provided confirmation of the results observed in the twinned sample and hold prospect for further studies, particularly of the effect of doping on the transition to square. Lastly,

measurements by inelastic neutron scattering of the spin fluctuations at the metamagnetic field in $Sr_3Ru_2O_7$ were shown. These important experiments have demonstrated the first microscopic evidence for a wholesale change in the character of the spin correlations at the metamagnetic field.

Acknowledgements

It has been said that tradition is force to be reckoned with, and so as is customary, I wish to thank foremost my Ph.D. supervisor Prof. Ted Forgan. However, it is not just due to thesis protocol that Ted deserves primacy in these acknowledgements: I am indebted to Ted for his sage advice (Ted has a *vast* knowledge of physics) and his support throughout my time at Birmingham.

The last four years have also been greatly enhanced by the members of the Condensed Matter Physics group at Birmingham. I would particularly like to thank Demetris Charalambous for mentoring me in the early stages of my Ph.D., introducing me to the crash-free world of Linux and providing many enlightening physics discussions. I was lucky to have such a patient co-worker as Emma Jones, and I have her to thank for preventing me from destroying Tubby Tesla before the data presented in this thesis was collected! There has never been a dull moment working in the "Ted" sub-group — well, perhaps I exaggerate, but I would like to acknowledge present and past members anyway. These include: Daniel Ucko (for his appreciation for fine coffee and sitting in pubs watching football), Silvia Ramos (who single-handedly fostered a collective social life amongst the oddballs of the group), Rich Lycett a.k.a. "Dick Lyce" (for his cheery northern banter), Charlotte Bowell (for tolerating my sick mind) and Mark Laver (for being just as haphazard and dangerous in the lab as me). The daily toil in the office was made much more pleasurable by interactions with the other Ph.D. students in the group; for this I thank Jon Fenton (where's my youthful exuberance now, eh?), Suz Gildert, Mugdha Joshi, Philip Baker, Sean McMitchell, Xuefeng Deng and last, but certainly not least Tim Barraclough: I would like to thank Tim for sharing the vast quantities of beer and take-aways that fuel Ph.D. research, for being a considerate flatmate (except the day when he stole all the knives!) and for being a good friend. My acknowledgements of the group would not be complete without mentioning the more experienced members. Chris Muirhead, Mark Colclough, Colin Gough, Joe

Vinen and Alistair Rae have broadened my mind with various seminars on interesting physics. I have greatly enjoyed talking to Chris and Mark about a very diverse range of subjects during their brief transits past my desk to collect tea.

It has been a privilege to work with a number of very talented international collaborators, some of whom have contributed towards this work, and it would be remiss not to thank them. Amongst these are (in no particular order): Raffi Gilardi, Joel Mesot, Bob Cubitt, Charles Dewhurst, Stephen Hayden, Andrew Wildes, Vladimir Hinkov, Stephen Lee and Alan Drew.

Finally, some personal acknowledgements are due. I would like to thank and dedicate this thesis to: my parents, for all their support (particularly during my undergraduate degree); my fiancée, Anna Marshall, for support and trying to read this thesis; and the rest of my family.

CHAPTER I

The vortex lattice

1. Introduction

The existence of the vortex lattice in type-II superconductors was promulgated by Abrikosov (1957) after he examined solutions of the Ginzburg-Landau equations in an applied field for a case that was hitherto believed unrealistic. Before that time, the Ginzburg-Landau equations had been successful in describing the properties of type-I superconductors near the critical temperature, $T_{\rm c}$. The theory contains two important length scales: the length λ over which magnetic field variations occur inside a superconductor, and the length ξ over which the superconducting order parameter varies. Prior to Abrikosov's work, only solutions of the Ginzburg-Landau equations with the ratio of the length scales $\kappa = \lambda/\xi < 1/\sqrt{2}$ were considered. For $\kappa > 1/\sqrt{2}$ (the type-II regime — see section 4), it was found that the energy of a domain boundary between normal and superconducting regions can be negative (for fields above the first critical field, $H_{\rm c1}$ — see below) which was, at that time, considered unphysical. However, Abrikosov succeeded in solving the Ginzburg-Landau equations in the presence of an applied field in this regime and discovered that close to $T_{\rm c}$ the superconducting order parameter has a periodic solution. This admitted the interpretation that a magnetic lattice is formed such that flux penetrates at positions in the superconductor where the order parameter vanishes. The flux is quantised in units of the so-called flux quantum:

$$\Phi_0 = \frac{h}{2e} = 2.07{\cdot}10^{-15}\,\mathrm{Wb} \tag{1.1}$$

Surrounding each unit of flux are circulating currents (vortices) that tend to shield the rest of the superconductor from the penetrating flux.

In a type-II superconductor, the Abrikosov vortex lattice is only realised at high temperatures or high magnetic fields; at sufficiently low temperatures and inductions,

type-II superconductors are found to behave similarly to type-I superconductors, *i.e.* they exhibit the Meissner effect (total flux expulsion). The reason for this is that the formation of vortices represents a trade-off between an increase in the free energy due to a loss of condensation energy, and a decrease in the free energy from allowing flux to enter the superconductor. At low temperatures and low inductions the loss of condensation energy proves too great and it is not auspicious for vortices to form. Therefore, unlike type-I superconductors, which have only one critical field, $H_{\rm c}$, at which superconductivity vanishes, type-II superconductors have *two* critical fields, $H_{\rm c1}$ and $H_{\rm c2}$, such that $H_{\rm c1} < H_{\rm c} < H_{\rm c2}$ *. Up to the first critical field, $H_{\rm c1}$, the behaviour of a type-II superconductor is identical to a type-I (see figure 1.1). Beyond the first critical field vortices penetrate the sample and their density increases until the second critical field, $H_{\rm c2}$, at which point the superconductor returns to its normal state.

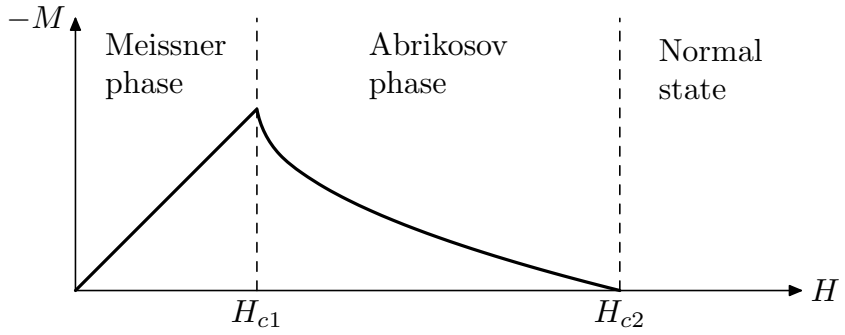

Fig. 1.1: Magnetisation as a function of applied field for a type-II superconductor.

In this chapter, a selection of theoretical tools used to model the vortex lattice is reviewed. These tools range from the simple-minded London approach, which is nonetheless applicable in many circumstances (see section 2), to more sophisticated theories that elucidate the intricate effects associated with unconventional superconductivity. It is impossible to do justice to the vast body of material on the vortex lattice, therefore only those theories with direct relevance to the material of this thesis will be discussed.

* Assuming a comparison is being made between a type-II to a type-I superconductor with the same value of condensation energy per unit volume at $(H, T) = (0, 0)$. For a type-II superconductor, $H_{\rm c}$ still has the interpretation of being a measure of condensation energy even though nothing "interesting" happens at this field.

2. The London theory of type-II superconductors.

The London theory (London & London, 1935) was the first successful phenomenological explanation of the electrodynamics of superconductors and — at a time when type-II superconductivity was unknown — provided a bridge between the two principal electromagnetic properties of type-I superconductors: perfect conductivity and the Meissner effect. The London theory builds the bridge on the foundation of classical electronic conduction, which is described by the Drude model:

$$m\left(\dot{\mathbf{v}} + \frac{\mathbf{v}}{\tau}\right) = -e\mathbf{E}. \tag{2.1}$$

Equation 2.1 is simply the equation of motion for an electron with velocity $\mathbf{v}$ under the influence of an electric field, $\mathbf{E}$ undergoing collisions with a characteristic time τ. Clearly, the property of perfect conduction implies that the damping term is zero, *i.e.* $\tau \to \infty$. Rewriting equation 2.1 (without the damping term) in terms of the magnetisation current density, $\mathbf{J}(\mathbf{r}) = \mu_0^{-1}\nabla \times \mathbf{B}$, results, after some trivial manipulation, in the expression:

$$\Lambda\nabla \times \mathbf{J} + \mathbf{B} = \mathbf{K}(\mathbf{r}), \qquad \Lambda = \frac{m}{ne^2}, \tag{2.2}$$

where $\mathbf{K}(\mathbf{r})$ is an arbitrary function of position resulting from integrating with respect to time. This equation governs the magnetic response of a perfect conductor, but is too general as a description of a superconductor. The most important difference between a perfect conductor and a superconductor is that in the former, magnetisation currents will be generated to oppose any change in flux, whereas the magnetisation currents in the latter act to exclude flux from the bulk regardless of its history. This property is known as the Meissner effect and to account properly for it requires that all time-independent solutions, which would define a history, are rejected. Therefore the function $\mathbf{K}(\mathbf{r})$ is set to zero. That the resulting form of equation 2.2 accords with the Meissner effect is easily verified: consider an area Σ, bounded by a path Γ, that lies deep within the bulk of a superconductor. Integration of equation 2.2 over this surface yields zero for both the first term (since there is zero current density deep within the bulk) and second term (since no flux is present in the superconductor). A non-zero value for $\mathbf{K}(\mathbf{r})$ inside the superconductor would imply the existence of a time-independent flux in disagreement with the Meissner effect.

F. and H. London took equation 2.2 with $\mathbf{K}(\mathbf{r}) = \mathbf{0}$ as being a fundamental equation governing the electromagnetic response of a type-I superconductor. Using the differential form of Ampère's law and $\nabla \cdot \mathbf{B} = 0$ equation 2.2 can be recast into the more familiar form

$$\lambda_{\mathrm{L}}^2 \nabla^2 \mathbf{B} = \mathbf{B}, \qquad \lambda_{\mathrm{L}}^2 = \frac{m}{\mu_0 n e^2}, \tag{2.3}$$

where λ_{L} is the so-called London penetration depth, which gives the length scale over which an external applied field is exponentially attenuated inside the superconductor* — typically $\sim 10^{-7}\,\mathrm{m}$.

Although the nature of the vortex state in type-II superconductors was first appreciated by studying the Ginzburg-Landau equations (Abrikosov, 1957), many useful results may be obtained by examining a modified version of the simpler London theory. The necessary amendments can made by re-examining the function $\mathbf{K}(\mathbf{r})$ in equation 2.2, which was previously set to zero to account for the Meissner effect. The nucleation of vortices in a type-II superconductor is clearly beyond the assumptions under which 2.3 was derived, so they must be introduced by brute force. A single vortex at the origin may be modelled by $\mathbf{K}(\mathbf{r}) = \Phi_0 \delta(\mathbf{r}) \hat{\mathbf{z}}$, which generates a single flux quantum. Hence, the London equation, modified for the mixed state of a type-II superconductor, can be written

$$\lambda_{\mathrm{L}}^2 \nabla^2 \mathbf{B} - \mathbf{B} = \Phi_0 \sum_i \delta^{(2)}(\mathbf{r} - \mathbf{r}_i)\, \hat{\mathbf{z}}, \tag{2.4}$$

where the set of vectors $\{\mathbf{r}_i\}$ denote the positions of the vortices.

Since the vortex lattice is a periodic structure it is more convenient to rewrite the London equation (2.4) in terms of reciprocal space. To do this the magnetic field, $\mathbf{B}(\mathbf{r})$, is written as a Fourier sum:

$$\mathbf{B}(\mathbf{r}) = \sum_{\mathbf{G}} \mathbf{B}_{\mathbf{G}} \exp(\mathrm{i}\, \mathbf{G} \cdot \mathbf{r}). \tag{2.5}$$

Substituting the Fourier sum for $\mathbf{B}(\mathbf{r})$ into equation 2.4 and integrating over one primitive unit cell provides the values of the Fourier components:

$$\mathbf{B}_{\mathbf{G}} = \frac{\langle B \rangle \hat{\mathbf{z}}}{1 + \lambda_{\mathrm{L}}^2 G^2}, \tag{2.6}$$

* Although this result is well-known in Condensed Matter Physics, it has only fairly recently been *directly* measured using slow muons (Jackson *et al.*, 2000)

where $\langle B \rangle$ is the average induction in the superconductor. At large inductions where the inter-vortex spacing is much larger than the penetration depth (*i.e.* $\lambda_{\mathrm{L}}^2 G^2 \gg 1$), the unity in the denominator may be disregarded. Since $G \propto \sqrt{B}$, in this limit the London Fourier components are field independent.

Inevitably, a price must be paid for the simplicity of the London description of the vortex lattice. In particular the free energy*,

$$F = \frac{1}{2\mu_0} \int B^2 + \lambda_{\mathrm{L}}^2 \left(\nabla \times \mathbf{B}\right)^2 \, \mathrm{d}^3 r, \tag{2.7}$$

is divergent. This malaise arises because the London theory tacitly assumes that the superconducting condensate is "rigid" with respect to perturbations. Rigidity implies that on application of a magnetic field the canonical momentum of the electron pairs is conserved. To keep the canonical momentum constant, the gauge-invariant superfluid velocity, $\mathbf{v}_{\mathrm{s}}$, changes in concert with the vector potential and thus the response in the London limit of the eletron superfluid to an applied field may be written as a local relation of the form $\mathbf{J} = -\Lambda^{-1}\mathbf{A}$, which is equivalent to the London postulate (Schrieffer & Tinkham, 1999). So although London theory may be derived from the classical theory of electromagnetism and a few empirical assumptions, it can also be viewed as a limiting case of a fully-blown quantum theory of superconductivity if excitations can be ignored.

Rigidity leads to a rather unphysical picture of vortices in type-II superconductors. A London vortex can be pictured as truly singular with only an infinitesimal filament along which superconductivity is suppressed and a logarithmically divergent field at the core. (This divergence is responsible for the field independence of the Fourier components seen in equation 2.6.) In reality, supercurrent flow causes quasi-particles to be excited out of the condensate, which increases the free energy thus attaching an extra penalty to large current densities in addition to the kinetic energy term (the second term in equation 2.7). This removes the field divergence and spreads the core over a finite volume.

Despite the shortcomings of London theory, the London free energy is still a useful quantity to calculate so long as the vortex core size can be neglected with respect to

* Euler-Lagrange minimisation of the London free energy provides an alternative route to equation 2.3

the penetration depth and, concomitantly, contributions near to the vortex core are somehow removed. For studies of the vortex lattice it is most beneficial to do this in reciprocal space. Integrating equation 2.7 by parts and disposing of the surface term, which is negligible for a large vortex lattice, yields, after substituting equation 2.4 and converting into reciprocal space quantities via equation 2.5:

$$\mathcal{F} = \frac{\langle B \rangle}{2\mu_0} \sum_{\mathbf{G}} \hat{\mathbf{z}} \cdot \mathbf{B}_{\mathbf{G}}, \tag{2.8}$$

where $\mathcal{F}$ is the free energy density. The quantity $\mathcal{F}$ is formally (logarithmically) divergent for the same reasons that equation 2.7 is. As has already been alluded, this necessitates a remedy that is most conveniently dispensed in the form of an arbitrary Gaussian cut-off at large wavevectors (Brandt, 1995). (This result, which is valid near H_{c2}, is derived from Ginzburg-Landau theory and represents the real space vortices by Gaussian source terms. At low fields the cut-off may be approximated by an exponential (Yaouanc *et al.*, 1997).) The cut-off is applied to each Fourier component multiplicatively, *i.e.* $\mathbf{B}_{\mathbf{G}} \rightarrow \mathbf{B}_{\mathbf{G}} \exp(-G^2\xi^2)$. The width of the Gaussian distribution, $\approx \xi^{-1}$, is taken so as to exclude contributions to the free energy at length scales less than the width of the vortex core, $\approx \xi$, which is the length scale at which London theory breaks down. With this *ad hoc* amendment the London free energy converges and is minimised for a vortex lattice with triangular coordination. Since the free energy (equation 2.7) is invariant with respect to rotation of the coordinate system, there is a degeneracy in the orientation of the vortex lattice. This degeneracy is a simple consequence of the isotropic nature of the free energy and may be removed, in some instances, by anisotropy (see section 3).

In figure 1.2 is shown a contour plot of the field distribution given by the London model with the Gaussian cut-off described above. The parameters have been chosen such that the lattice represented in the figure is similar to the vortex lattice formed in $YBa_2Cu_3O_7$ at 1 T, *i.e.* with the inter-vortex spacing approximately $0.3\lambda_L$ (λ_L =140 nm) — see figure caption for details. The noteworthy features of the London vortex lattice are: the saddle points, lying in between neighbouring vortices; the minima, which occupy positions interstitial to three neighbouring maxima; and the maxima whose divergence is suppressed by the convolution of the "ideal" London lattice by a Gaussian of width ξ as outlined above.

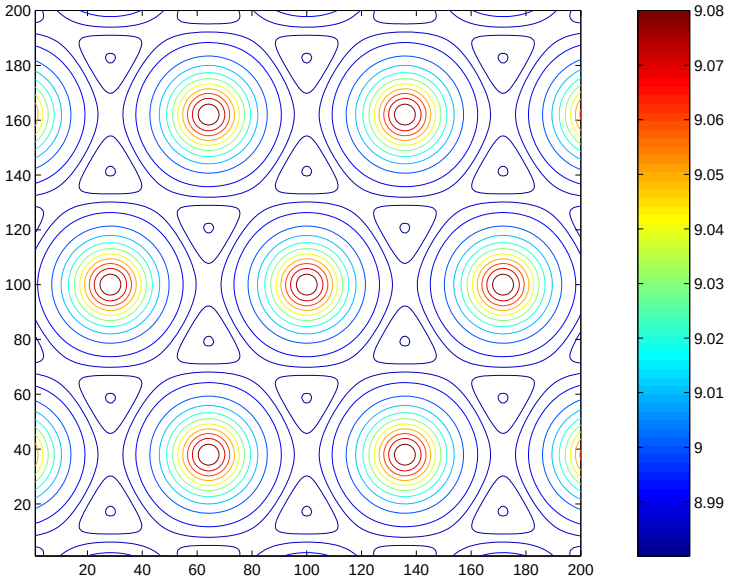

Fig. 1.2: Numerical calculation of the field distribution given by London theory (equation 2.5), with a Gaussian cut-off. The calculation is performed in units such that the flux quantum is unity and lengths are measured relative to the London penetration depth. In these normalised units $B = 9$, which corresponds to an inter-vortex spacing of approximately $0.3\lambda_{\mathrm{L}}$, and $\xi = 0.02$ ($\kappa = 50$), giving a cut-off range of 25 reciprocal lattice vectors. The lattice sum was taken to 100 reciprocal lattice vectors in each direction.

3. Anisotropic London theory

The range of application of equation 2.4 can be easily extended to take into account electronic anisotropy, which is of particular relevance to the study of high-T_{c} materials due to their layered structure. This is accomplished by inserting a normalised effective-mass tensor, $\boldsymbol{\mathcal{M}}$, into the expression for the free energy (equation 2.7) such that the kinetic energy term remains invariant:

$$F[\mathbf{B}(\mathbf{r})] = \frac{1}{2\mu_0} \int B^2 + \lambda_{\mathrm{L}}^2 (\nabla \times \mathbf{B}) \cdot \boldsymbol{\mathcal{M}} \cdot (\nabla \times \mathbf{B}) \, \mathrm{d}^3 r. \tag{3.1}$$

In the above expression λ_{L} is calculated for the geometric mean mass and the normalised effective-mass tensor in the frame of an orthorhombic crystal is given by:

$$\boldsymbol{\mathcal{M}} = (m_a m_b m_c)^{-1/3} \begin{pmatrix} m_a & 0 & 0 \\ 0 & m_b & 0 \\ 0 & 0 & m_c \end{pmatrix}, \tag{3.2}$$

where the effective masses, m_i, are calculated in the usual way, *i.e.* from the Fermi-surface average $\langle v_i^2 \rangle$. (v_i is a component of the Fermi velocity.)

To obtain the anisotropic version of the London equation, the free energy functional (equation 3.1) is minimised with respect to $\mathbf{B}(\mathbf{r})$, whereupon, after inserting the vortex source terms (Dirac delta-functions), the equation

$$\mathbf{B} + \lambda_{\mathrm{L}}^2 \nabla \times [\boldsymbol{\mathcal{M}} \cdot (\nabla \times \mathbf{B})] = \Phi_0 \sum_i \delta^{(2)}(\mathbf{r} - \mathbf{r}_i)\, \hat{\mathbf{z}}, \tag{3.3}$$

is obtained.

It is easy to appreciate that when the magnetic field is applied along a crystal axis, the effect of electronic anisotropy on the vortex lattice is simply a scale transformation. Since the vortices interact magnetically, the scale transformation depends on the ratio of the penetration depths in the plane perpendicular to the vortex. (The penetration depth ratios are, according to equation 2.3, proportional to the square-root of the mass ratios.) For example, if the field is applied along the crystal c-axis then the resulting vortex lattice may be formed by taking the standard isotropic vortex lattice and scaling it in real space by $\gamma_{ab}^{-\frac{1}{2}} = \sqrt{\lambda_b/\lambda_a}$ along the crystal a-direction and by $\gamma_{ab}^{\frac{1}{2}} = \sqrt{\lambda_a/\lambda_b}$ along the crystal b-direction. If $m_a > m_b$ the resulting distortion is that depicted in figure 1.3. Note that the definition of anisotropic penetration depths used here gives the magnetic penetration depth in the direction *perpendicular* to the relevant effective mass (*e.g.* $\lambda_a \propto \sqrt{m_a}$ gives the screening length along the b-direction). The relationship between mass anisotropy and field anisotropy is just a consequence of Ampère's law and is shown in figure 1.4.

When the field is applied at some angle to a principal axis, the diagonal components of the effective-mass tensor mix also, resulting in distortion of the vortex lattice (Kogan, 1981). For simplicity, consider the case of uniaxial anisotropy where $m_a = m_b < m_c$ (see section 20 for an example in practice). If the field is applied at an angle Θ to the c-axis by rotation about the a-axis (see figure 1.4) then it will mix m_b and m_c into the effective mass in the y'-direction; the effective mass in the x'-direction is unchanged. The anisotropy experienced by the supercurrents flowing in the $y'x'$ plane (perpendicular to z' vortex direction) is easily calculated by rotating the effective-mass

tensor. The relevant scale factor is

$$\epsilon(\Theta) = \sqrt{\cos^2\Theta + \gamma_{ac}^2 \sin^2\theta}, \tag{3.4}$$

where in the real space vortex frame the vortex lattice (*i.e.* the field distribution) is scaled by $\epsilon^{-\frac{1}{2}}$ in x' and by $\epsilon^{\frac{1}{2}}$ in y' (see figure 1.4).

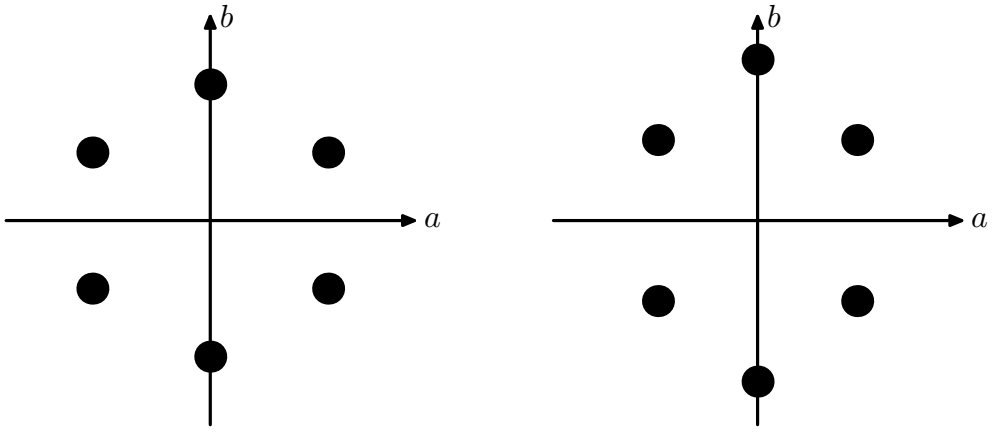

Fig. 1.3: Effect of anisotropy in real space for the "diagonal" case: turning on the anisotropy scales the isotropic lattice left by a factor $\gamma^{-\frac{1}{2}}$ along the a-direction and $\gamma^{\frac{1}{2}}$ along the b-direction. Here $\gamma = 1.4$.

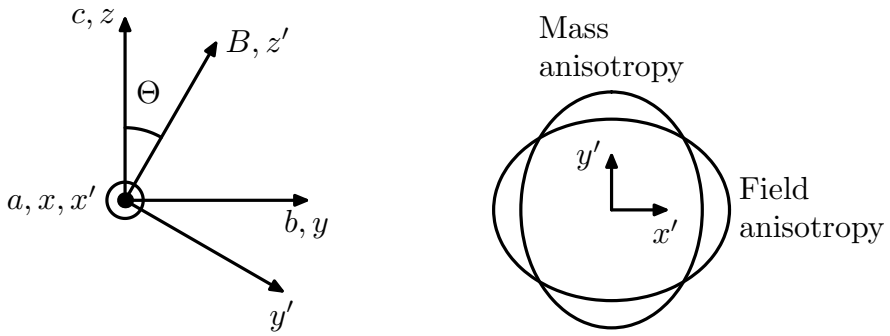

Fig. 1.4: Left: frames of reference: initially the crystal frame (a, b, c) and the vortex frame (x, y, z) coincide; this is the "diagonal case". The primed frame (x', y', z') is the vortex frame after rotation by Θ about the crystal a-axis. Right: relationship between the anisotropy in effective mass and field in the plane perpendicular to the vortex.

Effects subtler than than those described above arise when the magnetic field is applied along an arbitrary direction because the effective-mass tensor is no longer diagonal in the vortex frame. Firstly, there is a preference for the vortex lattice to align such that the nearest-neighbour direction corresponds to the direction perpendicular to the

axis of rotation, which also corresponds to the direction of shortest magnetic penetration length in the plane perpendicular to the vortex direction (Campbell *et al.*, 1988). Clearly, no such alignment occurs in the isotropic case; nor does it in the anisotropic case when the mass tensor is diagonal in the vortex frame. It might be thought that in the latter case the vortices *would* have their nearest-neighbour direction along the direction of shortest penetration depth: the rapid spatial variations along this direction would be facilitated by currents going along an "easy" direction of little kinetic energy cost. However, a scale transformation maps a diagonal anisotropic system back to an orientationally degenerate isotropic system and so no orientation should be preferred. The difference between diagonal and non-diagonal vortex directions in an anisotropic superconductor can be accounted for by the coupling of supercurrent density along different crystallographic directions.

The second effect of applying a field at an arbitrary direction in the crystal frame is that field components, $\mathbf{B}_{G_{x,y}}$, transverse to the vortex axis may be induced (Thiemann *et al.*, 1989). Naturally, the average of these components over a unit cell must be zero to satisfy flux quantisation. In a simple-minded picture of a uniaxial system these components are generated because the supercurrents will not flow in the plane perpendicular to the vortex, but will be tilted towards the easy plane. Indeed, Campbell *et al.* (1988) have shown that when $m_c \gg m_{a,b}$ in a uniaxial system, the magnetisation currents are almost exclusively confined to the basal plane for all orientations of applied field except when it is close to perpendicular to the c-axis.

In general, both these effects may be deduced by minimising the free energy, which assumes the same form as the isotropic case (equation 2.8). The Fourier components are obtained by a similar method as the isotropic case, but the resulting tensor expression, which defines $\mathbf{B_G}$ implicitly, is in general somewhat more complicated:

$$B_{\mathbf{G},i} - \lambda^2 \epsilon_{isl} G_s m_{lk} \epsilon_{ktj} G_t B_{\mathbf{G},j} = \langle B \rangle \hat{l}_i. \tag{3.5}$$

Here the components of the effective-mass tensor are given by m_{lk}, $\hat{l}_i$ are the components of the unit vector parallel to the vortices; $\langle B \rangle$ is the induction averaged over one unit cell; and ϵ_{ijk} is the fully-antisymmetric (Levi-Civita) tensor.

Burlachkov (1989) has calculated the free energy density corresponding to the

Fourier coefficients of equation 3.5. He found:

$$\mathcal{F} = \frac{\langle B \rangle^2}{2\mu_0} \sum_{\mathbf{G}} \left\{ 1 + \lambda_{\mathrm{L}}^2 [\mathbf{G} \times \hat{\mathbf{l}}] \cdot \boldsymbol{\mathcal{M}} \cdot [\mathbf{G} \times \hat{\mathbf{l}}] - \frac{\lambda_{\mathrm{L}}^4 G^2 \left([\mathbf{G} \times \hat{\mathbf{l}}] \cdot \boldsymbol{\mathcal{M}} \cdot \hat{\mathbf{l}} \right)^2}{\left(1 + \lambda_{\mathrm{L}}^2 G^2 [\hat{\mathbf{l}} \cdot \boldsymbol{\mathcal{M}} \cdot \hat{\mathbf{l}}] \right)} \right\}^{-1}, \quad (3.6)$$

where $\hat{\mathbf{l}}$ is the unit vector specifying the vortex direction. The vortex lattice structure in an anisotropic system may be determined by minimising equation 3.6. Naturally, a cut-off is required to prevent divergence due to the singular vortex cores. It might be thought that an anisotropic version of the Gaussian cut-off proposed in section 2 that takes into account the effective mass in the plane perpendicular to the vortices would be appropriate. However, Kogan (1981) has pointed out that such a cut-off constitutes an attempt to correct the London model in a regime where it is no longer valid. In this respect, it is important to bear in mind the limitations of London theory and not to treat large-wavevector cut-offs as a panacea. Many dubious conclusions have been reached due to the misappropriation of cut-offs. For example, Sardella & Moore (1993) mention that tilt-wave instabilities can be induced in the vortex lattice by unphysical cut-offs. (See section 20 for another example.)

4. Ginzburg-Landau theory

Like the London equations, the Ginzburg-Landau equations are phenomenological. However, unlike the former, which are based on a classical electrodynamic description of superconductivity, the latter are derived from a proper *thermodynamic* theory of the superconducting state. Furthermore, due to the judicious choice of order parameter, Ginzburg-Landau theory contains many of the quantum-mechanical aspects of superconductivity that are either ignored in the classical derivation of London theory or, from a quantum mechanical view of London theory, lost in making the approximation that the superconducting state is perfectly rigid. The inherently quantum-mechanical nature of the Ginzburg-Landau equations yield great dividends such as the prediction of the vortex state (see section 5), which can only be incorporated into London theory by hand. For these reasons Ginzburg-Landau theory is more complete and in some senses superior to London theory. However, Ginzburg-Landau theory in its simplest form is only valid quite close to T_{c}. At low temperatures it is often easier to use the

London equations (assuming they are valid in the regime under consideration) perhaps with corretions to handle small perturbations to the superconducting wavefunction (see section 7). Nevertheless, Ginzburg-Landau theory remains a useful tool, particularly in studying unconventional vortex structures (section 8), where the full microscopic description is often unwieldy.

Ginzburg-Landau theory is based on the more general Landau theory of second-order phase transitions, a basic tenet of which is the concept of the order parameter: a quantity whose value is zero above the transition temperature, T_c, and non-zero below it. Landau theory has been brought to bear on a plethora of different phase transitions. In each case the procedure is first to select an appropriate mathematical object (*e.g.* scalar function) to play the role of the order parameter and then to expand the free energy in terms of this order parameter, ensuring that the symmetry of the system with respect to the order parameter is obeyed. In the case of superconductivity, the order parameter is chosen to be a complex function of position, $\psi(\mathbf{r})$, in analogy with a quantum-mechanical wave function. The function $n = |\psi(\mathbf{r})|^2$ can then be interpreted as the number density of particles (Cooper pairs — see section 6) in the superfluid. The free energy density expansion to quartic order for a uniform superconductor in zero applied field is given by

$$\mathcal{F}(T, |\psi|) = \mathcal{F}_0(T) + \alpha(T)\,|\psi|^2 + \frac{\beta(T)}{2}\,|\psi|^4 + \cdots, \tag{4.1}$$

where $\mathcal{F}_0(T)$ is the free energy density of the normal state. This form is chosen to give the correct spontaneous-symmetry-breaking behaviour at T_c and complies with the criteria that the free energy should be invariant with respect to the phase of the order parameter and that it should be an analytic function of the order parameter. The coefficients of the second two terms, $\alpha(T)$ and $\beta(T)$, are chosen such that the free energy is minimum for $|\psi| = 0$ above T_c and $|\psi| > 0$ below T_c, as shown in figure 1.5. This is accomplished if $\alpha(T) \propto (T - T_c)$ and $\beta(T)$ is a constant, whereby minimising the free energy with respect to $|\psi|$ below T_c yields*:

$$|\psi|^2(T) = -\frac{\alpha(T)}{\beta(T)}. \tag{4.2}$$

* The complex nature of the order parameter is ignored here since the phase is only important when discussing non-uniform superconductivity.

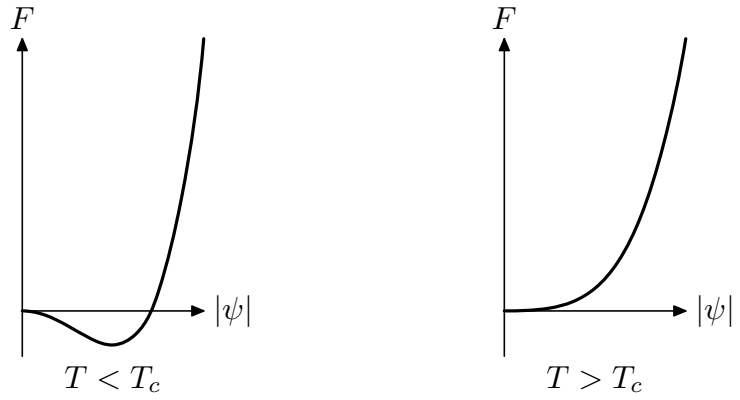

Fig. 1.5: Free energy as a function of $|\psi|$ below (left) and above (right) T_c. For the definitions of α and β in the text the free energy is minimum for $|\psi| = 0$ above T_c, but is minimum at $|\psi| > 0$ below T_c.

When studying the behaviour of superconductors under the influence of an applied field two modifications need to be made to equation 4.1: firstly, the field energy density needs to be added and secondly, a gradient term needs to be added to allow for non-uniformity (as is the case in the vortex state). The gradient operator selected is analogous to the momentum operator in quantum mechanics. The gauge-invariant form of this operator, $(\nabla - \frac{2ie}{\hbar}\mathbf{A})$, is chosen to take into account the effect of an applied field. The factor of 2 in the term containing the vector potential is consistent with the charge carriers being the paired electrons (Cooper pairs) predicted by BCS theory (section 6). Inserting these two terms into the free energy density gives:

$$\mathcal{F}(T) = \mathcal{F}_0(T) + \alpha(T)\left|\psi\right|^2 + \frac{\beta(T)}{2}\left|\psi\right|^4 + \frac{\hbar^2}{2m}\left|\left(\nabla - \frac{2ie}{\hbar}\mathbf{A}\right)\psi\right|^2 + \frac{1}{2\mu_0}B^2, \qquad (4.3)$$

where m is the mass of a Cooper pair. The free energy is given by the functional:

$$F\left[\psi(\mathbf{r}), \psi^*(\mathbf{r}), \nabla\psi(\mathbf{r}), \nabla\psi^*(\mathbf{r}), \mathbf{A}(\mathbf{r})\right] = \int \mathcal{F}(T)\mathrm{d}^3r, \qquad (4.4)$$

which can be minimised using the Euler-Lagrange technique with respect to ψ (and its complex conjugate) and $\mathbf{A}$ to give the Ginzburg-Landau equations:

$$-\frac{\hbar^2}{2m}\left[\nabla - \frac{2ie}{\hbar}\mathbf{A}\right]^2\psi + \alpha\psi + \beta\left|\psi\right|^2\psi = 0, \qquad (4.5)$$

$$\nabla \times \mathbf{B} = \mu_0\mathbf{J} \quad \text{where} \quad \mathbf{J} = \frac{ie}{m}\left(\psi\nabla\psi^* - \psi^*\nabla\psi\right) - \frac{2e^2}{m}\left|\psi\right|^2\mathbf{A}. \qquad (4.6)$$

Equation 4.5 is reminiscent of the time-independent Schrödinger equation, but contains an extra non-linear term, $\beta|\psi|^2\psi$, which tends to favour solutions with uniform $|\psi|$ (Tinkham, 1996). Equation 4.6 is identical to Ampère's law with the corresponding current density being of a quantum-mechanical nature. Therefore these equations demonstrate that although Ginzburg-Landau theory is based on the theory of phase transitions and is hence under the remit of thermodynamics, the quantum nature of the superconducting state is built in by the choice of the order parameter and form of the free energy density.

Two length scales arise naturally out of equations 4.5 and 4.6. The first of these has its origin in equation 4.5 and is known as the coherence length:

$$\xi_{\mathrm{GL}}(T) = \sqrt{\frac{\hbar^2}{2m|\alpha|(T)}}. \tag{4.7}$$

The coherence length is the length scale over which the order parameter varies when subjected to a perturbation. It can be formally related to H_{c2} by linearising equation 4.5 and solving for the lowest Landau level, giving

$$H_{\mathrm{c2}}(T) = \frac{\Phi_0}{2\pi\xi^2_{\mathrm{GL}}(T)}. \tag{4.8}$$

This expression may be appreciated more intuitively by regarding H_{c2} as being set by the flux density at which the closest possible vortex spacing, *i.e.* $\approx \xi$, is realised.

The second length scale is the penetration depth, which is defined in analogy with the London penetration depth equation 2.3 and arises from equation 4.6:

$$\lambda_{\mathrm{GL}}(T) = \sqrt{\frac{m}{4\mu_0 e^2 n(T)}} \quad \text{where} \quad n(T) = |\psi|^2(T) = \frac{-\alpha(T)}{\beta}. \tag{4.9}$$

The relative size of the coherence length and penetration depth dictates to which type a given superconductor belongs. Since both length scales diverge as $(T - T_{\mathrm{c}})^{-1/2}$ at T_{c}, their ratio is a temperature-independent parameter:

$$\kappa = \frac{\lambda}{\xi}. \tag{4.10}$$

The demarcation between type-I and type-II behaviour occurs at $\kappa = 1/\sqrt{2}$, with larger values of κ leading to type-II behaviour and smaller values giving type-I behaviour.

5. The Abrikosov vortex lattice

Abrikosov's seminal 1957 paper (Abrikosov, 1957) provided the first successful interpretation of the Ginzburg-Landau equations in the type-II limit ($\kappa > 1/\sqrt{2}$). This solution was realised by solving the Ginzburg-Landau equations perturbatively. Firstly, he took the solution to the linearised version of equation 4.5, which had already been discovered in the original Ginzburg-Landau paper (Ginzburg & Landau, 1950) in the context of evaluating H_{c2}. This solution is obtained in the gauge $\mathbf{A} = B_0 x\hat{\mathbf{y}}$ (correspoding to a uniform magnetic field along the z-axis; this is in the London gauge). For mathematical expediency, the units are normalised such that lengths are measured in terms of the penetration depth, λ_{GL}; the magnetic field is in units of $\sqrt{2}B_c$; and the order parameter is measured relative to the bulk value at zero temperature so that near T_{c}, $\psi \ll 1$. The resulting linearisation of equation 4.5 gives rise to a differential equation whose solution is written most generally as:

$$\psi(x,y) = \sum_{n=-\infty}^{\infty} C_n \psi_n(x,y)$$

$$\psi_n(x,y) = \exp(\mathrm{i}kny) \exp\left[-\frac{\kappa^2}{2}\left(x - \frac{kn}{\kappa^2}\right)^2\right], \tag{5.1}$$

where C_n and k are arbitrary constants, but will be determined later by the perturbation solution. This solution is valid only very close to $H_{c2}(T)$ where $\psi \ll 1$. The amount by which the nascent superconductivity reduces the magnetic field within the bulk of the superconductor is determined by substituting equation 5.1 into the second Ginzburg-Landau equation (4.6):

$$B = B_0 - \frac{|\psi|^2}{2\kappa} \quad \Longleftrightarrow \quad A = B_0 x - \frac{1}{2\kappa}\int |\psi|^2 \mathrm{d}x. \tag{5.2}$$

The perturbation solution for ψ now proceeds by substituting equation 5.2 into the first Ginzburg-Landau equation (4.5) — complete with the non-linear term — to calculate the small first-order corrections to the ψ_n terms in equation 5.1. The resulting solution ψ can still be represented by equation 5.1, but in order to minimise the free energy, the coefficients C_n and k are constrained to minimise the famous Abrikosov parameter, β_{A}, given by:

$$\beta_{\mathrm{A}} = \frac{\langle|\psi|^4\rangle}{\langle|\psi|^2\rangle^2}. \tag{5.3}$$

Furthermore, in order to get a periodic solution for ψ a recurrence relation is expected between the coefficients C_n:

$$C_{n+N} = C_n. \tag{5.4}$$

Due to a numerical error in evaluating β_{A} for the triangular lattice, Abrikosov found that the square vortex lattice ($N = 1$) had the lowest free energy corresponding to $\beta_{\mathrm{A}} = 1.18$. However, it was later discovered that the triangular lattice ($N = 2$ and $C_1 = \mathrm{i}C_0$) is more favourable since in this case $\beta_{\mathrm{A}} = 1.16$. That there is so little difference in β_{A} for these two configurations evinces the fact that only very small higher-order terms in the free energy can give a propensity for an unconventional vortex lattice; indeed triangular Abrikosov-like vortex lattices are in practice rarely observed!

It is of interest to calculate from the Ginzburg-Landau theory the Fourier components of the internal field distribution as these are related to the neutron scattering amplitude (see section 11). H. Brandt has performed these calculations (Brandt, 1995) in the regime $B > 0.5B_{\mathrm{c2}}$ for an arbitrary arrangement of vortices, parameterised by the set of reciprocal lattice vectors $\mathbf{G}_{mn} = (2\pi/x_1y_2)(my_2, -mx_2 + nx_1)$. (The real-space vortex lattice has basis vectors $(x_1, 0)$ and (x_2, y_2).) He found:

$$|\psi(\mathbf{r})|^2 = \frac{1 - \langle B\rangle/B_{\mathrm{c2}}}{[1 - 1/(2\kappa^2)]\beta_{\mathrm{A}}} \sum_{\mathbf{G}} a_{\mathbf{G}} \cos(\mathbf{G}\cdot\mathbf{r})$$

$$B(\mathbf{r}) = B_0 - (\Phi_0/4\pi\lambda^2)|\psi(\mathbf{r})|^2. \tag{5.5}$$

The Fourier coefficients $a_{\mathbf{G}}$ are given by

$$a_{\mathbf{G}} = (-1)^{m+mn+n} \exp(-G_{mn}^2 x_1 y_2/8\pi). \tag{5.6}$$

The solution presented in equation 5.5 is plotted in figure 1.6 with the same value of the coherence length ($\xi = 0.02$) as in figure 1.2 and in the same dimensionless units. The value of $\langle B\rangle = 300$ is chosen such that the criterion $0.5B_{\mathrm{c2}} < B < B_{\mathrm{c2}}$ is satisfied.

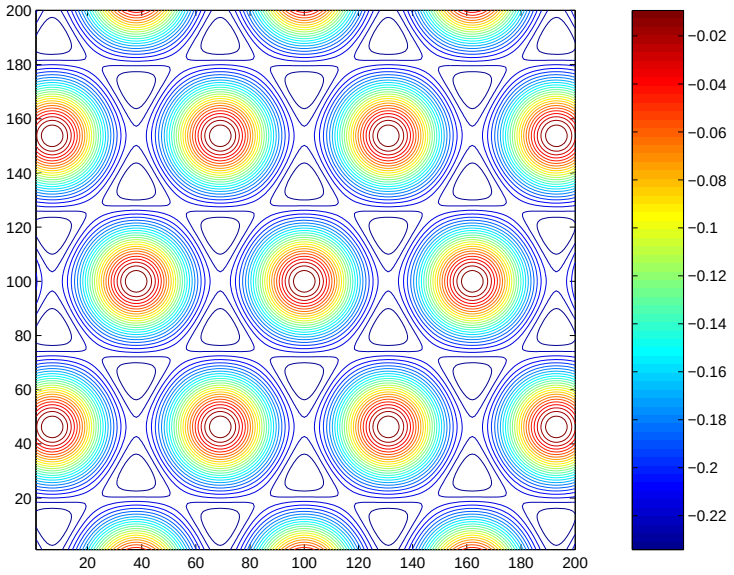

Fig. 1.6: Numerical calculation of the local magnetisation given by Brandt's solution (1995) of the Ginzburg-Landau equations. The calculation is evaluated in dimensionless units such that $\Phi_0 = 1$ and lengths are measured relative to the penetration depth. In these normalised units $B = 300$, corresponding to an inter-vortex spacing of roughly 0.06λ, and $\xi = 0.02$ ($\kappa = 50$ and $B/B_{c2} \approx 0.75$). The figure is $0.2\lambda \times 0.2\lambda$ in size.

6. An outline of microscopic theory

Various techniques have been developed to tackle problems in vortex physics from first principles. These are derived from the quantum- and statistical-mechanical behaviour of strongly interacting electrons which, in some materials at least, can form Cooper pairs and become superfluid. There is an obvious inherent difficulty with such a complete description of the superconducting state and this is reflected by the fact that microscopic theory has yet to supplant in practice the more tractable and more intuitive phenomenological theories. In most cases, the solution of a microscopic model of the vortex lattice must be done numerically and therefore does not lend itself easily to a simple physical interpretation. In this section, the essentials of some of these microscopic techniques are sketched. As this is a highly specialised field, no attempt here is made to solve any of these problems; an interested reader should consult some of the references presented in sections 8 and 24 or the book by Kopnin (2001) for more details.

The first successful microscopic assault on the problem of superconductivity was achieved by the ground-breaking work of Bardeen, Cooper and Schrieffer (1957). Their work was based upon the solution of an interacting-electron model Hamiltonian:

$$\hat{H} = \sum_{\mathbf{k},\sigma} \left(\frac{\hbar^2 k^2}{2m_e} - \mu \right) \hat{c}^\dagger_{\mathbf{k},\sigma} \hat{c}_{\mathbf{k},\sigma} + \frac{1}{2} \sum_{\substack{\mathbf{k}_1,\sigma_1 \\ \mathbf{k}_2,\sigma_2 \\ \mathbf{q}}} \hat{c}^\dagger_{\mathbf{k}_1+\mathbf{q},\sigma_1} \hat{c}^\dagger_{\mathbf{k}_2-\mathbf{q},\sigma_2} V_{\mathbf{k}_1,\mathbf{k}_2,\mathbf{q}} \hat{c}_{\mathbf{k}_2,\sigma_2} \hat{c}_{\mathbf{k}_1,\sigma_1}, \quad (6.1)$$

where $c_{\mathbf{k},\sigma}$ ($c^\dagger_{\mathbf{k},\sigma}$) annihilates (creates) an electron in momentum state $\mathbf{k}$ with spin σ; μ is the chemical potential; and $V_{\mathbf{k}_1,\mathbf{k}_2,\mathbf{q}}$ is the matrix element of the two-body electron-electron interaction potential that scatters an electron from state $\mathbf{k}_1$ to $\mathbf{k}_1 + \mathbf{q}$ and (to conserve momentum) another electron from state $\mathbf{k}_2$ to $\mathbf{k}_2 - \mathbf{q}$. A prerequisite for superconductivity is that the latter term gives rise to an attractive interaction, which in standard phonon-mediated superconductivity is due to "overscreening" by the ionic cores of the normally repulsive Coulomb interaction (Waldram, 1996).

Bardeen, Cooper and Schrieffer (BCS) found an approximate solution for the ground state of equation 6.1 consisting of an ensemble of phase-coherent opposite-spin electron pairs each with the same pair momentum, $\mathbf{s}$:

$$|\mathrm{BCS}\rangle = \prod_{\mathbf{k}} \left(u_{\mathbf{k}} + \exp(\mathrm{i}\theta) v_{\mathbf{k}} \hat{c}^\dagger_{\mathbf{k}+\mathbf{s},\downarrow} \hat{c}^\dagger_{-\mathbf{k}+\mathbf{s},\uparrow} \right) |0\rangle, \quad (6.2)$$

where θ is the phase of the superfluid and the wavefunctions, $v_{\mathbf{k}}$ and $u_{\mathbf{k}}$, obey the normalisation condition $u^2_{\mathbf{k}} + v^2_{\mathbf{k}} = 1$. When $u_{\mathbf{k}} = 0$ for $|\mathbf{k}| < k_\mathrm{F}$ this wavefunction just gives a filled Fermi sea*, but when $u_{\mathbf{k}} \neq 0$ for $|\mathbf{k}| < k_\mathrm{F}$ the electron and hole states become mixed and the occupation becomes more diffuse near the Fermi surface. This is a characteristic property of the paired electrons in the BCS theory.

Despite being only an approximation, the wavefunction in equation 6.2 is very successful in predicting the qualitative properties of the superconducting state. For example, the superconducting gap, $\Delta_{\mathbf{k}}$, emerges naturally when computing the energy, $E_{\mathbf{k}}$, required to make a single particle excitation in the superfluid:

$$E_{\mathbf{k}} = \sqrt{\left(\frac{\hbar^2 k^2}{2m_e} - \mu \right)^2 + \Delta^2_{\mathbf{k}}}. \quad (6.3)$$

* The precise condition on $u_{\mathbf{k}}$ and $v_{\mathbf{k}}$ for a filled Fermi sea is: $u_{\mathbf{k}} = 0$ and $v_{\mathbf{k}} = 1$ for $|\mathbf{k}| < k_\mathrm{F}$, and $u_{\mathbf{k}} = 1$ and $v_{\mathbf{k}} = 0$ for $|\mathbf{k}| > k_\mathrm{F}$.

It turns out that these excitations are neither exactly electron-like nor exactly hole-like. Their nature depends on exactly where in **k**-space (*i.e.* the values of $u_{\mathbf{k}}$ and $v_{\mathbf{k}}$) they are created, according to the "Bogoliubov" creation and annihilation operators for the excitations:

$$\begin{aligned}\hat{\gamma}^{\dagger}_{\mathbf{k},\downarrow} &= u_{\mathbf{k}}\hat{c}^{\dagger}_{\mathbf{k},\downarrow} - \exp(-\mathrm{i}\theta)v_{\mathbf{k}}\hat{c}_{-\mathbf{k},\uparrow} \\ \hat{\gamma}_{\mathbf{k},\downarrow} &= u_{\mathbf{k}}\hat{c}_{\mathbf{k},\downarrow} - \exp(+\mathrm{i}\theta)v_{\mathbf{k}}\hat{c}^{\dagger}_{-\mathbf{k},\uparrow}.\end{aligned} \tag{6.4}$$

The BCS formulation of the superconducting state presented so far makes no account for cases where superconductivity is non-uniform. Fortunately, it is possible to generalise the formalism above and bring the tools of microscopic theory to bear on the vortex lattice. In a fairly straightforward generalisation, the Bogoliubov operators (equation 6.4) can be extended to take into account spatial variations (Waldrum, 1996):

$$\begin{aligned}\hat{\gamma}^{\dagger}_{n,\downarrow} &= \int \left[u^{*}_{n}(\mathbf{r})\hat{\psi}^{\dagger}_{\downarrow}(\mathbf{r}) - v^{*}_{n}(\mathbf{r})\hat{\psi}^{\dagger}_{\uparrow}(\mathbf{r})\right] \mathrm{d}^3 r \\ \hat{\gamma}_{n,\downarrow} &= \int \left[u_{n}(\mathbf{r})\hat{\psi}_{\downarrow}(\mathbf{r}) - v_{n}(\mathbf{r})\hat{\psi}^{\dagger}_{\uparrow}(\mathbf{r})\right] \mathrm{d}^3 r,\end{aligned} \tag{6.5}$$

where the operators $\hat{\psi}^{\dagger}_{\sigma}(\mathbf{r})$ and $\hat{\psi}_{\sigma}(\mathbf{r})$ respectively create and destroy an electron with spin σ at position $\mathbf{r}$ and are the Fourier transforms of the number-representation operators $c^{\dagger}_{\mathbf{k},\sigma}$ and $c_{\mathbf{k},\sigma}$. The quasi-particle states created/destroyed by $\hat{\gamma}^{\dagger}_{n,\downarrow}$ and $\hat{\gamma}_{n,\downarrow}$ are labelled using the index n.

As a natural consequence of the position-dependent creation and annihilation of quasi particles using the operators above, the superconducting gap is no longer uniform, but is instead a function of position related to the following expectation value:

$$\Delta(\mathbf{r}) \propto \langle\hat{\psi}_{\downarrow}(\mathbf{r})\hat{\psi}_{\uparrow}(\mathbf{r})\rangle. \tag{6.6}$$

This muddies the interpretation of Δ as the magnitude of the superconducting energy gap, but equation 6.6 provides other physical insights. Firstly $\Delta(\mathbf{r})$ may be interpreted as a local field in the spirit of mean field theory and can therefore be related to the complex order parameter, $\psi(\mathbf{r})$, of the Ginzburg-Landau theory. Furthermore, the form of equation 6.6 suggests that correlations between spin-up and spin-down electrons is important for superconductivity, which is a well-known property of the phenomenon.

The most important feature of a position-dependent gap function is that it gives a handle on solving non-uniform problems. One such method is via the Bogoliubov-de

Gennes equations (Ketterson & Song, 1999), which are a set of eigenvalue equations for the hole and particle wavefunctions $u_n(\mathbf{r})$ and $v_n(\mathbf{r})$ which are coupled by $\Delta(\mathbf{r})$:

$$\begin{aligned}(\hat{H}-\mu)u_n(\mathbf{r})+\Delta^*(\mathbf{r})v_n(\mathbf{r}) &= E_n u_n(\mathbf{r}) \\ -(\hat{H}-\mu)v_n(\mathbf{r})+\Delta(\mathbf{r})u_n(\mathbf{r}) &= E_n v_n(\mathbf{r}).\end{aligned} \tag{6.7}$$

Solution of these equations is in general a difficult task except for the simple case of uniform superconductivity (*i.e.* constant Δ) in which case $u_n(\mathbf{r})$ and $v_n(\mathbf{r})$ assume plane-wave forms (Waldram, 1996). However, since superconductors quite generally have much larger coherence lengths than Fermi wavelengths (quasi-particle wavelength) a quasi-classical approximation in often used (Kopnin, 2001). In this approximation the momentum dependence of the pairing potential is treated separately to the variation of order parameter in the solutions for $u_n(\mathbf{r})$ and $v_n(\mathbf{r})$. The validity of the approximation depends on the smallness of the ratio Δ/E_F. For low-T_c materials this is well obeyed ($\Delta/E_\mathrm{F} \sim 10^{-3}$), but in high-$T_\mathrm{c}$ materials, which have large gaps, the approximation is less good.

Green's functions are another powerful tool for microscopic investigations of the vortex lattice. Here too, great simplifications are made assuming a quasi-classical picture. Eilenberger (1968) applied this approximation to the Green's functions of BCS theory, which were derived by Gor'kov (1958). Like the Bogoliubov-de Gennes equations, Eilenberger's theory has found extensive application in the field of unconventional superconductivity (see sections 7 and 8).

7. Non-local London theory

Common to both the London and Ginzburg-Landau theories of the vortex lattice is the *local* nature of the electrodynamics, *i.e.* the local relationship between the current and vector potential of the form $\mathbf{J}(\mathbf{r}) \propto \mathbf{A}(\mathbf{r})$. However, in reality a non-local relation between $\mathbf{J}(\mathbf{r})$ and $\mathbf{A}(\mathbf{r})$ is expected because when the superfluid is subjected to a perturbation (*e.g.* in the vicinity of a vortex) its response will be spread out over a distance equal to the coherence length. The size of the coherence length relative to the electrodynamic length scale (*i.e.* the penetration depth) is what determines the importance of non-local effects in a given superconductor. Thus non-locality is more pronounced in materials with low values of κ, but, conversely, non-locality is less of an

issue in high κ materials. In the high-κ regime non-locality may be neglected because the superfluid wavefunction is rigid with respect to perturbations and London theory may be applied. (In the extreme type-II limit ($\kappa \to \infty$) this approximation becomes exact.) However, at high inductions where the vortices come into close proximity and the perturbations are large, non-local corrections are required for a satisfactory explanation of the properties of the vortex lattice. In this section the impact on the vortex lattice of the non-local corrections to the London theory is considered.

The non-local relationship between current and vector potential in an isotropic superconductor may be written in terms of a convolution of a spatially-invariant kernel, $K(\mathbf{r}-\mathbf{r}')$:

$$\mathbf{J}(\mathbf{r}) \propto \int K(\mathbf{r}-\mathbf{r}')\mathbf{A}(\mathbf{r}')\mathrm{d}^3\mathbf{r}'. \tag{7.1}$$

This non-local relation complicates matters considerably compared to the simple London expression. However, for many superconductors κ is sufficiently large that only the first non-local correction to the London theory is required. In this case the kernel, $K(\mathbf{r}-\mathbf{r}')$, is expected to be sharply peaked about $\mathbf{r}=\mathbf{r}'$ allowing significant simplification of equation 7.1. Since $K(\mathbf{r}-\mathbf{r}')$ is sharply peaked it may be Taylor expanded about $G=0$ in reciprocal space, giving to leading order:

$$\mathbf{J}(\mathbf{G}) = K(\mathbf{G})\mathbf{A}(\mathbf{G}) \approx \left[1+\epsilon G^2\right]\mathbf{A}(\mathbf{G}). \tag{7.2}$$

(Note that there is no term in G due to the symmetry of the kernel.) In real space such an expansion corresponds to the inclusion of gradient terms, such that $\mathbf{J}(\mathbf{r}) \propto \mathbf{A}(\mathbf{r}) + \epsilon\nabla^2\mathbf{A}(\mathbf{r}) + \cdots$.

From the point of view of the vortex lattice, the non-local term in equation 7.2 simply modifies the form of the lattice in the vicinity of each vortex core. Of greater interest is the effect of non-locality when there is an underlying electronic anistropy. The obvious heuristic generalisation of the G^2 term in equation 7.2 involves the contraction of a fourth-rank tensor with $\mathbf{G}$ (twice) and the vector potential. In reciprocal space this may be written:

$$\mu_0 j_i = -\lambda^{-2}(m_{ij}^{-1} - \lambda^2 n_{ijlm}G_lG_m)a_j, \tag{7.3}$$

where m_{ij}^{-1} is the inverse-effective-mass tensor; λ is the penetration depth calculated from the geometric-mean mass, *i.e.* $(\lambda_a\lambda_b\lambda_c)^{1/3}$; and the singularities at the vortex

cores are removed by defining a new vector potential $\mathbf{a} = \mathbf{A} + \Phi_0 \nabla\phi/2\pi$. Kogan *et al.* (1996) have justified this form via the quasi-classical Eilenberger equations enabling, in principle, the calculation of the tensor n_{ijlm} in terms of purely microscopic parameters, in particular the fourth moment of the Fermi velocity:

$$n_{ijlm} = \frac{\hbar^2 \langle v_i v_j v_l v_m \rangle \gamma(T,\tau)}{4\Delta_0^2 \lambda^2 \det\langle v_i v_j \rangle^{1/3}}, \tag{7.4}$$

where v_i is the ith component of the Fermi velocity and Δ_0 is the magnitude of the superconducting gap at zero temperature. The constant of proportionality, $\gamma(T,\tau)$, depends on scattering and is proportional to Δ_0^2 (see Kogan *et al.* (1996) for details).

To obtain the form of the vortex lattice arising from the transport equation 7.3, the Fourier coefficients of the field distribution need to be calculated. This is achieved in the same fashion as for the local London theory. The vortex source terms are re-inserted via the flux-quantisation condition, which is given by $\mathbf{B} = \nabla \times \mathbf{a} + \Phi_0 \sum_i \delta(\mathbf{r} - \mathbf{r}_i)\hat{\mathbf{z}}$ for vortices directed along the z-axis, giving rise to the expression:

$$B_r + \mu_0 \lambda^2 \epsilon_{rsj} G_s K_{ij}^{-1}(\mathbf{G}) \epsilon_{imn} G_m B_n = \Phi_0 \hat{z}_r. \tag{7.5}$$

Assuming the non-locality is small, the inverted kernel $K_{ij}^{-1}(\mathbf{G})$ may be approximated by the Taylor expansion:

$$K_{ij}^{-1}(\mathbf{G}) \approx m_{ij} - \lambda^2 m_{ir} m_{sj} n_{rsmn} G_m G_n. \tag{7.6}$$

The configuration actually adopted by the vortex lattice within this theory may be determined by the minimisation of the free energy density given by equation 2.8, which requires solving equation 7.5 for $\mathbf{B}_\mathbf{G}$. Unlike the local London free energy, the non-local free energy is convergent by virtue of the non-local correction term, which gives rise to Fourier components that vary as G^{-4} at large G. Nonetheless, despite the inclusion of the leading-order non-local correction, equation 7.5 is only a good approximation for $G < \xi^{-1}$ and hence the reciprocal sum must be ameliorated by some kind of cut-off for the same reason the local theory is.

The principal effect the non-local corrections have is to couple the vortex lattice to the underlying electronic anisotropy in a way that cannot be "scaled away" *even* when the vortices lie along a crystal axis. To illustrate this point consider the vortex

lattice in a tetragonal superconductor (which symmetry dictates that $\lambda_a = \lambda = \lambda_b$) such that the vortices lie along the c-axis. Solving equation 7.5 in terms of $\mathbf{B_G}$ in this high-symmetry situation gives (Kogan, 1997):

$$\mathcal{F} = \frac{\langle B \rangle^2}{2\mu_0} \sum_{\mathbf{G}} \frac{1}{1 + \lambda^2 G^2 + \lambda^4 \left[n_2 G^4 + (2n_1 - 6n_2) G_1^2 G_2^2 \right]}, \tag{7.7}$$

where $n_1 \propto \langle v_1^4 \rangle \equiv \langle v_2^4 \rangle$ and $n_2 \propto \langle v_1^2 v_2^2 \rangle$. The term containing $G_1^2 G_2^2$ in this expression is responsible for anisotropy. At high fields this term favours a square vortex lattice oriented such that the nearest-neighbour direction corresponds to that of the Fermi velocity minima.

8. The vortex lattice in a d-wave superconductor

In an isotropic s-wave superconductor, the attractive electron-electron interaction, $V_{\mathbf{kk'}}$, is isotropic and results in a superconducting gap, $\Delta_{\mathbf{k}}$, that is uniform over the Fermi surface. Most materials have far from spherical Fermi surfaces so the magnitude of the superconducting gap is modulated due to the variation of the density of states over the Fermi surface. This gives rise to the effects described in the previous section, but in many superconductors the gap itself exhibits a large degree of intrinsic anisotropy. Indeed, there is good evidence for the existence of both p-wave and d-wave superconductivity. These have an unconventional pairing symmetry entirely different to s-wave. Rather than being isotropic and fully gapped, p- and d-wave pairing gives rise to nodes at certain points of the Fermi surface. These nodes radically alter the superconducting properties because quasi particles may be excited along these directions even well below T_c. In this section, the implications of d-wave pairing* on the superconducting state is briefly discussed and a survey of various theoretical studies of d-wave vortices and vortex lattices is presented.

* Since the cuprate high-T_c superconductors, including the subject of this thesis ($YBa_2Cu_3O_7$), are most likely d-wave, only pairing through this channel is discussed here. Pairing is also possible through the p-wave channel (for example in Sr_2RuO_4) in which electrons are paired in a triplet state to satisfy the fermion antisymmetry of the pair wavefunction.

Although the exact mechanism of superconductivity in the cuprates is still the subject of controversy, the symmetry of the crystal* imposes constraints on the pairing potential and hence also on the gap function. In fact a whole class of different gap functions compatible with the crystal symmetry are possible. These may be determined by expanding $\Delta_{\mathbf{k}}$ in terms of the basis functions that represent the crystal symmetry (Tsuei & Kirtley, 2000a). For a cuprate material one such gap "wavefunction" is given by:

$$\Delta_{\mathbf{k}}^{d_{x^2-y^2}} = \Delta_0(\cos k_x - \cos k_y) + \dots \ . \tag{8.1}$$

This is known as the $d_{x^2-y^2}$ gap function (since it has the same symmetry as the basis function x^2-y^2) and it is apparent that it is compatible with the C_{4v} point symmetry of the CuO_2 planes which are ostensibly responsible for superconductivity in the cuprates. Equation 8.1 is plotted in figure 1.7. Not only does $\Delta_{\mathbf{k}}^{d_{x^2-y^2}}$ exhibit nodes along the $\{110\}$ directions, but also changes phase by π in going between adjacent lobes. (This property is exploited in measurements of the gap symmetry using tricrystal junctions — see Tsuei & Kirtley (2000a) for more details.)

The presence of nodes in the superconducting gaps of the cuprates turns out to be just as important for the vortex lattice as it does for the other superconducting properties. Since the nodes give the superconducting gap "100%" anisotropy it is expected that their influence will be just as great as other sources of anisotropy, if not more so. Therefore it is vital to include the form of the gap when constructing a theory of the vortex lattice. In the Ginzburg-Landau theory, it boils down to choosing correctly the terms in the free energy expansion. In a bulk d-wave superconductor the expansion should contain higher-order gradient terms like $(\partial_x^2 - \partial_y^2)^2$ in addition to the isotropic terms contained in equation 4.3. The higher-order terms reduce the symmetry of the free energy to four-fold. Moreover, the presence of vortices breaks the translational symmetry of the crystal lattice and in general it is expected that in the vicinity of a vortex core an s-wave component will be induced. This has been

* Other symmetries, such as time reversal and spin symmetry, are also involved. The symmetry of the superconducting state will in general be a subset of the normal state symmetry since there is spontaneous breaking of symmetry at T_c. (In an s-wave superconductor global gauge symmetry is broken at T_c.)

verified by Soninen *et al.* (1994) who examined the structure of a single vortex line in a $d_{x^2-y^2}$ superconductor using the Bogoliubov-de Gennes equations with an attractive pairing interaction operating on nearest-neighbour electrons on a square lattice. The vortex structure determined by this calculation is very rich. They identified three regions: an inner core analagous to that of an s-wave superconductor in which the order parameter is suppressed; an outer core where there is coexistence of s- and d-wave order parameters; and a bulk region where the order parameter relaxes into a pure d-wave state. The outer core region is of greatest interest because the coexistence of the two order parameters bestows anisotropy on the vortex core, which as Soninen *et al.* point out must lead to an angular variation in the inter-vortex interaction. This basic theoretical observation, which has been reported by a number of authors, underpins the natural tendency for d-wave vortices to organise into unconventional lattices.

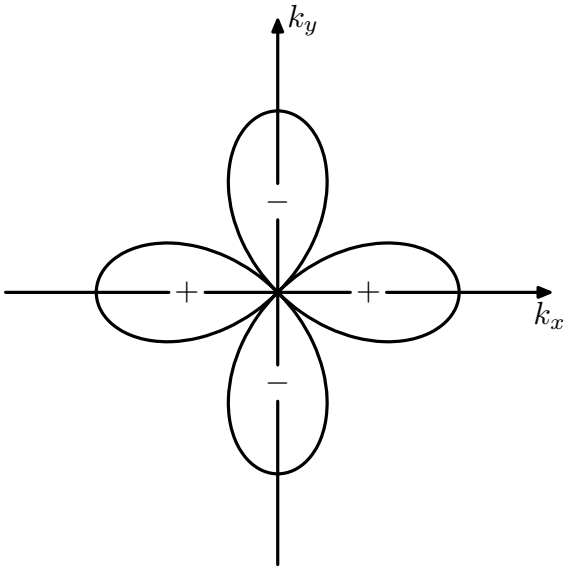

Fig. 1.7: A plot of the $d_{x^2-y^2}$ magnitude of the gap function, $\Delta_{\mathbf{k}}^{d_{x^2-y^2}}$, about the Fermi surface; the phase of each lobe is also indicated. There are nodes along $k_x = k_y$ about which the phase of the gap (order parameter) changes by π.

In their analysis, Soninen *et al.* (1994) also wrote down a Ginzburg-Landau expansion containing the higher-order gradient terms described above. Following their microscopic calculations the free energy expression contains *two* order parameters*, s

* These order parameters naturally have different T_c's. In a d-wave superconductor $T_d > T_s$.

and d:

$$\begin{aligned}\mathcal{F} =& \frac{B^2}{2\mu_0} + \alpha_s|s|^2 + \alpha_d|d|^2 + \beta_1|s|^4 + \beta_2|d|^4 + \beta_3|s|^2|d|^2 \\ &+ \beta_4(s^{*2}d^2 + \text{c.c.}) + \gamma_s\left|\mathbf{\Pi}s\right|^2 + \gamma_d\left|\mathbf{\Pi}d\right|^2 \\ &+ \gamma_\nu\left(\Pi_y s \Pi_y d^* - \Pi_x s \Pi_x d^* + \text{c.c.}\right),\end{aligned} \tag{8.2}$$

where c.c. stands for the complex conjugate of the preceeding term and the operator $\mathbf{\Pi}$ is the gauge-invariant momentum operator (see equation 4.3). The terms with coefficients α_s, α_d, β_1, β_2, γ_s and γ_d are all recognisable as the terms needed for separate expansions of the Ginzburg-Landau free energy in the s- and d-wave order parameters. The other terms provide coupling between the two order parameters. For example, the mixed gradient terms are responsible for generating the s-wave component near a vortex core. Ren *et al.* (1995) derived equation 8.2 from the Gor'kov equations and discovered that the s-wave component decays over a distance comparable with the magnetic penetration depth. Therefore even for moderate inductions ($\xi \ll a_0 \ll \lambda$) the s-wave component persists everywhere in the mixed state.

Berlinksy *et al.* (1995) and Franz *et al.* (1996) have made further analyses of vortices using the Ginzburg-Landau expansion shown in equation 8.2. The topological structure of the s-wave order parameter elucidated by these calculations exhibits a complicated configuration of five vortex cores arranged with one at the vortex centre surrounded by four symmetrically-placed vortices with opposite winding. This is essentially the same anisotropy discussed by Soninen *et al.* (1994) and, perhaps predictably, has the effect of enforcing its four-fold symmetry on the vortex lattice, albeit at distances much further than the extent of the induced s-wave vortices. (In this respect the s-wave vortices are more of a symptom of the unconventional nature of d-wave vortices than a cause of an unconventional vortex lattice.) Berlinsky *et al.* (1995) have minimised the free energy for the vortex lattice using a variety of strengths of the coupling parameter γ_ν. For small values of γ_ν, the standard triangular vortex lattice appears to be preferred, but as γ_ν is increased, the equilibrium vortex lattice becomes at first oblique and then square at some critical value that depends upon the value of the other parameters in equation 8.2. Franz *et al.* (1996) examined the dependence of the square vortex lattice free energy on its orientation relative to the crystal axes. By defining a coordinate system rotated by an angle α relative to the crystal {110}

direction and studying its effect on the mixed gradient term (the only term in equation 8.2 that is not invariant under rotation), they found that the free energy is minimised for $\alpha = 0, \pm\pi/2, \cdots$, *i.e.* the vortex lattice aligns itself along {110}.

Affleck *et al.* (1997) have also studied the vortex lattice using the Ginzburg-Landau free energy expansion shown in equation 8.2. Their approach differs from earlier works. Instead of deriving and solving the Ginzburg-Landau equations arising from equation 8.2, they first simplified the problem by integrating out the s-wave component. This was accomplished by deriving the Ginzburg-Landau equation in s and substituting it back into the free energy expansion, which to leading order gives:

$$\mathcal{F}' = \frac{B^2}{2\mu_0} + \alpha_d|d|^2 + \beta_2|d|^4 + \gamma_\nu \left[|\mathbf{\Pi} d|^2 - \frac{\gamma_\nu^2 \gamma_d}{\gamma_s} \left| (\Pi_x^2 - \Pi_y^2) d \right|^2 \right]. \tag{8.3}$$

In making this approximation structural information on the scale of ξ is lost, but it is not important considering that most investigations of the vortex lattice in high-T_c materials occur well below B_{c2}. With this in mind Affleck *et al.* made the further approximation that the magnitude of the order parameter, d, was constant. Writing the superfluid velocity as $\mathbf{v}(\mathbf{r}) = \nabla\theta(\mathbf{r}) - \frac{2e}{\hbar}\mathbf{A}(\mathbf{r})$ (where $\theta(\mathbf{r})$ is the phase of d) this yields an expression reminiscent of the standard London free energy (equation 2.7), but with higher-order terms in the kinetic energy part:

$$\mathcal{F}_{\mathrm{L}} = \frac{B^2}{2\mu_0} + \gamma_\nu d_0^2 \left\{ v^2 - \frac{\gamma_\nu^2 \gamma_d}{\gamma_s} \left[(v_x^2 - v_y^2)^2 + (\partial_y v_y - \partial_x v_x)^2 \right] \right\}. \tag{8.4}$$

Although this London-like expression does not contain the rich detail of the vortex cores, it is sufficiently accurate to calculate the morphology of the vortex lattice. Minimising the free energy yields the same lattice configuration as the microscopic and pure Ginzburg-Landau studies. The Fourier coefficents within this extended-London model are given by

$$\mathbf{B}(\mathbf{G}) = \langle B \rangle \frac{\exp(-G^2\xi'^2)}{1 + \lambda^2 G^2 + 4\epsilon\lambda^2\xi^2 G_x^2 G_y^2}, \tag{8.5}$$

where $\epsilon = 3\alpha_d\gamma_\nu^2/\alpha_s\gamma_d^2$. The Gaussian term in the numerator of this expression originates in the choice of vortex source term and is purely phenomenological (see section 2). Note the near isomorphism of the terms in equation 8.5 with those from the non-local London theory of a tetragonal superconductor (the terms in the sum of equation 7.7). The close correspondence is no accident. In the standard London and Ginzburg-Landau

equations the electrodynamics are local. Adding the first corrections to the kernel in non-local London theory or higher-order gradient terms in the d-wave Ginzburg-Landau theory both have similar effects, even though the physical basis for each is quite different. Put more intuitively, in the d-wave Ginzburg-Landau theory the order parameter nodes can be thought of as inducing non-locality since along these directions the coherence length is infinite. Therefore, in some systems it may not be possible to discern, based solely on qualitative observations, whether "plain" non-locality or d-wave effects are responsible for unconventional vortex lattices.

The quasi-classical Eilenberger equations have been used extensively to make highly detailed calculations of the nature of d-wave vortices and their lattices. The Eilenberger formulation has the advantage over Ginzburg-Landau because it is valid over the whole (H, T) plane (not just near $H_{c2}(T)$) and because it does not rely on phenomenological expansion coefficients; but it is disadvantaged by the lack of a simple physical picture and the inherent difficulty of the calculations, which mostly require numerical solution. Nevertheless, such calculations have been performed with great success. Ichioka *et al.* (1996a) have undertaken calculations to find out the structure of a vortex in a $d_{x^2-y^2}$ superconductor in which there is finite pairing in the s-wave and d_{xy}-wave channels. Their results give good agreement with the Bogliubov-de Gennes and Ginzburg-Landau models cited above. In another study by the same group (Ichioka *et al.*, 1996b), a single $d_{x^2-y^2}$-wave vortex was investigated in the absence of other induced components. Their results demonstrate the four-fold symmetry of a vortex even without the other components. This is reflected in the local density of quasi-particle states, which at low quasi-particle energy extend along the {110} directions for many coherence lengths. These quasi-particle tails do not feature in s-wave vortices in which the density of quasi-particle states peaks isotropically (*i.e.* as a circle) around an isolated vortex as a function of energy. The effect of these quasi-particle tails on the vortex lattice was worked out by Ichioka *et al.*(1999). When d-wave vortices are packed together close enough, tunnelling between vortex cores of the quasi-particles is enhanced if the vortices are arranged such that the nearest-neighbour direction is along the d-wave order parameter node ({110}). Therefore, there is a term in the free energy that favours a square arrangement of vortices oriented along {110} due to the reduction of

the quasi-particle kinetic energy by tunnelling along this direction. The free energies of square and triangular vortex lattices with nearest-neighbour along either {100} or {110} have been computed at $T = 0.5T_c$ by Ichioka *et al.* (1999) using the Eilenberger formalism with material parameters corresponding closely to those of $YBa_2Cu_3O_{7-\delta}$. At low fields the triangular vortex lattice is preferred (both orientations have the same free energy), but at $H > 0.15H_{c2}$ the square lattice oriented along {110} is stabilised as expected from the preceeding argument. (The other orientation of square lattice has the highest free energy for all values of H.) No other vortex lattice configurations were tested due to the intensive nature of these numerical calculations, but it is reasonable to suspect a continuous transformation from an isotropic triangular vortex lattice to a square one as predicted by Berlinsky *et al.* (1995).

9. The non-ideal vortex lattice

Underpinning the theory presented so far is the rather false ideal of the vortex lattice as an infinite structure with perfect translational order. Not only does this view inadequately reflect the reality of experiments, but it also neglects the physics of disorder and imperfections, which can give rise to rich physics in their own right. Therefore the ideal of a perfect vortex lattice will be abandoned; in the remainder of this thesis the phrase "vortex lattice" will assume a more colloquial meaning, *i.e.* the structure formed by an ensemble of vortices, as opposed to the rigorous meaning implied by the technical definition of "lattice". In this section some aspects of the theory of the non-ideal vortex lattice will be reviewed.

The simplest cause of loss of perfect translational order in the vortex lattice is sample geometry. In the general case, a sample will posess a non-zero demagnetisation coefficient, which will tend to cause the flux going through the sample (*i.e.* the vortices) to bend in order for the electromagnetic boundary conditions to be satisfied. This macroscopic bending becomes more important for samples with large magnetisations (*i.e.* far below H_{c2}).

A more interesting and considerably less trivial cause for imperfections in the vortex lattice is caused by disorder in the underlying crystal. Defects in a crystal (precipitates, vacancies, impurities *etc.*) suppress superconductivity in their vicinity,

forming centres onto which vortices may be "pinned". Pinning occurs because it is advantageous for a vortex to form on a site that confers no increase in the free energy due to the local suppression of superconductivity by the vortex core (superconductivity is already suppressed by the pinning centre).

Pinning plays an important role in determining the properties of a superconductor. In the mixed state even a DC current may be dissipated by the movement of the vortices by the Lorentz force. Pinning defeats this process and superconductors with many pinning centres will generally have large effective critical current densities (the current density at which point the Lorentz force overcomes the energy barriers of the pinning centres). Thus the study of pinning and the flux flow state is technologically important.

Pinning also influences the static magnetic properties of type-II superconductors. Strong pinning will hinder the flow of vortices into the sample as the applied field is increased, hence increasing the magnetisation. (It can be a surface and/or a bulk effect.) In a "hard" superconductor (strong pinning) this process may be described by the Bean model (Bean, 1964) in which flux enters at the sample edges and is pushed inside the superconductor such that the field gradient is equal to the critical current density. This is often called the critical state model because at all points in the superconductor the vortices are just on the edge of flux flow.

Several types of pinning site are possible, but the commonest are point pinning-centres. Since vortices are one-dimensional objects, a vortex may be pinned along its length by many point pinning-centres. The route that a vortex takes through a sample depends on the balance of the energies associated with gain in condensation energy from the pinning centre, the vortex line tension and the interactions with other vortices. An expression governing this behaviour is easily written down: in the continuum limit, the Hamiltonian (Giamarchi & Bhattacharya, 2001;Giamarchi & Le Doussal, 1997) can be written in terms of the vortex displacement vector field $\mathbf{u}(\mathbf{r})$, the elastic response tensor c_{ij} and a random potential, $V(\mathbf{r})$, which models the pinning sites:

$$H = \frac{1}{2\Omega} \sum_{ij} \sum_{\mathbf{G}} c_{ij}(\mathbf{G}) u_i(\mathbf{G}) u_j(\mathbf{G}) + \int \left[V(\mathbf{r}) \sum_i \delta^{(2)}(\mathbf{r} - \mathbf{R}_i^0 - \mathbf{u}_i) \right] \mathrm{d}^2 r, \qquad (9.1)$$

where $\mathbf{R}_i^0$ are the positions of the vortices in the absence of disorder. Due to the highly

non-linear coupling of the vortex displacements, $\mathbf{u}_i(\mathbf{r})$, to the Hamiltonian, the solution of equation 9.1 represents a formidable problem in statistical mechanics. Fortunately, some progress has been made, particularly by Larkin (1970), who has calculated the form of the relative vortex-displacement correlation function:

$$b(r) = \langle [u(\mathbf{r}) - u(\mathbf{0})]^2 \rangle. \tag{9.2}$$

In this analysis the integral of the disorder term in equation 9.1 was expanded to first-order in the displacement field, $\mathbf{u}(\mathbf{r})$, yielding the surprising result that the relative vortex-displacement function grows algebraically as a function of distance. It might be concluded from this statement that arbitrarily weak disorder destroys the long-range translational order of the vortex lattice. However, as Larkin first realised, the expansion is only valid up to distances R_c such that $u(R_\mathrm{c}) \approx \xi$, which is well below the length at which dislocations start to appear (of the order or greater than the inter-vortex spacing). Beyond R_c, $b(r)$ grows slightly more slowly and — vitally to the existence of the vortex lattice — $b(r)$ grows only logarithmically beyond R_a, which is the distance at which $b(r) = a$. Therefore, as long as the pinning is not too strong, the vortex lattice may retain long-range order. Long-range order is able to survive in part by virtue of the periodicity of the vortex lattice: each vortex will accommodate pinning sites close to it, but there is no incentive for any particular vortex to make a displacement of more than one vortex spacing. This results in a vortex phase that exhibits perfect topological order. Such a vortex lattice phase is known as the Bragg glass phase and is responsible for the observation of strong Bragg peaks in neutron scattering (see section 11).

The realisation of the Bragg glass in a type-II superconductor depends upon a number of factors. Obviously, a sample with strong pinning will be more susceptible to disorder. Indeed, dislocations will occur if the inter-vortex spacing becomes comparable with R_a. The Bragg glass is also sensitive to the value of the induction in the sample. At low values of induction the inter-vortex separation may be too great for the inter-vortex interaction to organise effectively the vortices into a lattice. In contrast, the Bragg glass is also destroyed by large inductions. This transpires due to the fact that the strength of the disorder term in equation 9.1 increases with induction more than the elastic term. In this regime the vortices form a glassy phase (the vortex glass), which is riddled with dislocations. Furthermore, thermal fluctuations at large temperatures

may induce the Bragg glass to melt into a vortex liquid or gas. Therefore, insofar as disorder is concerned, the phase diagram for vortices in a type-II superconductor may be represented rather generally as in figure 1.8.

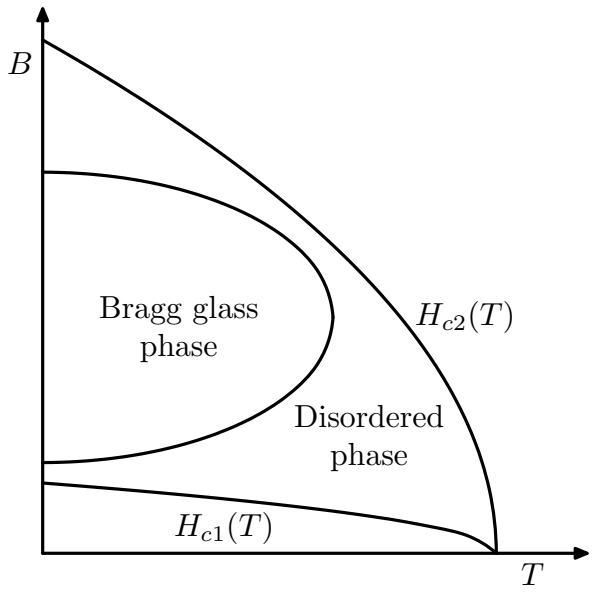

Fig. 1.8: A cartoon of the generic disorder phase diagram of a type-II superconductor. The ordered phase (the Bragg glass) is confined to an intermediate field range and low temperatures. Surrounding this ordered phase are either glass-like or liquid-like disordered phases.

Another type of pinning, which is particularly pertinent to high-T_c materials, is pinning due to twin planes. Twin planes are extended planar crystal defects. They arise in materials which have a transition from a tetragonal phase at high temperatures to an orthorhombic phase at low temperatures, which has basal plane lattice parameters that are similar in size. As the sample cools through this transition, the degeneracy in the two basal plane lattice parameters is removed and the sample is divided into two types of domain at roughly 90° to each other (see figure 1.9). Due to their planar nature, these defects form very effective pinning sites. Even when the density of twin planes is low compared to the density of vortices, they can still exert a strong influence by pinning vortices along a line and thus imposing an orientation on the vortex lattice. In this case two types of vortex lattice domain, mutually orthogonal to each other, is realised. The orientation of the vortex lattice by twin planes is generally much stronger than any other source because the energy involved is the condensation energy, albeit for only some of the vortices in a domain, rather than the very subtle energy balances

typical of coupling to crystal anisotropy.

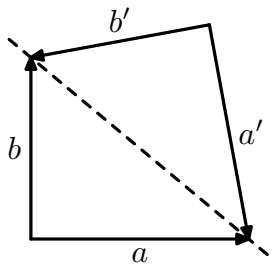

Fig. 1.9: A schematic of a twin boundary in an orthorhombic crystal. The dashed line indicates the twin boundary, either side of which the basal plane axes are exchanged. In this figure $a = 1.2b$, which is highly exaggerated (for clarity) compared to typical differences between a and b of just a few percent.

CHAPTER II

Small-angle neutron scattering

10. Introduction

Small-angle neutron scattering (SANS) is an elastic neutron-scattering technique used to probe mesoscopic systems whose characteristic length scales are in the range 10–1000 nm. Colloids, precipitates in alloys and the vortex lattice are all examples of systems that fit within this broad remit. Studying such systems using neutron scattering requires an instrument that is well-adapted to handle large-scale structures. To illustrate these requirements, consider the d-spacing of a triangular arrangement of vortex lines, a representation of which is shown in figure 2.1. Flux quantisation gives:

$$d_{\triangle} = \sqrt{\frac{\sqrt{3}\Phi_0}{2B}}. \tag{10.1}$$

Even at relatively high inductions, *e.g.* 1 T, where $d_{\triangle}$ is approximately 40 nm, this is at least two orders of magnitude larger than that in a typical crystal! To cope with the extremely small momentum transfers involved in this type of scattering, SANS instruments utilise long-wavelength ($\lambda_{\mathrm{n}} \approx 1\,\mathrm{nm}$) neutrons. Nevertheless the angle of scatter, 2θ, which is given by the famous Bragg law:

$$2d \sin\theta = \lambda_{\mathrm{n}}, \tag{10.2}$$

is still only of the order of a degree. Hence SANS instruments are also characterised by their large sample-detector distances.

The use of SANS to study the vortex lattice was pioneered by Cribier *et al.* in 1964 (Cribier *et al.*, 1964). Since then it has become a ubiquitous and indispensible tool for vortex physics and, with the discovery of unconventional superconductivity, has

enjoyed somewhat of a renaissance during the last fifteen or so years. Recent examples of its application include measurements of the vortex lattice in high-T_c cuprates, heavy fermion materials, the borocarbides and Sr_2RuO_4.

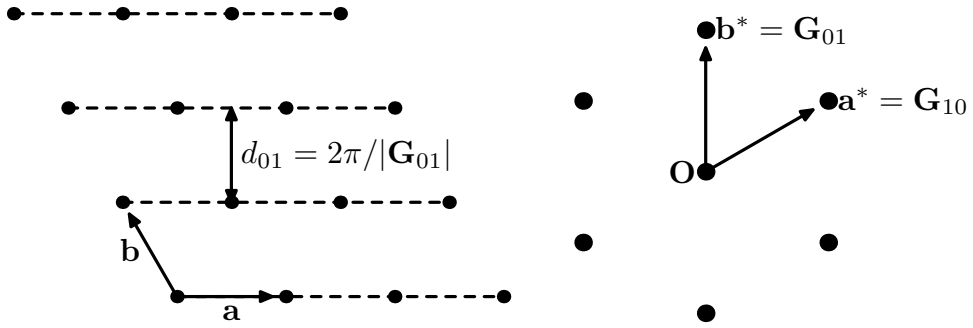

Fig. 2.1: The Bragg picture of the vortex lattice. Shown on the left in real space is a region of a triangular-coordinated vortex lattice with a set of planes indicated. On the right is shown the equivalent picture in reciprocal space.

The purpose of this chapter is to provide a thorough review of SANS measurements on the vortex lattice with particular emphasis on the methodology and the theory that underpins it. For a broader research-based review of recent SANS results in high-T_c materials the reader is directed to the excellent review by Forgan (1998a).

11. Basic scattering theory and geometry

Making full use of information gleaned by SANS requires the development of a proper quantum-mechanical theory of the scattering of neutrons from the vortex lattice. The Hamiltonian describing this may be written in terms of the interaction between the neutron magnetic moment and the local induction:

$$\hat{H} = -\frac{\hbar^2}{2m_n}\nabla^2 - \boldsymbol{\mu}_n \cdot \mathbf{B}(\mathbf{r}), \tag{11.1}$$

where the neutron magnetic moment is $\mu_n = 9.66 \times 10^{-27}\,\mathrm{JT}^{-1}$. An important simplification can be made in this analysis: the kinetic energy of a neutron of wavelength 1 nm (typical in SANS) is $\sim 1 \times 10^{-22}$J whereas the potential energy of a neutron in a field of 1 T is only $\sim 1 \times 10^{-26}$J. Therefore the potential term in the Hamiltonian may be regarded as a perturbation and the problem may be solved using the well-known first Born approximation (Merzbacher, 1998) in which the differential cross-section is

calculated from the Fourier transform of the scattering potential:

$$\frac{\mathrm{d}\sigma}{\mathrm{d}\Omega} = |f(\mathbf{q})|^2 \quad \text{where} \quad f(\mathbf{q}) \approx \frac{m_n}{2\pi\hbar^2} \int \boldsymbol{\mu}_n \cdot \mathbf{B}(\mathbf{r}) \exp(-\mathrm{i}\mathbf{q} \cdot \mathbf{r}) \mathrm{d}^3 r, \tag{11.2}$$

where $f(\mathbf{q})$ is the scattering amplitude for a neutron undergoing scattering with momentum transfer $\hbar\mathbf{q}$. (Note that there is zero energy transfer in this type of scattering because the scattering potential is time-independent.)

It is instructive to examine equation 11.2 for the case of a vortex lattice with perfect translational order, which may be represented by the Fourier sum $\mathbf{B}(\mathbf{r}) = \sum_{\mathbf{G}} \mathbf{B}_{\mathbf{G}} \exp(\mathrm{i}\,\mathbf{G} \cdot \mathbf{r})$. Calculating the differential cross-section in this idealised scenario gives:

$$\frac{\mathrm{d}\sigma}{\mathrm{d}\Omega}(\mathbf{q}) = (2\pi)^3 \left(\frac{\gamma}{4}\right)^2 \frac{V}{\Phi_0^2} \sum_{\mathbf{G}} |\mathbf{B}_{\mathbf{G}}|^2 \, \delta(\mathbf{q} - \mathbf{G}), \tag{11.3}$$

where V is the sample volume and γ is the neutron magnetic moment in nuclear magnetons. Despite its apparent complexity, this equation embodies two simple conditions for diffraction, which provide an intuitively appealing geometric picture of SANS and, indeed, diffraction in general:

$$|\mathbf{k}_{\mathrm{in}}| = |\mathbf{k}_{\mathrm{out}}|, \quad \mathbf{k}_{\mathrm{out}} - \mathbf{k}_{\mathrm{in}} = \mathbf{q} \tag{11.4}$$

The first of these relations expresses the elastic nature of the scattering; the second, which is a consequence of the delta functions in equation 11.3, is just Bragg's law. These criteria can be represented pictorially as in figure 2.2, in which the incoming neutron wavevector $\mathbf{k}_{\mathrm{in}}$ is directed at the origin of the two-dimensional reciprocal space and the outgoing neutron wavevector, $\mathbf{k}_{\mathrm{out}}$, lies on the Ewald sphere (the locus of elastic scattering). In a SANS experiment, the direction of $\mathbf{k}_{\mathrm{in}}$ is fixed and in the "standard" geometry the field is applied nominally *parallel* to the neutron beam. The plane containing the reciprocal lattice vectors of the two-dimensional vortex lattice is therefore nominally *perpendicular* to the neutron beam (see figure 2.2). To satisfy the conditions for diffraction (equation 11.4) the vortex lattice must be rotated — or "rocked" in diffraction patois — until a reciprocal lattice vector spans the Ewald sphere.

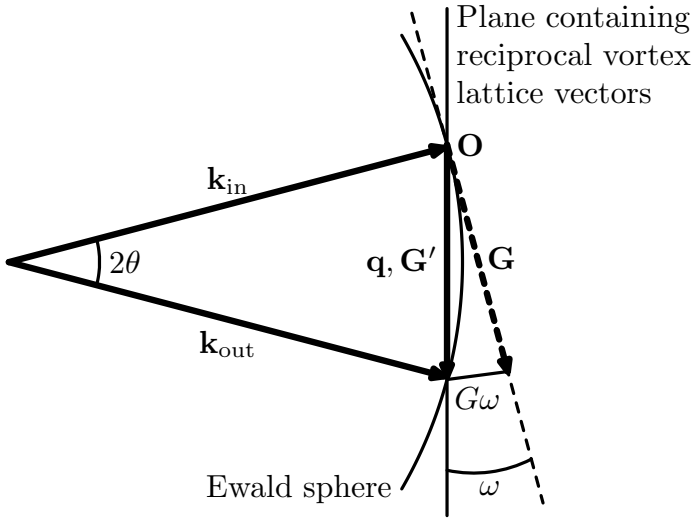

Fig. 2.2: A simple picture of the scattering geometry described by equation 11.3. The Bragg condition is fulfilled when a reciprocal lattice vector forms a chord of the Ewald sphere. For this to occur, the reciprocal vortex lattice plane (represented by a line) is rocked (rotated) from its zero-angle position (dashed line) until the angle of rock, ω, is equal to the Bragg angle, θ. For clarity the angle of scatter has been exaggerated: in a real SANS experiment the Bragg angle, θ, is typically of the order of a degree and the neutron wavevector is much larger than $\mathbf{q}$.

In a real experiment the intensity of a Bragg peak integrated over all solid angles and all rocking angles, ω, is measured, rather than the differential cross-section. The integrated intensity may be calculated easily from equation 11.3, taking just the Dirac delta-function corresponding to the Bragg peak of interest. The intensity is then given by

$$\mathrm{d}I(\mathbf{q},\omega) = \phi \frac{\mathrm{d}\sigma}{\mathrm{d}\Omega} \mathrm{d}\Omega \mathrm{d}\omega, \tag{11.5}$$

where ϕ is the neutron flux. In the case of a perfect vortex lattice, the integral over solid angles will only have contributions when the argument of the delta function $\delta(\mathbf{q}-\mathbf{G})$ is zero, which occurs when the sample is rocked by the Bragg angle, θ. From figure 2.2 the distance between $\mathbf{q}$ and $\mathbf{G}$ in the small-angle limit is given by $G\omega$, where ω is the angle of rock. The small-angle limit allows the three-dimensional delta function to be expanded as a product of delta functions, one in the plane containing the reciprocal vortex lattice vectors (two-dimensional) and one perpendicular to it (one-dimensional). The latter integral, which can be represented as $\delta(G(\omega-\theta))$ is performed first. Making a change of variables and integrating yields a factor G^{-1} in the integrated intensity.

The integration over the remaining two dimensions of the delta function is done easily by converting it to an integral over the area of the Ewald sphere, which near to the reciprocal lattice vector is approximately parallel to the plane of the reciprocal vortex lattice (in the small-angle limit). This entails the change of variables $\mathrm{d}\Omega \rightarrow k^{-2}\mathrm{d}A$, providing a factor of λ_{n}^2. The final result, as first quoted by Cribier *et al.* (1964), is:

$$I_{\mathbf{G}} = 2\pi\phi \left(\frac{\gamma}{4}\right)^2 \frac{V\lambda_{\mathrm{n}}^2}{\Phi_0^2 G} \left|\mathbf{B}_{\mathbf{G}}\right|^2 . \tag{11.6}$$

Therefore, in addition to the kinematic factor λ_{n}^2/G, the integrated intensity depends upon the neutron flux, ϕ, and the sample volume, V in the manner expected. The only other factor of interest is the vortex form-factor, $|\mathbf{B}_{\mathbf{G}}|$, for which various theoretical models exist, but whose effect on the integrated intensity may be illustrated using the London model as a starting point. The London model is often a decent approximation in the region of phase space (H, T) accessible to SANS. In this theory, the form-factors, $\mathbf{B}_{\mathbf{G}} \approx \langle B \rangle \hat{\mathbf{z}}/(1 + \lambda_{\mathrm{L}}^2 G^2)$ (equation 2.6) are field *independent* for $B \gg B_{\mathrm{c1}}$, which simply expresses the fact that no field contrast is lost in going to large inductions because of the logarithmic divergence of the field at the vortex cores. Hence, the only loss in integrated intensity experienced from increasing field is a rather slow ($B^{-\frac{1}{2}}$) kinematic one. However, the effect of the penetration depth, λ_{L}, on the scattered intensity is extremely strong: $\lambda_{\mathrm{L}}^{-4}$! This makes the study of superconductors with long penetration depths extraordinarily difficult. Unfortunately many of the currently *en vogue* superconductors (*e.g.* high-T_{c} and heavy fermion) fall into this category.

12. SANS instrumentation, set-up and technique

The specialisation of SANS instruments to large-scale structures — and hence low momentum transfers — means that they are quite different from their large-momentum-transfer brethren in both appearance and operation. In figure 2.3 is shown a schematic that typifies modern SANS instruments, which are now commonly found at both reactor-based and spallation-based neutron sources*. In order to maximise

* The measurements presented in this thesis were obtained from D11 and D22 at the Institut Laue-Langevin (ILL), Grenoble, France and SANS-I at the Paul Scherrer

the angle of scatter, SANS instruments utilise cold neutrons produced by the moderation of fission neutrons, typically in liquid deuterium at a temperature of around 20 K, which corresponds to a typical wavelength of the order of 0.1 nm. Cold neutrons can be transmitted by multiple critical reflection through a so-called "supermirror" neutron guide. These guides have walls consisting of a highly polished nickel surface deposited on top of a multilayer giving an effective critical angle of a few degrees, thus enabling neutrons to be delivered to the experimental area.

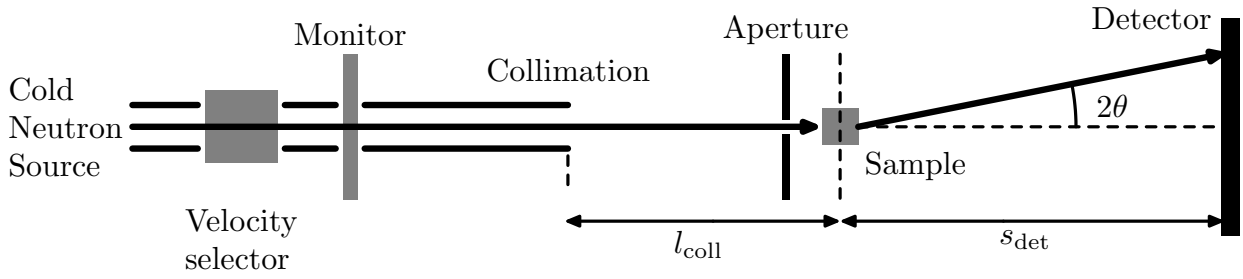

Fig. 2.3: A schematic of a SANS instrument. The neutrons are extracted from the cold source by a neutron guide (parallel lines) and a wavelength, λ_{n}, is selected by a mechanical velocity selector. The two other important instrument parameters are the collimation length, l_{coll}, and the detector distance, s_{det}.

Before the neutrons are scattered from the sample it is first necessary to select a wavelength band from the cold thermal spectrum produced by moderation. The choice of wavelength is a crucial one: larger wavelengths yield proportionately larger Bragg angles, but since SANS invariably uses the low-energy tail of the Maxwell-Boltzmann distribution, which varies as $\lambda_{\mathrm{n}}^{-4}$, a significantly lower flux must be tolerated. (A small recompense to this is the λ_{n}^{2} dependence of the integrated intensity — see equation 11.6.)

Wavelength selection is accomplished by mechanical velocity selection. The neutron beam passes through a turbine of neutron-absorbing blades that transmits a mean wavelength inversely proportional to the angular velocity (typically around 10,000 revolutions per minute) with a fractional spread of $\Delta\lambda_{\mathrm{n}}/\lambda_{\mathrm{n}} \approx 10\%$. This large spread is one cause of the rather poor resolution of SANS instruments since, from Bragg's law,

Institut (PSI), Villigen, Switzerland. The ILL is a 54 MW reactor-based source and at PSI spallation neutrons are produced from a 590 MeV proton beam incident on a lead target.

it translates to a 10% spread in 2θ. (See section 14.)

Directly after the velocity selector lies the monitor. The monitor is a low-efficiency detector and its purpose is to facilitate normalisation since the total number of monitor counts during a run reflects the total number of neutrons incident on the sample. This is of particular importance in a spallation-based neutron source where the beam intensity may be subject to very large fluctuations. In such cases, it is more prudent to count to a set number of monitor counts rather than a set time.

In addition to wavelength spread, another important factor in the resolution of a SANS instrument is beam divergence. On a SANS instrument, collimation is effected by removing some of the neutron guide near the sample and by using a source aperture. The angular divergence of the beam can be reduced in a linear fashion by increasing the length, l_{coll}, over which the beam is collimated, but this comes at the expense of neutron flux at the sample which decreases with l_{coll}^{-2}.

After the collimation, the beam passes through a sample aperture, which defines the beam size on the sample. The sample resides inside a cryomagnet (or a thin-tailed cryostat placed inside the bore of an electromagnet), which provides the magnetic field and the low temperatures required for superconductivity. Substantial care must be taken with this arrangement. Most importantly, every effort should be made to limit the amount of material (other than the sample) lying in the beam's path because it will contribute to the background signal; anything necessarily in the beam should be constructed from a material with a low absorption and low incoherent scattering cross-section such as pure aluminium, and should be as free as possible from precipitates and defects, both of which give rise to significant small-angle scattering. This places constraints on the mechanical design of the cryomagnet. Furthermore, parts of the walls of the cryostat through which the beam passes are often replaced by sapphire (Al_2O_3) windows because aluminium alloy used in cryostat construction contains precipitates.

Where possible, the sample itself should comply with the guidelines above, and if the sample contains a strongly absorbing isotope then it should be not be made thick relative to the attenuation length*. For sample mounting, a *thin* layer of glue may

* Clearly an attempt is made to maximise the total signal which will increase linearly with the sample volume, but decrease exponentially with its thickness.

be used. This practice would seem an anathema to an inelastic neutron scatterer due to the strong incoherent scattering from hydrogen in the glue, but in SANS bigger problems arise from precipitate scattering, which is not distributed over all solid angles like incoherent scattering from hydrogen. As a final precaution against background scattering components in the beam (such as the plate onto which the sample is mounted) are masked with a neutron-absorbing material such as cadmium, and samples with flat faces may have their edges masked to prevent unwanted reflections. (A paint made from gadolinium oxide is convenient for this.)

To maximise flux incident on the sample for a particular set of instrument parameters (wavelength, collimation, *etc.*), both sample and sample aperture should be well positioned with respect to the beam. The neutron intensity drops quite rapidly off axis so even displacements of a few centimetres can give rise to changes in flux by small integer factors.

Neutrons scattered from the sample pass through an evacuated tank in which resides a position-sensitive detector placed at a (variable) distance, s_{det} from the sample (see figure 2.3). In common with most modern neutron detectors, SANS detectors are based on the absorption of neutrons by ^{3}He:

$$^3\mathrm{He} + \mathrm{n} \rightarrow ^3\mathrm{H} + ^1\mathrm{H} + 764\,\mathrm{keV}. \tag{12.1}$$

The reaction produces a charge pulse that is amplified by a cascade process similar to that in a Geiger counter and is detected by a series of horizontal and vertical wire anodes maintained at high voltage relative to a cathode at the back of the detector. The position of the neutron is given by the indices of the horizontal and vertical wires that recorded the charge pulse. The count rate of the detector is limited to about 50 kHz because only one neutron can be counted at once by the detector. Therefore to prevent excessive dead-time (or even damage to the detector) the strong undiffracted beam is terminated by a cadmium beam-stop placed just in front of the detector. Recently, SANS detectors have been developed that consist of a series of vertical wire anodes in tubes. In this arrangement, the horizontal position of the detected neutron is determined by which wire the charge pulse is measured on and the vertical position is determined by charge division between the two ends of each wire anode. Typically a count rate of about 50 kHz per wire can be achieved in these detectors.

Two stepper motors facilitate the rocking of the cryomagnet about two mutually orthogonal axes perpendicular to the beam. In SANS these degrees of freedom are conventionally denoted ω (rotation about the vertical axis) and ϕ (rotation about the horizontal axis perpendicular to the beam). Most SANS instruments are endowed with a good deal of automation and the instrument may be programmed to scan through the Bragg condition by sequentially moving one or both motors and then counting. (In diffraction parlance such a scan is known as a rocking curve.) It is good practice always to scan these motors in the same direction to avoid problems arising from backlash. This is done not just for the obvious reason that the Bragg condition will move due to backlash, but also because more often than not background measurements need to be subtracted to see clearly the signal from the vortex lattice. Background measurements can be obtained either by performing the same scan with zero applied field or, more commonly, by taking the sample above its critical temperature. A high degree of scan repeatability is desirable because the background signal, which has its origins in, *e.g.*, precipitates, may be *very strongly* angle-dependent.

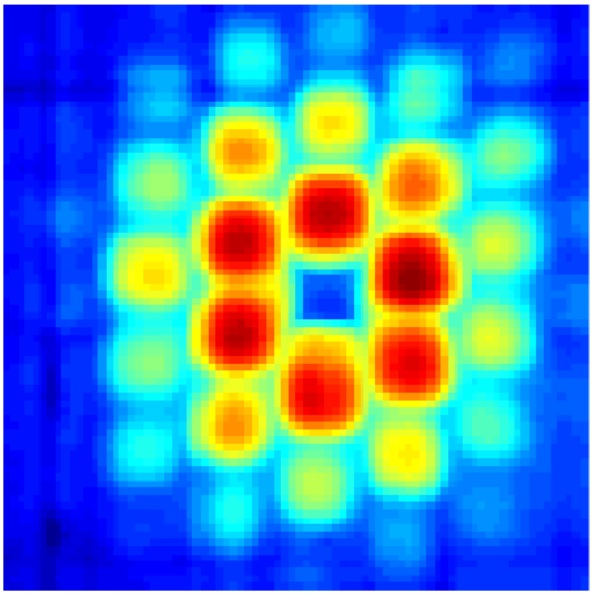

Fig. 2.4: An example of data obtained using SANS: a diffraction pattern of the vortex lattice in niobium with a field of 0.2 T applied parallel to the crystal (110) direction. The picture shows the logarithm of the sum over many rocking angles showing several orders of diffraction. The two dark bands are due to bad "lines" on the detector and the lack of counts in the centre square is due to the beam-stop.

An example of a SANS diffraction pattern is shown in figure 2.4. These data were obtained from the vortex lattice in niobium formed by field-cooling in 0.2 T. The sample was rocked in such a way as to satisfy the Bragg condition for the first few orders of diffraction. Although taken under relatively low resolution conditions, the diffraction pattern in figure 2.4 demonstrates the often poor resolution of SANS measurements.

13. Bragg's law revisited: specialisation to SANS

Before explaining the effects of finite resolution, it is worth reappraising the Bragg conditions for scattering (equation 11.4) for the case of the vortex lattice. The vortex lattice is a two-dimensional entity thus in general all the scattering vectors, **q**, lie in the plane containing the reciprocal lattice vectors, **G**. (The exact arrangement of **G**-vectors in this plane is not important to what follows.) The Bragg conditions stipulate that the locus of scattered neutrons is formed by the intersection of the Ewald sphere (locus of elastic scattering) with the plane of **G**-vectors. This intersection is obviously a circle whose radius in reciprocal space depends upon the wavelength, $\lambda_{\rm n}$, and the rocking angles, ω and ϕ; for brevity this locus will named the Ewald circle. The equation of the Ewald circle in reciprocal space is easily calculated using simple coordinate geometry: assume the vortex lattice **q**-vectors lie in the q_y-q_z plane and that when $\omega = 0 = \phi$, the incoming neutron wavevector lies along the q_x-axis. Rocking the sample corresponds to rotating in reciprocal space the incoming neutron wavevector about the q_z-axis by ω and about the q'_y-axis by ϕ:

$$\mathbf{k}_{\rm in} = \frac{2\pi}{\lambda_{\rm n}} \begin{pmatrix} 1 \\ 0 \\ 0 \end{pmatrix} \longrightarrow \frac{2\pi}{\lambda_{\rm n}} \begin{pmatrix} \cos\omega\cos\phi \\ \sin\omega \\ \cos\omega\sin\phi \end{pmatrix} \tag{13.1}$$

(Note that the order of rotation is not important because rotation is commutative in the small angle limit to be applied shortly.) Intersecting equation 13.1 with the vortex lattice plane, $q_x = 0$, provides the equation for the Ewald circle, which in the small-angle limit is:

$$(q_y - k_{\rm in}\omega)^2 + (q_z - k_{\rm in}\phi)^2 = k_{\rm in}^2(\omega^2 + \phi^2), \tag{13.2}$$

where $k_{\rm in} = 2\pi/\lambda_{\rm n}$. Equation 13.2 is plotted in figure 2.5, which also shows an example of a two-dimensional **q**-vector that satisfies the Bragg condition (*i.e.* lies on the Ewald circle).

The projection of the Ewald circle onto the detector is a circle. To map a point in reciprocal space onto the detector the two Bragg angles, $\theta_{\mathrm{B},x}$ and $\theta_{\mathrm{B},y}$, corresponding to the two components of the **q**-vector are calculated independently:

$$\theta_{\mathrm{B},x} = \frac{\lambda_{\mathrm{n}} q_r \cos q_\theta}{4\pi} \quad \text{and} \quad \theta_{\mathrm{B},y} = \frac{\lambda_{\mathrm{n}} q_r \sin q_\theta}{4\pi}. \tag{13.3}$$

The position on the detector is given by $\mathbf{r}_{\mathrm{det}} = 2s_{\mathrm{det}}(\theta_{\mathrm{B},x}, \theta_{\mathrm{B},y})$, as is shown on the right-hand diagram of figure 2.5. Figure 2.5 provides a nice geometrical picture of diffraction in SANS: as the sample is rocked the Ewald circle expands and any Bragg peaks lying underneath it are projected on the detector. (In the figure, **q** is mapped to $\mathbf{r}_{\mathrm{det}}$.) This picture is limited in the sense that it ignores resolution effects; these will be included in the next few sections.

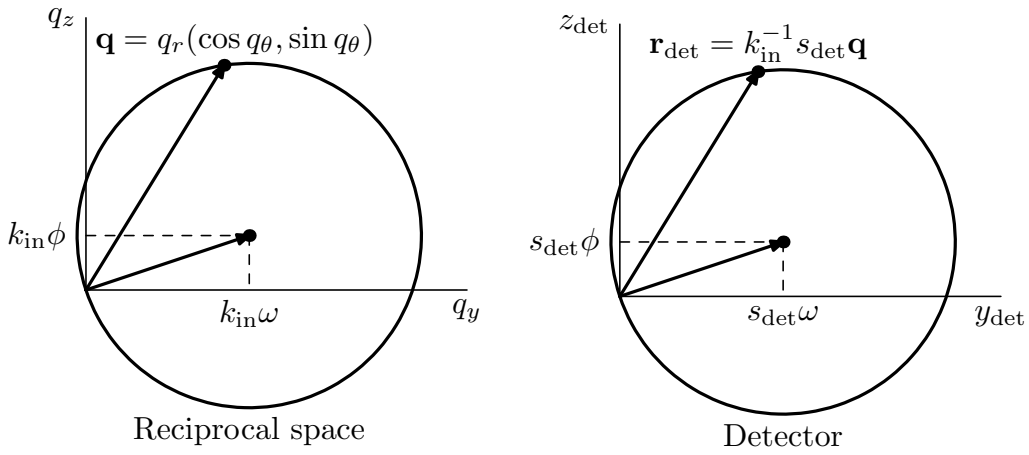

Fig. 2.5: The Ewald circle — the locus of points in reciprocal space (left) that are able to scatter a neutron of wavelength $\lambda_{\mathrm{n}} = 2\pi/k_{\mathrm{in}}$. On the right is shown the locus of points on the detector (placed at a distance s_{det}) where the neutrons land. The sample has been rotated by (ω, ϕ).

Equation 13.2 can be generalised to three dimensions, thus removing the earlier restriction that the **G**-vectors lies in a plane. This is most naturally done in spherical polar coordinates by introducing an azimuthal angle q_ω (in addition to the in-plane coordinates q_r and q_θ) that specifies the orientation of a particular plane under consideration. The angle q_ω corresponds to a rotation about the q_z-axis, which is in the *same* direction as the sample rotation angle ω. Therefore, for the purpose of specifying the Bragg condition, these parameters may be lumped into a single parameter $\omega' = \omega - q_\omega$. The assumptions under which equation 13.2 was derived are not affected

because although both ω and q_ω can be large, the criterion for small-angle scattering is still satisfied if their difference is small. This reflects closely the reality of SANS experiments where rotations by ϕ are generally small — for technical reasons — whereas rotations in ω, which are effected by a sample turn-table can be large ($\omega \in [-\pi, \pi]$ under ideal circumstances) allowing large-scale structures to be probed in different directions. The Bragg condition for small-angle scattering off $\mathbf{q} = (q_r, q_\theta, q_\omega)$ may hence be written:

$$\lambda_\mathrm{n} q_r = 4\pi \left[(\omega' + \alpha) \cos q_\theta + (\phi + \beta) \sin q_\theta \right]. \tag{13.4}$$

In the expression above, the angles α and β have been added preemptively to ω' and ϕ (respectively) to take into account diffraction from a beam rotated by α and β away from the nominal beam direction. These angles alter the radius and centre of the Ewald circle in an obvious manner. This generalisation will be needed later in the discussion of beam divergence.

14. Resolution of SANS

The low-resolution nature of a typical SANS set-up is a double-edged sword: on the one hand it can be a blessing, allowing in many cases the simultaneous measurement of multiple Bragg peaks and hence offering good neutron economy; on the other hand it can be a curse if, for example, Bragg peaks overlap on the detector (see, *e.g.*, section 23), or if instrumental effects need to be deconvolved to obtain intrinsic information. In either case, a proper understanding* of resolution effects is requisite to making the best use of SANS data. In this section, the two instrumental sources of finite resolution,

* The resolution effects described here and in the next section are based upon a simple set of rules developed by Brown (2001), which also demonstrates an example of their application in correcting measurements for sampling bias. The current presentation (sections 14 and 15) is a more mature and extended version of that earlier work and is further supplemented by the calculation of the instrumental resolution function (appendix A) and the reciprocal-space sampling function (appendix B). In comparison to the pioneering work in this area by Cubitt *et al.* (1992), the present work takes a more general three-dimensional view of the scattering of neutrons from the vortex lattice (see the discussion at the end of section 15).

wavelength spread and beam divergence, are evaluated. First, their effects are dealt with separately by considering how each contributes to the region of reciprocal space accessible in a single measurement; to where on the detector this region is mapped; and how the rocking curve is affected by each. Next, their combined effect is exposed in terms of the resolution function, which maps a single point in reciprocal space onto the detector.

Figure 2.5 provides a means to examine finite-resolution SANS. The first resolution effect to be considered is wavelength spread, which is illustrated in figure 2.6 for the generalised vortex lattice plane described above. The dashed scattering triangle corresponds to a wavelength shorter (larger $\mathbf{k}_{\text{in}}$) than the solid triangle, which denotes the nominal wavelength. It is easily seen that the former surveys a larger-radius circle of reciprocal space than the latter. In reality, there is a distribution of wavelengths thus the accessible region of reciprocal space will be crescent-shaped rather than the idealised Ewald circle shown in the previous section. However, the cones of scatter from each wavelength all subtend the *same* angle. Therefore, the scattering from the crescent region of reciprocal space is distributed over a single circle on the detector as shown in the bottom right diagram of figure 2.6. In this way wavelength spread convolves the scattering from $\mathbf{q}$-vectors with the same q_θ, but different q_r. Note though, that for fixed rocking angles wavelength spread alone cannot smear the scattering from a given $\mathbf{q}$-vector over the detector. This only occurs for a combination of wavelength spread and beam divergence (see the resolution function later in this section) or if data at different rocking angles are added (see below).

Wavelength spread plays a crucial role in determining the width of the rocking curve of a reciprocal lattice vector. Differentiating Bragg's law gives $\delta\theta/\theta = \delta\lambda/\lambda$. Therefore although beam divergence is often the dominant instrumental contribution to rocking curve width, the constant fractional spread due to the velocity selector (normally about 10%) becomes more important with increasing q because beam divergence gives a constant absolute spread. Furthermore, as the sample is rocked through the Bragg condition for the mean wavelength, the position of the diffracted spot will move radially outwards; figure 2.7 illustrates the idea. The upshot of this is that scattering from a single point in reciprocal space will give a radial smear of intensity on the

detector when summed over a rocking curve even for a perfectly collimated beam.

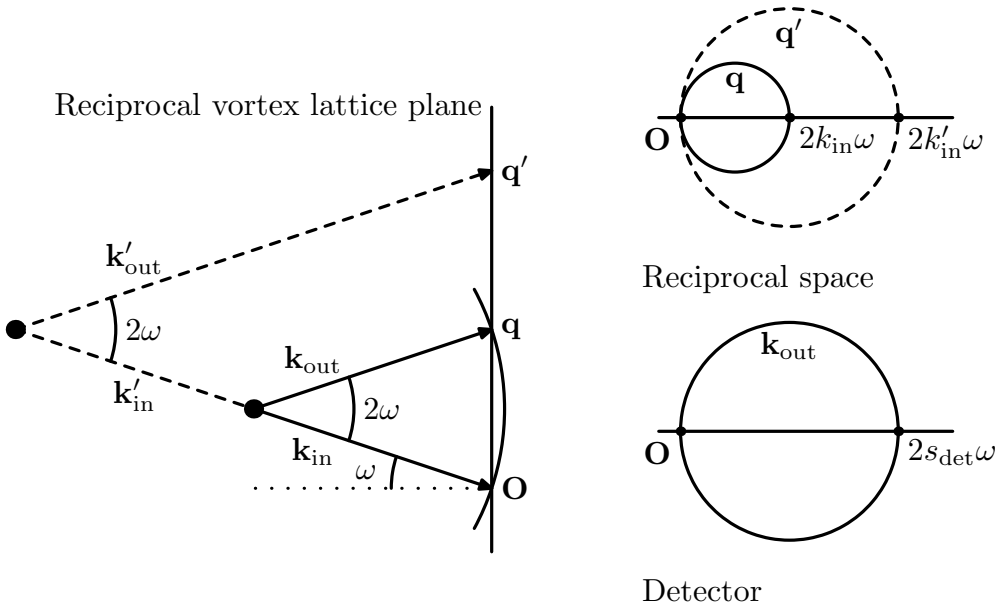

Fig. 2.6: Scattering from two different wavelengths for a sample rocked by ω (ϕ ignored for clarity). Shown on the left are the two scattering cones and on the right are diagrams equivalent to figure 2.5. The two different wavelengths see different parts of reciprocal space given by the locii $\mathbf{q}$ and $\mathbf{q}'$. However, when projected onto the detector both cones of scatter coincide.

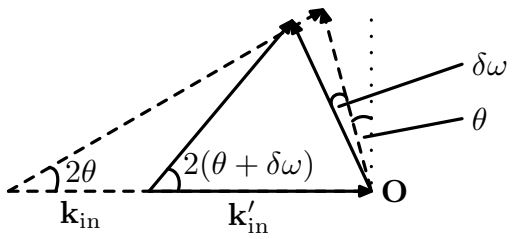

Fig. 2.7: The effect of wavelength spread on the rocking curve. The dashed triangle represents the rocked on case (for λ_{n}) and the solid triangle is the scattering from the same $\mathbf{q}$-vector rocked off slightly. In the latter case a longer wavelength satisfies Bragg's law and the scattering angle is increased commensurately.

The second instrumental contribution to resolution is beam divergence, which may be described by two angles, α and β, that quantify the direction of a given neutron wavevector by rotations about the vertical and horizontal axes (respectively) relative to the nominal beam. The resolution effects associated with beam divergence are demonstrated in figure 2.8. On the left diagram of that figure the vortex lattice plane

normal is rotated by the rocking angle ω away from the nominal beam direction, $\mathbf{k}_{\mathrm{in}}$. Also shown is another neutron wavevector, $\mathbf{k}'_{\mathrm{in}}$, with the same wavelength as $\mathbf{k}_{\mathrm{in}}$, but at an angle α to the latter. From this geometry, it is evident that the radius of the circle in reciprocal space to which $\mathbf{k}'_{\mathrm{in}}$ is sensitive is just proportional to the sum $\omega + \alpha$ in accordance with equation 13.4. Therefore, beam divergence resembles wavelength spread in that it samples a crescent-shaped region of reciprocal space. However, in contrast to the latter, the projection of this crescent on the detector is not just a circle because each orientation of wavevector has a different cone of scattering. Instead, each incident wavevector is scattered onto a circle of radius $s_{\mathrm{det}}(\omega + \alpha)$ centred at $-s_{\mathrm{det}}\alpha$. (Note that the centre of the circle moves such that the Ewald circle encompasses zero-$\mathbf{q}$ scattering which does not divert the beam.) Therefore the diffracted neutrons land on an annular band on the detector. In this respect, beam divergence needs to be treated with some care and does *not*, for example, simply correspond to sample rotation: although in reciprocal space only relative orientations are important, the detector does have an absolute measure of orientation — the nominal beam direction, which accounts for the difference according to the detector between rotating the beam and rotating the sample.

Like wavelength spread, at fixed rocking angles it is impossible for beam divergence alone to give a diffraction peak radial width as it is forbidden by the Bragg condition. (Although radial width may be effected when they act in concert — see below.) However, Bragg's law makes no proscription concerning scattering tangent to a reciprocal lattice vector and is in fact automatically satisfied by any degree of divergence perpendicular to $\mathbf{G}$. Physically, divergence perpendicular to $\mathbf{G}$ corresponds to rotating the scattering triangle about $\mathbf{G}$, which obviously cannot cause a violation of Bragg's law (see figure 2.10); this idea is fleshed out more mathematically in the derivation of the resolution function (appendix A). Thus a diffraction peak may be endowed with tangential width. Here collimation has found a niche as there in no mechanism by which wavelength spread can influence the tangential width of a Bragg peak.

From the point of view of the rocking curve, beam divergence gives scattering over a range of rocking angles just like wavelength spread, though the effect is somewhat different as shown in figure 2.9. If the sample scatters the nominal wavevector of

wavelength λ_n by 2θ when rocked on, then when it is rocked off by $\delta\omega$ the component of the beam that scatters is that propagating at $\delta\omega$ to the nominal beam. This wavevector will be scattered by $2\theta + \delta\omega$, in contrast to the $2(\theta + \delta\omega)$ obtained with wavelength spread.

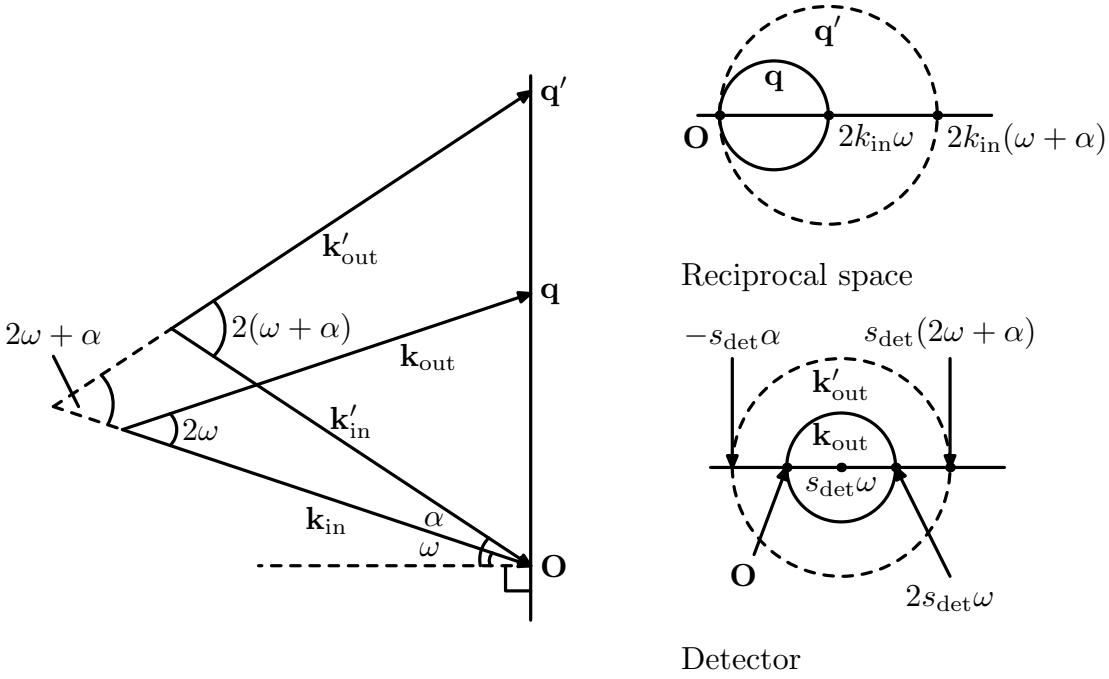

Fig. 2.8: A schematic showing the effect of beam divergence on resolution. The nominal beam has been rocked by ω and the divergent beam is at an angle α to it (see left). (Both wavevectors are equal in magnitude.) The circles sampled in reciprocal space and scattered to (on the detector) are shown in the top right and bottom right diagrams respectively.

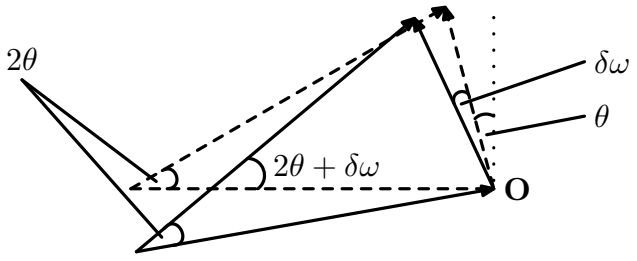

Fig. 2.9: The impact beam divergence has on the rocking curve of a $\mathbf{q}$-vector. The dashed triangle is taken as the centre of the rocking curve and the solid triangle corresponds to the sample rocked by $\delta\omega$. The wavelength of both scattering triangles is the same. Hence the component of the beam giving scattering in the rocked off case is rotated relative to the main beam by $\delta\omega$. The scattering from this wavevector is $2\theta + \delta\omega$.

Wavelength spread and beam divergence are the two instrumental parameters that define the resolution in a SANS experiment. Their combined effect is to "smear" a point in reciprocal space over the detector both radially to **q** (a combination of wavelength spread and beam divergence) and tangentially (beam divergence only). Figure 2.10 illustrates this process in one dimension. The nominal beam is rocked on to the **q**-vector giving scattering at $2\theta = 2\omega$ relative to the nominal beam direction. A larger wavelength (smaller $\mathbf{k}_{\mathrm{in}}$) neutron may also satisfy the Bragg condition if the beam divergence angle, α, is such that the Bragg condition is satisfied. That neutron will be scattered by $2\omega + \alpha$ relative to the nominal beam direction and therefore the diffraction peak will have a radial spread. In two dimensions, the diffraction peak will also have a tangential spread as discussed above. This is easy to appreciate by inspecting figure 2.10 since rocking tangentially to **q** (*i.e.* out of the page) satisfies the Bragg condition (equation 13.4) for arbitrary rocks.

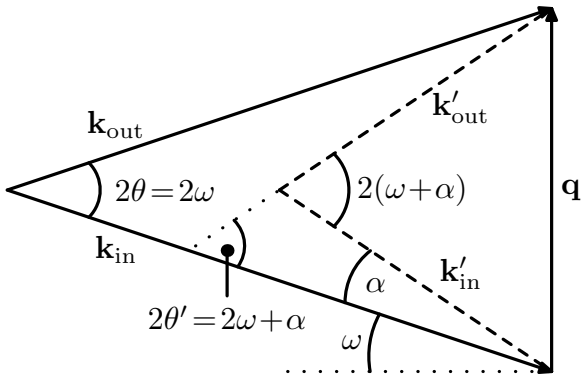

Fig. 2.10: Geometry for scattering off a single **q**-vector by neutrons with different wavevectors. The solid scattering triangle represents scattering of neutrons with the nominal wavelength, λ_{n}, directed at an angle ω (the rocking angle) to the sample. The dashed triangle represents scattering from the same **q**-vector of neutrons of a larger wavelength at an angle α to the nominal beam. The latter neutrons are scattered by $2\theta' = 2\omega + \alpha$ relative to the nominal beam direction ($\mathbf{k}_{\mathrm{in}}$)

The resolution function for SANS is computed in appendix A in two dimensions for arbitrary ω and ϕ (*i.e.* not necessarily rocked on). Performing the calculation requires knowledge of the form of the distributions in wavelength and beam divergence. In principle these may be measured, but it is often sufficient to assume that they are Gaussian, which have the advantage of mathematical convenience because they are

easily integrated:

$$P(\lambda) \propto \exp\left(-\frac{(\lambda-\lambda_{\rm n})^2}{2\sigma_\lambda^2}\right), \quad P(\mathbf{d}) \propto \exp(-\mathbf{d}\cdot\boldsymbol{\mathcal{D}}\cdot\mathbf{d}). \tag{14.1}$$

Here, $\mathbf{d} = (\alpha, \beta)$ is the beam divergence vector and the beam anisotropy is given by the matrix $\boldsymbol{\mathcal{D}}$, which is taken to be diagonal (since the principal axes of the instrument are horizontal and vertical). The general resolution function describing scattering from a two-dimensional $\mathbf{q}$-vector (q_r, q_θ) (using polar coordinates) is given by:

$$\begin{aligned} R_{\mathbf{q}}(\theta_x,\theta_y) \propto & \exp\left(-\frac{1}{2\sigma_\lambda^2}\left[\frac{4\pi}{q_r}\left(2\theta_x\cos q_\theta + 2\theta_y \sin q_\theta - \omega\cos q_\theta - \phi\sin q_\theta\right) - \lambda_{\rm n}\right]^2\right) \\ & \times \exp\left(-\frac{1}{\sigma_\alpha^2}\left[\theta_x(\sin^2 q_\theta - \cos^2 q_\theta) - 2\theta_y\cos q_\theta \sin q_\theta + \omega\cos^2 q_\theta + \phi\cos q_\theta \sin q_\theta\right]^2\right) \\ & \times \exp\left(-\frac{1}{\sigma_\beta^2}\left[\theta_y(\cos^2 q_\theta - \sin^2 q_\theta) - 2\theta_x\cos q_\theta \sin q_\theta + \phi\sin^2 q_\theta + \omega\cos q_\theta \sin q_\theta\right]^2\right), \end{aligned} \tag{14.2}$$

where (θ_x, θ_y) are the scattering angles and σ_i $(i \in \lambda, \alpha, \beta)$ are the widths of the distributions.

To see the effect of resolution, consider scattering from a $\mathbf{q}$-vector with $q_\theta = 0$ at $\phi = 0$. A much simpler equation results, which is easier to interpret:

$$R_{\mathbf{q}}(\theta_x,\theta_y) \propto \exp\left(-\frac{1}{2\sigma_\lambda^2}\left[\frac{4\pi}{q_r}(2\theta_x - (2\tilde{\omega} + \delta\omega))\right]^2 - \frac{1}{\sigma_\alpha^2}\left[\omega - \theta_x\right]^2 - \frac{\theta_y^2}{\sigma_\beta^2}\right). \tag{14.3}$$

Here $\tilde{\omega}$ is the value of ω that satisfies the Bragg condition for the mean wavelength, $\lambda_{\rm n}$, and $\delta\omega$ is some arbitrary deviation from this angle. Equation 14.3 comprises three terms: the first two define the radial width and the last term contains the tangential dependence. The radial and tangential factors are plotted in figures 2.11 and 2.12 respectively. From equation 14.3 it is clear that the contributors to radial spot-width (wavelength spread and horizontal beam divergence) modulate each other and the net width is dominated by the narrower of the two distributions. This is reflected in figure 2.11 in which the width is significantly smaller than the beam divergence and in fact is attributable to the 1 Å spread in λ, which in angular terms is equivalent to 0.05°*.

* The width of the λ distribution measured in the same units as beam divergence (*i.e.* radians) is obtained by dividing by the factor $4\pi/q$.

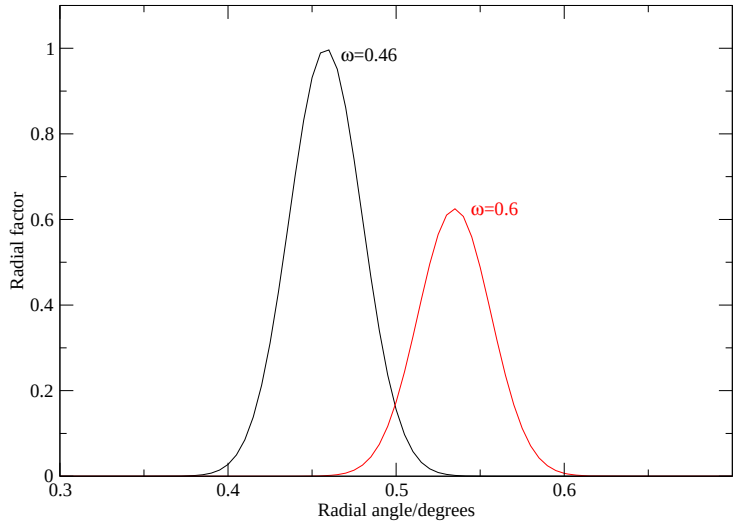

Fig. 2.11: The radial part of equation plotted using the values $\lambda_n = 10\,\text{Å}$, $q_r = 10\,\text{mÅ}^{-1}$, $\sigma_\lambda = 1\,\text{Å}$ and $\sigma_\alpha = 0.1°$. The black curve corresponds to being rocked on ($\omega = 0.46°$) and the red curve corresponds to being slightly rocked off ($\omega = 0.6°$).

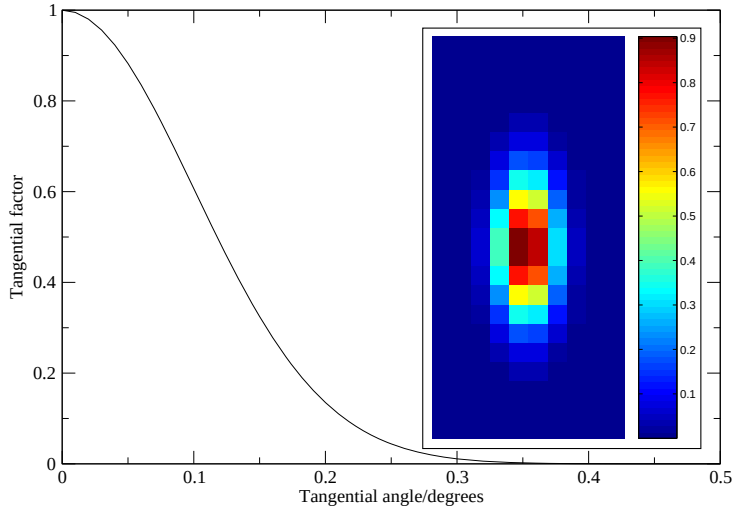

Fig. 2.12: The tangential part of equation 14.3 plotted for $\sigma_\beta = 0.1°$. In the inset is shown a two-dimensional plot of the full resolution function using the $\omega = 0.46°$ of figure 2.11.

Also shown in figure 2.11 is the effect of rocking on the spot position measured on the detector. In this regard there are two clearly identifiable limits: the limit of perfect velocity selection ($\sigma_\lambda \to 0$, thus the first term is dominant) and the limit of perfect collimation ($\sigma_\alpha \to 0$, hence the second term prevails). In either case, the spot will be shifted according to the mechanism associated with the widest distribution.

For example, by inspection of equation 14.3 it is clear that when rocked off the Bragg condition by $\delta\omega$ good collimation favours a "λ-type" spot shift of $\delta\theta = \delta\omega$ (see figure 2.7). In contrast, the shift bestowed when wavelength is well-defined is just half of the latter: $\delta\theta = \delta\omega/2$ (see the "beam divergence-type" shift in figure 2.9). In figure 2.11 where the wavelength distribution is comparatively narrow, the shift of the rocked off (red) curve is about $\delta\omega/2 \approx 0.07°$.

15. Effects of imperfections on resolution

The final resolution effect to be discussed is due to the sample itself. Though not a strictly extrinsic source, the sample gives rise to similar effects as the instrumental agents. To understand this, consider the differential cross-section, which is proportional to the Fourier transform of the auto-correlation function of $B(\mathbf{r})$:

$$\frac{\mathrm{d}\sigma}{\mathrm{d}\Omega} \propto B(\mathbf{q})B(-\mathbf{q}) \equiv \hat{F}\{B(\mathbf{r}) \odot B(\mathbf{r})\}. \tag{15.1}$$

If the correlations of the vortex lattice along the induction (the z-axis) are independent of those perpendicular to it then the differential cross-section may be factorised as $B(\mathbf{q})B(-\mathbf{q}) = B(\mathbf{q}_{xy})B(-\mathbf{q}_{xy})B(q_z)B(-q_z)$. Physically, this corresponds to a vortex lattice whose vortex lines meander through the sample without affecting the in-plane structure; thus, it may be thought of as a "mosaic" of crystallites with some distribution of orientations (see figure 2.13). The resulting reciprocal vortex lattice is quasi two-dimensional. In other words, the two-dimensional lattice structure is retained, but the spots now have some out-of-plane width.

Independence of correlations along the induction from those perpendicular to it is not a good assumption to make in general. For example, pinning certainly does not adhere to this ideal since the displacement of a vortex to accommodate a pinning site involves all the elastic moduli of the vortex lattice, not just the "tilt" modulus. Isotropic systems are particularly susceptible because there is no mechanism by which in-plane orientation is enforced and the shear modulus is substantially smaller than the tilt modulus (Brandt, 1995). So in general, reciprocal space ought to be considered in truly three-dimensional terms, *cf.* the Vortex glass state in section 9, and lattice effects cannot rigorously be described in the language of resolution. However, there

are cases when reciprocal space may be reduced to the quasi-two-dimensional space described above, *e.g.* when there is a macroscopic curvature of the applied field or a small demagnetisation effect in a sample with low pinning. This is demonstrated in figure 2.13, where the magnitude and in-plane orientation of the reciprocal lattice vector, **G**, is unchanged, but it gently tilts as a function of position along the induction axis.

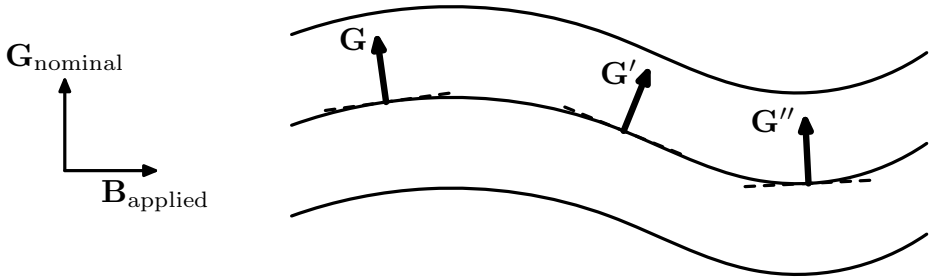

Fig. 2.13: An illustration of mosaic spread in the vortex lattice. The vortex lines meander along the field direction giving rise to a distribution in orientation of **q** along the vortex lines.

In figure 2.14 is shown the consequence of vortex-lattice mosaic spread on resolution in SANS. A neutron of wavevector $\mathbf{k}_{\text{in}}$ may be scattered off any of a distribution of reciprocal vortex-lattice planes, each with identical in-plane structure. The length of the in-plane reciprocal lattice vector grows in proportion with the angle γ, by which that scattering plane differs from the nominal plane direction. For example, in figure 2.14 $\mathbf{k}_{\text{in}}$ can be scattered by either **q** (small Ewald circle) or $\mathbf{q}'$ (large Ewald circle). Therefore mosaic spread acts similarly to instrumental effects in that it causes a crescent shaped area of the vortex reciprocal-lattice plane to be sampled (top right of figure 2.14). The crescent maps onto another crescent on the detector (bottom right of figure 2.14), in contrast to both beam divergence and wavelength spread. Note that each circle of scatter on the detector passes through the undiffracted beam as expected (bottom right diagram of figure 2.14).

Mosaic spread has an identical impact on rocking curve width as beam divergence. This transpires because both cases correspond to a relative rotation of sample and beam. However, unlike beam divergence mosaic spread does not cause a diffraction spot to move during rocking. For a well-collimated monochromatic beam, rocking a mosaic simply moves the reciprocal lattice vector, **G**, of a different two-dimensional

crystallite onto the Ewald sphere. Since the different **G**-vectors are all related by rotation in this sense, the resulting scattering triangles are all identical. An illustration is shown in figure 2.15 in which rocking the sample to get any of the dashed/dotted **G**-vectors to satisfy Bragg's law will leave the scattering triangle unchanged.

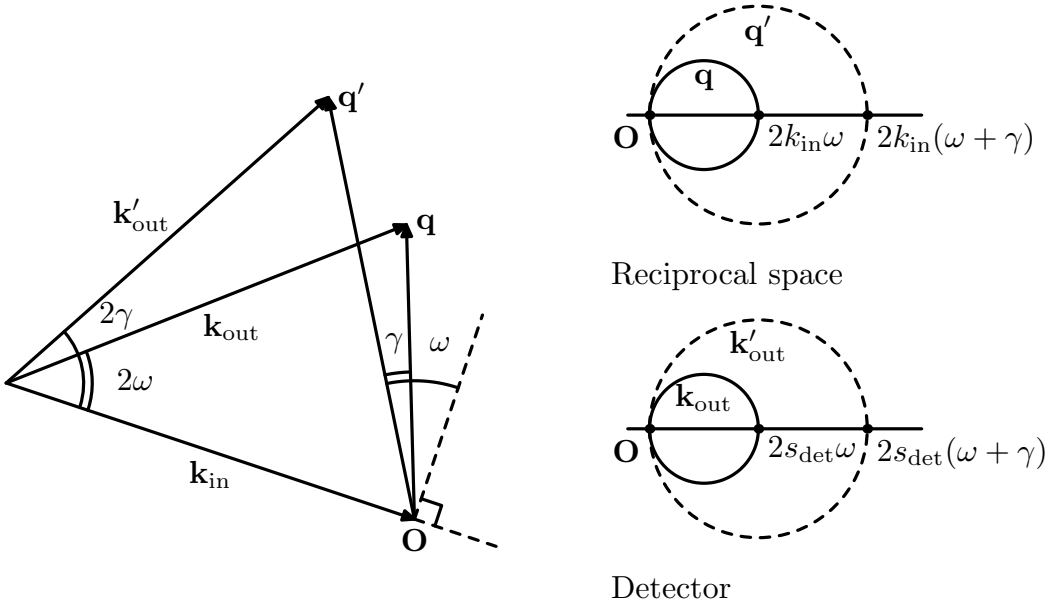

Fig. 2.14: An illustration of the contribution of mosaic spread to resolution. Neutrons of wavevector $\mathbf{k}_{\mathrm{in}}$ are diffracted by two different $\mathbf{q}$-vectors corresponding to two different orientations of Bragg planes. One Bragg plane is the nominal Bragg plane (rotated by the rocking angle, ω, from parallel to $\mathbf{k}_{\mathrm{in}}$) and the other is at an angle γ to the latter.

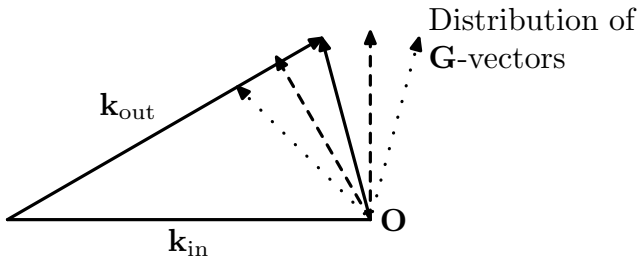

Fig. 2.15: Effect of mosaic spread on the rocking curve. The Bragg condition is satisfied by a range of **G** so the rocking curve width is increased, but all of these form the same scattering triangle therefore the peak intensity does not shift.

Mosaic spread may also be incorporated into an expression for resolution in the quasi two-dimensional limit, which was achieved by Cubitt *et al.* (1992). They have calculated the radial spot width including the effects of mosaic spread. Furthermore,

they have allowed for a variation in the d-spacing in their sample, which is easily done because it has precisely the same effect as wavelength spread and the two can be combined in quadrature. In this respect their expression is not really a resolution function like equation 31.10, but it is arguably more useful as it predicts the radial width of the spot in terms of the wavelength spread, beam divergence and sample characteristics. Since the former two can be measured, intrinsic sample properties can be deduced from the spot width.

16. Summary of resolution considerations

In common with most experiments dealing with scattering from condensed matter, it is vital in SANS that decisions involving the set-up of the instrument are tailored towards the measurement. Since wavelength spread is normally fixed to around 10%, these decisions generally boil down to the choice between low flux and high collimation or vice-versa. In this section, the concepts of the previous few sections are summarised and paraphrased into a loose set of rules governing best practice.

A pictorial summary of how each of the agents involved in resolution affect the measurement of correlation lengths is shown in figure 2.16. The three correlation lengths of interest are: the radial correlation length (δq_{rad}), which corresponds to a variable d-spacing in the sample; a tangential correlation length (δq_{tang}), which quantifies orientational order (with respect to rotations of the vortex lattice about the induction); and an out-of-plane correlation length (δq_{norm}), which in this scattering geometry measures the meandering of the vortex lines along the direction of the induction (see figure 2.13). Measurements of these intrinsic length scales will be contaminated by extrinsic sources. For example, the radial and out-of-plane correlation lengths will both be convolved with beam divergence and wavelength spread and together these determine both the radial width on the detector and the rocking curve width in a rather complicated way described in the previous two sections.

To measure the radial and out-of-plane correlation lengths via the rocking curve width using the expression due to Cubitt *et al.* (1992) the collimation should be set to a sufficiently high degree such that the width of the rocking curve is not resolution limited. However, not much is to be gained by going below the width due to wavelength

spread because this sets the minimum extrinsic width of the rocking curve and neutrons will be wasted.

If the radial spot width is used to deduce the correlation lengths then the choice of collimation is largely arbitrary because, from Bragg's law, the radial spot width cannot be larger than the narrowest of the distributions contributing towards resolution. Nevertheless, using this technique requires performing a rocking curve to establish the Bragg angle so it is still worth setting the collimation to be comparable in effect to that of wavelength spread.

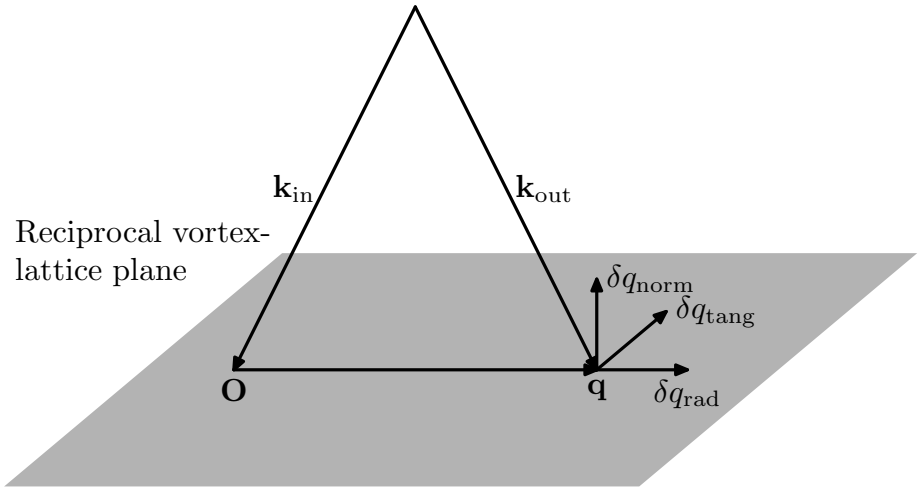

Fig. 2.16: The measurement of correlation lengths in different directions. The radial and out-of-plane correlation lengths, δq_{rad} and δq_{norm}, both lie in the scattering plane and hence convolve with wavelength spread and radial beam divergence to define the radial spot width and rocking curve width. The tangential correlation length, δq_{tang}, is convolved with the tangential beam divergence to give the tangential spot width.

Only if good tangential resolution is required is it worth increasing the collimation any further. The tangential correlation length will be convolved with the beam divergence to give the measured tangential width on the detector and wavelength spread plays no role at all. On occasion it may be worth sacrificing neutron flux if, for example, the diffraction pattern consists of many domains and resolving spots becomes an issue. Though in general, if good tangential resolution is needed it may be worth performing the experiment in the geometry where the field is applied perpendicular to the incoming beam. In this geometry, the scattering triangle (figure 2.16) lies in the plane containing the reciprocal lattice vectors and diffraction peaks that were separated

by only a few degrees azimuthally on the detector are now separated by a few degrees in *rocking angle*.

Once the instrument has been set-up and the appropriate resolution realised, it is useful to have a picture of how much of reciprocal space the diffractometer is sensitive to in any given measurement. The net effect of the three contributions to resolution (wavelength, collimation and mosaic spread) described above is to sample a finite crescent-shaped region of reciprocal space. The function $S_{\lambda_n \omega \phi}(q_x, q_y)$ describing this has been calculated assuming Gaussian distributions of the relevant quantities (see appendix B). A plot of $S_{\lambda_n \omega \phi}(q_x, q_y)$ for a rock in ϕ from $-0.8°$ to $0.8°$ in $0.2°$ steps is shown in figure 2.17. The other angle (ω) is fixed at zero for the duration of the rock and $\lambda_n = 10\,\text{Å}$. The wavelength spread is chosen to be 10% and the standard deviations in beam divergence and mosaic spread (both horizontally and vertically) are all $0.14°$. The figure demonstrates clearly the "fuzzy" Ewald sphere sweeping through the "fuzzy" vortex lattice plane and at each rocking angle a distribution of the in-plane structure is sampled. The last plot (bottom right) is of the sum over the entire rock from which it can be seen that any diffraction peaks lying along the horizontal (*i.e.* orthogonal to the direction of rocking) are well illuminated. This is an example of the virtue of poor resolution in that it allows many Bragg peaks to be observed simultaneously. Indeed when working at low inductions — and hence low q — it is often sufficient to measure at $\omega = 0 = \phi$ if only structural information is sought. However, at high q the temptation to use poor resolution as an economy is best avoided because of the shifting of spots as a function of rocking angle, which will give false structural information. Indeed, it is normally well worth rocking through a diffraction peak rather than making an educated guess of the Bragg angle (*e.g.* by assuming an isotropic triangular vortex lattice) and measuring there.

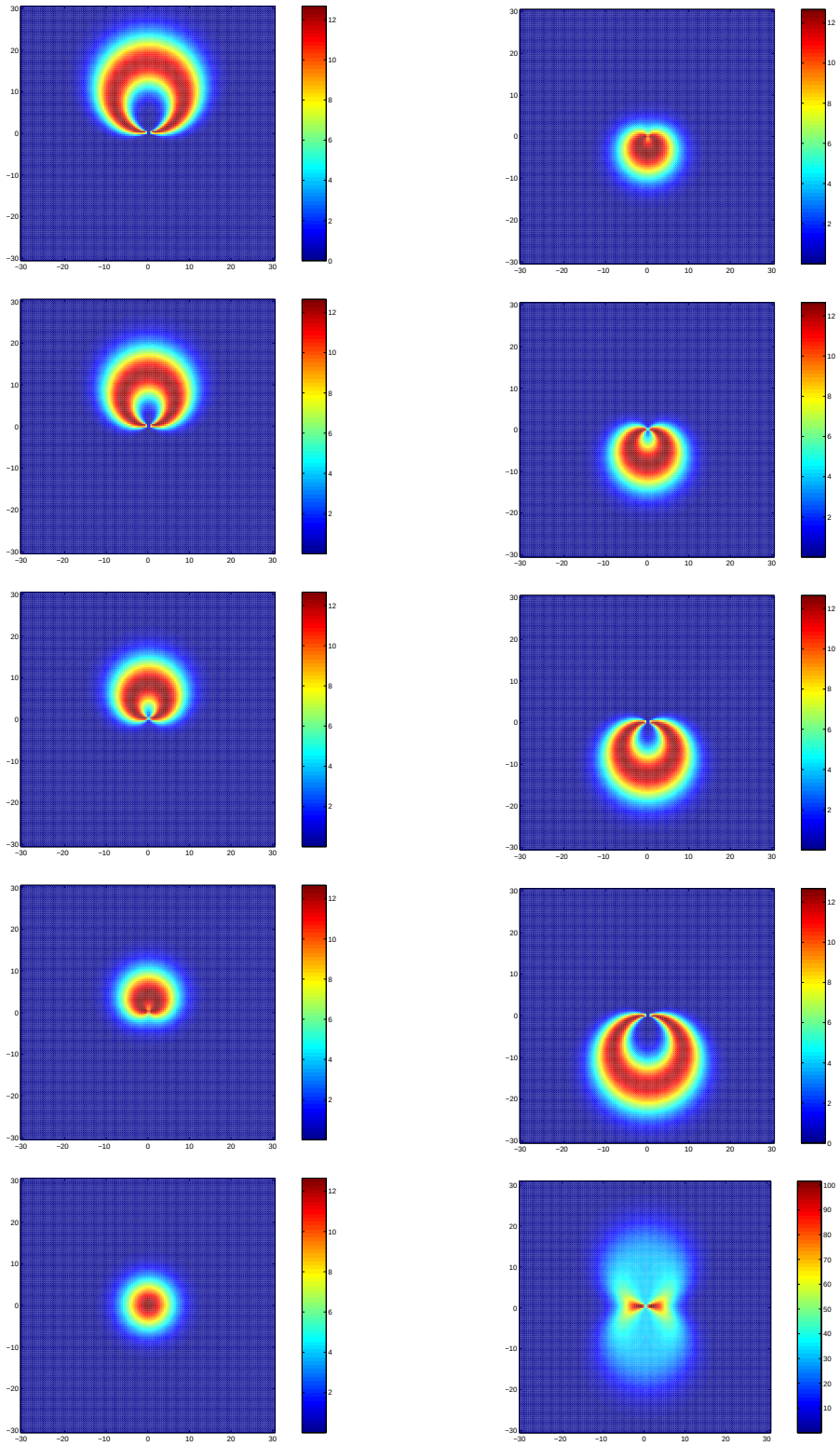

Fig. 2.17: Plots of the reciprocal space sampling function (arbitrary) units for the sequence $\phi = -0.8°, -0.6°, -0.4°, -0.2°, 0°, 0.2°, 0.4°, 0.6°, 0.8°$. The other parameters are $\omega = 0$, $\lambda = 10\,\text{Å}$, $\sigma_\lambda = 1\,\text{Å}$, $\sigma_\zeta = 0.2° = \sigma_\eta$ (see appendix B). Bottom right plot is the sum of plots. The plot axes are in mÅ^{-1}.

17. Other probes of the vortex lattice

SANS is not the only weapon in the vortex physicist's armoury. A plethora of other techniques are employed, each with their own advantages and disadvantages with respect to SANS. In this section, a brief review of a selection of these techniques and their application to structural studies of the vortex lattice is presented.

One strategy for extracting information about the vortex lattice is to look for its effect on macroscopic sample properties. Near a vortex structural phase transition a jump in the free energy or its derivative is expected. Thus the measurement of a thermodynamic quantity, such as heat capacity ($C_H = -T(\partial^2 G/\partial T^2)_H$) or magnetisation ($M = -(\partial G/\partial H)_T$), may pin-point the location of a structural phase transition in reversible (low pinning) samples. For example, Park *et al.* (2005) have recently used both magnetisation and specific heat measurements to identify a re-entrant triangular-square-triangular phase transition in the vortex lattice of $LuNi_2B_2C$. (This type of transition, common in the borocarbides, is related to non-local effects — see section 7). Magnetisation has also been exploited in identifying vortex lattice melting in high-T_c materials (see, for example, Zeldov *et al.*, 1995). So too have thermal measurements: in $YBa_2Cu_3O_{7-\delta}$, Schilling *et al.* (1997) have used a differential heat-capacity technique to establish the melting line. (Vortex lattice melting in high-T_c materials is first-order and is manifest by a peak in both the magnetisation and the heat capacity.)

In non-reversible samples, features in the magnetisation may also indicate a vortex matter transition. A second peak in the irreversible part of the magnetisation curve can be attributed to a sudden increase in pinning (section 9). Such peaks have been observed in $YBa_2Cu_3O_{7-\delta}$ (Deligiannis *et al.*, 1997) and $Bi_2Sr_2CaCu_2O_8$ (Khaykovich, 1996) and were attributed to a transition from weak disorder (Bragg glass) to strong disorder (vortex glass). The magnetisation data are supported by resistivity measurements (*e.g.* Shibata, 2002), which provide a good measure of the strength of pinning.

The principal drawback to thermodynamic and transport measurements is that although they can provide useful information (such as the order of a phase transition), they do not measure the vortices directly. Therefore any interpretation regarding the nature of the transition is subject to speculation and inference. For example, Rosenstein and Knigavko (1999) have interpreted the second peak in the magnetisation of

$YBa_2Cu_3O_{7-\delta}$ as due to a structural phase transition (from distorted triangular to square) in the vortex lattice, which softens the vortex lattice and hence increases the propensity for it to pin. In such instances, structural information gleaned from SANS can resolve ambiguities (see chapter III).

Vortices may be imaged directly using a class of local magnetic probes (see Bending (1999) for a review). Amongst these techniques is the so-called Bitter decoration technique which was used by Essman and Traüble (1967) to see vortex lines on the surface of a type-II superconductor. The Bitter decoration technique works by decorating with a fine magnetic powder the ends of vortices as they emerge from the sample; an electron microscope is then used to study the resulting pattern. This enables the structure of the vortex lattice to be examined over a small surface region ($\approx 30 \times 30$ vortex lines), which reveals both the local coordination and the presence of pinning centres and dislocations. At larger scales, magneto-optical imaging provides similar information. It relies on the Faraday rotation by the local magnetic field of a circularly polarised light beam passing through a magneto-optical layer deposited on the sample surface. Although it cannot be used to image individual vortex lines, it can discern microstructural features such as domains or flux penetration at sample edges.

Other local magnetic probes work on the principle of scanning rather than imaging. These include scanning hall-probe microscopy and magnetic force microscopy (Bending, 1999). Scanning hall-probe microscopy is particularly useful in that it directly measures the local field profile at the sample surface. (Magnetic force microscopy also, in principle, measures the local field, but obtaining it from the raw data is more difficult due to the complex magnetic interaction between the sample surface and the microscope tip.) However, all these local probe techniques (scanning and imaging) suffer from the constraint that their spatial resolution is poor (particularly true for magneto-optical imaging). They are therefore limited to low field studies which renders many of the phase transitions associated with unconventional superconductivity or non-local effects inaccessible. The fact that they only measure the vortex lattice at the surface (not the bulk) and only sample a small region are additional objections that may favour the use of SANS for structural studies.

Scanning tunneling microscopy (STM) is a local technique that is not constrained

to low inductions. STM measures the differential conductance as a function of sample bias and is essentially a spectroscopy of the quasi-particle states. In the bulk (where the order parameter is constant) the differential conductance will exhibit a peak at a bias equivalent to the superconducting gap. However, inside a vortex core there are bound quasi-particle states (with energy $\sim \Delta^2/2E_{\mathrm{F}}$) and STM can also probe these states (Hess *et al.*, 1990). By scanning the tip of the microscope at a fixed bias corresponding to these bound states, a map of where the vortices lie can be obtained. STM has atomic resolution therefore there is no practical limitation to the induction at which this technique can be used.

Since STM measures the local density of states of quasi particles, it is quite complementary to SANS and μSR (see below), which are sensitive to the magnetic properties of vortices. In particular, STM allows a more direct measurement of the symmetry of the order parameter by its effect on the local density of states near a vortex core (see, for example, Shibata, 2003a). In a fairly recent development Pan *et al.* (2000) have investigated the vortex lattice in $Bi_2Sr_2CaCu_2O_{8+\delta}$ with a dilute concentration of Zn atoms, which act as pinning centres. By performing separate scans over the surface at energies corresponding to the vortex bound states and to the Zn impurities they were able to obtain indepedent images of both the pinning centres and the vortices.

Despite its apparent superiority over other local probes, STM still suffers from only being able to sample a *small region* of the *surface*, rather than the sample-averged bulk measurements provided by SANS and μSR. However, STM remains a valuable tool for structural studies and the spectroscopic information it also furnishes is a welcome bonus, if not the principal reason for employing the technique.

Like SANS, μSR is sensitive to the magnetism of the vortices and is a bulk measurement (see Sonier *et al.*(2000) for a review of μSR applied to the vortex lattice). In μSR the muons incident on the sample are produced by pion decay with a kinetic energy of roughly 4 MeV and their polarisation opposite to their momentum. After the muon has come to rest (a process which is very quick and preseves spin direction) it precesses in the local field according to its Larmor frequency, $\gamma_\mu/2\pi = 135.5342\,\mathrm{MHz.T^{-1}}$ until it decays (with a mean lifetime of about $2.2\,\mu$s). When it decays, the muon emits a positron preferentially in the direction in which its spin was pointing. The asymme-

try in emission allows muons to measure the local field. By implanting muons into the sample at random positions* one by one and measuring by two (or more) oppositely placed detectors the asymmetry in emitted positrons as a function of time after implantation, μSR gives the probability density for local internal fields (known as the lineshape). For example, consider the simple case of a uniform field applied to a sample with no magnetisation. The muons all precess at the same frequency and therefore the asymmetry spectrum will just be sinusoidal (after corrections for the muon lifetime, which will multiply the asymmetry by an exponential damping term). If the field is non-uniform (as is the case when a vortex lattice is present) then the sinusoidal asymmetry spectrum will be depolarised. Inverse Fourier transforming the time dependent muon polarisation measured in this way gives the muon lineshape, $P(B)$. The form of the lineshape depends on the details of the vortex lattice structure and, unlike SANS, structural information cannot be immediately gleaned from the lineshape. Rather, it is neccessary to calculate the lineshape from theory and compare.

Due to its relative simplicity, SANS would appear to be the experiment of choice for most structural studies of the vortex lattice. There are, however, many occasions when μSR measurements provide useful complementary information for SANS. One such example is provided by the work of Kealey *et al.* (2000) in which both the magnitude *and* the sign of the vortex lattice Fourier components in Sr_2RuO_4 were deduced. SANS alone cannot measure the sign of the Fourier component because the intensity of scatter is proportional to the modulus squared, but by guessing the signs (or taking them from theory) the real space vortex lattice can be reconstructed from which the muon lineshape may be calculated and compared with experiment.

There are even instances when muon experiments are preferred to SANS. The scattered intensity from SANS is proportional to λ^{-4} so SANS may not be viable in samples with very long penetration depths. μSR, on the other hand, has much less constraint as the penetration depth affects the width of the muon lineshape by $\langle B^2 \rangle \propto \lambda^{-4}$.

* Actually, the positively-charged muon is most likely to bind to a negatively-charged ion, but this does not matter for vortex lattice studies because the intervortex distance is much larger than the interatomic spacing. Therefore the field is sampled randomly.

Another experiment that is worth mentioning — purely on the merit of its ingenuity — is the novel atomic-beam magnetic-resonance technique utilised by Hauglin *et al.* (2003) to study the low-field vortex lattice in $YBa_2Cu_3O_{7-\delta}$. In these experiments a thermal beam of ^{39}K atoms in the lower of two hyperfine-split levels is prepared by optical pumping. Passing the beam over the surface of a type-II superconductor in the mixed state causes the atoms in the beam to experience a time dependent B-field that drives the transition to the higher hyperfine state ($f = 462\,\mathrm{MHz}$). The probability of transition depends upon not only the field distribution of the vortices (*i.e.*, to leading order the inter-vortex spacing), but also on the velocity of a given atom in the thermal spectrum. Therefore, after passing through a Stern-Gerlach magnet, which rejects atoms still in the lower hyperfine state the number of excited atoms needs to be detected as a function of velocity. This is accomplished through resonant fluorescence, which may be tuned to a particular velocity by the Doppler shift.

The atomic-beam magnetic-resonance technique suffers a number of disadvantages: it only measures in one-dimension; is confined to low fields and only looks at the surface. Its main advantage with respect to gaining structural information is that it is a sample-averaged experiment. Furthermore, it is has one important advantage over SANS: it is much more sensitive to the vortex lattice close to T_c.

CHAPTER III

Vortex lattice transition in YBCO

18. Introduction

In this chapter the main results of the thesis are presented. The principal result is the observation by SANS of a field-induced transition to square coordination in the vortex lattice in a fully oxygenated sample of $YBa_2Cu_3O_{7-\delta}$ (YBCO). This has been supplemented by additional measurements on the dependence of this transition on temperature and applied field direction.

The motivation for the measurements has been provided by the need to understand how the unconventional nature of *d*-wave superconductivity in materials such as YBCO affects the vortex state. There has been much theoretical speculation concerning the stability of the square vortex lattice in *d*-wave materials and these measurements are amongst the first to corroborate the theoretical investigations; other similar investigations have been carried out on $La_{1.87}Ca_{0.17}CuO_4$ (Gilardi *et al.*, 2002), $CeCoIn_5$ (Eskildsen *et al.*, 2003) and $Nd_{1.85}Ce_{0.15}CuO_4$ (Gilardi *et al.*, 2004 and section 29 of this thesis).

Very much related to *d*-wave anisotropy are non-local effects in *s*-wave materials (see section 7). Here too are often seen unconventional square vortex lattices. In high-T_c materials, both *d*-wave and non-local effects are, in principle, at play. In $La_{1.87}Ca_{0.17}CuO_4$ it appears that the Fermi surface anisotropy is sufficient to countermand the order parameter anisotropy (Gilardi *et al.*, 2002).

This chapter will begin with a brief overview of the properties of YBCO* and previous measurements of the vortex lattice therein, with emphasis placed on structural

* See, *e.g.*, Waldram, 1996 and Burns, 1991 for a more elaborate account of the material presented there including similar material on high-T_c materials in general. The material presented in section 19 is intentionally biased towards vortex physics.

studies of static vortex lattices. Next, the experimental results and data analysis will be presented in detail, starting first with the field-dependent transition before exploring the other directions of parameter space, namely temperature and field angle.

19. YBCO: history and basic properties

YBCO is one of the most famous and well-studied members of the family of high-temperature cuprate superconductors. The first high-temperature (high-T_c) superconductor to be discovered was $La_{2-\delta}Sr_\delta CuO_4$ (Bednorz & Müller, 1986), which when optimally-doped has a T_c of 30 K. YBCO was discovered by Wu *et al.* (1987) about one year later and its relatively high T_c of 93 K (at optimal doping) is partly responsible for its ubiquity in studies of high-T_c materials. In addition to its high T_c, YBCO is also renowned for its extremely large H_{c2}, which, depending on oxygen doping, can easily exceed 100 T with the field applied parallel to the crystal c-axis. Such figures are typical of high-T_c compounds and are indicative of the large values of κ in these materials.

With such favourable superconducting properties relative to low-T_c materials, it might seem surprising that high-T_c compounds have failed to encroach into some of the areas of application of superconductors (such as superconducting magnets, for instance). A significant obstacle to this goal is their crystal structure: they are all ceramic materials (perovskites), which are neither malleable nor ductile and extremely difficult to synthesise as wires on an industrial scale. Nevertheless, the remarkable properties of high-T_c superconductors arise out of their complicated structure and therefore an appreciation of the complex crystallography is essential.

Figure 3.1 shows the crystal structure of $YBa_2Cu_3O_6$ and $YBa_2Cu_3O_7$ (Burns, 1991). Both have a perovskite-like crystal structure consisting of CuO_2 planes separated by BaO or Y layers. These two compounds sit at opposite ends of the oxygen doping scale of the parent compound, $YBa_2Cu_3O_6$. The electronic properties of YBCO are dominated by the CuO_2 planes, which form electronic states due to the overlap of the $3d$ orbitals of copper and the $2p$ orbitals of oxygen; the remainder of the electrons may be neglected as they are too strongly involved in ionic bonding*. In $YBa_2Cu_3O_6$, which

* An exception is electrons from dopant atoms (*e.g.* Ca in $La_{2-\delta}Ca_\delta CuO_4$). These

is tetragonal, there is one hole per CuO_2 plane per unit cell, but at low temperatures it is an insulating antiferromagnet. This is the so-called Mott insulating state and it occurs in systems with low carrier density where Coulomb repulsion overcomes the desire to form a Fermi liquid with a partially-filled band.

When oxygen is added to $YBa_2Cu_3O_6$, they occupy sites interstitial to the Cu atoms sandwiched between the BaO planes. For large enough concentrations of these oxygen "impurities" two things occur. Firstly, it causes the compound to become orthorhombic (at low temperatures) and in doing so forms the CuO chain structures running parallel to the crystal b direction. The very slight orthorhombicity, which sets in below about 500°C, is responsible for the appearance of twin planes (see section 9 and Forgan *et al.*, 1998b). The formation of twin planes may be suppressed by applying uniaxial pressure to a sample along one of the basal plane axes in the tetragonal phase and maintaining the pressure during cooling. The uniaxial pressure causes the b-direction to form preferentially perpendicular to the force applied; this trick may be applied to "de-twin" other cuprate superconductors.

The second effect of the extra oxygen atoms is electronic in nature. Since the oxygen atoms form O^{2-} ions, each oxygen takes two electrons that come from changes in valence of the copper atoms. This creates holes and thus alters the electronic properties of YBCO profoundly. As δ is decreased from 1 to 0, $YBa_2Cu_3O_{7-\delta}$ evolves from a low-temperature antiferromagnetic ground state to a superconducting ground state, which appears at around $\delta = 0.4$. At this point the Néel temperature collapses and T_c begins to rise. (The maximum value of T_c occurs at around $\delta = 0.04$.) Such behaviour is common to all cuprate high-T_c materials and in this doping regime the normal state appears to be metallic, but in a quite unconventional sense as it does not fit nicely into the Fermi liquid picture of metals. For example, resistivity is found to be linear in temperature above T_c. That could easily be interpreted in terms of the standard phonon-dominated scattering rate, but microwave measurements indicate that the eletron-electron scattering is the dominant process (Schofield, 1999). The linear dependence disagrees with the T^2 scattering rate predicted by Fermi liquid theory. However, a T^2 dependence *is* observed in experiments on the Hall effect (Waldram,

types of non-oxygen dopants may also be substituted into YBCO (see section 30).

1996). The apparent contradiction between resistance and Hall-effect measurements is one of the outstanding problems in understanding the normal state properties of the cuprates, which is seen as vital in gaining understanding of the superconducting state.

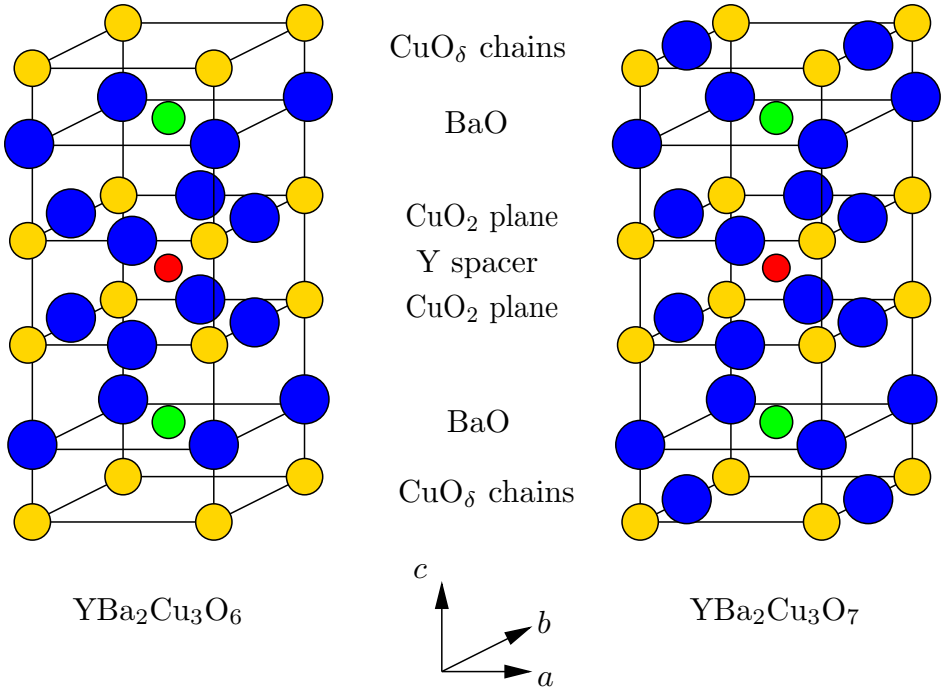

Fig. 3.1: The crystal structures of $YBa_2Cu_3O_6$ (left) and $YBa_2Cu_3O_7$ (right). The Y (●), Ba (●), Cu (●) and O (●) atoms are represented by spheres. The lattice parameters for $YBa_2Cu_3O_6$ are roughly $a = 3.8\,\text{Å} = b$ and $c = 11.6\,\text{Å}$. In the fully oxygenated compound b is larger than a by roughly 1%.

Despite the difficulties in applying Landau's Fermi liquid theory to YBCO, a band theory description does have some success in explaining its electrical properties for values of δ close to zero. However, there is a paucity of good experimental evidence on the Fermi surface due to the difficulty in measuring the de Haas-van Alphen oscillations. (de Haas-van Alphen experiments need to be performed at low temperatures and hence require very large fields to suppress superconductivity.) Photoemission experiments (see Liu *et al.*, 1992; Schabel *et al.*, 1998a and 1998b) have led the way in this field and, surprisingly, reveal good agreement with calculations based on an independent electron model. The Fermi surface is found to consist of four pieces. Two of these are roughly cylindrical hole surfaces and are mostly associated with the CuO_2 planes. An example of one of these surfaces is shown in figure 3.2. Within a tight binding picture, the distortion of this surface from a perfect cylinder is due to anti-bonding overlaps

forming S. As a result, the anisotropy of the Fermi surface velocity is such that it is large along the (100) and (010) directions compared to the (110) direction. This is relevant in vortex physics because non-local corrections to the London theory depend upon the anisotropy of the fourth moment of the Fermi velocity (see section 7), which is non-zero for the type of distortion shown in figure 3.2 since $3\langle v_{\mathrm{F},x}^2 v_{\mathrm{F},y}^2\rangle \neq \langle v_{\mathrm{F},x}^4\rangle$.

The other two pieces are associated with the CuO chains. The presence of the CuO chains gives rise to non-zero anisotropy of the second moment of the basal plane Fermi velocity. (The highly schematic Fermi surface shown in figure 3.2 has an isotropic second moment of Fermi velocity, *i.e.* $\langle v_{\mathrm{F},x}^2\rangle = \langle v_{\mathrm{F},y}^2\rangle$.) This has an impact upon the vortex lattice even within the simple local anisotropic London theory (section 3) and the penetration depth along a and b will be unequal as a result of the fact that $v_{\mathrm{F},a} \ll v_{\mathrm{F},b}$. Measurements of the anisotropy of penetration depth, γ_{ab}, ($\gamma_{ab}^2 = m_a/m_b$) typically give values of around 1.2–1.4, depending on the degree of doping (see, for example, Dolan *et al.*, 1989; Sun *et al.*, 1995 and Wang *et al.*, 1998).

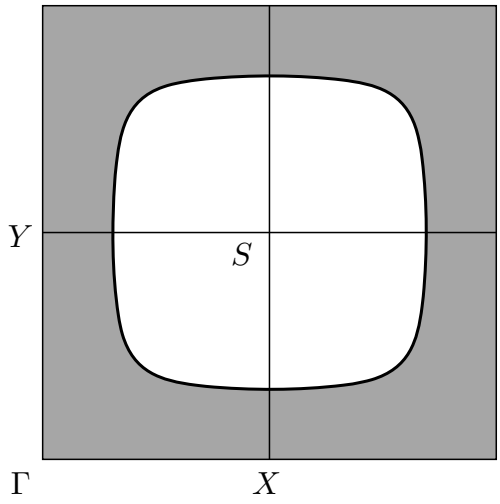

Fig. 3.2: Schematic of one of the cylindrical hole Fermi surfaces in YBCO. The points Γ, X, Y and S define the vertices of the first Brillouin zone.

None of these pieces of Fermi surface has much dispersion along the k_z direction, which is reflected by the rather two-dimensional character of YBCO's electrical properties. Indeed the effective mass is much larger along the c-axis than along a or b. Typically $\gamma_{ac} \approx 5$, which translates to an effective mass anisotropy of 25 between the c-axis and basal plane. The large c-axis effective mass can have an even greater effect on the vortex lattice than the basal plane anisotropy (see the next section and references

therein).

In its superconducting state, YBCO exhibits typical high-T_c behaviour, *i.e.* large H_{c2} and a large κ (≈ 100). As a consequence of the latter, the penetration depth is long ($\lambda_{ab} \approx 150\,\mathrm{nm}$) and the coherence length is short ($\xi_{ab} \approx 2\,\mathrm{nm}$). The superconducting properties of YBCO are heavily influenced by the electronic structure described above. The coherence length displays a similar degree of anisotropy as the penetration depth and is typically very short along the c-axis ($\xi_c \approx 0.5\,\mathrm{nm}$). Although short, it is still considerably larger than the distance between CuO_2 planes and hence YBCO is nowhere near as two-dimensional as other high-T_c superconductors such as $La_{2-\delta}Sr_\delta CuO_4$ (LSCO) or $Bi_2Sr_2CaCu_2O_{8+\delta}$ (BSCCO) (which is particularly anisotropic). Therefore, vortices in YBCO may be regarded as fully three dimensional objects over a large field range and there is no need to consider the Josephson coupling between adjacent planes as is done in the Lawrence-Doniach model (Lawrence & Doniach, 1971). In contrast, the vortices in BSCCO are more weakly coupled between adjacent planes and can decouple into "pancake" vortices at sufficiently high fields (Cubitt *et al.*, 1993).

Another important property of YBCO vis-à-vis the vortex lattice is the unconventional nature of the superconductivity and the non-s-wave symmetry it confers. Measurements by Tsuei *et al.* (1994), which show a non-integer multiple of the flux quantum threading a specially arranged junction of three crystals, assert that YBCO is a d-wave superconductor. There is more or less a consensus on the d-wave nature, but there are still detractors. Müller (2002) has suggested that d-wave effects in high-T_c materials are a surface phenomenon and that high-T_c materials are in fact bulk s-wave superconductors. This has some support from measurements of the penetration depth in YBCO using muons (Harshman *et al.*, 2004), but the general view seems to be in favour of d-wave pairing.

20. Vortex lattice structure in YBCO

To date there have been numerous structural investigations of the vortex lattice in YBCO at low fields. Amongst the first of these is the decoration experiments by Gammel *et al.* (1987), which show a well-ordered triangular lattice at low fields. These

measurements have been improved upon by Dolan *et al.* (1989) who, using the same method, were able to extract the anisotropy in the basal plane ($\gamma_{ab} = 1.15 \pm 0.02$) and the anisotropy of the basal plane with respect to the c-axis ($\gamma_{ac} = 5.5 \pm 1$).

In 1990 YBCO became the first high-T_c vortex lattice to be investigated by SANS (Forgan *et al.*, 1990). The success of this and many subsequent neutron studies on the intrinsic behaviour of the vortex lattice has been fuelled by the availability of good-quality single-crystal samples of YBCO — in particular, samples free from precipitates and impurity phases, which may obscure the intrinsic structure of the vortex lattice by inducing disorder (see section 9) or stymie SANS measurements by giving too much background (see the guidelines laid out in section 12). However, even good-quality crystals of YBCO contain twin planes and vortices are very susceptible to pinning by these (section 9 for an explanation of pinning due to twin-planes). When the field is applied parallel to these extended planar defects, a four-fold diffraction pattern ensues due to pinning along the {110} (twin plane) directions, which when viewed along the (001) direction has four-fold symmetry in the approximately tetragonal crystal. This can be very pronounced in heavily twinned samples and they often *appear* to have a square vortex lattices as was demonstrated by Yethiraj *et al.*(1993a). In the same study, it was shown that by rotating the field away from parallel to the c-axis the influence of the twin planes is degraded. More recent SANS measurements (Simon *et al.*, 2004) have explored this effect further. In that study, the vortices were found to pin to twin planes for rotations of the field away from the twin plane direction less than some critical angle (about 10° in their sample). Beyond the critical angle the vortices were found to meander through the sample, *i.e.* locally following a twin plane, but crossing over to the next twin plane in order to keep the global direction of the vortex parallel to the applied field.

Despite the inherent difficulties imposed by sample limitations, SANS has led the way in understanding the intrinsic structure of the vortex lattice in YBCO. At intermediate fields, where $H_{c1} \ll H \ll H_{c2}$, a high-κ superconductor like YBCO would be expected to follow quite accurately the London model. (Recall that a large κ translates to small ξ and large λ. In this regime the intervortex spacing, a_0, is large enough for the order parameter to remain constant except for a small region $\sim \xi \ll a_0$

near the core, but the spacing is small enough for the vortices to overlap magnetically ($\lambda \gg a_0$) and therefore interact strongly.) Experimentally, the London model has been reasonably well established at low fields, but there is evidence that this behaviour is perturbed slightly by unconventional sources (see later).

An early SANS investigation of the vortex structure in YBCO was undertaken by Yethiraj *et al.* (1993b). They observed the vortex lattice in a twinned crystal in a modest applied field of 0.8 T. The value obtained for the c-axis anisotropy, γ_{ac}, was 4.5 ± 0.5, which is in agreement to that determined by decoration. Moreover, they studied the variation of the vortex lattice anisotropy with angle of applied field from parallel to the c-axis, to 80° to the c-axis. It was found that the anisotropy of the vortex lattice varies with angle of induction as predicted by anisotropic London theory (section 3). The orientation of the vortex lattice in this experiment was found not to agree with that predicted by Campbell *et al.* (1988), but it was attributed simply to twin plane pinning, which has a much stronger effect on orientation than does the rather weak London correction. Therefore in *lightly* twinned samples (as opposed to *heavily* twinned samples such as the ones used in the experiments by Yethiraj *et al.* (1993a) and Simon *et al.* (2004)) the structure of the vortex lattice agrees with the predictions of London theory, but the orientation is determined by twin-plane pinning.

Unfortunately, Yethiraj *et al.* (1993b) were unable to deduce γ_{ab} due to its small value and the complications of twinning. The basal plane anisotropy has been measured with SANS by Johnson *et al.* (1999) using a detwinned crystal. They obtained a value of $\gamma_{ab} = 1.18 \pm 0.02$, which is similar to most estimates (see section 19), but note that since basal plane anisotropy comes from the presence of the CuO chains, γ_{ab} depends strongly on the oxygen doping.

In addition to measuring the basal plane anisotropy, Johnson *et al.* were able to observe the intrinsic orientation of some domains of the vortex lattice. With a field of 0.5 T applied parallel to the crystal c-axis, they saw four well-formed vortex-lattice domains, each with a distorted triangular configuration. Two of these originated from residual twin-plane pinning and were "removed" by applying the field at a small angle (1.5°) to the c-axis. (The domains pinned to the twin planes do not disappear; instead, they form 1.5° away in rocking angle from those domains whose vortices are parallel to

the applied field and can therefore be separated out of the diffraction pattern containing the intrinsic domains.) The other two domains, which were found to be equally populated, were aligned with the crystal axes and their distorted triangular structures were found to be static up to the highest field investigated (4 T). Consequently, Johnson *et al.* concluded that these were entirely conventional London-like vortex lattice domains. However, the fact that these well-ordered domains are both found to be oriented along the crystal axes implies that they are not strictly conventional because there is no preferred orientation in either the local London and Ginzburg-Landau theories. The reason for this has already been discussed in the context of the London theory (see section 3). In the Ginzburg-Landau theory it arises because the relevant interaction length scales (λ and ξ) scale in the same way with the anisotropy in the diagonal situation. (If the anisotropies in λ and ξ were different then scaling away the anisotropy would be impossible.) Although the exact nature of the alignment discovered by Johnson *et al.* is unclear, it is presumably due to coupling of the vortex lattice with the underlying crystal lattice and it therefore seems natural that both domains should align with the major symmetry directions of the crystal.

More satisfying evidence for unconventional behaviour in the low-field vortex lattice in $YBa_2Cu_3O_{7-\delta}$ was found by Johnson *et al.* when they applied the field at an angle to the *c*-axis. Here anisotropic London theory *does* make a prediction as to which orientation the vortex lattice will favour (in addition to the effect on the structure of coupling the large *c*-axis effective mass to that of the basal plane) (Campbell, 1988). Although $YBa_2Cu_3O_{7-\delta}$ is biaxial, the argument outlined in section 3 still holds, but the conclusion is slightly modified. The vortex lattice will still be oriented perpendicular to the axis of rotation. However, this may not necessarily correspond to the short magnetic direction because if *a* is the axis of rotation, then the effective mass given by coupling the *b*- and *c*-axes may still be smaller than the effective mass along *a*. This alignment was indeed observed at low fields (0.2 T) by Johnson *et al.*. With *a* as the axis of rotation they discovered a tendency for the vortex lattice oriented along *b* (or its projection perpendicular to the field) to gain intensity with increasing angle, at the expense of the *a*-oriented domain*. However, at higher fields (above 3 T) they observed

* Johnson *et al.* (1999) indulge in a confusing habit of describing a vortex lattice

a transition from the predicted anisotropic London orientation to one where the vortex lattice is oriented along the crystal a-direction. No explanation was offered by the authors (and indeed, according to the present author, none has ever been forthcoming), but it seems sensible to suspect that this effect derives from vortex core interactions, which though negligible at low inductions, ought to become more important as the field is increased and the vortices experience greater overlap.

Curiously, the results with b as the axis of rotation were less conclusive and only a polycrystalline ring of scattered intensity was observed. This was attributed by Johnson *et al.* to some unqualified effect of the CuO chains, but note also that in this configuration the mixing of the c-axis mass with the a-axis mass enhances the basal plane anisotropy making the penetration depth along the b-axis (*i.e.* perpendicular to the predicted nearest-neighbour direction) significantly longer. Since the vortex lattice elastic moduli are proportional to λ^{-2} (Brandt, 1995) the vortex lattice should be softer and the vortices more susceptible to disorder-induced displacements perpendicular to the theoretical nearest-neighbour direction.

In summary, the results of Johnson *et al.* seem to imply a more-or-less anisotropic London-like vortex lattice at low fields ($< 4\,\mathrm{T}$) in which the orientation is governed by small perturbations. The work of Kealey *et al.* (2001) can be interpreted as broadly agreeing with this assessment. In that experiment, the transverse field components arising from applying the magnetic field at an angle to the c-axis (see section 3) were measured by their ability to spin-flip neutrons. The sample used was the same as that used in Johnson *et al.* (1999) and exhibited the expected anisotropic-London dependence of vortex lattice distortion as a function of angle of applied field. However, the magnitude of the transverse field components, which may be measured by the ratio of spin-flip to non-spin-flip scattering, was found to be inconsistent with the values pre-

---

domain with, for example, a scattering vector, $\mathbf{q}$ parallel to the a-axis as being "a-oriented". This is not rigorously true: such a $\mathbf{q}$-vector implies that a set of vortex lattice *plane normals* are oriented along a; the vortex nearest-neighbour direction is actually *perpendicular* to this. Such muddling of real and reciprocal space is avoided here and vortex lattice orientation is defined in terms of a nearest-neighbour direction in real space *not* reciprocal space, unless explicitly stated.

dicted by anisotropic London theory (Thiemann *et al.*, 1989; Kealey *et al.*, 2001) given the measured value of $\gamma_{ac} = 4.5$. Reconciliation is possible, but only if a much larger value of γ_{ac} (about 50) is assumed. Kealey *et al.* pointed out that this discrepancy could be due to the fact that the structure of the vortex lattice is frozen in at the irreversibility temperature, which is rather higher than those at which the experiment was performed. (It is the generally accepted dogma in SANS that experiments should be performed at low temperatures where the penetration depth is shorter and, as a consequence, the scattering stronger.) On the other hand, the transverse field components will reflect more truthfully the intrinsic low-temperature behaviour, which, it appears, is far more two-dimensional and unconventional than at high temperatures.

Not all measurements of the vortex lattice structure in $YBa_2Cu_3O_{7-\delta}$ concur with a London-like picture. For example, Keimer *et al.* (1994) believed they had found evidence for unconventional behaviour, which they associated with gap anisotropy. This was based on the observation of four oblique lattices (with an angle of 74° between equal length lattice vectors) at fields of up to 5 T. Keimer *et al.* rejected the thesis that these domains could be attributed to conventional triangular lattices that were distorted by basal plane anisotropy and pinned by twin planes. Instead, they presented an argument based on the flawed evaluation of the London Gibbs free energy as a function of angle between reciprocal lattice vectors, which misleadingly showed an increasing instability of the minimum (60° for an isotropic vortex lattice) with increasing applied field. They wrongly assigned this to a failure of London theory to account accurately for their data. That conclusion was refuted by Forgan & Lee (1995), who demonstrated that the calculation of the Gibb's free energy was tainted by numerical artefacts generated by an inappropriate sharp cut-off. Walker & Timusk (1995) employed a simple argument based on symmetry, which states that any orientation-favouring pertubation of an undistorted vortex lattice cannot simultaneously give the alignment and the structure in the distorted frame as seen by Keimer *et al.*. Instead Walker and Timusk claim, quite correctly, that Keimer's data can be interpreted simply in terms of mass anisotropy and twin-plane pinning. More recent measurements (Johnson *et al.*, 1999; Brown *et al.*, 2003 and section 22) have reinforced these views.

Scanning tunnelling microscopy (STM) studies of the vortex lattice structure of

$YBa_2Cu_3O_{7-\delta}$ have also hinted at departures from simple anisotropic London theory. In an early study, Maggio-Aprile *et al.* (1995) discovered in an applied field of 6 T a structure similar to that observed by Keimer *et al.*, which they also interpreted — probably incorrectly as explained above — as a distorted square vortex lattice. These data are not very reliable measurements of the vortex structure because a region containing only 5×5 vortices was sampled. Moreover, the vortex lattice, by their own admission, was very disordered ("glass-like" in their words) and within the sampled region the density of vortices was found to correspond to an induction *greater than* the applied field. However, assuming that the extent of the low energy states is $\approx \xi$, these STM measurements do provide a unique measurement of the anisotropy in the basal-plane coherence length ($\xi_a/\xi_b = 0.67$). This value is consistent with the broad range of values (see the previous section), but it would be of great interest to have measurements in the same sample of the anisotropy in *both* the penetration depth and the coherence length to see whether a scalable London or Ginzburg-Landau picture really was valid.

Other STM investigations of the structure have been performed by Fischer *et al.* (1997) at 6 T and Shibata *et al.* (2003b) at 1 T. Fischer *et al.* state that after the effects of anisotropy are undone their results are consistent with a square vortex lattice. Shibata *et al.* are somewhat more ambivalent in this respect and more concious of the fact that STM samples only a small region of sample. Indeed, they turn this fact to their advantage by examining the influence of a twin plane on the vortex lattice. (Other local probes are capable of this — see section 17 — but they are restricted to much lower fields than STM.) Their results indicate that the vortex lattice is severly distorted in the vicinity of a twin plane, but that the distortion persists only for roughly five vortex spacings, which is much shorter than the typical twin plane distance in their lightly twinned sample. The influence of a twin plane on orientation stretches much further, though, and is seen by Shibata *et al.* to still be controlling the vortex lattice orientation at distances of order 1 μm away. This provides a beautiful microscopic confirmation of similar conclusion made from SANS experiments (*e.g.* Yethiraj *et al.* (1993b), Johnson *et al.* (1999) and Brown *et al.* (2004)).

21. High-field vortex lattice studies: set-up

The wealth of theoretical work concerning the impact of non-local and d-wave effects on the vortex lattice in YBCO — and the corresponding lack of good experimental evidence for these structures — has motivated a programme of research exploiting SANS to study the vortex lattice in YBCO at high fields. Although structural phase transitions have been discovered in similar materials at lower fields (*e.g.* below 1 T (Gilardi, 2003) in $La_{2-x}Sr_xCuO_4$), much higher fields are demanded in YBCO because loosely speaking, the field at which such a transition occurs is expected to scale with H_{c2}, which can be as much as 150 T for YBCO (approximately a factor 3 higher than $La_{2-x}Sr_xCuO_4$). Anticipating that the field range of interest for YBCO will be roughly 1–10 T a high-field SANS facility has been commissioned* on the SANS-I instrument at the Paul-Scherrer Institut, Villigen, Switzerland. Central to the facility is a custom-made horizontal-field cryomagnet manufactured by Oxford Instruments (U.K.). This magnet is composed of a Helmholtz pair and is capable of delivering fields of up to 10 T with a field uniformity of 0.2% over a 1 cm sphere, which easily encompasses the sample used here. The maximum field can be improved by pumping on a lambda-stage to reduce the temperature of the coils and increase their critical current, allowing fields as large as 11 T.

The sample environment is provided by a variable-temperature insert, which is cooled by pumping helium through a needle valve in an arrangement similar to many cryostats. (During operation, a small amount of helium exchange gas (about 50 mbar at 100 K) is left in the sample space to ensure good thermal contact with the gas being pumped through the tail.) The temperature is computer controlled via a Lakeshore temperature controller and, for well-adjusted PID values, is stable to within 0.1 K. The system is very versatile and allows sample temperatures from room temperature down to about 1.5 K to be attained, thus making it ideal for studies of temperature dependence.

* This venture was initiated by a collaboration lead by E.M. Forgan of the University of Birmingham with substantial resources from the Paul-Scherrer Institut, The University of Zürich and Warwick University.

When in use, the cryomagnet is mounted on top of the sample turntable and goniometer, which facilitate rocking onto the Bragg condition (goniometer tilts of up to 10° are possible). Care has to be taken with the motors driving the turntable and goniometer due to the potentially very large stray field. In particular, magnetic shaft encoders cannot be used and must be replaced with optical ones. The stray fields generated by the cryomagnet are even sufficient to affect adversely the operation of the motors themselves. This has necessitated the positioning of the motors at fairly large distances from the magnet and the use of long drive shafts.

The other important element in these high-field measurements is the sample itself. It has already been explained in section 12 that good sample quality is a must for favourable signal-to-noise ratios in SANS. Likewise, since the intrinsic properties of the vortex lattice are of primary interest, a sample with as little disorder as possible is desirable. To this end, a small (36 mg) high-quality single-crystal of overdoped YBCO (T_c =86 K) was used. The sample was grown by A. Erb from a melt in a $BaZrO_3$ crucible, which is known to provide very low-impurity samples. (See Erb *et al.*, 1996 for a description of the growth process.) To reduce pinning even further the sample was oxygenated close to O_7, freeing the CuO chains of oxygen vacancies that might pin vortices. However, the sample is not pinning free and does contain a low density of twin planes. These complicate matters slightly by giving correlated pinning (which is to be avoided when looking at intrinsic properties) and presumably contribute to the small-angle background scattering, but on balance, they are better than random point disorder, which would reduce the signal from the vortex lattice by increasing the rocking curve width.

The sample was mounted on an aluminium plate and surrounded by a cadmium mask according to the recommendations of section 12. The sample was oriented with its *c*-axis perpendicular to the backing plate and the whole assembly was constructed such that it was easy to swap between having {100} horizontal/vertical or {110} horizontal/vertical. The alignment was checked using by taking an X-ray Laue pattern, after which the sample assembly was fixed to a "sample stick" and installed in the cryomagnet with the *c*-axis was parallel to the applied field. By attaching a laser pointer to the top of the stick and projecting the laser spot on a wall some distance away,

accurate rotations of the c-axis with respect to the field could be achieved using the magnet turntable. (Naturally, any rotation was performed *above* T_c!)

In most measurements, the vortex lattice was formed by cooling through the irreversibility line with a field applied. (The experiments were performed at a "base" temperature of 4 or 5 K.) This offers an obvious advantage over the converse, namely applying a field after cooling, because not only will sample irreversibility inhibit flux penetration into the sample in the latter case, but the vortex lattice is also likely to be better ordered. Some authors (*e.g.* Dewhurst *et al.*, 2003) have reported an improvement in vortex lattice order by oscillating the applied field by some small amount (typically 10%) whilst going through the irreversibility line to "wiggle" the vortex lines into their equilibrium position. No benefit was found in this procedure here, which is probably testament to a comparatively high degree of reversibility in the sample.

22. Low field measurements

Before embarking on an examination of the high-field vortex lattice, it was necessary first to characterise the sample by studying the vortex lattice at lower fields. The sample was mounted with B parallel to the c-axis and the {110} (twin plane) directions horizontal/vertical, and was cooled to 4 K in an applied field of 1 T. From the work of Johnson *et al.* (1999) it is expected that anisotropic London theory will be a good description of the vortex lattice in this regime, although as pointed out in section 20 there is still controversy surrounding this issue so these measurements will provide a good check.

At 1 T the d-spacing for the undistorted triangular lattice is $d_\triangle$ =42 nm, hence at a wavelength of λ_n =8 Å a Bragg angle of about $\theta_\triangle = 0.5°$ is expected. Since the basal plane anisotropy is small, this gives a good guide to a suitable range of rocking angles. To reach the rocking curve peak of all the diffraction spots the sample was rocked over the range $[-1°, +1°]$ in 0.1° steps in both ω and ϕ (separately). Following the discussion in section 16, it is evident that in these scans the resolution volume will pass directly through the Bragg condition for **q**-vectors along {110}, but **q**-vectors lying along {100} will only be caught by the "side" of the Ewald circle. It transpires that this is sufficient because at the extremes of the rocks the component of the Ewald

circle along {100} is $1^\circ/\sqrt{2} = 0.7^\circ$, which just covers the Bragg angle for the spots in this direction (assuming not too much distortion).

In figure 3.3 is shown the sum of the data acquired in the rocking curves described above, minus background rocks taken at 100 K (well above T_c). (In these measurements the detector was placed at 12.7 m from the sample and the beam was collimated over 11 m; this proved sufficient to resolve the spots clearly.) Subtracting backgrounds is an efficient way of removing the strong background signal from the sample. Nevertheless, near to the beam centre the small-angle background scattering becomes very large (it varies as an inverse power law in q) therefore even subtraction leaves a residual background from the statistical fluctuations arising from the subtraction of two large signals. Furthermore, there are systematic remanents of the background due to thermal expansion of the sample stick which alters the background between low and high temperatures. In figure 3.3 pixels near the centre of the pattern containing this detritus have been zeroed.

The pattern shown in figure 3.3 clearly has the same four-fold symmetry as the (twinned) sample and bears considerable resemblence to the patterns obtained by Keimer *et al.* (1994). Twenty distinct spots are identifiable, four of which are significantly stronger than the other sixteen and lie along {110}. Their arrangement is highly suggestive of four anisotropic-London vortex lattice domains pinned to the twin planes. The origin of each of these domains is illustrated schematically in figure 3.4. The twin planes divide the sample into two orientations of crystallographic domain with interchanged anisotropy and so there exist two different environments in which the vortex lattice can form. The presence of strong spots along {110} indicates that the orientation of each vortex domain is controlled by the twin planes. The microstructural measurements of Shibata *et al.* (2003b) demonstrate that the twin planes exert an influence on the vortex lattice over large distances. Presumably then, two different vortex domains will exist in the vicinity of a twin plane with interchanged anisotropy either side of the twin plane. Within a given crystallographic domain, it is most probable that there exist a number of vortex domains with the same anisotropy, but oriented in different directions as prescribed by the orientation of the twin planes that define the borders of the crystal domain. Therefore, four different domains are expected from

the two possible anisotropies and two possible twin plane orientations.

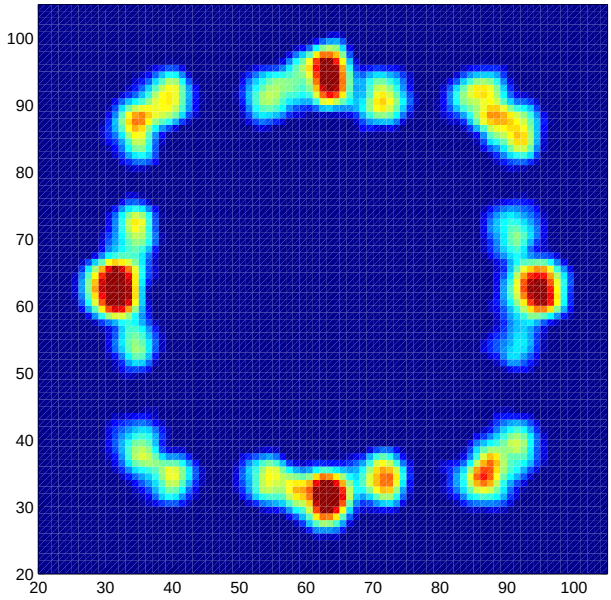

Fig. 3.3: Sum of the horizontal and vertical rocks described in the text showing the vortex lattice in the $YBa_2Cu_3O_7$ sample at 1 T. A background above T_c has been subtracted and the the centre of the diffraction pattern has been masked by software. The data have also been smoothed numerically by convolving twice the raw data with a 3×3-pixel pseudo-Gaussian kernel.

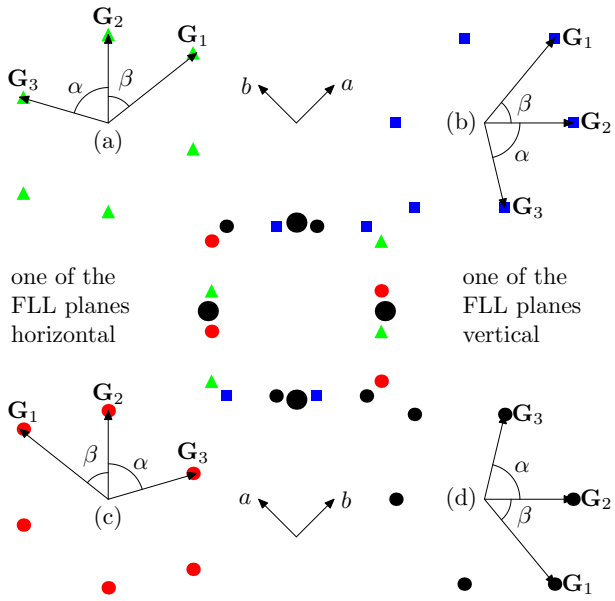

Fig. 3.4: A schematic showing how the four vortex lattice domains in figure 3.3 are formed. Twinning in the crystal gives rise to two different anisotropies and two possible orientations enforced by the twin planes. The spots along the twin plane direction are stronger in part due to the fact that two vortex lattice domains contribute to each.

Few would argue with the statement that the twin planes control the orientation of the vortex lattice, but the fidelity of the other part of the preceding hypothesis, that the vortex lattice structure is given by London theory, can only be established by more detailed analyses. The positions on the detector of the twenty spots have been calculated by fitting each spot to a two-dimensional Gaussian — a procedure used extensively throughout this work*. There is no particular justification for this choice of fitting function; indeed the exact shape of a Bragg peak will depend upon the forms of the distributions in wavelength, beam divergence and mosaic spread (section 14). Regardless of these exact forms, a Gaussian will give a reliable estimate of the width of a spot and a very good estimate of its position for all reasonable distributions. The Gaussian fitting function is defined by six parameters: height, A; x-position, x_0; y-position, y_0; (nominally) minor width, σ_1; (nominally) major width, σ_2 and angle of orientation, ϕ:

$$G(x,y) = A \exp\left(-\frac{[r(x,y)\cos\zeta(x,y)]^2}{2\sigma_1^2}\right) \exp\left(-\frac{[r(x,y)\sin\zeta(x,y)]^2}{2\sigma_2^2}\right), \qquad (22.1)$$

where $r(x,y) = \sqrt{(x-x_0)^2 + (y-y_0)^2}$, $\zeta = \text{atan}[(y-y_0)/(x-x_0)] - \phi$ and (x,y) is the position of the spot on the detector. The fitting routine allowed a variable background, but it was set *a priori* to zero since its effect has already been countered by the background subtraction. Due to the close proximity to one another of spots on the detector, the spots could not be fitted separately. Instead, by selecting an appropriate fitting region, fits were done on four groups of three spots for the spots along {110} (top, bottom, left and right in figure 3.3) and four groups of two spots

* The data reduction presented in this thesis was performed using SANSAN, a text-based menu-driven FORTRAN SANS analysis programme evolved at Birmingham by generations of experimenters — including the present author — under Prof. E.M. Forgan. A rival programme called GRASP developed by C. Dewhurst at ILL, Grenoble was also used. It has most of the functionality and reliability of SANSAN, but beats its older redoubtable brother in terms of useability: it has a graphical user interface. At the time of writing, details of SANSAN are obtainable from Prof. E.M. Forgan at the University of Birmingham and GRASP is available from the ILL website (http://www.ill.fr/lss/grasp/grasp_main.html).

for the spots along {100} (along the diagonals of the figure). In each case, only data taken near the peak of the rocking curve for a particular group were utilised thus simultaneously minimising the fractional error in the data and preventing any of the systematic errors described in section 16. The rocking curves for two ensembles of spots (top and top-left) are shown in figure 3.5.

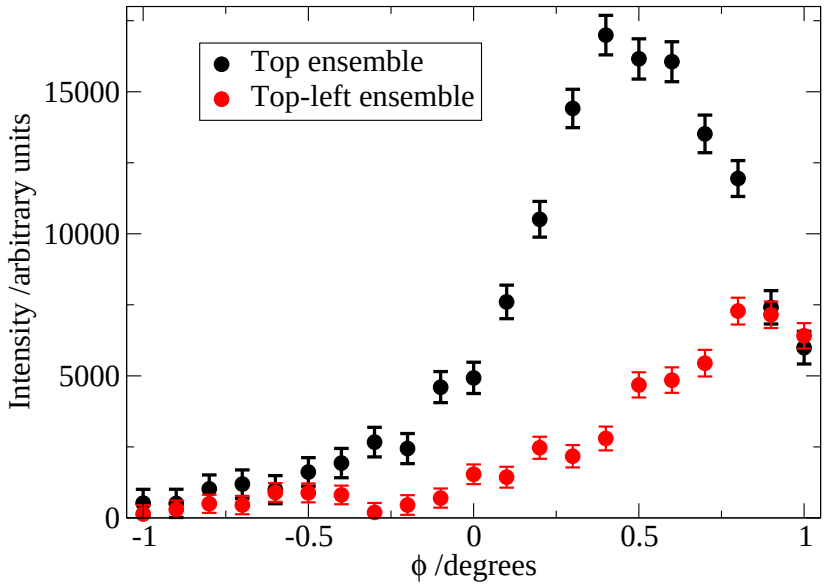

Fig. 3.5: Rocking curves as a function of ϕ for two of the sets of spots shown in figure 3.3. The curves were obtained by summing as a function of angle the foreground minus background counts over a box encompassing the spots.

Once the spot positions had been obtained, the spots were all mapped onto the same anisotropy by taking the spots associated with one orientation of anisotropy (the red and black domains at the bottom of figure 3.4) and shifting their angular position by 90°. This mapping brings all of the spots onto the same ellipse whose eccentricity, ϵ, can then be fitted. For convenience the fit was done to r^{-2}, which is linear in $\cos^2\theta$:

$$\frac{1}{r^2} = \frac{(1-\epsilon)^2}{R^2}\cos^2\theta + \frac{\epsilon^2}{R^2}, \tag{22.2}$$

where (r, θ) are the polar coordinates of the spot relative to the detector centre, which was determined self-consistently by averaging over pairs of $\mathbf{q} \leftrightarrow -\mathbf{q}$ symmetry-related spots (and checked against a centre-of-gravity fit of an attenuated image of the direct beam) and R is the "radius" of the ellipse. The fit yields a value of $\epsilon \equiv \gamma_{ab} = 1.28(1)$ for

the anisotropy. This value is quite similar to the one obtained by Johnson *et al.* (1999), but larger (statistically significant), which almost certainly reflects the higher degree of anisotropy due to the well-oxygenated CuO chains in the stoichiometric sample used here.

To verify the London nature of these vortex domains, the anisotropic London vortex lattice structure was calculated by minimising numerically the free energy (equations 2.8 and 3.5) using the measured value γ_{ab}. The minimisation was performed subject to the constraint that one of the reciprocal lattice vectors, $\mathbf{G}_2$, lies along $\{110\}$. This is tantamount to infinitely strong pinning by twin planes, which is a reasonable approximation given the ambivalence to orientation of the London vortex lattice. The calculation was performed for a flux density corresponding to an inter-vortex distance of $0.1\lambda_{\mathrm{L}}$. As discussed in section 2, an *isotropic* Gaussian cut-off was used to force convergence of the free energy sum. The cut-off was implemented with a coherence length, $\xi = 0.02\lambda$, or equivalently, $\kappa = 50$, which is within the extreme type-II limit.

The computer programme listed in appendix C performs the minimisation by exploring a reasonable region of the vortex-lattice-structure parameter space. The two variable parameters in the problem are the angle, β, between the primitive reciprocal lattice vectors and the length of $\mathbf{G}_2$ (see figure 3.4) measured with respect to the length of the corresponding isotropic triangular lattice (the lengths of the other two vectors, $\mathbf{G}_1$ and $\mathbf{G}_3$ are fixed by flux quantisation). The parameter space surveyed was $\beta \in [40^\circ, 80^\circ]$ and $G_2 \in [0.8, 1.2]$ with a granularity of $(\delta\beta, \delta G_2) = (1.0^\circ, 0.025)$. Summing over 100 reciprocal lattice vectors in each direction (sufficient given the chosen value of ξ) determined the equilibrium vortex lattice structure to be that defined by $\beta = 52^\circ$ and $G_2 = 0.975$. Therefore the other angle, α, defined in figure 3.4 is $\alpha = 73^\circ$ and the other vector lengths are $G_1 = 1.127$ and $G_3 = 0.934$ (see table 3.1 for a summary). (Summing over 1000 vectors gave the same answer with no difference in the free energy to one part in 10^{10}.)

The equilibrium London vortex lattice structure may also be determined by a simple scaling argument that only works when the induction is along a principal axis as in the present case. Scaling works by taking an isotropic vortex lattice (equal-length basis vectors each spanned by angles of 60°) and distorting it by the anisotropy in

the penetration depth. Consider an isotropic vortex lattice in reciprocal space (or real space, since the two structures are related by a 90° rotation); the lattice vectors are given by:

$$\begin{aligned} \mathbf{G} &= G_0[\cos(\psi)\hat{\mathbf{x}} + \sin(\psi)\hat{\mathbf{y}}] \\ \mathbf{G}_\pm &= G_0[\cos(\psi \pm 60^\circ)\hat{\mathbf{x}} + \sin(\psi \pm 60^\circ)\hat{\mathbf{y}}] \end{aligned} . \tag{22.3}$$

In equation 22.3 the vector $\mathbf{G}$ lies at an angle ψ to the (isotropic) horizontal basal plane axis and two other basis vectors of the same length, $\mathbf{G}_\pm$, lie at 60° relative to $\mathbf{G}$. The distortion is applied by scaling by $\gamma_{ab}^{\frac{1}{2}}$ in along $\hat{\mathbf{x}}$ and $\gamma_{ab}^{-\frac{1}{2}}$ along $\hat{\mathbf{y}}$ (for an anisotropy γ_{ab}):

$$\begin{aligned} \mathbf{G}' &= G_0 \left[\gamma_{ab}^{\frac{1}{2}} \cos(\psi)\hat{\mathbf{x}} + \gamma_{ab}^{-\frac{1}{2}} \sin(\psi)\hat{\mathbf{y}}\right] \\ \mathbf{G}'_\pm &= G_0 \left[\gamma_{ab}^{\frac{1}{2}} \cos(\psi \pm 60^\circ)\hat{\mathbf{x}} + \gamma_{ab}^{-\frac{1}{2}} \sin(\psi \pm 60^\circ)\hat{\mathbf{y}}\right] \end{aligned} . \tag{22.4}$$

The angle ψ is still a free parameter because of the orientational degeneracy of the London vortex lattice. However, twin-plane pinning requires that $\mathbf{G}'$ lies at an angle of 45° to the anisotropic basal plane axes, which determines the angle ψ in the isotropic frame:

$$\tan(\psi) = \gamma_{ab} \tan(45^\circ) \tag{22.5}$$

Using the measured anisotropy of $\gamma_{ab} = 1.28(1)$, a vortex lattice pinned along the twin plane direction may be derived by scaling an isotropic vortex lattice with a basis vector at $\psi = 52^\circ$ to the basal plane axes. (By inspecting figure 3.4 it can be seen that $\mathbf{G}'$ may be identified with $\mathbf{G}_2$ (the reciprocal lattice vector along the twin plane direction) and $\mathbf{G}'_+$ and $\mathbf{G}'_-$ are equivalent to $\mathbf{G}_3$ and $\mathbf{G}_1$ respectively.) The results are summarised in table 3.1, which demonstrates the equivalence of the scaling and numerical techniques apart from slight differences caused by the granularity of the numerical technique.

The values derived from the scaling argument and the numerical minimisation of the anisotropic London free energy are found to be in good agreement with the experimental values deduced from the fitted positions of the spots. Since four degenerate vortex lattice domains are observed, the structure was calculated from experimental data by averaging over symmetry-related spots. The results are summarised in table 3.1 alongside the theoretical predictions. All show very good agreement with the theoretical values, but there appears to be a slight systematic discrepancy (about 1%) between the the calculated and measured values of G_1 (and as, a consequence, the other

reciprocal lattice vector lengths). The origin is unclear, but given the good agreement of the other values it is unlikely that this affects the conclusion that the 1 T data are consistent with London theory. It is most likely due to miscalibration of either the sample-detector distance ($G_1 \propto s_{\mathrm{det}}$), the mean wavelength ($G_1 \propto \lambda_{\mathrm{n}}$) or the applied field ($G_1 \propto B^{-1/2}$). (Resolution effects are an unlikely cause since the spots were fitted using data symmetric about the rocking curve.)

Low-field vortex lattice ($\gamma_{ab} = 1.28(1)$)			
Parameter	Measured	Numerical	Scaling
G_1 /m$\mathring{A}^{-1}$	17.0(1)	16.72	16.73
G_1/G_2	1.149(8)	1.156	1.144
G_1/G_3	1.21(4)	1.21	1.222
α	73(2)°	73°	72.3°
β	51(1)°	52°	51.3°

Table 3.1: Summary of the structural parameters of the low field vortex lattice derived from numerical minimisation of the London free energy, a scaling argument and data taken at 1 T. Differences between the numerical and scaled values can be attributed to the finite parameter step-size in the minimisation programme.

23. Field-dependent structural phase transition

Having established the London nature of the low-field vortex lattice in the over-doped YBCO sample, measurements were undertaken to examine its field dependence up to the highest available field (11 T). As before, the vortex lattice was formed by field-cooling, done at intervals of 1 T over the field range 1–11 T (field applied parallel to the crystal c-axis).

The first indication of a field-dependent structural phase transition is given by the data taken at 4 T, which are displayed in figure 3.6. These data were taken with 6 m collimation, a sample-detector distance of 8 m (reduced from the value used at 1 T to account for the factor two increase in q) and a mean wavelength of 8 Å. The reduction in collimation compared to the 1 T data was necessary in order to gain good statistics over a reasonable amount of time. (Recall, that even assuming London-like vortices, which do not suffer a form-factor drop-off with field in their integrated intensity, there

is still a $B^{-1/2}$ dependence on the scattered intensity in equation 11.6 and so a factor two decrease relative to 1 T is expected in the very least.)

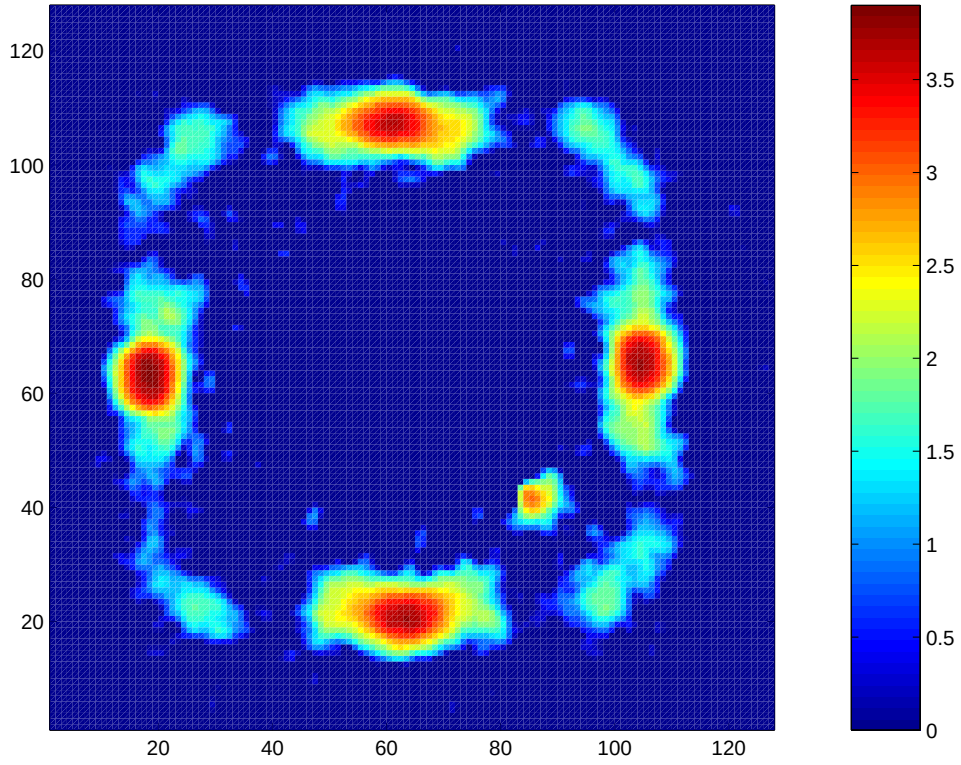

Fig. 3.6: Vortex lattice diffraction pattern taken at 4 T and a temperature of 5 K. The asymmetrically located bright spot in the bottom-left corner of the pattern results from poor background subtraction in that region and was observed at the same place on the detector in data taken at different applied fields using the same backgrounds. Careful inspection reveals a very slight misalignment ($\approx 1^\circ$) of the twin planes relative to the horizontal/vertical of the detector; it is of no importance to the nature of these measurement since the experiment has effective cylindrical symmetry with B parallel to the crystal c-axis.

Rather than rocking by simply ω and ϕ, the data at 4 T are acutally formed from a sum of *diagonal* scans designed to rock directly through the Bragg condition of the weak spot ensembles in the corners of the pattern. For the diffractometer set-up given above a Bragg angle of $\theta_\triangle = 1.1^\circ$ is expected, but due to the distortion of the vortex lattice, which tends to push the spots into the corner, the diagonal scan was done such that $\omega = \phi \in [0.9^\circ, 1.1^\circ]$ in 0.1° steps. (Obviously in terms of an absolute "diagonal"

angle, this corresponds to a range $\sqrt{2}$ larger than these numbers.) These short rocks were intended to gain as much structural information in as little time as possible: at 0.9° the "corner" spots are rocked on (this was verified by a rock down to $\omega = \phi = 0.5°$ at low statistics and with no backgrounds) and at 1.1° the spots horizontal and vertical in the pattern (*i.e.* those due to the twin planes) were rocked on.

Although some of the difference between the diffraction pattern at 4 T (figure 3.6) and that at 1 T (figure 3.3) can be attributed to the poorer resolution of the former, there are clear intrinsic differences too. The pattern is visually more square with the corner spots positioned further towards the vertices of the square whose basis vectors consist of equal combinations of the horizontal and vertical spot q-vectors. The spots have also coalesced somewhat, although it is not immediately discernible due to the decrease in resolution and requires further quantitatve analysis (see later).

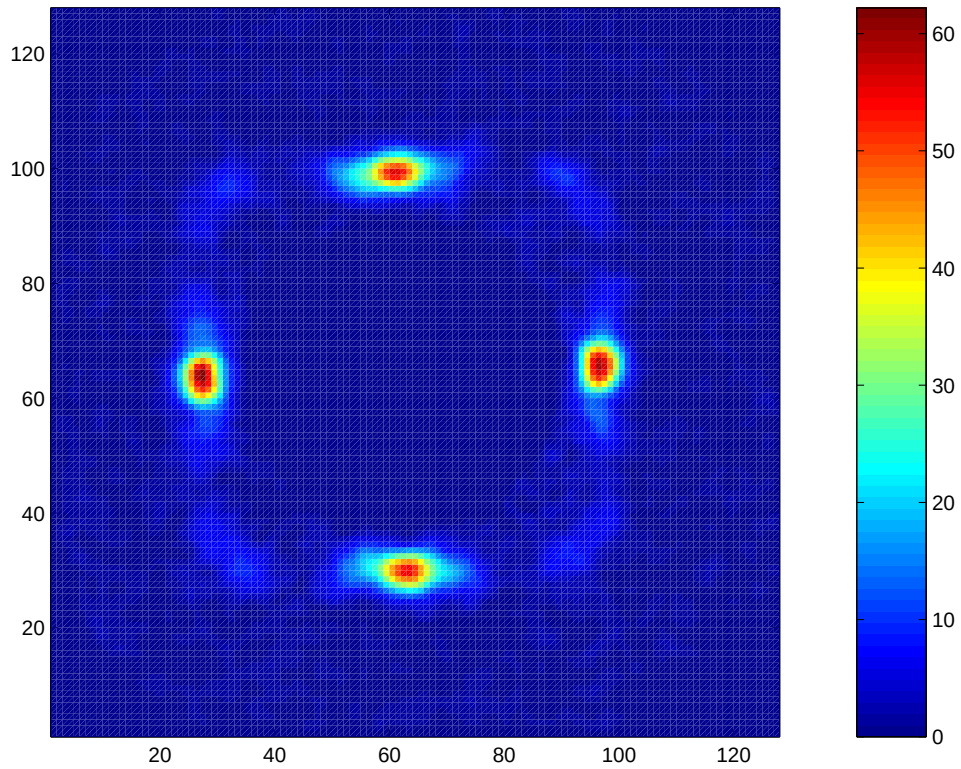

Fig. 3.7: Vortex lattice diffraction pattern taken at 6 T. Negative values, arising from statistical fluctuations in the background, have been zeroed in addition to those near the centre.

The evolution in vortex lattice morphology continues as the applied field is increased. In figure 3.7 is shown the diffraction pattern at an applied field of 6 T. These data were taken in a similar fashion as the data at 4 T, but the range of rocking angles was increased to $\omega = \phi \in [1.1°, 1.3°]$ (in 0.1° steps) to allow for the expected increase in the Bragg angle; the sample-detector distance was commensurately reduced to 6 m. The arrangment of the reciprocal lattice vectors at 6 T is very similar to that at 4 T, though the spots appear to have coalesced further. However, the intensity of the reflections lying directly along {110} has increased relative to the intensities of the other spots. It seems that even without much apparent change in the positions of the reciprocal lattice vectors, the observation of much stronger scattering along {110} indicates that nearest-neighbour correlations of vortices lying on a square lattice are becoming more important in determining the vortex structure. Next-nearest-neighbour correlations (corner spots) do not seem to be as prevalent as they scatter less (by roughly a factor four), probably due to a field-dependent reduction in the vortex form-factor along this direction (see figure 3.15 and discussion thereof).

The diffraction pattern at 7 T exhibits a remarkably different structure to those at 6 T and 4 T. In this pattern, which is shown on a logarithmic scale in figure 3.8, there is significant overlap of the spots. To combat the difficulty arising from the spot ensembles smearing into single entities, the collimation length was increased to 8 m*; naturally, the scattered intensity was reduced by a factor $(6/8)^2 \approx 0.5$. Despite the greater resolution of these measurements, there is still a much greater degree of coalescence of the spots. Each of the ensembles of three spots lying near the {110} direction appears to be converging into a single spot, as are the two-spot ensembles in the corners of the picture. The latter spots have also moved further out to the corner of the square and have become noticeably weaker compared to the same reflections observed at low fields (figure 3.8 is on a natural logarithmic scale). The implication is that each of the four vortex lattice domains present in the twinned sample is distorting into a square lattice.

* A slightly larger collimation length might have been chosen, but the next (larger) value was 11 m, which would result in an unacceptable reduction in count rate.

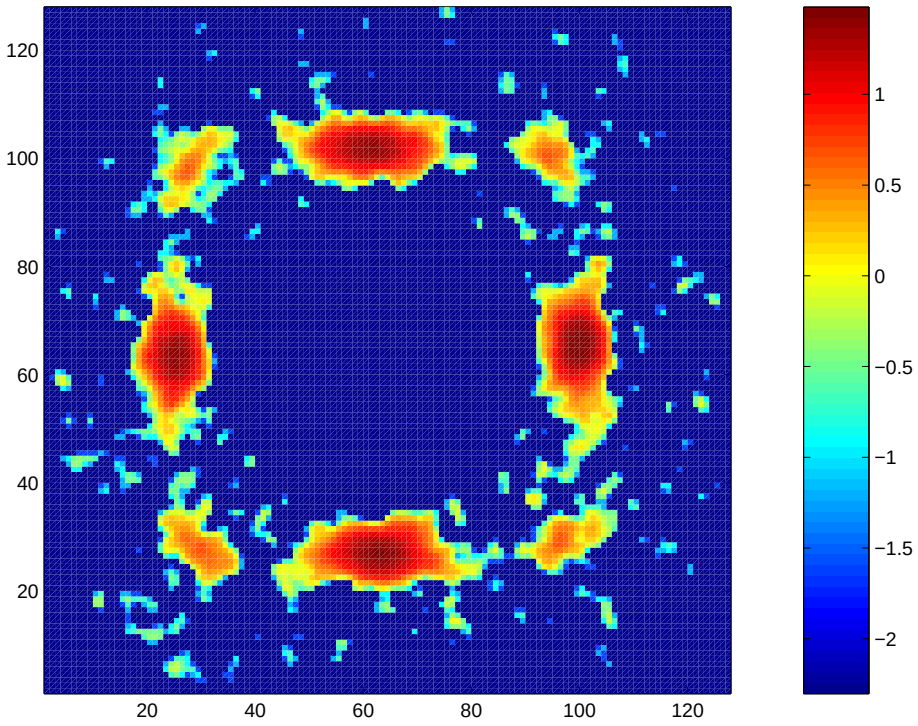

Fig. 3.8: Natural logarithm of the vortex-lattice diffraction pattern taken at 7 T.

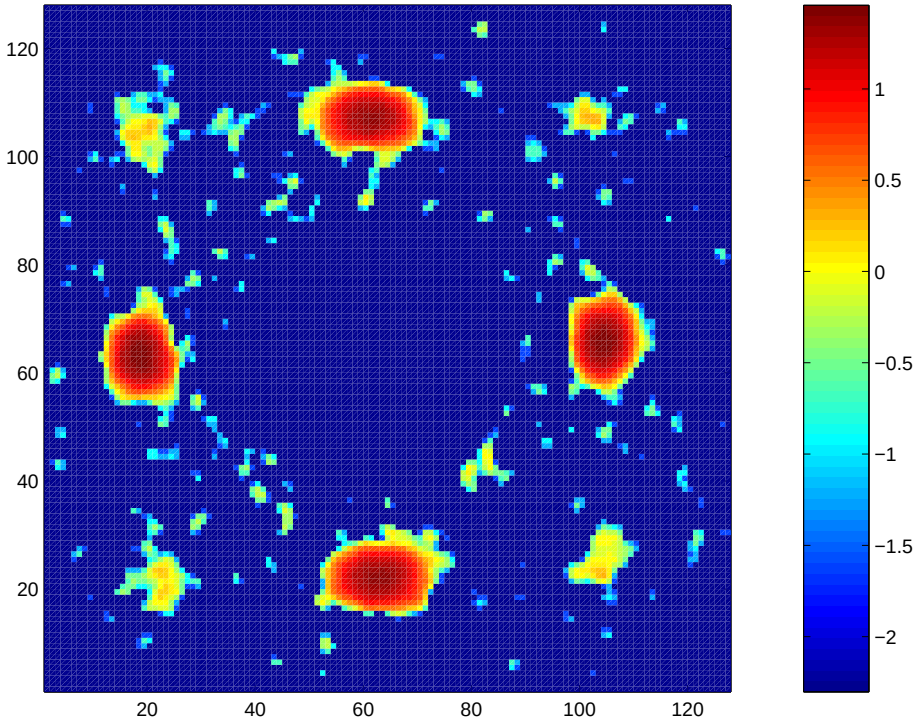

Fig. 3.9: Natural logarithm of the vortex lattice diffraction pattern taken at 9 T.

At 9 T (figure 3.9) the vortex lattice domains have a distinctly square structure. There appears only one spot along each {110} direction in these data; if these spots are composed of more than one reflection then they are resolution limited. The collimation has been relaxed to 6 m for these measurements since even at 8 m the spots would not be resolved into their putative components. It is likely that the degree of collimation required to remedy this would reduce the scattered intensity to intolerably low levels.

Note also that the diffraction peaks along the diagonal directions are weaker and tangentially narrower than in the 7 T data. These spots appear to have evolved into the second-order spots of a single-orientation square vortex-lattice domain. This is even clearer in the data taken at 11 T (figure 3.10) in which these spots are weaker still.

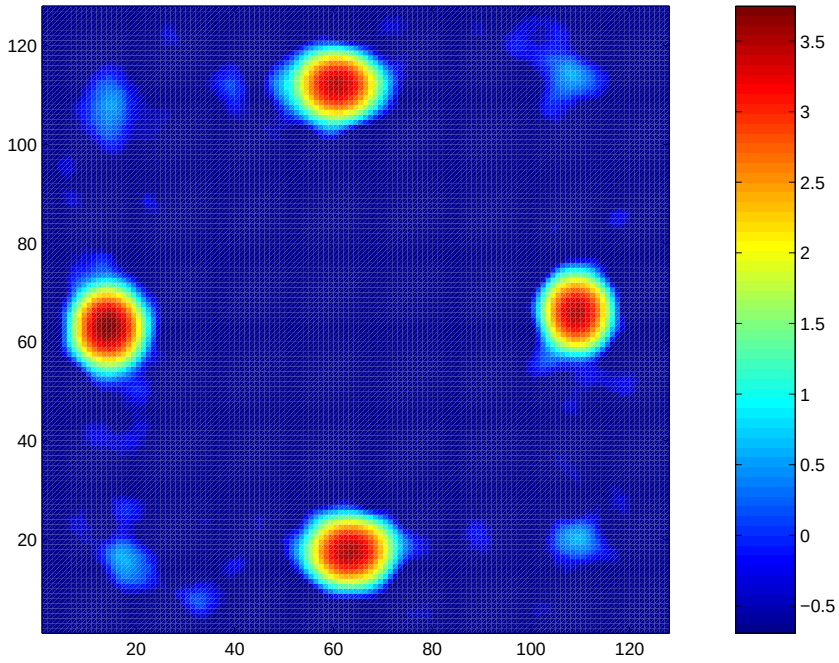

Fig. 3.10: Natural logarithm of the vortex lattice diffraction pattern taken at 11 T. To make the weak spots in the corner of this pattern more visible the data have been truncated above a threshold and numerically smoothed a further two times.

In the present experimental set-up there is no real hope of resolving the structural evolution of the vortex lattice beyond about 6 T. Partly, this is due to the poor resolution of SANS, which is inescapable, but it is also due to the degeneracy in orientation of the vortex lattice domains caused by the twin planes. Therefore the strategy to advance from that unsatisfactory position was to attempt to remove the degeneracy.

This was accomplished by rotating the sample about the vertical axis by a *small* angle such that the twin planes that were vertical ran instead at some angle to the applied field. It was found that rotating by only 5° vitiated the ability of the vertical twin planes to pin the vortex lattice. (The horizontal twin planes were unaffected because after rotation the applied field was still within these planes.) The rotation should also affect the intrinsic properties of the vortex lattice, but it is reasonable to suspect that such effects will be negligible because their dependence on the applied field direction is much less sensitive than that of the twin planes. For example, London theory predicts a change in distortion (equation 3.4) approximately proportional to $\cos\theta$; for $\theta = 5°$ it gives a difference of only 0.4%, which is a change smaller than the statistical error on the measurement of γ_{ab} quoted in section 22. Similarly, effects associated with non-local corrections to the London model and d-wave phenomena are also expected to deviate very little from their behaviour with B paralllel to the c-axis for small rotations of the sample.

In figure 3.11 is shown the result of the rotation described above on the vortex lattice diffraction pattern at 7 T. The figure shows data summed over an ω rocking curve through the spots near the horizontal ($\omega \in [\pm 0.9°, \pm 1.9°]$ in 0.1° steps) and a ϕ rocking curve through the vertical spots ($\phi \in [\pm 0.9°, \pm 1.9°]$ in 0.1° steps). Both scans were done with $s_{\mathrm{det}} = 6\,\mathrm{m}$ and $l_{\mathrm{coll}} = 6\,\mathrm{m}$, and backgrounds were re-taken above T_{c} since the slight sample rotation was expected to alter the background significantly. It is clear that the rotation has had the desired effect of removing two of the domains from the diffraction pattern. Those domains giving rise to strong scattering along the horizontal {110} direction (see figures 3.8 and 3.4) are not apparent in figure 3.11. It is not quite clear what happens to these domains. If they were replaced completely the remaining two domains would yield twice the scattered intensity. This does not appear to be the case, although there is a significant increase in the intensity of these spots. Rocking the sample further in ω around the position that the horiztonal spots would be expected to appear if they were still pinned to the twin planes produced no peak in the rocking curve (as might be predicted in a strongly twinned sample such as the one studied by Simon *et al.* (2004)). It is possible, given the frustration induced by the sample rotation that the flux associated with these twin planes forms a highly

disordered vortex state with a very wide rocking curve and hence immeasureably small Bragg peaks at any given angle. Inspecting figure 3.11 reveals very faint scattering distributed around a ring with roughly the correct **q**-value for 7 T, but no structure is discernible.

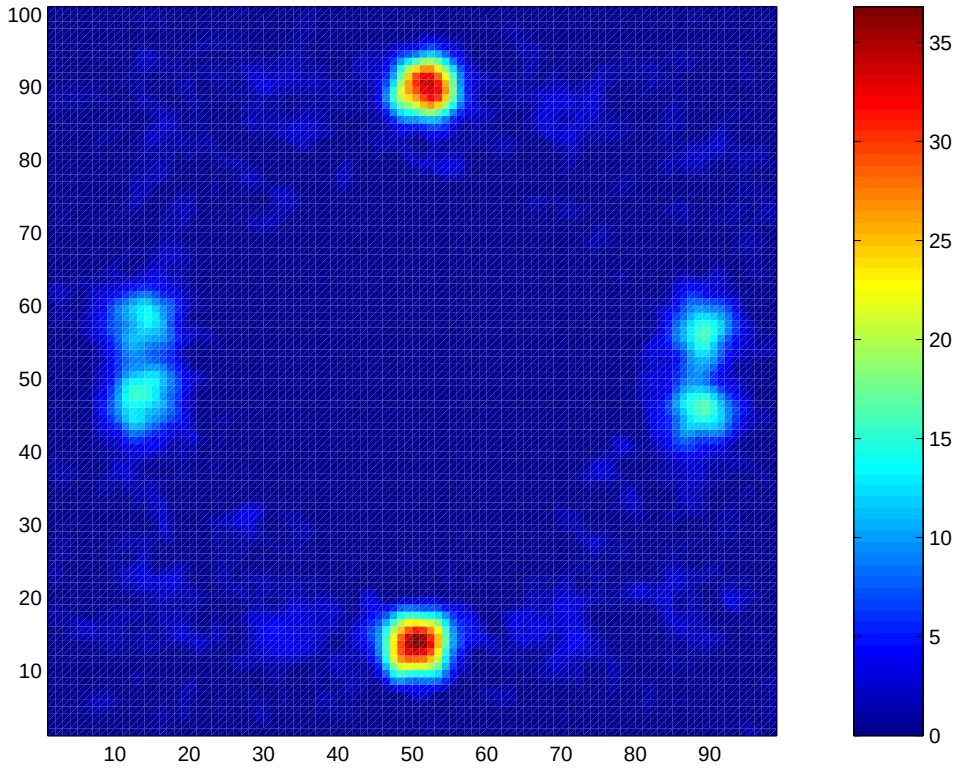

Fig. 3.11: Vortex lattice diffraction pattern taken at 7 T with **B** applied at 5° to the crystal c-axis. The diffraction pattern is composed of ω and ϕ rocks through the bottom/top and left/right spots taken with λ_{n} =8 Å, s_{det} =6 m and l_{coll} =6 m.

As a result of the sample rotation, the two Bragg peaks either side of the (now absent) horizontal twin-plane peak are clearly resolved enabling the vortex lattice structure to be obtained quantitatively. The spots in the corners are also absent, but only due to the fact that neither the ω-scan nor the ϕ-scan gets close enough to the Bragg condition for these weak reflections to be visible in the data. Nothing is lost though, because fitting just two reciprocal lattice vectors is sufficient to determine the Bravais structure of the vortex lattice. (In principal, diagonal scans could have been performed, but a considerable time investment would be required to measure the corner

spots, which has already been achieved in the case with **B** parallel to the c-axis. From the perspective of measuring the structure from the top/bottom and left/right spots, straightforward ω- or ϕ-scans are preferred to diagonal ones since they rock *directly* through those spots.)

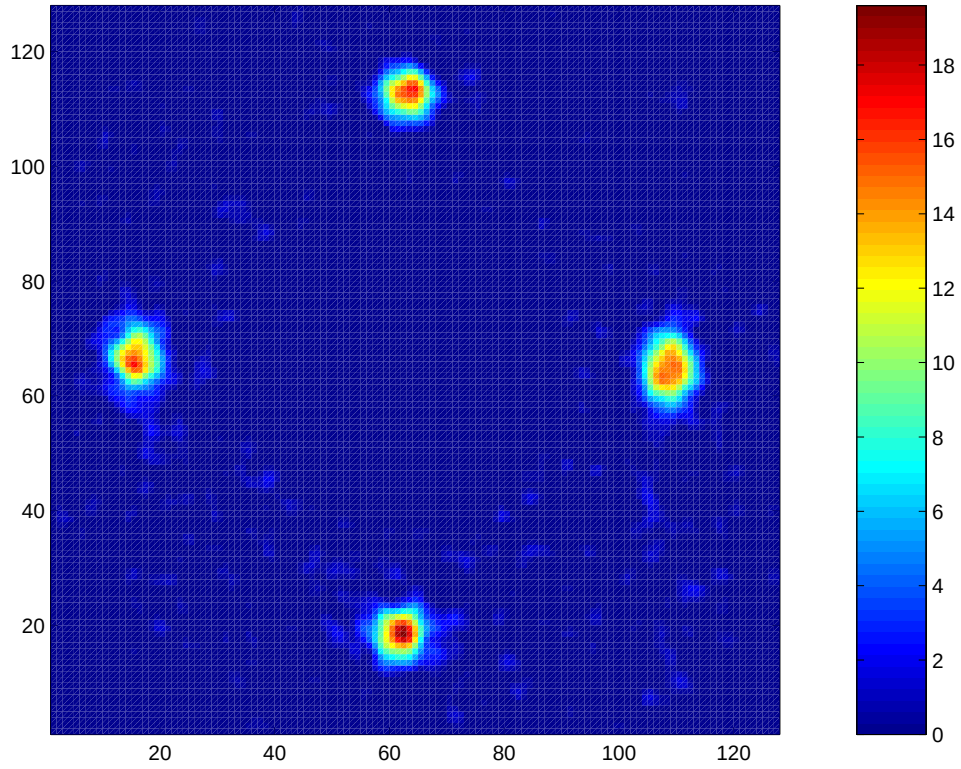

Fig. 3.12: Vortex lattice diffraction pattern taken at 10.8 T with **B** applied at 5° to the crystal c-axis, taken under the same conditions as figure 3.11, but with appropriately larger rocking angles to compensate for the larger Bragg angle at this field.

The diffraction pattern taken at 10.8 T and under the same conditions as above provides satisfying confirmation that the high-field vortex lattice does indeed have square-like morphology. These data are shown in figure 3.12, which is on a linear scale. The square structure is realised by a continuous deformation from the anisotropic triangular structure just as was seen in the data with B parallel to the crystal c-axis. It is not clear, however, whether at 10.8 T the domains are truly square or the spots along the horizontal axis of figure 3.12 are actually unresolved double spots. The tangential width of the left/right spots is larger by a factor 1.7(1) than the tangential width of the

top/bottom spots, which may imply a slight splitting in the latter spots if it is *assumed* that the correlation length transverse to the q-vectors is the same for both types of reflection. The presence of twin planes would argue against this being the case, but making the assumption that these correlation lengths are identical allows the fitting of two peaks for each of the horizontal spots by fixing their tangential width to that of the fitted value for the top and bottom spots. This gives an estimate of the angle α when the measurements become resolution limited.

With the sample in its new orientation, data were taken at a variety of fields with the view to use the greater effective resolution to map out the field-dependent vortex structure. The resolution-enhanced data complement the data taken with B parallel to the c-axis, which despite the complications of orientational degeneracy are still useful up to about 6 T.

In figure 3.13 is shown the evolution as a function of field of the angles α and β, which define the vortex lattice structure for vortices aligned along the {110} direction. The data shown are a mixture of the B-parallel and 5° data. For $B < 6$ T the curve of $\alpha(B)$ is derived from data with B parallel to the c-axis, but at larger fields, where it becomes difficult to resolve adjacent spots, data taken at 5° was used, which is why the datum at 7 T has such small error bars. Similarly, the low field data ($\leq$9 T) of the $\beta(B)$ curve were taken with the field aligned with the c-axis. At higher fields, the data displayed are calculated from the 5° data by adding the two measured reciprocal lattice vectors to form the vector in the corner of the diffraction pattern. (The results gave reasonable agreement with fits of the diagonal scans with B parallel to the c-axis, but at high fields the two spots in the corner are very close and *very* weak, therefore fitting them from the experimental data is not as reliable as the above method.)

Even at the highest available applied field (11 T) the transition is not quite complete and plateaux are not observed in either curve of figure 3.13. Strictly speaking, a single perfectly square vortex lattice domain would not be expected to exist due to the very slight orthorhombicity of the sample. In its stead, one rectangular vortex lattice domain should occupy each of the two types of crystallographic domain shown in figure 3.14. The domains are expected to form with one nearest-neighbour direction along a twin plane direction, which run horizontally in the present case. Therefore

both domains share common top/bottom reflections, but have different side spots corresponding to the differing anisotropy of the underlying crystal domains. An upper limit on the distortion (*i.e.* the ratio of the sides of the rectangular unit cell) of the high-field rectangular lattice can be obtained from the highest field datum of figure 3.13. The distortion obtained from the datum at 10.8 T is 0.972(5). (At 11 T this corresponds to a difference in vortex lattice parameters of only 4 Å — comparable with the size of the basal-plane crystal parameters!)

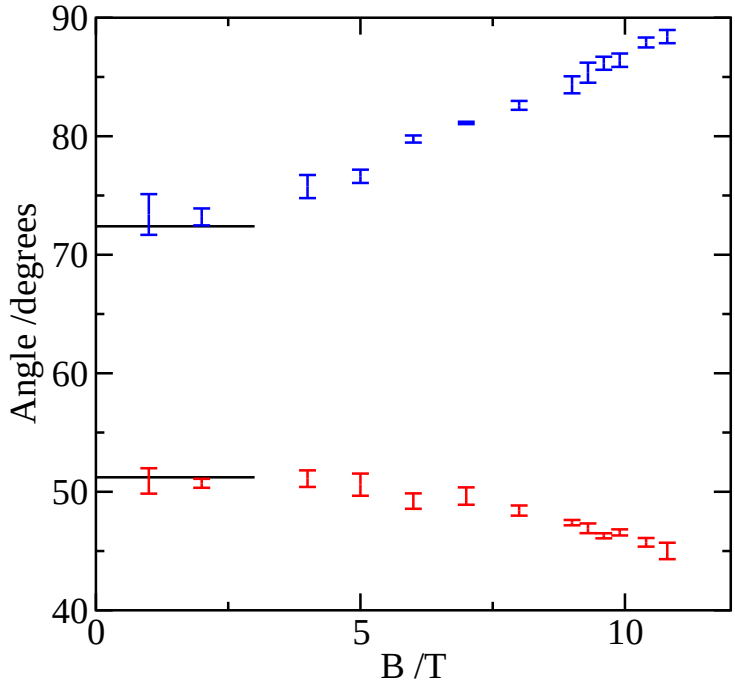

Fig. 3.13: The variation with applied field of the angles α (blue curve) and β (red curve) defining the vortex lattice structure (see figure 3.4). At low fields the data are consistent with anisotropic London theory (horizontal lines), but tend towards the values for an isotropic square vortex lattice ($\alpha = 90°$, $\beta = 45°$) at higher fields. (For an isotropic triangular arrangement of vortex lines $\alpha = \beta = 60°$.)

The structural transformation presented so far is just one facet of the transition to a square vortex lattice. Since the transition to square is driven by anisotropy in the vortex-vortex interaction (see the following section), it might also be expected to have an influence on the form-factor. Some evidence of this can be seen in the field-evolution of the relative spot intensities, but the data collected here is geared primarily

towards a structural study, thus there is a lack of complete rocking curves from which the form-factor could be calculated using equation 11.6.

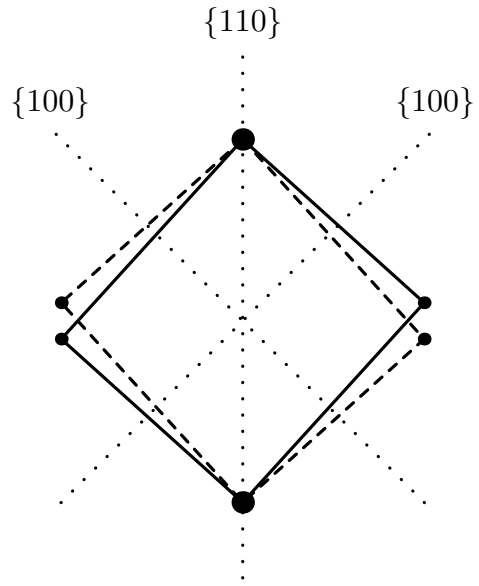

Fig. 3.14: The two possible distorted square reciprocal vortex lattices expected from symmetry when the field is applied at 5° to the sample c-axis (vertical axis of rotation). The squares are elongated along the basal plane direction due to the presence of the CuO chains. (Note: with the field applied *parallel* to the c-axis four domains would be expected; the other two may be constructed by rotating this figure by 90°.)

There is clearly motivation to perform complete rocking curves of the first-order triangular reflections since some evolve into second-order square reflections, but it would be time consuming and only realistic for a limited set of fields. In the absence of such data, some idea of the behaviour of the form-factor can be extracted from the existing data set under some assumptions. For example, if a constant rocking curve width for all diffraction spots at all fields is assumed, then the integrated intensity is just proportional to the peak intensity and the absence of complete rocking curves is not a problem. In reality, the rocking curve width *will* have a field dependence and matters are complicated by the use of different instrument set-ups at different fields, which also change the rocking curve width. However, if all that is required is the relative form-factors (*i.e.* their ratio), then an approximation may be obtained from the ratio of the peak intensities of the spots. This approximation becomes exact if all the spots in some

data set at a particular field have the same rocking curve width, which may not be a water-tight assumption (particularly in the presence of twin planes), but is much less rigid than the assumption of equality of *all* rocking curve widths. There is one caveat, however: it cannot be guaranteed on the basis of a partial rock, which perhaps consists of only a few points covering only a fraction of the rocking curve width, that the peak has been reached. Fortunately, for the diagonal scans (done with B parallel to the c-axis) the positions of the spots are such that they all lie nearly simultaneously under the sampling function so that the three-point rocks around the calculated Bragg angle are flat for all the spots, which is a good indication of being at the peak. Low resolution has undoubtably also helped in this respect, but it has hindered too: with B applied parallel to the c-axis, the degeneracy of vortex lattice domain orientation ensures that the reflections overlap over the entire field-range studied. Therefore, calculating the peak intensity in the usual way — *i.e.* by summing over a region on the detector around the spots — will give rise to systematic errors due to contamination from nearby spots. Instead, the intensity must be derived from *fitting* multiple spots that coalesce.

The procedure outlined above has been carried out for data taken with B parallel to the c-axis. The intensities of the strong doubly-degenerate spots along the {110} directions (vectors $\mathbf{G}_2$ in figure 3.4) and the weak corner spots (vectors $\mathbf{G}_1$ in figure 3.4) were calculated and a ratio of the two was formed at each field (under a given set of experimental conditions). (The intensity of the other spots, which are satellites of the main {110} spots, is less interesting as they eventually merge with the {110} spots and thus are very similar to the latter over the whole field range.) At high fields it becomes impossible for the fitting routine to resolve the three spots near {110} and the two corner spots. Here, single spots were fitted and the intensities were divided by a factor two to account for field-induced degeneracy. (Recall that the spots lying directly along {110} are doubly degenerate at low fields and thus their intensity is divided by a factor four at high fields.)

The form-factor ratio, $|\mathbf{B}_{\mathbf{G}_1}| \,/\, |\mathbf{B}_{\mathbf{G}_2}|$, of the reflections $\mathbf{G}_1$ and $\mathbf{G}_2$ are displayed in figure 3.15 as calculated from the diagonal scans (as before, the results have been averaged over symmetry-related reflections). The relationship between the measured

integrated intensity and form-factor was derived in equation 11.6 and can be expressed:

$$|B_{\mathbf{G}}| \propto \sqrt{I_{\mathbf{G}}\,|\mathbf{G}|}. \tag{23.1}$$

The data shown in figure 3.13 were used to obtain the ratio $|\mathbf{G}_2|\,/\,|\mathbf{G}_1|$ required in calculating $|\mathbf{B}_{\mathbf{G}_1}|\,/\,|\mathbf{B}_{\mathbf{G}_2}|$ from $I_{\mathbf{G}_1}/I_{\mathbf{G}_2}$. It should be reiterated that these are not the *true* form-factor ratios, but are subject to the assumptions described above that underpin the calculation of the intensity ratio.

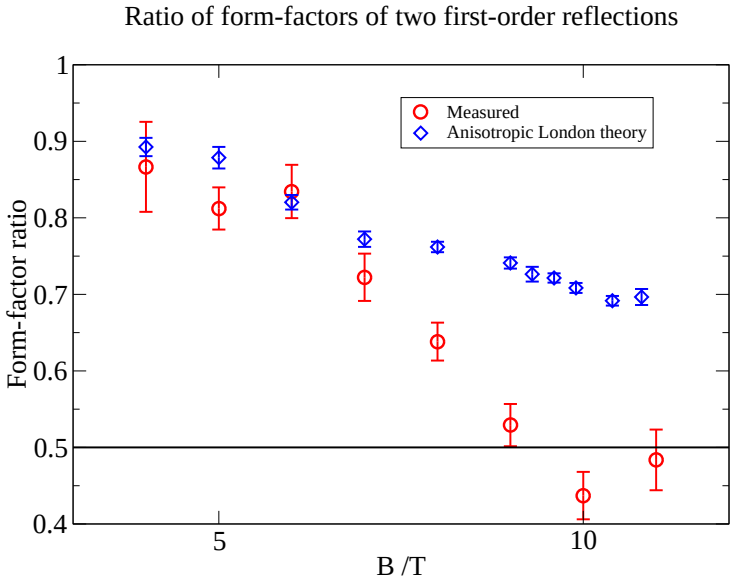

Fig. 3.15: The estimated form-factor ratio $|\mathbf{B}_{\mathbf{G}_1}|\,/\,|\mathbf{B}_{\mathbf{G}_2}|$ as a function of field (see figure 3.4 for the definition of $\mathbf{G}_1$ and $\mathbf{G}_2$). Both the observed ratio (approximated by the calculation discussed in the text) and the ratio calculated from the London form-factor are shown. The latter was calculated from the measured structure shown in figure 3.13. The horizontal line at 0.5 indicates the prediction for an isotropic square London vortex lattice.

Also shown in figure 3.15 is the intensity ratio predicted by anisotropic London theory with a basal plane anisotropy of $\gamma_{ab} = 1.28$. The London form-factor for an anisotropic superconductor is given by equation 3.5, which when B is parallel to the c-axis may be written:

$$B_{\mathbf{G}} = \frac{\langle B \rangle}{1 + \lambda_{\mathrm{L}}^2 (G_x^2 m_{yy} + G_y^2 m_{xx})}, \tag{23.2}$$

where the unity in the denominator may be disregarded (see section 2). The data in figure 3.13 was used to calculate the field evolution of the London form-factor for

the observed vortex structure (even if that structure was not the one predicted by London theory)*. Comparing these data with the experimental ones reveals that the diminished intensity of the corner spots at high fields is not simply a consequence of the larger ratio of $|\mathbf{G}_2| / |\mathbf{G}_1|$ and its concomitant effect on the anisotropic London form-factor, nor the G^{-1} geometrical dependence of the integrated intensity (equation 11.6 or 23.1). However, it should be pointed out that the results do agree with the ratio of the second-order to first-order form-factors of an isotropic square lattice. (An isotropic square London lattice has $G_{11} = \sqrt{2}G_{10}$ and therefore the form-factor ratio of these two spots is 0.5.) While this may indicate that vortices have London-like magnetic properties, even the existence of a square vortex lattice, let alone a field-dependent change in the electronic anisotropy, is beyond London theory.

24. Interpretation of the square vortex lattice

Figure 3.13 gives clear indication of a continuous transition from the conventional distorted triangular vortex lattice at low-fields to what appears to be an unconventional square vortex lattice at high fields, with nearest-neighbours along the {110} direction. This begs the question: what causes the anisotropy that is responsible for the high-field square vortex lattice? It cannot be described simply in terms of anisotropic London theory because even allowing a field dependence to the London anisotropy, it is impossible to get a square lattice from a distorted triangular one by a simple scale transformation. In addition, figure 3.15 shows a marked departure of the form-factors from the anisotropic London model.

The other possible candidates comprise both intrinsic and extrinsic sources: non-local effects (see section 7), *d*-wave effects (see section 8) and twin-plane pinning (see section 9). Twin planes almost certainly have influence on the structure of the vortex lattice because even though only a small fraction of the vortices are directly affected, the energy involved is comparable with the condensation energy for each vortex. It is

* In an isotropic triangular vortex lattice the ratio $|\mathbf{B}_{\mathbf{G}_1}| / |\mathbf{B}_{\mathbf{G}_2}|$ is identically unity. The same is true for the predicted London structure with B parallel to the c-axis because the scale transformation that converts the isotropic lattice to the anisotropic one preserves the degree of magnetic contrast along any direction in real space.

unlikely, however, that the twin planes are responsible for the transition to the square vortex lattice even though it might be thought that their arrangement would enhance square-like vortex correlations along {110}. Clearly, the twin-planes do not achieve this at "low" fields, *e.g.* 1 T, although they do appear to control the orientation. To conclude that the twin planes *increase* their influence as a function of field so as to favour a square arrangement of vortices is unnatural; that could only happen if the vortex lattice crossed over from a short-range weakly interacting system at low fields to a longer-range strongly-interacting system at high fields, which would propagate the twin-plane influence more effectively. That is not the case here: even at low fields the inter-vortex spacing is much smaller than the penetration depth ($a_0(1\,\mathrm{T}) \approx 40\,\mathrm{nm} \ll \lambda_\mathrm{L} \approx 150\,\mathrm{nm}$) therefore the vortices are already in the strongly interacting regime. If anything, it would be expected that increasing the induction would lead to a decrease in the relative contribution of the twin planes to the free energy since there are fewer twin planes per vortex at high fields.

Ruling out the effect of twin planes leaves the two intrinsic effects. As was stated in section 8, distinguishing between non-local effects and *d*-wave effects is a tricky and somewhat ill-defined problem because both correspond to non-locality (in some sense) and can sometimes give the same qualitative effects. Unfortunately, the vortex lattice in $YBa_2Cu_3O_7$ is one such case. In section 7, an expression for the London free energy including the leading-order non-local corrections was presented for a tetragonal superconductor and it was noted that, all things being equal, the free energy was minimised with the vortex nearest-neighbour direction along the minimum of the Fermi velocity. $YBa_2Cu_3O_7$ is not tetragonal, but since the degree of othorhombicity is small (see figure 3.14 and the related discussion) it should be resonable to assume it is approximately tetragonal and to consider just the principal Fermi surface associated with the CuO_2 planes (see figure 3.2). From this picture, it is clear that the minimum in the Fermi velocity occurs along {110} and therefore non-local London theory predicts that the square vortex lattice has its basis vectors along these directions. *d*-wave theory gives exactly the same prediction (recall the nodes are also along {110} in a $d_{x^2-y^2}$ superconductor).

One possible way to distinguish between non-local and *d*-wave effects is to calculate

from each theory the vortex form-factor and to compare it with the experimentally derived value. Unfortunately this task is difficult from both the experimental and theoretical sides. Firstly, the data available on the vortex form-factor (see figure 3.15) is, at present, incomplete and not totally reliable; and secondly, non-local London calculations of the vortex lattice structure in YBa_2Cu_3O have not yet been done and the required information on the electronic properties does not exist. There do exist theoretical results arising from *d*-wave theory. In the same paper that predicted through *d*-wave pairing the orientation of square vortex lattice observed here, Ichioka *et al.* (1999) have calculated ratios of the magnetic form-factors for variously oriented *s*- and *d*-wave vortex lattices. Of interest here is their calculation of $|\mathbf{B}_{11}|\,/\,|\mathbf{B}_{10}|$, which can be compared to $|\mathbf{B}_{\mathbf{G}_1}|\,/\,|\mathbf{B}_{\mathbf{G}_2}|$ of figure 3.15. Ichioka *et al.* (1999) found that in almost every vortex structure considered — except the square *d*-wave vortex lattice with nearest-neighbours along {110} that is stable at high fields — the magnitude of the ratio $|\mathbf{B}_{11}|\,/\,|\mathbf{B}_{10}|$ decreased monotonically. For the *d*-wave {110}-oriented square lattice, the ratio of the Fourier coefficients dips slightly at around $0.1H_{c2}$, but then *rises* monotonically (almost linearly) towards H_{c2}. The robustness at very high fields of $\mathbf{B}_{11}$ relative to $\mathbf{B}_{10}$ is probably due to the nodal reduction of the superfluid near {110}, which increases the magnetic penetration depth along $\mathbf{G}_{10}$ (recall that the vortex lattice reciprocal lattice vector $\mathbf{G}_{10}$ lies along the crystal {110} direction).

In the high-field region of the experiment ($\approx$11 T$\sim$ $0.1H_{c2}$, which corresponds to the low-field range of theory), the theoretical prediction (Ichioka *et al.*, 1999) for the {110}-oriented square lattice is $|\mathbf{B}_{11}|\,/\,|\mathbf{B}_{10}| \approx 0.5$, which agrees well with the experimental data of figure 3.15. However, direct comparison of the data in figure 3.15 with the numerical calculations of Ichioka *et al.* (1999) is not a trivial matter: notwithstanding the limitations of the experimental data (see discussion at the end of section 23), the calculations of Ichioka *et al.* were performed for an isotropic *d*-wave superconductor. Furthermore, the ratio $|\mathbf{B}_{11}|\,/\,|\mathbf{B}_{10}|$ for a square vortex lattice in an *s*-wave superconductor is very close to the *d*-wave value (for a vortex lattice oriented along {110}) and hence it is not even possible to distinguish between these from the present experimental data. Given the small difference in form-factor ratio between *d*-wave and *s*-wave pairing, it is likely that the form-factor ratio derived from non-local

London theory for a similarly configured vortex lattice will also be rather similar to the d-wave value at this field. Clearly more work is needed, both experimental (measuring complete rocking curves) and theoretical (calculating non-local London form factors), but it may prove quite difficult to differentiate between d-wave and non-local London theory in the present field range.

25. Temperature dependence

To map out the phase diagram of the vortex lattice morphology, temperature-dependent measurements have been undertaken. Since the square vortex lattice is realised only at high fields, these measurements were performed at applied fields of 4 T and larger. Furthermore, to allow accurate measurements of the angles between reciprocal lattice vectors, data were taken with the field applied at 5° to the crystal c-axis. In keeping with the previous methodology, the vortex lattice was formed by field cooling (as opposed to setting a sample temperature and then applying the field). Temperature scans were performed by both warming and cooling the sample; at no point in these investigations was any hysteresis observed despite the fact that some changes in vortex lattice structure occurred below the irreversibility temperature for macroscopic motion of vortex lines.

Figure 3.16 shows a series of diffraction patterns focused on the peaks appearing on the right-hand side of the 10 T diffraction pattern (*i.e.* those spots along the horizontal {110} direction, which due to the sample rotation do not arise from vortex lattice planes parallel to the twin planes). In the field-dependent data, this group of spots was manifest as a doublet at low fields (see figure 3.11), but at high field coalesced into a single mass corresponding to a single first order square peak or the very close unresolved peaks of two rectangular vortex lattices (see figures 3.12 and 3.14). The low temperature patterns (10 K, 30 K and 40 K) in figure 3.16 match the latter. However, as the temperature is increased, the vortex lattice appears to transform back into the low-field structure, *i.e.* distorted triangular vortex arrangements. This can first be seen at 45 K where there is a perceptible increase in the tangential width of the spot. (All the patterns shown in figure 3.16 were taken under the same conditions.) At 50 K the spot begins to separate into two. This trend continues with increasing temperature

and at around 60 K the spots are well separated and remain so up to about 75 K where the neutron signal from the vortex lattice disappears. The behaviour implies a temperature-induced transition back to a distorted triangular arrangement of vortices.

That the square vortex lattice is observed to transform back into a distorted triangular one with increasing temperatures provides confirmation of its intrinsic nature. The only effect temperature should have even on correlated pinning like twin plane pinning is on the correlation lengths, not the structure of the vortex lattice. However, from these data it would be still difficult to choose between the non-local and d-wave theories because both anticipate a transition back to the triangular vortex lattice. In d-wave theory, it occurs because of the tendency of thermal fluctuations to smear out the anisotropy in the the quasi-particle spectrum, which in turn reduces the anisotropy of the vortex-vortex interaction. From a Ginzburg-Landau viewpoint, high temperatures suppress the order parameter to the point that the higher-order terms become negligible, which reduces the free energy to a simple s-wave like expression.

Thermal fluctuations have a similar effect in the non-local London theory. The temperature dependence of the vortex lattice structure should depend upon the relative size in equation 7.3 of the non-local term ($\propto G^2\mathbf{a}(\mathbf{G})$) to the local term ($\propto \mathbf{a}(\mathbf{G})$). The local term depends only on the effective mass tensor so has no temperature dependence. The non-local term does have a temperature dependence and it transpires (Kogan *et al.*, 1996 and Kogan *et al.*, 1997) that it is contained entirely within the term $\gamma(T,\tau)$, which in the clean limit appropriate here is reduced only by a factor two between low temperatures and T_c. This counters the field-dependent increase in non-locality: the field dependence at constant low temperature of the ratio of the non-local term to the local one depends upon $G^2 \propto B$, which also changes by a factor ≈ 2 between low fields ($\leq$4 T), where a London structure is observed, and high fields ($\approx$10 T) where the square lattice is established. With more detailed theoretical analyses of systems with both Fermi surface and gap anisotropy (such as an equivalent YBCO version of the study by Nakai *et al.*, 2002), it might be possible to distinguish quantitatively between non-local London and d-wave theories based on the temperature dependence.

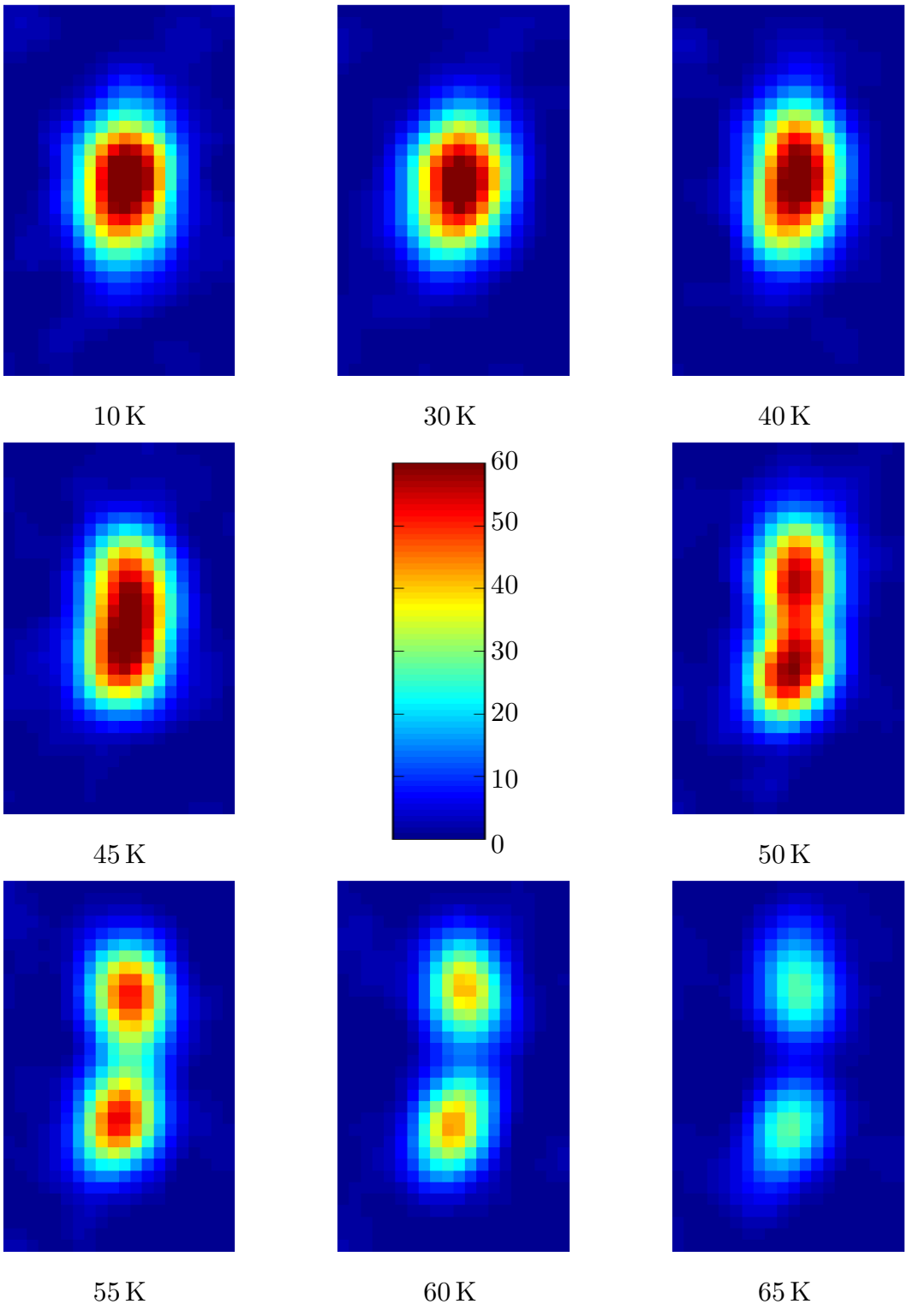

Fig. 3.16: Temperature scan at 10 T (applied at 5° to the *c*-axis) showing the temperature evolution of the right-hand diffraction peak(s). Each picture represents the same area of the detector and each share the same arbitrary-unit scale displayed in the centre.

The temperature-induced transition back to the distorted triangular vortex lattice can also be seen by its effect on the spots lying at the corners of the detector. Quantifying the transition using data from these reflections is obviously more difficult than using the Bragg peaks that scatter in the horizontal plane (see above) because the former are second-order reflections at low temperatures and hence they yield far weaker scattered intensity. Although these spots are less useful for measuring the vortex lattice structure, there exists a prospect that they exhibit an interesting temperature dependence: since they evolve from second-order spots at low temperatures to first-order spots of a triangular lattice at high temperatures, it is expected that their integrated intensity as a function of temperature will be non-monotonic. The plot of the peak intensity of these spots as a function of temperature (see figure 3.17) indicates the anticipated behaviour. Although the data are not the true *integrated* intensity, the corresponding trace for the right-hand spots shows no upturn that might arise from greater perfection of the vortex lattice due to annealing effects at higher temperatures.

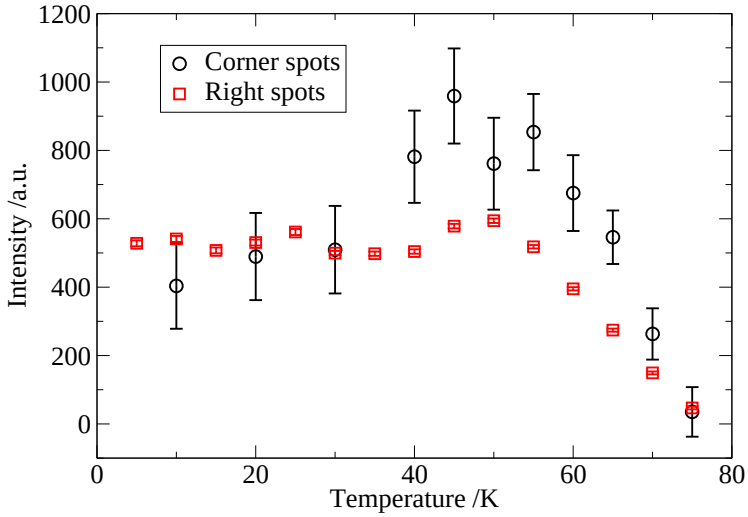

Fig. 3.17: A plot of the peak intensity of the corner spot(s) as a function of temperature, which exhibits non-monotonic behaviour. Shown for comparison is the peak intensity for the sum of the two right-hand spots divided by a factor five. (The intensity is in arbitrary units and normalised to a standard monitor.)

Measurements taken as a function of temperature at a number of applied fields allow the mapping of the intrinsic vortex lattice phase diagram. This was obtained by

repeating the temperature scan shown in figure 3.16 at a variety of fields and measuring the angle between the two reflections present in the patterns. Although the two spots belong to different vortex lattice domains, due to their symmetry relationship, the angle between them can be related to one of the true reciprocal lattice vector angles. The temperature dependence of the reciprocal lattice angle α (see figure 3.4) is plotted at 4, 7, 8, 9 and 10 T in figure 3.18. Not much temperature dependence is observed in this angle at low fields where the vortex lattice is London-like, but at higher fields, increasing temperature suppresses the tendency to form a square vortex lattice.

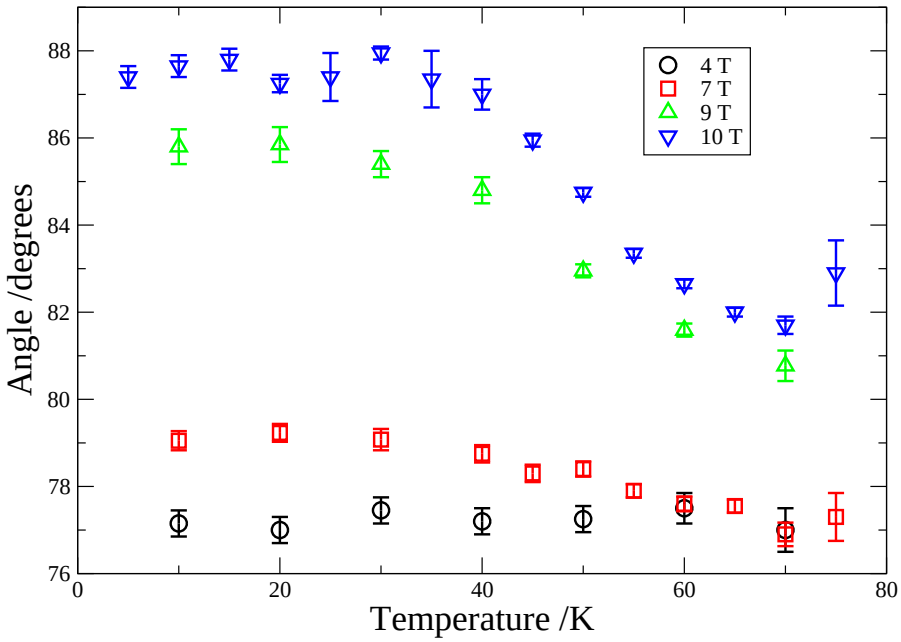

Fig. 3.18: The reciprocal lattice angle α as a function of temperature for various applied fields.

The temperature-dependent scans displayed in figure 3.18 were used to formulate a structural phase-diagram for the vortex lattice in $YBa_2Cu_3O_7$, which is shown in figure 3.19. Since the transition to a square (or rectangular) vortex lattice is a continuous one, the solid line of demarcation between the two phases in figure 3.19 represents the mid-point of the transition (defined as when $\alpha = 83°$). The phase diagram shows that at low temperatures (lower than about 20 K) the phase "boundary" is very flat and at $T = 0$ K the mid-point of the transition occurs at about 7.5 T. Only above roughly

20 K do thermal fluctuations start to become important for the vortex lattice structure. Near $H_{c2}(T)$ there is an upturn in the phase line with increasing temperature; this is entirely predictable given the proposed effects of thermal fluctuations reasoned earlier in this section. It is quite possible, in fact, that at higher fields the phase boundary bends backwards away from $H_{c2}(T)$ and towards the field axis, thus giving a small region near $H_{c2}(T)$ where the triangular lattice is preferred. This type of re-entrant transition is seen quite often, for example in the borocarbide $LuNi_2B_2C$ (Eskildsen *et al.*, 2001; Nakai *et al.*, 2002).

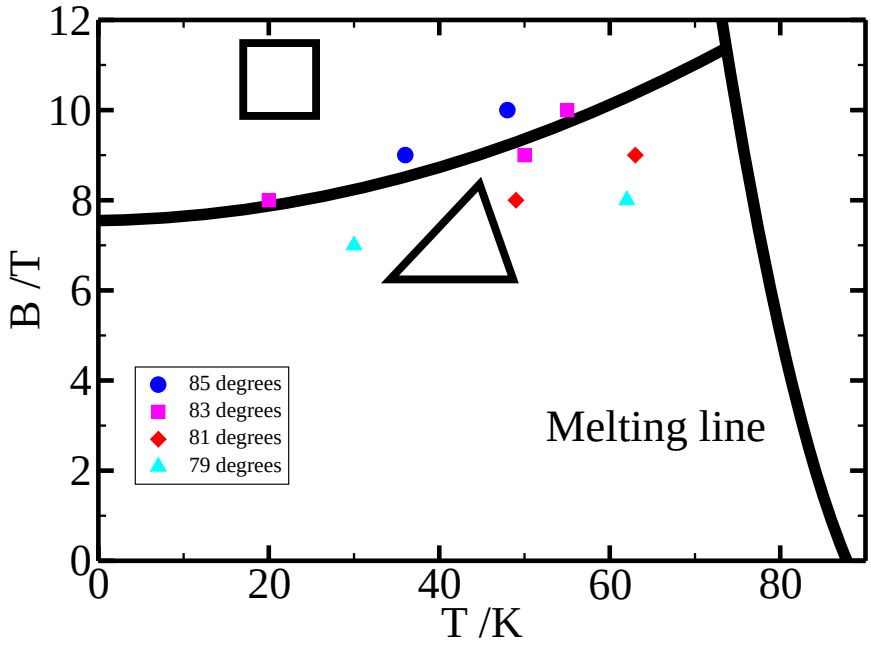

Fig. 3.19: The vortex structure phase diagram twinned of $YBa_2Cu_3O_7$. Both the triangular-square phase line and the vortex lattice melting line are shown. The latter was obtained from the crystal grower (Erb *et al.*, 1996) and the former is a guide to the eye showing where the angle α assumes the value of 83° (the mid-point of the transition). Points in phase space where α is 79°, 81°, 83° and 85° are also indicated. (These were taken by interpolating between the points of figure 3.18.)

26. Angle dependence

Based on the assumption that some kind of unconventional anisotropy in the basal plane — either non-local London-like or due to *d*-wave effects — is responsible for the appearence of a square vortex lattice at high fields, it follows that the angle of the applied field relative to the crystal axes should have an impact on the physics of the

high-field vortex lattice in $YBa_2Cu_3O_7$. To study the effect of angle of applied field, the sample geometry shown in figure 3.20 was employed. The sample was mounted initially with the basal-plane crystal axes horizontal/vertical and then rotated (above T_c) about the vertical axis by the required angle*. This geometry was chosen over the geometry used in the preceeding investigations (with the crystal axes at 45° to the horizontal/vertical before rotation) because rotations in the present configuration, which were not restricted to small angles as in earlier measurements, give a more "cleanly" coupled vortex frame: figure 3.20 shows that in the vortex frame there is coupling between either a or b (depending on the orientation of the crystal domain under consideration) and c along the horizontal, whereas vertically the electronic environment consists of a single uncoupled crystal axis; in contrast, the situation with a and b intially at 45° would involve coupling of the electronic properties along all three crystal axes. Another benefit of this geometry is that no {110} directions, along which the twin planes, order parameter nodes and Fermi velocity minima lie, are perpendicular to the vortex direction. Whilst this is likely to lead to a disordered vortex lattice at low fields (where the twin planes help to fix the orientation), at high fields it will show how much the rotation suppresses the square lattice, which following the discussion of section 24 forms due to the intrinsic preference of vortices to align along {110}.

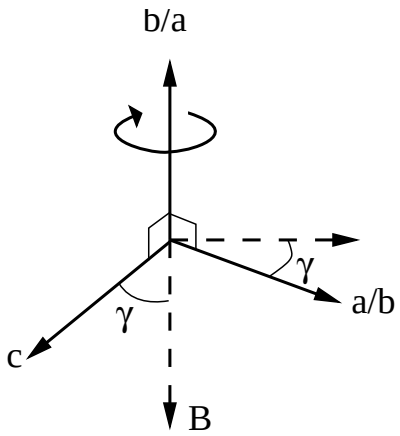

Fig. 3.20: Sample geometry used in the angle-dependence studies: the sample c-axis has been rotated in the horizontal plane by an angle γ away from parallel to the applied field, **B**.

* This necessitated taking separate backgrounds for each angle due to the possibly strong dependence on orientation of background scattering

In figure 3.21 is shown data taken at 5 K with a field of 5 T applied at 10°. The pattern is quite distinct from anything seen with B applied (nearly) parallel to the c-axis in the other sample orientation and comprises twelve clearly identifiable spots that belong to two domains of vortex lattice as illustrated in the figure. These lattices (hereon referred to by their identifying colour in figure 3.21) are both distorted hexagonal lattices. (By symmetry, the distortion has as its primary axes the vertical and horizontal of the diffraction pattern.) The black lattice is only slightly distorted from a perfect hexagon (squashed horizontally in the figure), with angles between the reciprocal lattice vectors (angles subtended by the vertices of the hexagon from its centre) of 54.2(6)° and 63.0(5)°. The magenta lattice, which is squashed vertically, is more distorted and its reciprocal lattice angles are 50.3(6)° and 64.9(3)°. Since the domains have either top/bottom or left/right spots, in real space they are oriented with their nearest-neighbour directions along a basal plane axis (black domain) or the projection of a basal plane axis onto the plane perpendicular to the applied field (magenta domain). (Obviously, the real-space nearest-neighbour directions of these two-dimensional lattices are perpendicular to the **q**-vectors; see also figure 3.20.) Furthermore, since the two domains are of nearly equal intensity they presumably each occupy one of the two types of crystal domain in the twinned sample. (In fact the black domain is slightly more intense than the magneta one; the reason for this will be made clear when looking at data taken at higher fields.) It follows that because the two domains are oriented 90° with respect to each another, and because the crystal domains are also 90° apart, the two vortex lattice domains must be oriented in the *same* way with respect to the axes within their respective crystallographic domain.

Given the above empirical observations, and the very plausible assumption that the two vortex lattice domains form in different crystallographic domains, it is interesting to consider why these two domains arise in such a configuration. They are certainly not conventional anisotropic London vortex lattice domains. If this were the case they would be expected to have very similar anisotropy because even at 10° the effect of coupling the c-axis effective mass is negligible ($\approx 2\%$) and the basal plane anisotropy dominates, which is the same for both vortex lattices if they are oriented similarly. In any case, the measurements on the sample reported here indicate that at 5 T the vortex

lattice does not behave very conventionally. (Recall that with B parallel to the c-axis the vortex lattices are part way through the transition to square.) Indeed, fitting the diffraction peaks to an ellipse gives eccentricities that are too small compared to that seen at 1 T applied parallel to the c-axis: the fits give $\epsilon = 1.14(2)$ (black domain) and $\epsilon = 1.229(6)$ (magenta domain) compared to $\gamma_{ab} = 1.28(1)$ at 1 T. Therefore, whatever agent is responsible for the occurrence of the nearly isotropic square lattice at high fields appears to be having the effect at this intermediate field of making the two hexagonal domains more isotropic than the bare London electrodynamic anisotropy.

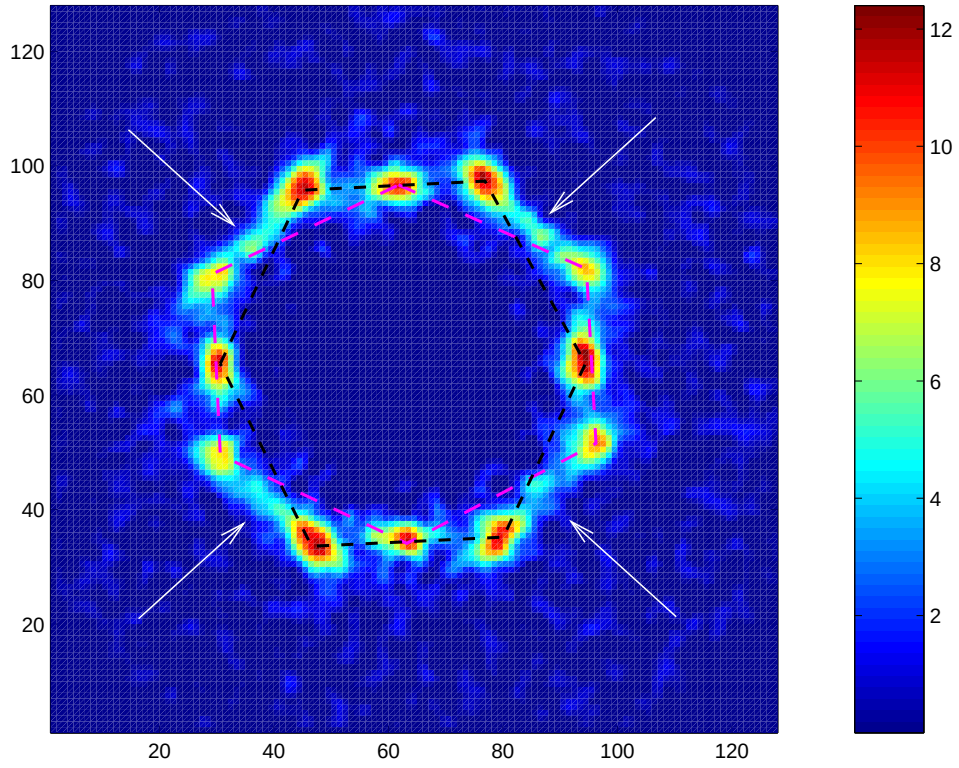

Fig. 3.21: Sum of diagonal rocks (linear scale) at 5 K with 5 T applied at 10° to the crystal c-axis. Two triangular vortex lattice domains are outlined and the white arrows indicate extra scattering along the lines running 45° radially from the centre of the diffraction pattern.

Despite the failure of London theory to account correctly for the distortion of either vortex lattice domain, its basic concepts concerning the effects of anisotropy can be used qualitatively to speculate as to which of the basal plane axes the observed domains are aligned. (The twinned nature of the sample means that this question cannot be resolved unambiguously.) If it is assumed that the basal plane anisotropy is

the leading factor in determining the distortion of the two domains, then the orientation of the distortion points to both vortex lattice domains being oriented with their nearest-neighbour direction along the crystal a-axis (black lattice) or its projection onto the plane perpendicular to the vortices (magenta lattice) — see section 3. That the two domains do not have the correct value of London distortion does not affect this qualitative argument.

It is unclear exactly what controls the nearest-neighbour directions in either vortex lattice domain. At first sight, the magenta domain seems to be oriented as predicted by anisotropic London theory*. However, it is unlikely, given the palpable departures from London theory already seen at 5 T, that the mechanism favouring a-axis orientation is the same as the London one. Similarly, there appears to be no explanation as to the orientation of the black domain. However, something similar to it has already been observed by Johnson *et al.* (1999) with a field of 3 T applied at 33° to c-axis (effected, as here, by rotating about the a-axis). They too were unclear as to its origin, but proffered that it may be due to an "unexpected influence" of the CuO chains. Given that based on a rather simplistic model of the properties of $YBa_2Cu_3O_7$, none of the unconventional theories documented here provides any clues, it is likely that a better understanding of the electronic structure of $YBa_2Cu_3O_7$ will be required to explain these effects.

Although the discrepancy between the London anisotropy and the distortion observed in the domains of figure 3.21 can be explained away in terms of the field-induced transition to a nearly isotropic square vortex lattice, that the distortions of these two domains are different from each other is an altogether more puzzling matter. Inspection of figure 3.21 reveals that the vortex lattice domain formed in the crystal domain with

* See Campbell *et al.* (1988) and the discussion in section 3. Note that Campbell's conclusion for a uniaxial superconductor — that the nearest-neighbour direction is along the axis perpendicular to the rotation — is unaffected by the biaxial nature of the sample here. This is true regardless of the value of effective mass along the axis of rotation since it is not coupled with the mass in any other direction. Recall that only the presence of *off-diagonal* terms in the mass tensor is able to effect a preferential orientation within the London theory.

the b-axis rotated by 10° (the black domain) is more isotropic. On the contrary, the magenta vortex lattice, which forms in crystal domains where the b-axis is perpendicular to the applied field, is less isotropic. London theory cannot account for the different distortions any more than it can account for the fact that both of the domains are more isotropic than expected because the 10° rotation is too small to give any measureable difference between the two. Curiously though, London theory does give the correct *qualitative* behaviour, *i.e.* that the black domain should be made more isotropic than the magenta one given some rotation (see figure 3.22). The enhancement of the angular dependence of distortion is clearly beyond the realms of anisotropic London theory, but may be explainable in terms of the extended Ginzburg-Landau or non-local London theories, which contain high-order powers of the effective-mass tensor and whose predicted distortion should vary with angle faster than the London $\cos(\theta)$. It is probably unnecessary to invoke a non-continuum theory such as the Lawrence-Doniach model (Lawrence and Doniach, 1971) because $YBa_2Cu_3O_7$ is only moderately anisotropic. (The cross-over to two-dimensional vortex line behaviour is expected at $B_{2D} \sim 100\,\mathrm{T}$ in $YBa_2Cu_3O_7$.)

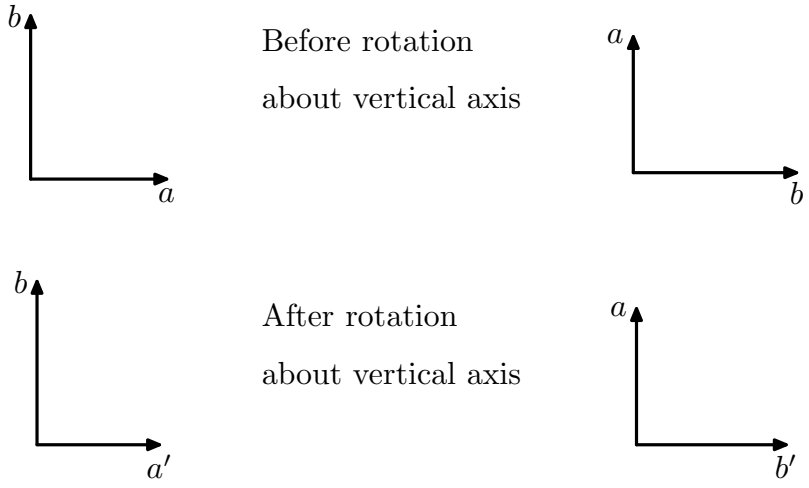

Fig. 3.22: The effect of rotation on the effective mass in the plane perpendicular to the vortex direction. (Large effective masses are represented by short arrows therefore the arrows give the actual real-space vortex-lattice distortion.) The primed axes are coupled to the c-axis.

Aside from the two strongly-scattering triangular vortex lattices, there is also present in the diffraction pattern shown in figure 3.21 significant scattering roughly along {110} as indicated by the white arrows. In a sample with much stronger pinning it may be feasible to attribute these to the tails of the wide rocking curves of vortices pinned to the twin planes, which are at 10° to the applied field direction. However the scattering along {110} appears to be centred at the Bragg angle expected given the q-value of these features, not at some large angle expected if the vortices ran along the twin planes. Rocking curves taken over small regions* encompassing the two diffraction peaks at the top-left of figure 3.21 and the weak intensity along {110} between them are shown in figure 3.23.

The origin of the weak interstitial spots in figure 3.21 is not immediately apparent. Although their arrangment is suggestive of a square vortex lattice domain, the measured q-value of $32.6(2)\,\mathrm{m\AA}^{-1}$ seems more consistent with the triangular value ($33.2\,\mathrm{m\AA}^{-1}$) than the square ($30.9\,\mathrm{m\AA}^{-1}$). Their angular coordinates are difficult to establish because there is a lot of overlap with the adjacent triangular peaks. The only way to get a satisfactory fit was to tie the tangential and radial widths of the trio of spots in the corners of the diffraction pattern; otherwise, the fitting routine attributed zero weight to the {110} spots. However, the angular positions of the spots measured in this way are unlikely to be reliable because of significant correlations in fitting between the angular position of the interstitial spots and the position and tangential widths of the strong spots. Thus, all that can really be deduced about the interstitial spots from the data is that they lie roughly along the {110} directions and have q-values too large for them to be the diffraction peaks of a square vortex lattice.

* Due to the overlap of the spots neither the rocking curve in figure 3.23 nor the rocking curve in figure 3.25 shows the total detector-integrated spot intensity as a function of angle. Instead, to avoid contamination from neighbouring spots, the intensity is integrated over similar-size areas around each peak. The results obtained this way allow a reliable comparison of the integrated intensity of different spots at the same field. Comparing the same spot at different fields is not so reliable, however, because the regions summed over are necessarily different.

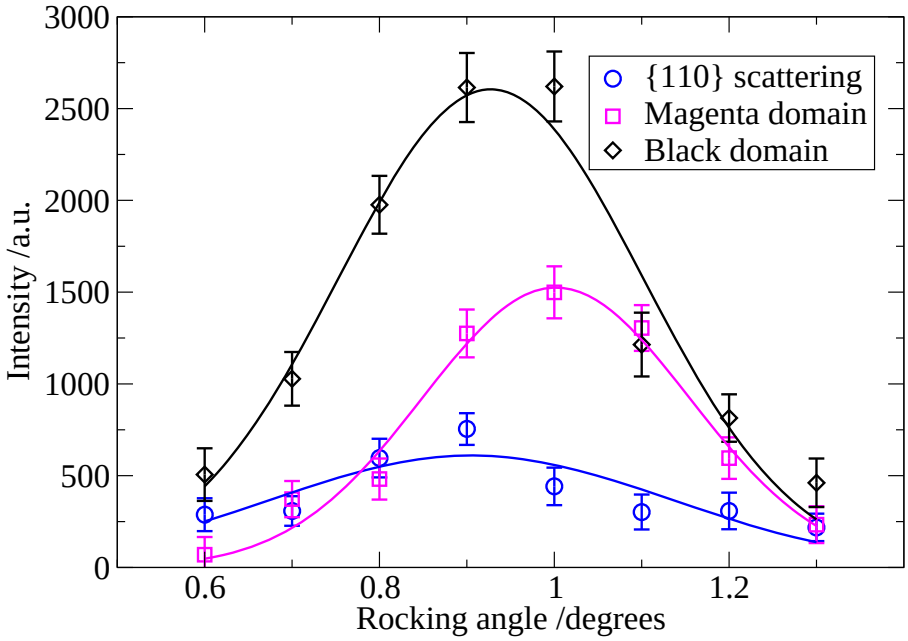

Fig. 3.23: Rocking curves as a function of "diagonal" rocking angle (*i.e.* $\omega = \phi$) of the three centres of intensity seen in the top-left of figure 3.21. (These rocking curves are representative of the ones done on identical spots in the other corners of the detector.) The two larger peaks correspond to the bright triangular domains and the smaller one to the diffuse scattering along the {110} direction. Also shown are Gaussian fits to the rocking curves; these fits give the following values for integrated intensity (in arbitrary units): 1.1(1) (black domain), 0.58(5) (magenta domain) and 0.35(8) ({110} domain).

One possible interpretation that is consistent with the facts is that they belong to four vortex lattice domains oriented along {110} similar to those seen at low fields with B-parallel to the c-axis. The absence of the other spots can be explained by the fact that they are much weaker than the four principal ones, which are doubly degenerate (see figure 3.3). Furthermore, the other spots would be expected to lie close to the positions of the strong peaks in the present diffraction pattern thus masking their presence (see figure 3.4). Even assuming the veracity of this hypothesis, it remains to be understood why the four putative domains orient along the projection of the {110} direction since the possibility that the vortex lines run along the twin planes has already been discounted. It may be that the twin planes still control the orientation of these domains if the vortices are pinned only at points where the twin planes intersect the CuO_2 planes but are otherwise straight and follow the applied field (Yethiraj *et al.*, 1993b). By this mechanism, a single vortex will be pinned by the intersection of

many twin planes as it threads the sample. Adjacent vortices will line up along the projection, ϕ_{twin}, of {110} onto the plane perpendicular to the vortex direction for a sample rotation of θ, simple geometry gives this to be:

$$\phi_{\text{twin}} = \arctan(\cos\theta \tan 45^\circ). \tag{26.1}$$

For small rotations, *e.g.* 10°, ϕ_{twin} is practically identical to 45° and is therefore in agreement with the position of the weak spots in figure 3.21. It should also be pointed out that similar reasoning should apply to the orientation of the nodes of the order parameter. Within the quasi-classical *d*-wave theory (Ichioka *et al.*, 1999), the free energy of a triangular arrangement of vortices aligned along {110} is very close to that of a similarly coordinated lattice aligned with the crystal axes.

Regardless of what causes the vortex lattice domains associated with the scattering along the diagonals of figure 3.21 it is quite possible that in each crystal domain there is a coexistence of two vortex lattice phases: one almost isotropic triangular (the black or magenta domains) and one with its nearest neighbour directions along {110}. Studying the field-evolution of the diffraction pattern gives good evidence of this. Figure 3.24 shows diffraction patterns taken at 7 T and 8.5 T. At 7 T the black domain of figure 3.21 is still clearly visible, but the magenta domain has become much weaker. This is verified by the rocking curves of these spots shown in figure 3.25. Compared to the rocking curves at 5 T (figure 3.23) the magenta domain is definitely diminished relative to the black domain. Unfortunately, the rocking curve of figure 3.25 did not go to sufficiently small angle to get a good estimate of the integrated intensity of the {110} spot, but it is nevertheless clear that its intensity has grown relative to the others'. In the very least it is of the same magnitude as the magenta domain, whereas at 5 T it was approximately half. The black vortex lattice domain seems unaffected at 7 T. However, at 8.5 T the black domain is now also weaker. The magenta domain is now completely invisible and both domains have been all but replaced by the now strong square-looking* domain oriented along the {110} direction. Also just visible at the

* Regretably, an error (discovered only after the experiment) in the data acquisition macro used to gather the high-field scans caused a systematic error in the rocking angles, which made all rocking angles $\sqrt{2}$ too large. As a result the q-values of the spots

very edges of this pattern along the horizontal axis are a pair of spots. These are the second order spots of the now bright {110} spots.

The only logical conclusion from the sequence of diffraction patterns at 5 T, 7 T and 8.5 T is that the region of sample occupied by the {110} domain(s) is growing at the expense of the other two domains, of which the magenta is the first to disappear, followed thereafter by the black domain. Curiously, this process occurs without much change in the shape of the these lattices. Table 3.2 shows the field dependence of the two angles between reciprocal lattice vectors of the black and magenta domain. Both domains have a more or less static structure, but there is a subtle tendency, measureable in the black domain, towards a more isotropic structure. It is probably simply a continuation of the trend towards more isotropic vortex lattice structures with increasing applied field whose ultimate manifestation is the square vortex lattice observed at high fields, which is visible in the data taken at 8.5 T. In this respect it is perhaps unsurprising that the magenta domain — whose distortion is larger than the black's — is the first to disappear.

measured on the detector are systematically too large due to the effects of resolution described in section 15, thus it is not possible to make the distinction between triangular and square q-values from these data. However, the structure of the diffraction pattern (*i.e.* the angles between reciprocal lattice vectors) is unaffected because the distortion due to resolution only affects the radial component of the reciprocal lattice vectors.

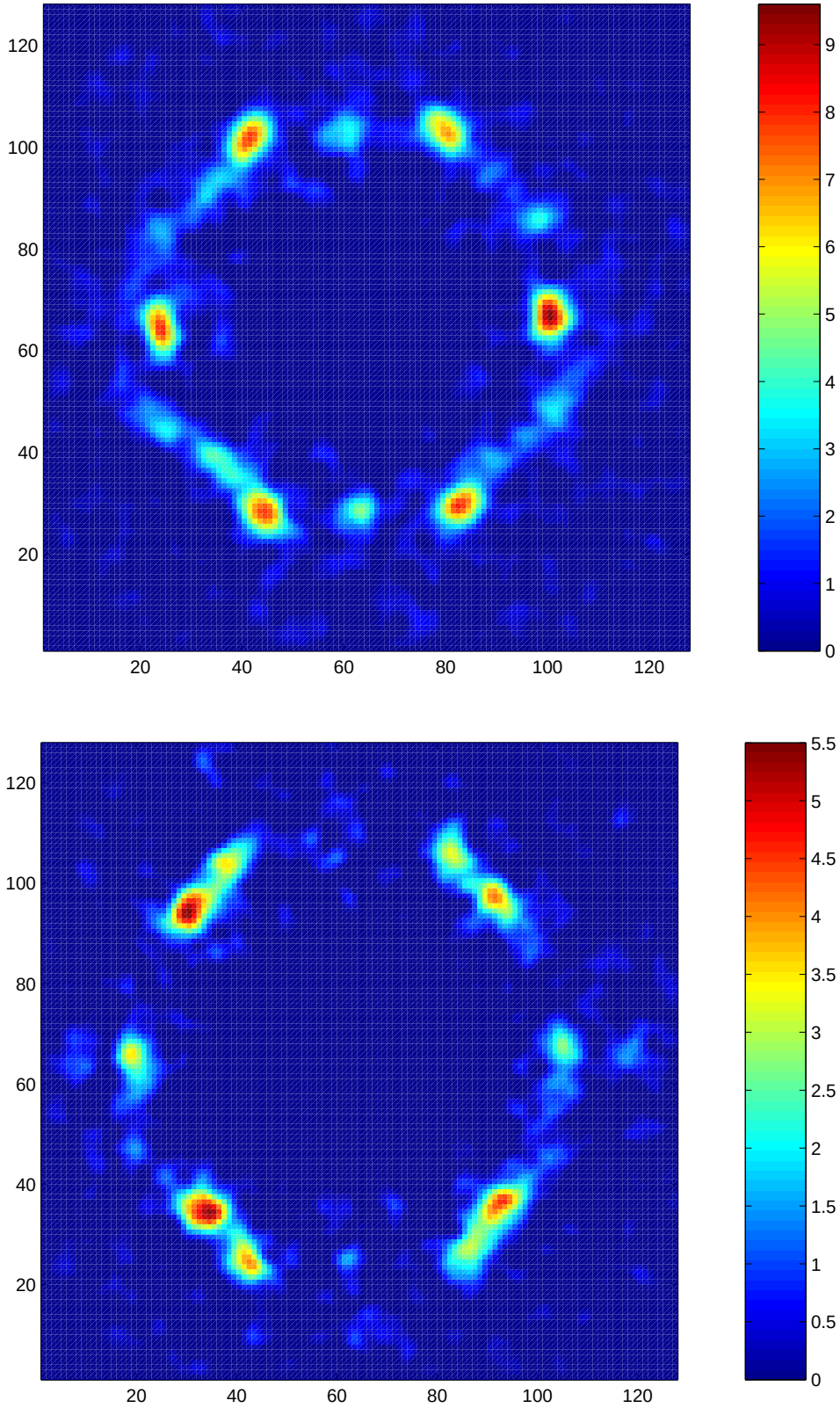

Fig. 3.24: Low-temperature diffraction patterns taken at 7 T (top) and 8.5 T (bottom). These patterns are sums over diagonal rocks.

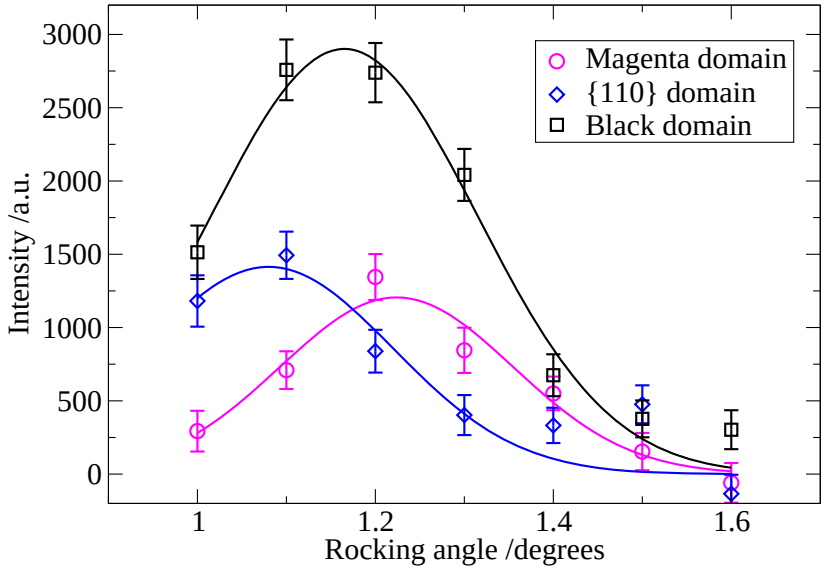

Fig. 3.25: Rocking curves of the three spots visible in the bottom-left sector of the data taken at 7 T. (The spots are denoted according to the convention of figure 3.21.) These rocking curves are representative of rocking curves of other symmetry-related spots. Also shown are Gaussian fits to these data. The fits yields integrated intensities (in arbitrary units) of 1.1(1) (black domain), 0.40(5) (magenta domain) and 0.50(5) ({110} domain). (The fit for the {110} domain is not very good owing to a lack of points on the left side of the rocking curve. The fit was performed assuming a width of 0.14°, which is the average of the other two curve widths (0.13° and 0.15°.))

Triangular vortex lattice structures ($\angle(\mathbf{B},\mathbf{c}) = 10°, \mathbf{B} \parallel (100)$)				
B/T	α_b	β_b	α_m	β_m
5	54.2(6)°	63.0(5)°	50.3(3)°	64.9(3)°
7	55.9(5)°	62.1(5)°	51(1)°	65(1)°
8.5	58.3(5)°	61.0(5)°	—	—

Table 3.2: The angles between reciprocal lattice vectors, α and β, defining the black and magenta domains in figure 3.21. (These are denoted by the subscripts "b" and "m" respectively.) At 8.5 T only the black domain was observable (see figure 3.24).

Figure 3.26 shows the diffraction pattern taken at 9 T in the configuration with the field applied at 10° to the crystal c-axis. From this it can be seen that even the black domain has practically vanished: the spots of this domain that are along the diagonals are still just visible, but the ones on the horizontal axis can only be seen amongst the

noise by the eye of faith. All that remains is a single (within resolution) square vortex lattice domain that presumably occupies both types of crystallographic domain. The distortion of the "square" lattice is very small. The two angles defining this lattice are those subtending the top-left and top-right spots, and the top-right and bottom-right spots. (By symmetry, the angles subtending the bottom-left and bottom-right, and the top-left and bottom-left are respectively equivalent to the former two.) Fitting the strong diffraction peaks of figure 3.26 gives these angles to be 90.8(3) and 89.2(3) respectively. The very small amount of distortion corresponds to a ratio of the sides of the rectangular unit cell of 0.986(4), which is a smaller distortion that that seen with **B** applied 5° away from the c-axis in the other sample orientation. However, the latter measurement was only an "upper" estimate of the distortion for **B** parallel to the c-axis (see section 23) and the true value is likely to be closer to unity.

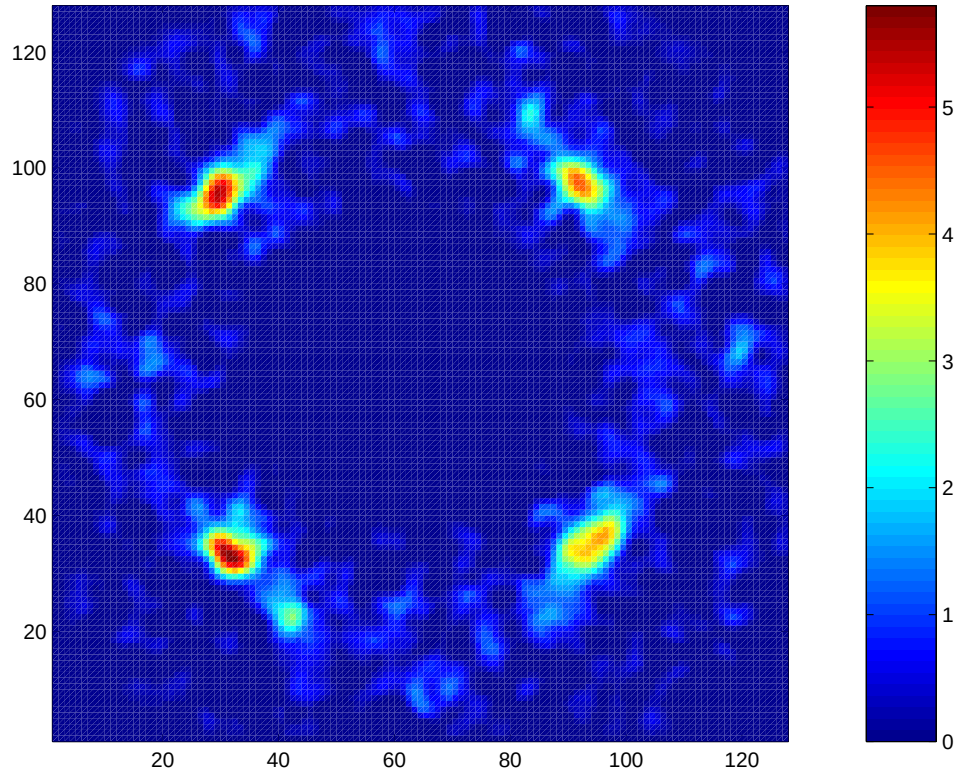

Fig. 3.26: Diffraction pattern obtained by diagonal rocks at 9 T.

The coexistence over a wide field-range of the square vortex lattice domain with the two hexagonal phases implies that the transition to square seen here is very different compared with the case where the field is applied parallel to the twin planes. It is most likely that in the present case the transition is first-order, which permits coexistence of two phases. If at a given applied field, the transition to square occurs somewhere below the irreversibility temperature (below which the vortex lattice structure is frozen) then pinning may be responsible for the survival of large regions of triangular vortex lattice in each of the crystallographic domains. Since the energy balance between different vortex configurations is usually very delicate and the energies involved in pinning are large (of the order of the condensation energy for each vortex pinned), it is quite possible that pinning may freeze in an unstable vortex lattice structure over a wide temperature range even in a sample with relatively low pinning like the present one.

A temperature scan was performed at 8.5 T in order to compare with the corresponding data taken with **B** applied along a twin plane direction. For expediency, the vortex lattice structure at each temperature was investigated by rocking onto the positions of the two diffraction peaks in the bottom-left of the diffraction pattern (see figure 3.24). To recap: at low temperatures the brighter of these two spots is the one associated with a square vortex lattice domain and the slightly less intense one belongs to the "black" triangular vortex lattice domain seen also at lower fields.

The temperature scan is shown in figure 3.27, in which is displayed the region around the two spots as a function of temperature all on the same linear colour-scale. The temperature scan was performed by cooling to 20 K in an applied field and then raising the temperature between each successive frame of figure 3.27 until the signal was lost (about 70 K); a couple of measurements were then taken going down in temperature for comparison. Notwithstanding changes in intensity due to the usual increase in penetration depth with increasing temperature, the structure of the pattern remains static (a fact that can be verified by fitting the spot positions). This is consistent with the conclusion stated above that the diffraction pattern in this orientation comprises two types of vortex lattice, separated by a first order transition, that coexist due to pinning. Furthermore, the occupation of the two domains is quite constant over the

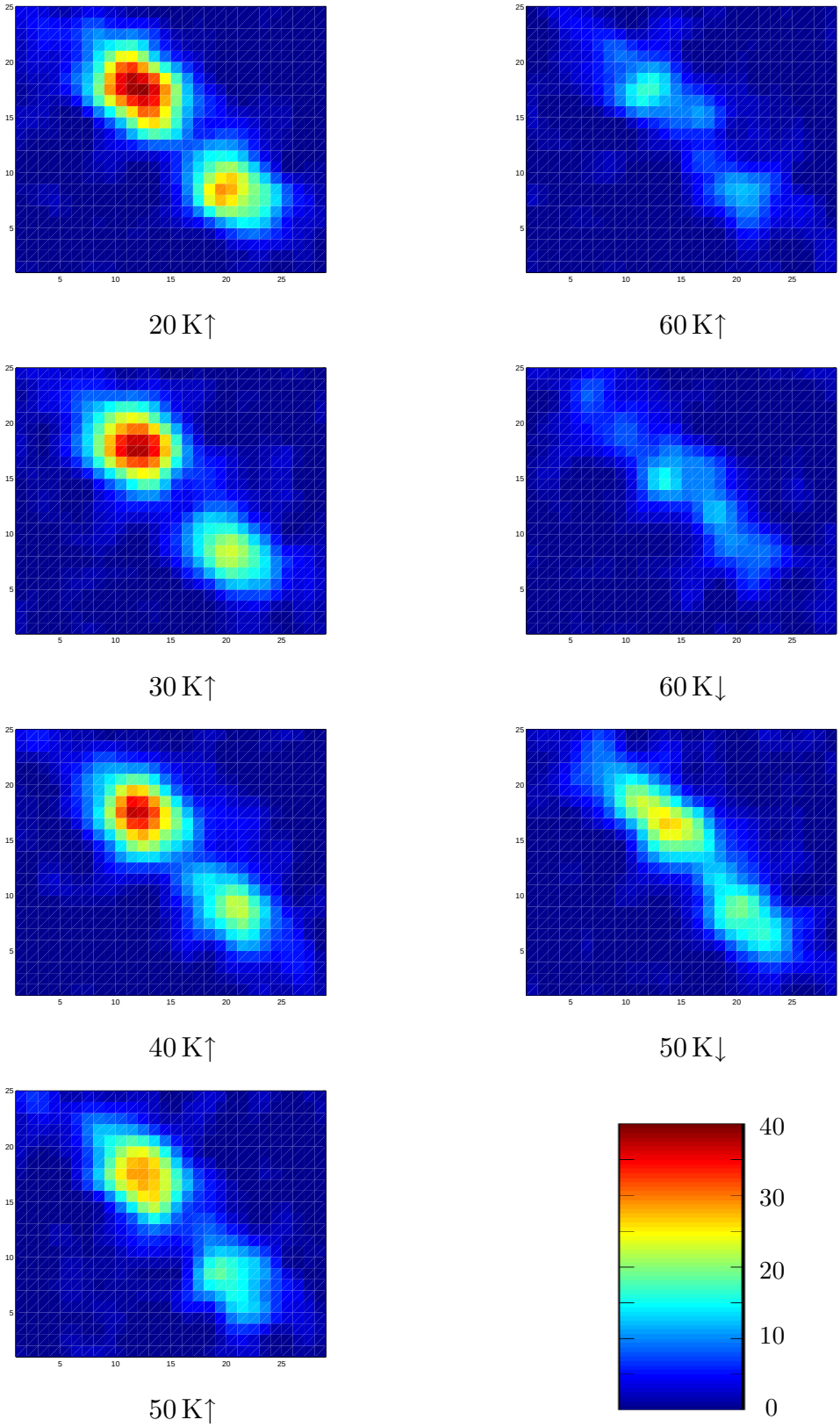

Fig. 3.27: Temperature scan on the bottom-left spots at 8.5 T going both up (↑) and down (↓) in temperature.

temperature range 20–50 K (the intensity ratio of the weaker domain to the stronger domain is about 0.7). However, there is some evidence of hysteresis at higher temperatures. At 50 K there is a difference between the "up" data and "down" data in the ratio of the intensities of the two spots, which are 0.6(1) and 0.8(1) respectively. That there is a larger volume of the triangular lattice relative to the square lattice in the data taken going down in temperature is consistent with the freezing-in of this type of domain below the transition to square.

To elucidate further the effect of applied field angle on the high-field vortex lattice in $YBa_2Cu_3O_7$, measurements were performed with the same sample orientation as above, but with an angle of 30° between the applied field and the crystal c-axis. In figure 3.28 is shown the diffraction pattern taken with 5 T applied at 30° to c. The pattern is composed of data taken by rocking the sample diagonally; neutrons of wavelength 8 Å were used and the sample-detector distance and collimation length were 6 m and 8 m respectively.

Figure 3.28 is quite a complicated diffraction pattern, but even at first sight a nearly isotropic triangular domain consisting of the six bright spots is clearly visible. This domain bears close resemblance to the domain coloured black in figure 3.21, but it is more isotropic and the angles defining this domain (59.4(2)° and 61.2(4)°) are closer to 60° than the corresponding angles of the lattice formed when **B** is only 10° from the c-axis (table 3.2). To an extent, this behaviour is expected from anisotropic London theory alone. The black domain forms with nearest-neighbours along the crystal a-axis, which is perpendicular to the applied field. On the other hand, the b-axis in this crystal domain is rotated towards the applied field due to the sample rotation. The effect of rotation is to couple the effective mass along the c-axis (the "hard" direction) with the effective mass along the b-axis (the "easy" direction). At around 30° (depending on oxygen doping) this coupling negates the basal plane coupling (Johnson *et al.*, 1999). For a biaxial superconductor, rotating the effective-mass tensor (equation 3.2) gives the distortion between the a-axis and the projection of the b-axis to be:

$$\epsilon = \sqrt{\gamma_{ab}^{-2}\cos^2(\theta) + \gamma_{ac}^{-2}\sin^2(\theta)}. \tag{26.2}$$

Using the value of $\gamma_{ab} = 1.28$ obtained at low fields (section 22) in this over-doped

sample and $\gamma_{ab} = 4.5$* gives $\epsilon_{\rm th}(30°) = 1.109$. (In this sample a perfectly isotropic vortex lattice arises when $\theta = 38°$, which is larger than the corresponding value of the sample used by Johnson *et al.* (1999) reflecting the lower oxygen doping in that sample.) Fitting the bright spots of figure 3.28 to an ellipse using the method of section 22 yields an experimental value of $\epsilon_{\rm exp}(30°) = 1.043(9)$. This is slightly less than the theoretical value suggesting that the anisotropy is to some extent suppressed by the same field dependent effect that gives rise to the high-field square lattice with **B** applied both parallel to the c-axis and at 10° to it.

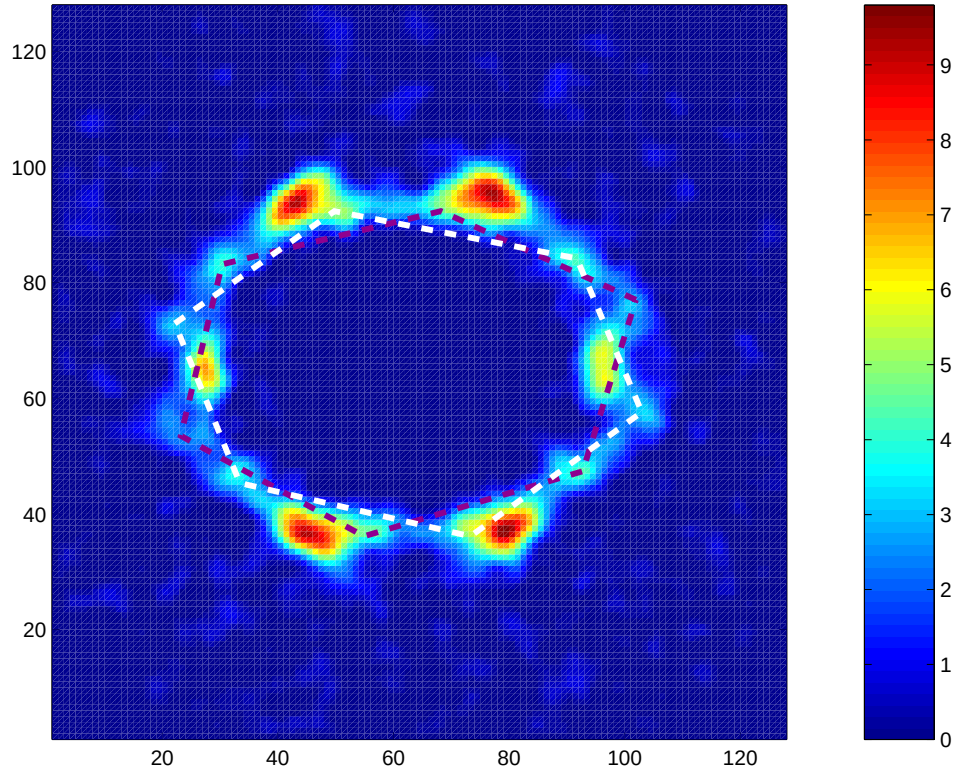

Fig. 3.28: Sum over diagonal rocks taken at 5 K with a magnetic field of 5 T applied at an angle of 30° to the crystal c-axis. In addition to the very clear triangular domain formed of the six strong diffraction peaks two further domains are marked out by the coloured hexagons.

* This quantity has not been determined at low fields for the present sample, but represents a rather typical value (see Yethiraj *et al.*, 1993). The precise value is not important because the second term in the surd is only a small correction.

In addition to the almost isotropic triangular domain, the diffraction pattern of figure 3.28 contains weaker scattered intensity that lies on an eccentric ring with its major axis horizontal in the pattern. If the bright isotropic triangular domain is related to the black domain in the diffraction pattern taken with **B** at 10° to c (figure 3.21), which forms in the crystal domain with the a-axis vertical in real space, then this extra scattering is associated with vortex structures that form in the other domain (the one with b vertical). However, this scattering bears no resemblence to the magenta domain of figure 3.21. Instead of just one nearly isotropic triangular domain, close inspection reveals that this scattering consists of two highly eccentric triangular domains (indicated by the dashed hexagons in figure 3.28). To verify these structures, the spots at the vertices of the hexagons were fitted. Unfortunately, the four spots associated with these domains residing at the top/bottom of the diffraction pattern were too close to the very strong spots of the intense domain to give a reasonable fit even though the odd shape of the strong spots gives good reason to suspect that they are composed of two diffraction peaks. Nevertheless, fitting the other two types of lattice vector in each domain and combining them appropriately gave a set of vectors which lie convincingly close to where by eye the top/bottom spots lie. Further credence is given to this conclusion by taking two of the fitted reciprocal lattice vectors from each domain and verifying that the proposed lattices obey flux quantisation.

The formation of the two eccentric triangular domains is presumably in response to the greater degree of rotation, which takes the a-axis in this crystal domain — along which the predecessor (magenta) vortex lattice was correlated — further away from being perpendicular to the applied field. These domains are similar in appearence to ones observed in another twinned stoichiometric $YBa_2Cu_3O_7$ sample with the field (0.8 T) applied at angles in the range $[45°, 80°]$ to the c-axis (Yethiraj *et al.*, 1993b). There it was claimed* that those structures were consistent with alignment along the intersections of the twin planes, which is not the case here. At $\theta = 30°$ equation 26.1 predicts that the twin-plane-correlated nearest-neighbour direction should be 41° to the vertical real-space axis. None of the reciprocal lattice vectors points to correlations

* No details of this calculation are presented in Yethiraj *et al.*(1993b), nor is the exact structure of any of the domains offered.

along this direction. The closest are the diffraction peaks lying roughly along the diagonal direction, whose corresponding angle is only 33°. Exactly what causes the orientation of the doubly degenerate domains is unclear, but again underlines the need for a good understanding for the intrinsic electronic properties of $YBa_2Cu_3O_7$ assuming extrinsic causes can be ruled out. Whatever the cause, it appears that the structure of these two vortex lattices follows fairly closely that prescribed by anisotropic London theory. To calculate this, the term γ_{ab}^{-2} in equation 26.2 is replaced with its reciprocal to allow for the interchanged a- and b-axes of this crystal domain relative to the former. The resulting distortion of $\epsilon_{\mathrm{th}}(30°) = 1.406$ is in rather good agreement of the measured value of $\epsilon_{\mathrm{exp}}(30°) = 1.39(7)$.

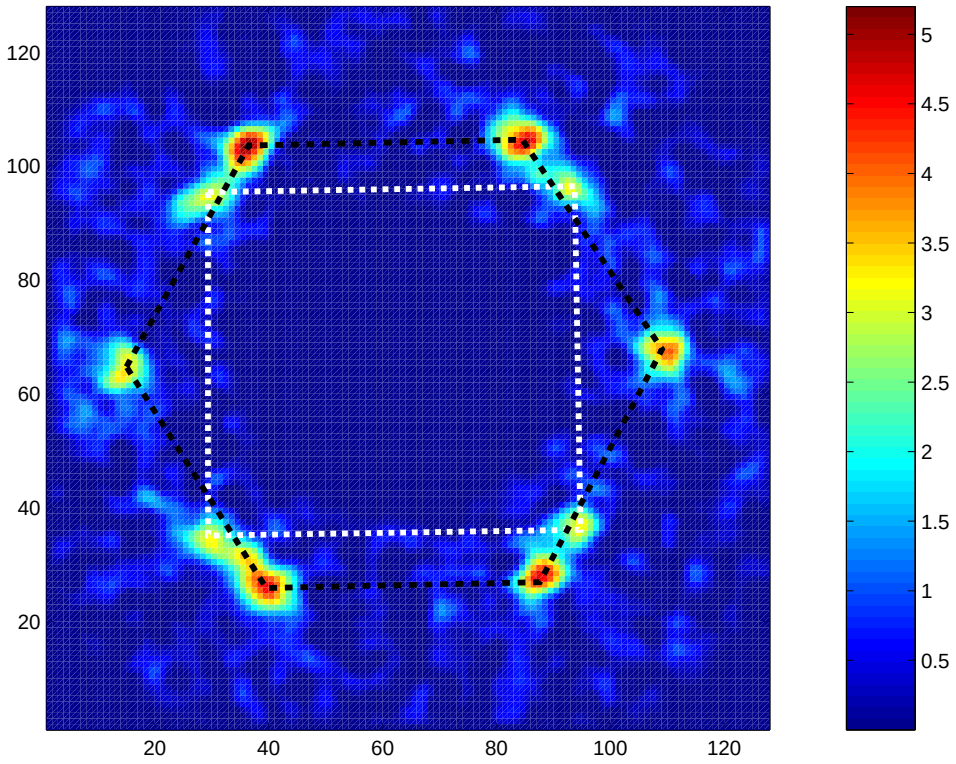

Fig. 3.29: Diffraction pattern obtained by diagonal rocks at 9 T applied at 30° to the crystal c-axis. The square and triangular domains present in the pattern are outlined. Following the discussion of the data with B applied at 10° to the c-axis, the two vortex lattice domains probably occupy separate crystal domains.

At high fields the behaviour of the vortices mimics closely that at 10°. Figure 3.29 shows the diffraction pattern taken at 9 T under the same conditions as the data taken at 5 T described above. Comparing these data with those of figure 3.26 demonstrates the similarities. Both patterns consist of the same two domains, one square and one triangular. The latter is the same "black" domain (oriented in real space with its nearest-neighbour direction along the crystal a-axis, which is vertical in this crystal domain) that has been seen throughout the angle-dependent studies. The former domain is the "final" square domain into which the low-field structures transform. Interestingly, the intensity of this domain relative to the surviving triangular domain is much weaker at 30° than it is at 10°. The implication of this observation is that increasing angle of applied field suppresses the square lattice. Such a conclusion is anticipated by both the d-wave and non-local London theories since the anisotropy that drives the vortices to a square arrangement is confined to the basal plane in both theories. Surprisingly though, the square vortex lattice domain is actually weaker than the "black" domain. If the volumes of the crystal domains are equal then at least equal populations of the two lattices would be expected if each resides in one of the two domains. (The "black domain might be slightly less populated if pieces of it had made the transition to square.) Clearly, more detailed investigations would be required to ascertain whether this is simply a form factor effect or whether disorder plays a role in reducing the scattered intensity.

That increasing the angle of the applied field suppresses the transition towards square is reinforced by figure 3.30. There are shown diffraction patterns taken at 10 T with the field appied at 20° and 30° to the crystal c-axis. (The data were obtained by rocking each of ω and ϕ separately over the range $[-3°, +3°]$ in 0.1° steps with $s_{\mathrm{det}} = 5\,\mathrm{m}, l_{\mathrm{coll}} = 6\,\mathrm{m}$ and $\lambda_{\mathrm{n}} = 8\,\text{Å}$.) Figure 3.30 demonstrates two things. Firstly by comparing the data taken at 10 T applied at 30° with the 9 T data of figure 3.29 it can be seen that in-line with the corresponding field dependence at 10° the triangular domain disappears with increasing field to the benefit of the square domain, whose scattered intensity increases. Secondly, comparing the diffraction patterns at 20° and 30° (both at 10 T) shows quite clearly that the transition to square is inhibited by increasing the angle of applied field. (The triangular domain is stronger at 30°.)

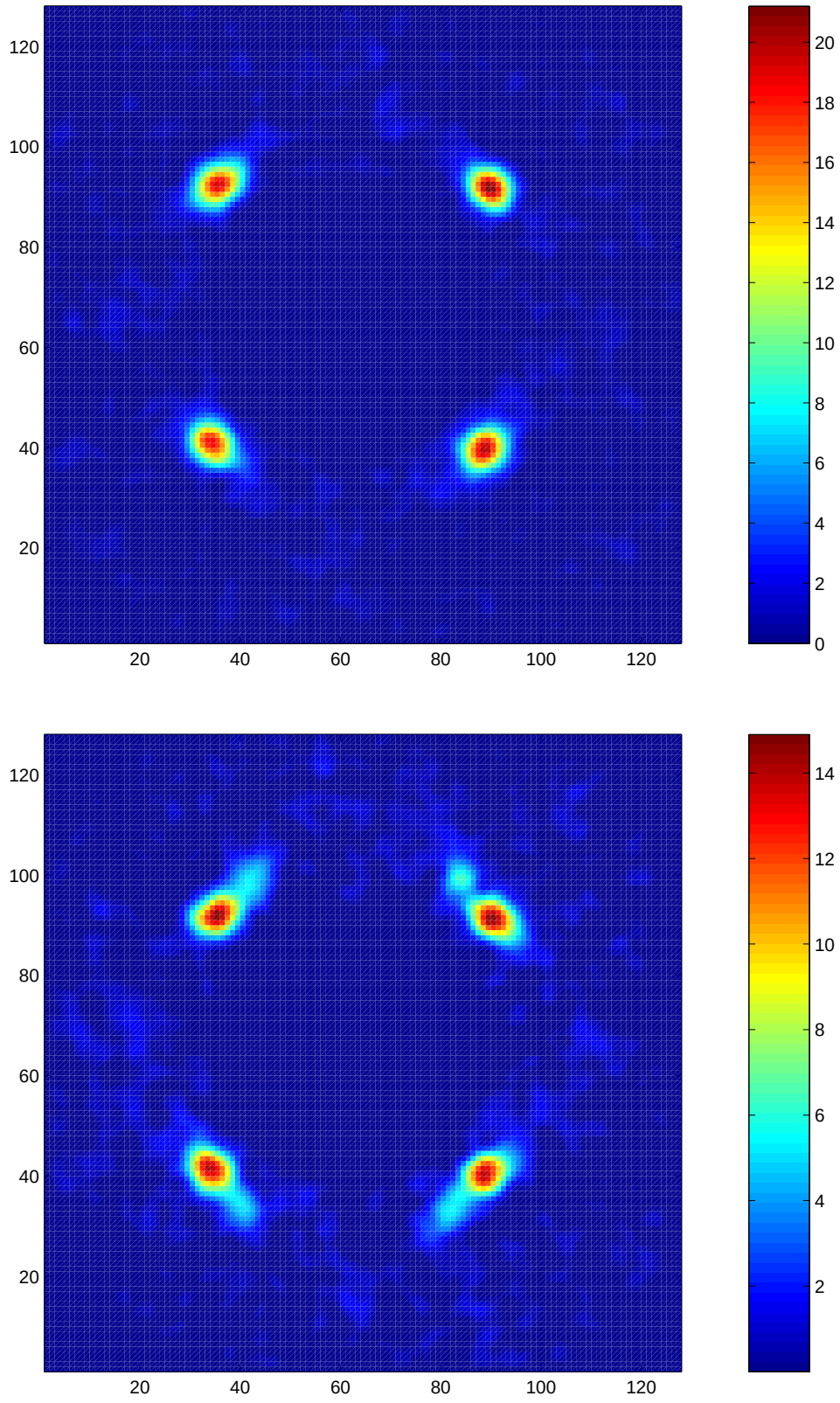

Fig. 3.30: Diffraction patterns at 10 T applied 20° (top) and 30° (bottom) to the *c*-axis.

It is also of interest to examine the dependence on applied field angle of the high-field square lattice distortion. Fitting the square spots visible in the diffraction patterns of figure 3.30 gives values of 0.956(3) and 0.934(6) for 20° and 30° respectively. The direction of these distortions is consistent with a larger effective mass along the horizontal direction perpendicular to the applied field (in real space) caused by the rotation about the vertical {100} direction. However, the degree of distortion seems to vary more slowly than that predicted by anisotropic London theory. In figure 3.31 the measured dependence of the square lattice distortion is compared with the anisotropic London prediction for $\gamma_{ac} = 4.5$ (Yethiraj *et al.*, 1993). Rather than use the experimentally determined value of the basal plane anisotropy (see section 22) an isotropic basal plane has been assumed because with **B** parallel to the c-axis an almost isotropic square lattice is observed. Unsurprisingly, the agreement between London theory and the measurements is poor, which emphasises the unconventional nature of the square vortex lattice observed at high fields in $YBa_2Cu_3O_7$.

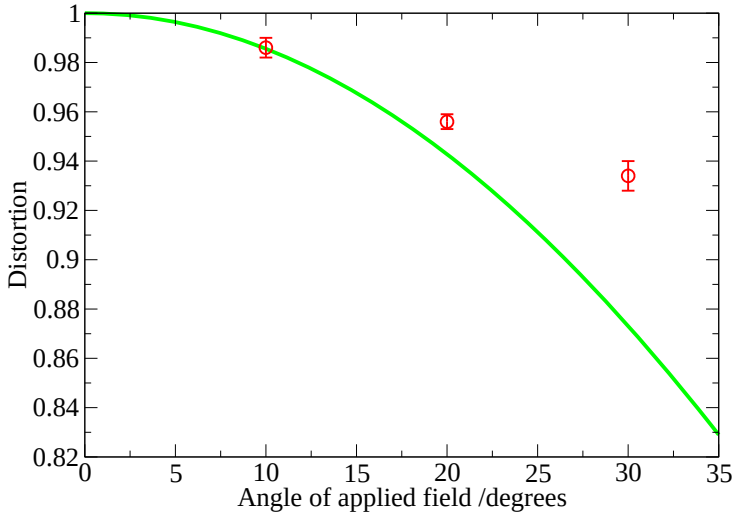

Fig. 3.31: Distortion of the high-field square vortex lattice as a function of applied field angle. The green curve shows the expected dependence from anisotropic London theory assuming that the basal plane is isotropic at $\theta = 0°$ and $\gamma_{ac} = 4.5$ (see equation 26.2).

27. Summary

In this chapter the first structural studies of the high-field vortex lattice in YBCO have been presented. The sample used in the investigations was lightly twinned (stoichiometric) $YBa_2Cu_3O_7$, which is over-doped relative to the optimum-T_c doping (which is seen in $YBa_2Cu_3O_{6.94}$). Consequently, a significant degree of basal plane anisotropy was expected compared to samples with lower oxygen doping (*e.g.* the one used by Johnson *et al.*, 1999). From a series of measurements at the relatively low field of 1 T, the ratio of basal-plane penetration depths was determined to be $\gamma_{ab} = 1.28(1)$, which is accordingly larger than values found in samples containing less oxygen.

The estimation of γ_{ab} relies on the validity of the anisotropic London model. In the London model, the vortices are approximated by singular zeroes of the order parameter (see section 2) and the anisotropy in the circulating super-current arises simply from the anisotropy in the effective electron mass in the plane perpendicular to the vortex. An important role fulfilled by the low field measurements was the verification of the validity of the London model in the low-field regime. It was found that the vortex structure observed at 1 T — namely distorted triangular vortex lattices — coincided well with the corresponding structure calculated both by numerically minimising the London free energy and by a simple scaling argument, if allowance is made for the twin planes, which are parallel to the crystal {110} direction and pin the orientation of the otherwise degenerate vortex lattice. The twin planes have the additional effect of dividing the crystal into small domains of interchanged basal plane axes and hence interchanged anisotropy. Therefore, a total of four degenerate domains (with overall four-fold symmetry) are observed because there are two orientations of twin planes separating the two crystallographic domains.

Given the large energy density involved in twin-plane pinning (of order the condensation energy density), it is most probable that the twin planes exert control over the orientation of the vortex lattice over all the field (applied parallel to the *c*-axis) and temperature range accessible to SANS. The experiments indicate that this is indeed the case: strong diffraction peaks due to vortex planes parallel to the twin planes are observed to the highest available field (11 T). However, the structure of the vortex lattice is not independent of field. Even at 4 T there is a subtle coalescence of

spots that evolves with increasing field until the four-fold symmetric structure of four distorted triangular domains is replaced with what appears within resolution to be a single square vortex lattice domain (section 23). Measurements taken with the field applied at 5° to the *c*-axis show evidence for a slight distortion (0.972(5)); thus the high-field configuration is actually rectangular as expected from the symmetry of the crystallographic domains.

Whilst the twin planes favour lines of vortices aligned along {110}, their role in the high-field square configuration was discounted (section 24). Instead, anisotropy in the vortex-vortex interaction induced by non-local effects arising from either Fermi surface anisotropy or *d*-wave effects were proposed as likely candidates. In $YBa_2Cu_3O_7$, both effects are expected to give rise to the same qualitative effect, *i.e.* a tendency for square-coordinated vortices with nearest-neighbours along {110}. It has not been possible to determine definitively to which anisotropy (Fermi surface or gap) the high-field vortex lattice structure owes its existence. In this regard, there is need for a theoretical study similar to the work on $LuNi_2B_2C$ by Nakai *et al.* (2002), but using realistic parameters for $YBa_2Cu_3O_7$. From an experimental point of view, more detailed measurements on the form-factor would be desirable. Present estimates of the form-factor (section 23) are consistent with *d*-wave theory, but no strong conclusion can be drawn because of the lack of knowledge about parameters needed for a non-local London calculation and the incompleteness of the experimental data.

The temperature dependence provides more compelling evidence that the high-field square vortex lattice arises from an intrinsic anisotropy rather than just twin-plane pinning. With increasing temperature, a continuous transition back to a distorted triangular arrangement is found to occur, although at high fields the vortex lattice was found never to return to exactly the low-field configuration, even at the highest temperatures for which the signal from neutron scattering was detectable. From these data, a phase diagram was constructed that showed the mid-point of this continuous transition bending upwards with increasing temperature. The prevalence of the triangular vortex lattice at high temperatures is indicative of thermal fluctuations "smearing out" the anisotropy responsible for the square configuration. Both non-local London theory and *d*-wave theory predict the same qualitative behaviour, but as is the case with the field

dependence, distinguishing between the two theories based on the experimental data would require more detailed calculations.

Since the field-induced anisotropy occurs in the basal plane, it was expected that changing the angle of the applied field away from parallel to the c-axis would result in suppression of the high-field square lattice. Measurements have verified that this is indeed the case, but during the angle-dependence investigations a veritable zoo of vortex structures was observed. With a modest field of 5 T applied at 10° to the crystal c-axis (rotated about {100} such that none of the twin plane directions was along the induction), two fairly isotropic ($\epsilon = 1.14(2)$ and $\epsilon = 1.229(6)$) triangular lattices are observed with their nearest neighbour directions along the crystal a-direction (or its projection onto the plane perpendicular to the applied field) that presumably populate the two different types of crystal domain available in the sample. (Similar structures to these were observed by Johnson *et al.* (1999) at lower fields (3.3 T) and larger angles of rotation (33°).) Anisotropic London theory is not able to account for either of these vortex lattice structures and the lower values of London distortion may reflect the basal plane anisotropy being to some extent cancelled by the anisotropy that prefers square coordination. Interestingly, neither triangular domain undegoes a continuous deformation to the high-field square lattice. Instead, weak scattering parallel to the crystal {110} directions, that appears to have a triangular q-value at low fields, gradually gets stronger at the expense of the two triangular vortex lattices. It eventually evolves into a square lattice at high fields very similar to that seen with B parallel to the c-axis. (The more anisotropic triangular lattice disappears first, followed by the more isotropic one, which is still just visible at 9 T. Neither of the strong triangular patterns seen at 5 T undergoes much change during this first-order transition.) At intermediate fields there is a coexistence in their respective crystal domains of the a-oriented vortex lattices with the vortex domain that eventually becomes square. Temperature dependent measurements suggest that pinning is responsible for the coexistence of the triangular vortex lattices (preferred at high temperatures and low fields) with the square structure (preferred at low temperatures and high fields).

The mechanism that gives rise to the a-oriented triangular vortex lattices is at present unknown, but is clearly associated to the properties of the basal plane. At 5 T

applied at 30° to the c-axis, only the vortex lattice domain occupying the crystal domain whose a-axis remains perpendicular to the field after rotation is observed. However, it is now very nearly isotropic due to the coupling of the large c-axis effective mass into the basal plane which cancels some of the anisotropy of the latter. The other is replaced by two highly distorted triangular structures similar to those seen by Yethiraj *et al.* (1993b) at much lower fields (0.8 T). These occupy the other type of crystal domain, which has its basal plane anisotropy enhanced by the coupling of the c-axis effective mass. The distortion of these two domains is in good agreement with the anisotropic London prediction at this angle ($\epsilon = 1.41$), but their orientation is not understood. It cannot be due to the intersection of twin planes with the CuO_2 planes as suggested by Yethiraj *et al.* (1993b) so is possibly intrinsic in nature.

The field evolution of the two eccentric triangular domains seen at 5 T applied 30° to c is not very different from that of the nearly isotropic one (found at smaller field angles) that they replace. However, as already suggested, the field at which the transition to square occurs is larger. There is also an increase in the distortion of the high-field square vortex lattice expected from the coupling of the c-axis effective mass, but it is found to be significantly smaller than that predicted by anisotropic London theory. This is another example of the non-scalable anisotropy in the vortex-vortex interaction at high fields acting in opposition to the scalable effective mass anisotropy, giving rise to a structure that is apparently more isotropic than expected from simple London theory.

CHAPTER IV

ADDITIONAL WORK

28. Introduction

The measurements and analyses presented in chapter III represent the principal results of this thesis, but they are only part of a broader programme at Birmingham whose aim is to study condensed matter systems (particularly superconductors) using neutrons, muons and X-rays. Common to each of these techniques is their ability to probe *microscopic* correlations making them ideal complementary partners to traditional lab-based experiments, which normally measure macroscopic and thermodynamic properties.

In this chapter is presented a brief tour through three other large-facility experiments in which this author has had an active role. The first two are SANS studies of the vortex lattice in $Nd_{2-x}Ce_xCuO_4$ and detwinned YBCO samples of different doping to the one studied in chapter III. Both of these are intimately related to the main work of this thesis, *i.e.* the study of unconventional vortex structures in *d*-wave superconductors. The third — the measurement of spin fluctuations in $Sr_3Ru_2O_7$ — is well off the beaten track of SANS measurements of the vortex lattice. Nevertheless, it is congruent with a broader theme: the study of strongly interacting systems. Many new oxide materials (including $YBa_2Cu_3O_{7-\delta}$, $Nd_{2-x}Ce_xCuO_4$ and $Sr_3Ru_2O_7$ amongst very many others) are characterised by their very strongly-interacting electrons, which exhibit radically different behaviour from the idealised Fermi liquid. Unconventional superconductivity and quantum-critical metamagnetism are two examples of the kind of emergent behaviour seen in complex condensed matter systems.

29. Square vortex lattice in NCCO

In this section are presented SANS measurements of the vortex lattice in the electron-doped high-T_c superconductor $Nd_{1.85}Ce_{0.15}CuO_4$ (Gilardi *et al.*, 2004), which were performed in close collaboration with R. Gilardi and J. Mesot of the Laboratory for Neutron Scattering, ETH Zürich. The work summarised here was published in Physical Review Letters in 2004 (Gilardi *et al.*, 2004).

In a similar fashion to their hole-doped counterparts, electron-doped high-T_c materials emerge from their antiferromagnetic parent compound (Nd_2CuO_4 in the case of $Nd_{2-x}Ce_xCuO_4$) by doping with charge carriers. However, as their name suggests, electron-doped superconductors are doped to have more free electrons per unit cell than the parent compound (Takagi *et al.*, 1989), which conspires to make the properties of electron-doped materials somewhat different from hole-doped varieties. For example, electron-doped materials tend to have comparatively low critical temperatures and upper critical fields (for $Nd_{1.85}Ce_{0.15}CuO_4$, $T_c \approx 20\,\mathrm{K}$ and $B_{c2} \approx 8\mathrm{T}$; *cf.* $T_c \approx 90\,\mathrm{K}$ and $B_{c2} \sim 100\mathrm{T}$ in $YBa_2Cu_3O_7$). Also, it has been shown by the inelastic neutron-scattering experiments performed by Yamada *et al.* (2003) that antiferromagnetism coexists with superconductivity in electron-doped cuprate superconductors.

Since both the electron- and hole-doped cuprates share similar crystal structures based on CuO_2 layers, it is inevitable that there are similarities between them too. In hole-doped systems, the CuO_2 planes play a crucial role in determining the symmetry of the superconducting order parameter for which there is substantial evidence favouring the *d*-wave picture (see section 19). In the electron-doped materials, many measurements gave indication of *s*-wave pairing, but more recent phase-sensitive measurements based on the half-flux-quantum effect (Tsuei & Kirtley, 2000b), which is probably the most reliable technique for determining the order parameter symmetry, were found to be consistent with *d*-wave pairing.

Interest in both hole- and electron-doped cuprates has been stimulated by the *d*-wave symmetry of the superconducting order parameters (see section 8), which can give rise to unconventional vortex lattice structures. Measurements showing the effects of the *d*-wave order parameter on the vortex lattice have already been reported in some hole-doped systems including $La_{1.87}Ca_{0.17}CuO_4$ (Gilardi *et al.*, 2002) and $YBa_2Cu_3O_7$

(see Brown *et al.*, 2004; Brown *et al.*, 2005; and this thesis); but there is a lack of equivalent data for electron-doped compounds like $Nd_{2-x}Ce_xCuO_4$, and thus there is motivation for an experiment.

The data presented here represent the first SANS measurements of the vortex lattice in the electron-doped material $Nd_{1.85}Ce_{0.15}CuO_4$. The experiments were carried out on the small-angle diffractometer D22 at Institut Laue-Langevin, Grenoble, France. Two samples were used, both grown in a mirror furnace and then annealed to give $T_c \approx 25\,K$ (Kurahashi *et al.*, 2002). The first was a bi-crystal cylinder of 5 mm diameter whose domains' c-axes were misaligned by a relative rotation of 7°. The second sample consisted of thin (≈ 1.5 mm) plates cut from a single-crystal cylinder using a diamond-blade circular saw and was intended to be used when scattering long-wavelength neutrons where attenuation becomes an issue. (Nd is quite a strong absorber of neutrons.) During the experiments, the samples were mounted in a cryostat in a similar arrangement to that discussed in section 21 (with the field parallel to the crystal c-axis (or bisecting the two c-axes in the bi-crystal). As before, the measurements were taken at low temperatures ($T = 2\,K$) and a background taken above T_c was subtracted.

In figure 4.1 are shown diffraction patterns at various magnetic inductions applied parallel to the c-axis. Despite the relatively large value of B_{c2} in NCCO, it was found that in the samples used here, the neutron signal from the vortex lattice was immeasurably small above about 400 mT. This point will be returned to later, but for now the structure of the vortex lattice at fields of 200 mT and below will be examined. In taking the data displayed in figure 4.1, measurements were made difficult at "high" fields due to the weakness of scattering. At the low end of the field range they were equally tricky due to the extremely low-q of the vortex lattice signal, which although stronger than the scattering at high fields, was swamped by a very large background signal that varies as q^{-n}. Of further concern was the change in background scattering between the low-temperature foreground scans and the high-temperature background scans caused by thermal expansion of the sample stick, which moved the sample vertically very slightly. To overcome this, a background shift was employed, which involved shifting the background pixel array relative to the foreground before subtraction. The

shift was calculated by a least-squares fitting algorithm that minimised according to the amount of shift the sum of residuals over an annulus around the detector centre in the background-corrected data. It might be thought that taking a zero-field background at low temperatures would be a better option, but in NCCO a field-dependence in the magnetic scattering is expected due to the tendency of anti-ferromagnetic ordering of both the Cu^{2+} moments and, at low temperatures, the Nd^{3+} moments (Yamada *et al.*, 2003).

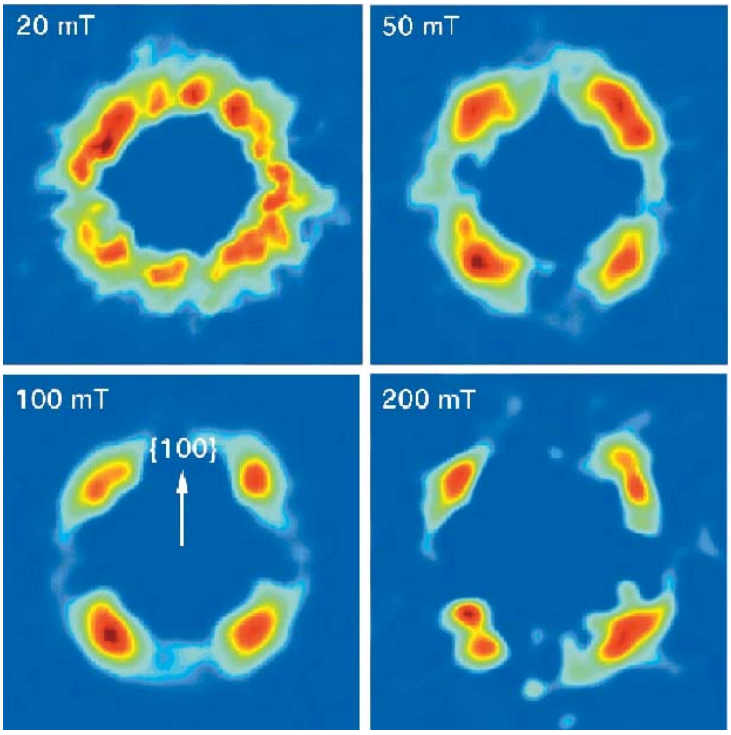

Fig. 4.1: (From Gilardi *et al.*, 2004.) Diffraction patterns of the vortex lattice in $Nd_{1.85}Ce_{0.15}CuO_4$ taken at 20 mT (top-left), 50 mT (top-right), 100 mT (bottom-left) and 200 mT (bottom-right). The crystallographic {100} directions are horizontal/vertical in this figure.

Figure 4.1 shows that the configuration adopted by the vortices at 50 mT, 100 mT and 200 mT is square with the vortex nearest-neigbour direction along {110}. The orientation coincides with both the nodes of the *d*-wave superconducting order parameter and the Fermi velocity minima, hence this configuration is anticipated by both *d*-wave (section 8) and non-local (section 7) theories of the vortex lattice. At 20 mT the pattern is ring-like and can be attributed to an orientationally disordered vortex phase, which is expected in the low field regime where the vortices are widely spaced

($\approx 300\,\mathrm{nm}$ at $20\,\mathrm{mT}$). However, a tangential sum as a function of the radial q-value of these data shows (figure 4.2) that the inter-vortex spacing as measured by the peak in the q-value is consistent with a square lattice, not triangular coordination. Magnetisation measurements show that at low fields the trapped flux is equal to within 1% to the value expected from the applied field. The difference in q-values between triangular and square configurations is roughly 7%, so any systematic error from this cause in discerning between the two can be ruled out.

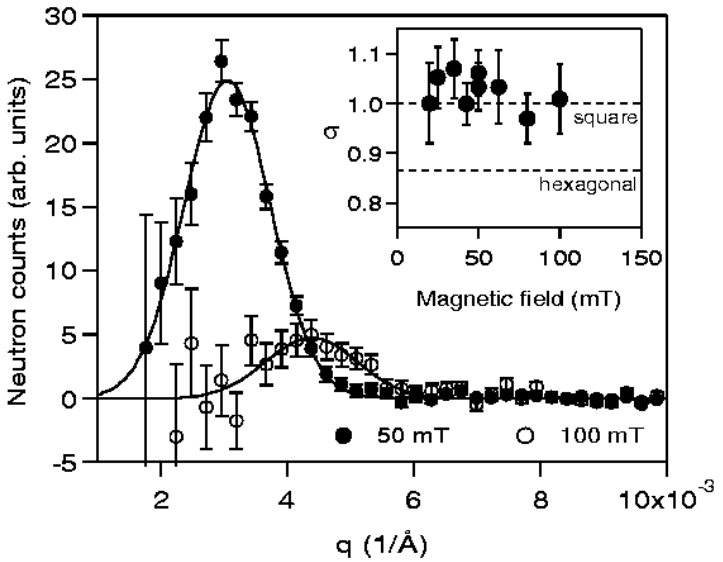

Fig. 4.2: (From Gilardi *et al.*, 2004.) Plots of the intensity as a function of the radial q-value calculated by summing the diffraction patterns tangentially. The inset shows a plot of the structure-dependent factor $\sigma = \sin(\alpha)$, where α is the angle between reciprocal-lattice basis vectors using the convention that $\alpha \in [0, 90°]$ and assuming an isotropic lattice (equal-length vectors). The factor α determines the length of the reciprocal lattice vectors via flux quantisation ($q = 2\pi\sqrt{B/\sigma\Phi_0}$). For a triangular lattice, $\sigma = \sqrt{3}/2$, whereas for square coordination, $\sigma = 1$.

It is a remarkable observation that the structure of the equlibrium vortex lattice in $Nd_{1.85}Ce_{0.15}CuO_4$ is square and remains so down to such low fields. This is in contrast to all of the other d-wave compounds in which a similar transition occurs at rather higher fractions of H_{c2}, and it also contrary to theories predicting the field scale of the the transition: d-wave theory predicts (Ichioka *et al.*, 1999) a transition field of $0.15H_{c2} \approx 1.2\,\mathrm{T}$ and a similar order of magnitude would be expected from non-local London theory. (The details would require detailed knowledge of the Fermi surface

— see Kogan *et al.*, 1997; the experimental evidence suggests that the Fermi surface in $Nd_{1.85}Ce_{0.15}CuO_4$ is an almost isotropic hole-like surface similar to YBCO (Darmascelli *et al.*, 2003)). It therefore seems that whatever drives vortices to assume a square arrangement is beyond the "simple" *d*-wave and non-local theories and could possibly have origins in the anti-ferromagnetic correlations present in the CuO_2 planes in $Nd_{2-x}Ce_xCuO_4$. In fact, the characteristic wave-vector of these correlations is along {110} (Yamada *et al.*, 2003), which coincides with the vortex nearest-neighbour direction.

Even more astonishing than the existence of the low-field square lattice is the fact that at 20 mT the vortex lattice has local square coordination, but appears to have no long-range orientational order. Degeneracy in orientation is a well-known feature in the isotropic London and Abrikosov theories (see sections 2 and 5) and can even occur in anisotropic London theory when the field is applied along a principal crystal direction (see section 3). However, every source of anisotropy that supports an unconventional square morphology — be it Fermi surface anisotropy or nodes in the superconducting order parameters — is coupled to the underlying crystal structure. So it is extremely surprising given the single/bi-crystal nature of the samples used (as verified by neutron Laue diffraction patterns) that the vortices should be so irresolute towards their relative orientation.

Another puzzle uncovered by these measurements is the rapid decay of the scattered intensity from the vortex lattice, which is graphed in figure 4.3. Strictly speaking, the integrated intensity should be calculated by integrating over the rocking curve, but that is impossible in these samples because the scattered intensity of the diffraction peaks shown in figure 4.1 was, within experimental errors, constant over a $\pm 4^\circ$ range of rocking angles. Therefore, with the measurement of complete rocking curves deemed impracticable, the integrated intensity as a function of field was represented by the intensity at a fixed angle, which gave the data of which figure 4.3 is comprised.

The "integrated" intensity shown in figure 4.3 exhibits a very rapid drop-off with increasing field that is not well described by an intrinsic decrease. Visually, a power law with exponent -2 gives a satisfying account of the data. The plain London theory patently fails to account correctly for the observed collapse of the intensity. In London

theory, the field diverges at each vortex core, thus there is no loss in magnetic contrast with increasing field and the only field dependence is the rather slow $B^{-\frac{1}{2}}$ whose origin is in the geometry of reciprocal space (see sections 2 and 11). It might be argued that correcting for the finite core size would improve matters, but this only generates Gaussian or exponential prefactors to the integrated intensity via the form factor (see section 2). Clearly, no amount of fiddling of coefficients can bring agreement of such expressions with the observed power law on the log-log plot of figure 4.3.

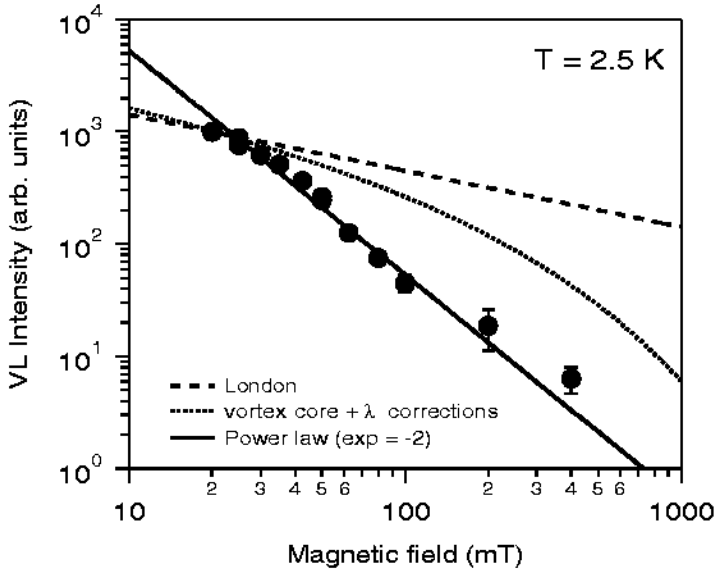

Fig. 4.3: (From Gilardi *et al.*, 2004.) The scattered intensity from the vortex lattice taken at $T = 2.5\,\mathrm{K}$. Also shown are theoretical predictions given by London theory (varying $\propto B^{-\frac{1}{2}}$; see section 11) and London theory with corrections for the vortex cores and the field-depedence of the penetration depth (see Gilardi *et al.* (2004) for details). Clearly neither of the dashed theoretical curves is able to reproduce the B^{-2} power law given by the data.

Another intrinsic source considered by Gilardi *et al.*(2004) as a candidate for the decrease in scattered intensity is the field dependence of the magnetic penetration depth. In a fully-gapped *s*-wave superconductor, the change in quasi-particle population from its ground state induced by the application of a field (via the resulting supercurrent flow) may often be neglected. An obvious exception occurs in the mixed state in the vicinity of a vortex core where the order parameter is suppressed; the vortex core corrections proposed above arise from this. However, the picture is much different in a *d*-wave superconductor whose order parameter nodes ensure that the quasi-particle

population will be affected by supercurrent flow even far from the vortex cores (Amin *et al.*, 1998). One way of looking at this is in terms of enhanced non-locality near the nodal directions (see section 8). There is evidence from μSR measurements (Sonier *et al.*, 1997) that the penetration depth varies linearly with field in the way predicted by Yip & Saul (1992):

$$\frac{\lambda(B)}{\lambda(0)} = 1 + \beta\frac{B}{B_0}, \tag{29.1}$$

where $B_0 = \Phi_0/(\pi^2\lambda\xi)$ is of the order of the thermodynamic critical field, $B_c \approx 0.3\,\mathrm{T}$, and the coefficent β was taken to be 7×10^{-2} (the value appropriate for YBCO) after Sonier *et al.* (1997). Like the finite-core correction, the correction due to the field-dependence of the penetration depth can be worked into the integrated intensity via the London form factor. The integrated intensity (equation 11.6) is proportional to λ^{-4}, therefore equation 29.1 cannot account for the data of figure 4.3. In addition, with $\beta = 7 \times 10^{-2}$, the correction at 200 mT to the plain London integrated intensity is only in the region of 20%. A value of β close to unity would be needed to get convergence of theory and data and it is not expected that this factor, which was measured in YBCO, should be vastly different for NCCO.

Having ruled out field-dependence of the vortex form factor as a probable cause, attention now turns to the effects of disorder on the structure factor (see section 9). First, it should be noted that a cross-over from three dimensions to two dimensions, such as that responsible for melting of the vortex lattice in $Bi_{2.15}Sr_{1.95}CaCu_2O_{8+x}$ (Cubitt, 1993), is unlikely in the field range of figure 4.3. (In fact, in $Nd_{1.85}Ce_{0.15}CuO_4$ the cross-over is expected at $B_{2D} \approx 13\,\mathrm{T} > B_{c2}$ (Gilardi *et al.*, 2004)). Instead, a transition to a three-dimensional vortex glass state like that observed in $La_{1.9}Sr_{0.1}CuO_4$ (Divakar *et al.*, 2004) seems more plausible. A similar rapid drop in integrated intensity has been observed in the vortex lattice of (K,Ba)BiO_3 (Joumard *et al.*, 1999 and Klein *et al.*, 2001). In those experiments, the peak of the rocking curve decreased with increasing magnetic field, but the width remained constant. Klein *et al.* (2001) attribute this to the Bragg glass state where the full-width at half maximum of the rocking curve is controlled by the constant experimental resolution. The peak height is determined by power laws in both the experimental resolution and the correlation length of the vortex lattice, which decreases with increasing field giving the observed decrease in intensity.

(Essentially, this occurs due to the form of the structure factor, which is a power law in q with a divergent peak and long tails — see Klein *et al.* (2001), Giamarchi & Le Doussal (1997) and Giamarchi & Bhattacharya (2001) for details.) The present data (figure 4.3 is only really comparable with the high end of the field range in the (K,Ba)BiO_3 studies where a transition from Bragg-glass behaviour to a more disordered state is seen. (At lower fields, the measurements of Klein *et al.* (2001) are resolution limited, which is a vastly different state of affairs than the vortex lattice reported here, whose width is in excess of 10°.)

In summary, the results presented here give firm evidence of a square vortex lattice in single-crystal $Nd_{1.85}Ce_{0.15}CuO_4$ at unprecedentedly low fields. As is the case with $YBa_2Cu_3O_7$, it is not possible to distinguish whether the origin of this is due to d-wave or non-local effects as both of these predict the observed configuration. Equally, neither theory can explain the adoption of the square configuration at such small fractions of H_{c2} and it remains an outstanding issue that may possibly require a theory taking into account the anti-ferromagnetic correlations in this material. Another unresolved point is the observation at 20 mT of an apparently square vortex lattice with no orientational order. Unconventional square lattices arise due to coupling between the vortices and the crystal lattice, which inherently impose a favoured orientation on the vortex lattice. If the term in the free energy favouring a square lattice oriented along {110} is frustrated by a much stronger disorder term, then why should the lattice keep a square q value rather than reverting to the triangular one?

Only a very small low-field range of the phase diagram has been explored so far and it goes without saying that further work at higher fields is desirable. The high-field SANS facility at PSI provides the possibility of measuring right up to $H_{c2}(T = 0)$, allowing the entire phase diagram to be explored unlike in $YBa_2Cu_3O_{7-\delta}$ and $La_{2-\delta}Sr_\delta CuO_4$ whose large upper critical field prohibit this. Before that can be achieved, an improvement in sample quality is necessary. The present sample presumably contains many pinning centres that are responsible for the very low field transition to a disordered vortex glass state.

30. SANS measurements on detwinned YBCO

The measurements presented in chapter III provide convincing evidence of a triangular to square transition in the vortex lattice structure in $YBa_2Cu_3O_7$, which may be understood in terms of either the non-local London theory or d-wave theory. Both those theories predict that the vortex nearest-neighbour direction lies along the {110} direction. This is indeed observed, however the presence of twin planes in that sample, which prefer orientation along {110}, somewhat undermines the direct relationship between the vortex lattice configuration and sources of intrinsic anisotropy. In addition, the twinned nature of the sample produced significant difficulty in accurately determining the vortex lattice structure as a function of field. It was in part to address these issues that further measurements on the vortex lattice in $YBa_2Cu_3O_7$ have been carried out on a set of detwinned samples. However, a greater motivation to perform more experiments was to extend the measurements: new samples have been grown with different hole dopings, which will add another dimension to the triangular to square phase diagram. In this section a glimpse of some of the next-generation SANS measurements on YBCO are presented. These measurements have been done in close collaboration with V. Hinkov and B. Keimer, who provided the samples and initiated the experiments. Since the investigations are still being actively pursued, only a small selection of the data will be presented; a complete fully-analysed account will be the subject of a future Physical Review Letter (Hinkov *et al.*, 2006a) and will form part of the Ph.D. thesis of V. Hinkov (Hinkov, 2006b).

The first detwinned sample used was of $YBa_2Cu_3O_{6.99}$, which should have comparable electronic properties to the twinned $YBa_2Cu_3O_7$ crystal used previously. Due to the difficulty in detwinning large single crystals, the sample was actually composed of ten small crystals (each $\approx 20\,\mathrm{mg}$) mounted in a well-aligned mosaic. The sample was mounted in the same cryomagnet used in the studies of the twinned sample with the field applied parallel to the crystal c-axis and the a-axis vertical relative to the detector. The diffraction pattern obtained from the vortex lattice in this sample at the relatively low field of 1 T is shown in figure 4.4. The pattern is hexagonal with the distortion expected from the basal plane electron effective-mass anisotropy. Each of the six spots has significant tangential width and moreover, some structure is evident,

indicating that the spots are in fact composed of multiple diffraction peaks. There are most probably a small number of residual twin planes that support distorted triangular vortex lattice domains pinned along the twin planes. (Recall that in the London regime the vortex lattice is orientationally degenerate thus even a very small number of twin planes can affect the orientation.) This is a similar situation to that depicted in figure 3.4, but with only *two* vortex lattice domains corresponding to the one dominant orientation of anisotropy. The pattern is also consistent with scattering from a vortex lattice domain with nearest-neighbours along the crystal b-direction, though it is difficult to resolve it. Rotating the c-axis by 10° away from the applied field direction to remove the influence of the twin planes does give clearly a b-oriented domain (Hinkov *et al.*, 2006a & 2006b). Johnson *et al.* (1999) observed a similar pattern at 0.51 T, but in that study there was another domain with nearest-neighbour aligned along the crystal a-axis. It is unknown whether that domain is suppressed here at 1 T, or whether its absence reflects the higher degree of oxygen doping in the present sample. It should also be pointed out that since this sample and the twinned sample of chapter III are very similar in doping, the b-oriented vortex lattice domain is the one preferred in the latter sample at low fields (although it is masked by twin plane pinning).

As the applied field is increased, the structure of the vortex lattice in the sample of $YBa_2Cu_3O_{6.99}$ undergoes a transition to square similar to that seen in the twinned sample (section 23). Figure 4.5 shows the diffraction pattern taken at 9 T. Here, the vortex lattice has a clear square structure with the vortex nearest-neighbour direction along the {110} direction in accordance with the predictions of d-wave theory and non-local London theory, as well as the experimental data on the twinned sample. These data provide satisying confirmation of the assertion in section 24 that the transition to a high field square vortex lattice has nothing to do with the presence of twin planes since there is expected to be a far smaller number of twin planes in the present sample.

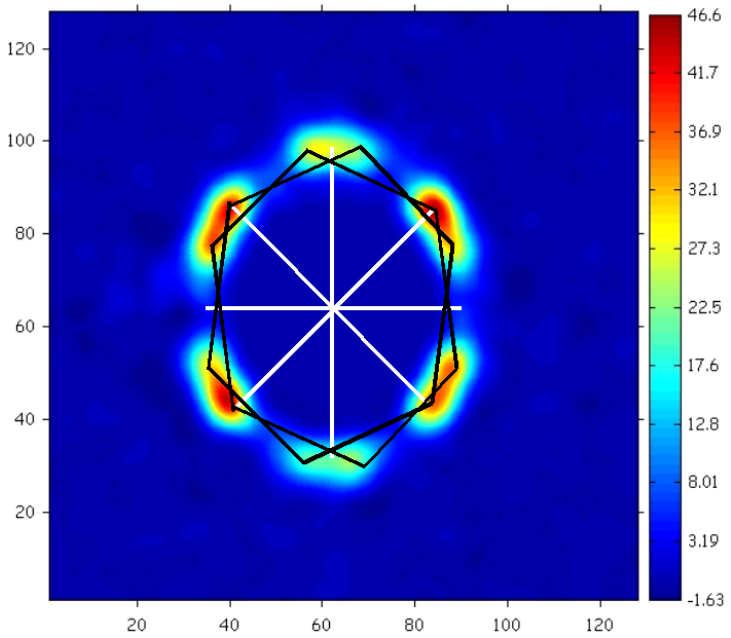

Fig. 4.4: Linear plot of the diffraction pattern obtained from the mosaic of $YBa_2Cu_3O_{6.99}$ crystals with a field of 1 T applied. The a-axis is vertical relative to the detector. The white lines superimposed on the pattern are parallel to the {100} and {110} crystal directions. The black hexagons represented distorted hexagonal vortex lattices pinned to a twin plane direction along {110}.

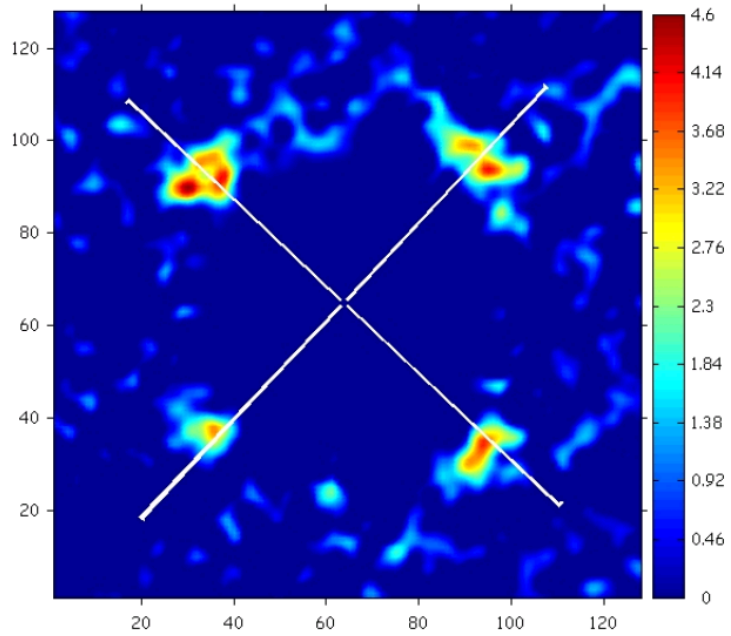

Fig. 4.5: Linear plot of the diffraction pattern obtained from the mosaic of $YBa_2Cu_3O_{6.99}$ at 9 T. The white lines are parallel to the crystal {110} directions.

Another sample used in the new studies consisted of small detwinned single crystals of calcium-doped $YBa_2Cu_3O_7$. Ca^{2+} ions are roughly the same size as Y^{3+} ions and therefore simply substitute yttrium in the crystal structure to form $Y_{1-y}Ca_yBa_2Cu_3O_7$. Since they are only bivalent, calcium ions donate one fewer electron than trivalent yttrium, therefore doping with calcium effectively adds holes, which increases the number charge carriers in $YBa_2Cu_3O_7$. The effect of this on the $YBa_2Cu_3O_7$ Fermi surface shown in figure 3.2 is to increase the cross-sectional area of the hole surface, which given the band structure will result in a more distorted square-shaped surface.

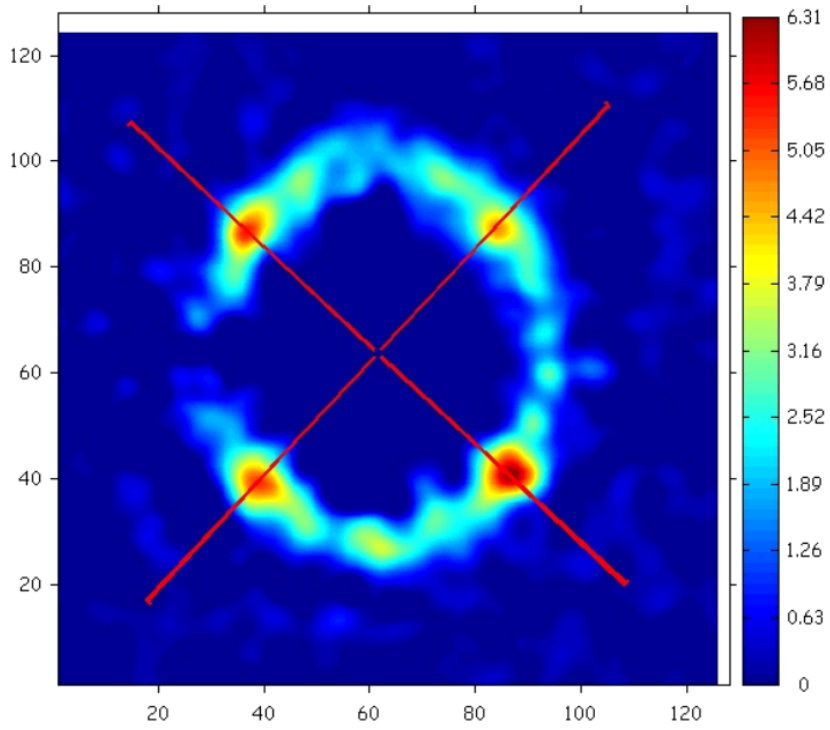

Fig. 4.6: Linear plot of the diffraction pattern obtained from the mosaic of $Y_{1-y}Ca_yBa_2Cu_3O_7$ at 1 T. The red lines lie roughly along the crystal {110} and the sample is mounted with the crystal a-axis vertical in the picture.

The diffraction pattern at 1 T obtained from the vortex lattice in the mosaic of single crystals of $Y_{1-y}Ca_yBa_2Cu_3O_7$ is shown in figure 4.6. The scattering lies on an ellipse oriented as expected from the basal plane anisotropy. Four strong spots lie on the ellipse along the {110} direction, which might arise from some kind of intrinsic ordering, but are most probably due to residual twin plane pinning. Some structure is discernible along the ring of scattering and bears resemblence to the two distorted triangular domains seen in the detwinned sample of $YBa_2Cu_3O_{6.99}$ (see figure 4.4).

However, figure 4.6 demonstrates that doping with calcium introduces more disorder than expected from the simple-minded view of calcium ions substituting yttrium ions.

Figure 4.7 shows the diffraction pattern from $Y_{1-y}Ca_yBa_2Cu_3O_7$ at 4 T. In this pattern, much of the scattered intensity distributed around an ellipse at 1 T is diminished and the features along {110} are more pronounced. At 7 T (figure 4.8) all that remains is the four spots along the diagonals, which imply a square vortex lattice structure. The field evolution of the data displays the classic signatures of a triangular to square transition and in many respects is the same as in the detwinned $YBa_2Cu_3O_{6.99}$ mosaic and the twinned $YBa_2Cu_3O_7$ crystal. What is surprising and different is that the transition appears to start and complete at significantly lower fields than in the other samples. Since the other two samples have very similar oxygen doping, this is presumably due to an effect of the increased carrier density and the enhanced Fermi surface distortion expected, which should give a greater propensity for a square {110}-oriented vortex lattice via the non-local London theory.

The work presented here represents only a small fraction of the data obtained so far and an even smaller fraction of the data in prospect. Further analysis is currently under way, which it is hoped will lead to a refinement of the conclusions presented in chapter III of this thesis. The detwinned samples have already yielded data comparable with the twinned sample. Unfortunately, residual twin planes in the detwinned samples will probably make measurements of the integrated intensity of individual reflections just as difficult as in the twinned sample. However, the range of differently doped samples becoming available will allow advances to be made, particularly with regards to the effect of Fermi surface morphology on the triangular to square transition.

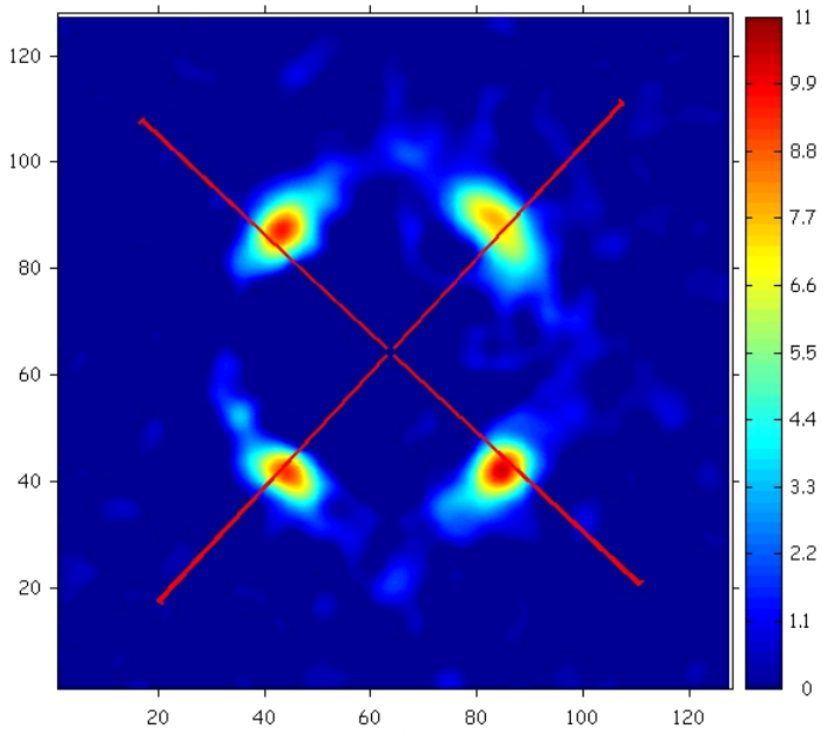

Fig. 4.7: Linear plot of the diffraction pattern obtained from the mosaic of $Y_{1-y}Ca_yBa_2Cu_3O_7$ at 4 T. The red lines lie roughly along the crystal {110} and the crystal a-axis is vertical in the picture.

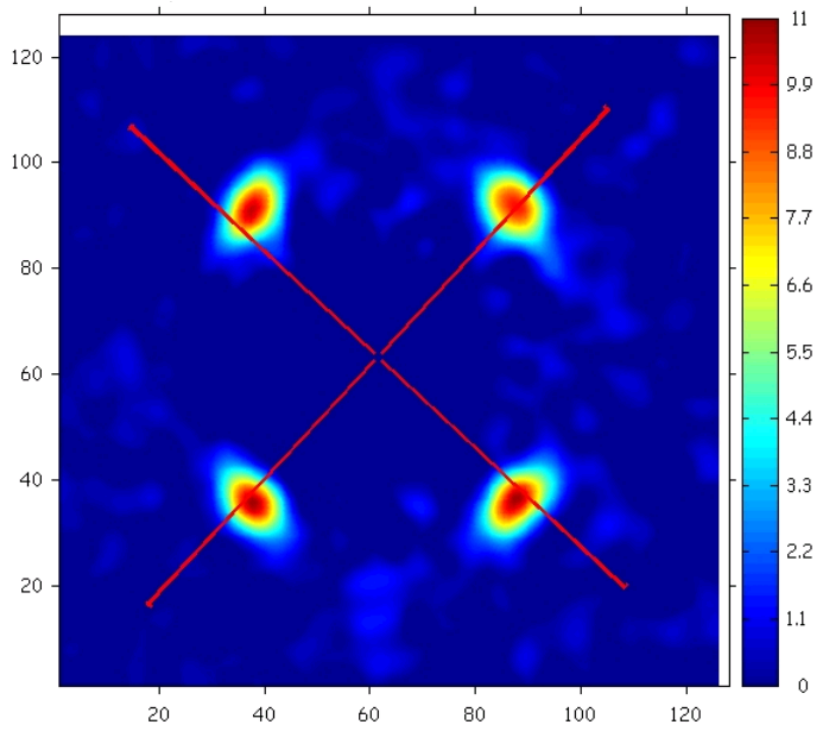

Fig. 4.8: Linear plot of the diffraction pattern obtained from the mosaic of $Y_{1-y}Ca_yBa_2Cu_3O_7$ at 7 T. The red lines lie roughly along the crystal {110} and the crystal a-axis is vertical in the picture.

31. Spin fluctuations in strontium ruthenate

The bi-layer ruthenate $Sr_3Ru_2O_7$ is the $n = 2$ member of the so-called Ruddleson-Popper series of materials given by $Sr_{n+1}Ru_nO_{3n+1}$. This family includes ferromagnetic $SrRuO_3$ ($n \to \infty$) and the p-wave spin-triplet superconductor Sr_2RuO_4 ($n = 1$), which has stirred great interest (MacKenzie & Maeno, 2003). It is because of $Sr_3Ru_2O_7$'s relationship to superconducting Sr_2RuO_4 and, to a greater degree, the observation of metamagnetism in $Sr_3Ru_2O_7$ (Perry *et al.*, 2001), which is believed to be related to a quantum-critical end-point (Grigera *et al.*, 2001), that $Sr_3Ru_2O_7$ has become so widely studied. As a result, there already exists a large body of measurements on $Sr_3Ru_2O_7$, including heat capacity, magnetisation and transport measurements, some of which are summarised below. The aim here is to complement the existing work, which is predominantly macroscopic in nature, with direct measurements of the spin fluctuations via inelastic neutron-scattering (INS). INS measures both the spatial and temporal dependence of the spin correlations, whose Fourier transform is related to the differential cross-section for scattering (Lovesey, 1987):

$$\frac{\mathrm{d}^2\sigma}{\mathrm{d}\Omega \mathrm{d}E} \propto \frac{1}{2\pi} \int \langle S(\mathbf{q},t) S(-\mathbf{q}) \rangle \exp(\mathrm{i}\omega t) \mathrm{d}t, \tag{31.1}$$

where $S(\mathbf{q},t)$ is the spin density function. The function $S(\mathbf{q},t)$ is of intrinsic interest because of its relation to the imaginary part of the susceptibility:

$$\frac{1}{2\pi} \int \langle S(\mathbf{q},t) S(-\mathbf{q}) \rangle \exp(\mathrm{i}\omega t) \mathrm{d}t \propto \frac{1}{\exp\left(\frac{\hbar\omega(\mathbf{q})}{k_\mathrm{B}T}\right) - 1} \chi''(\mathbf{q},\omega). \tag{31.2}$$

The INS measurements on $Sr_3Ru_2O_7$ has involved a collaboration led by E.M. Forgan of the University of Birmingham with assistance from the group of S. Hayden (University of Bristol) and samples from R. Perry and Y. Maeno (Kyoto University). Measurements of the spin fluctuations in zero field (in which this author played a role) have already been published (Capogna *et al.*, 2003). Further experimental data taken in an applied field is presented here. The analysis of these data is as yet only cursory; a fuller description will be published in the near future (Ramos *et al.*, 2006).

Before attempting to explain the properties of $Sr_3Ru_2O_7$ and various measurements thereof, it is worth examining the crystal structure from which they derive. In

figure 4.9 is shown the distinctive perovskite-like structure of $Sr_3Ru_2O_7$. Important to this structure are the RuO_6 octahedra that form the bi-layers, which in analogy with the CuO layers in high-T_c materials, are crucial in determining the electronic properties. In fact, only a portion of the true unit cell is shown in figure 4.9. At room temperature, $Sr_3Ru_2O_7$ is face-centred orthorhombic — not body-centred tetragonal as implied by figure 4.9 — due to the freezing-out of a rotational mode of the RuO_6 octahedra as shown in figure 4.10 (Shaked *et al.*, 2000). In the face-centred orthorhombic phase, each RuO_6 octahedron is rotated by 7° with nearest-neighbours rotated in the opposite sense to one another. Despite the rotation, the basal plane lattice constants are still equal within experimental error, but the unit cell is $\sqrt{2} \times \sqrt{2}$ larger and rotated by 45° relative to the undistorted unit cell.

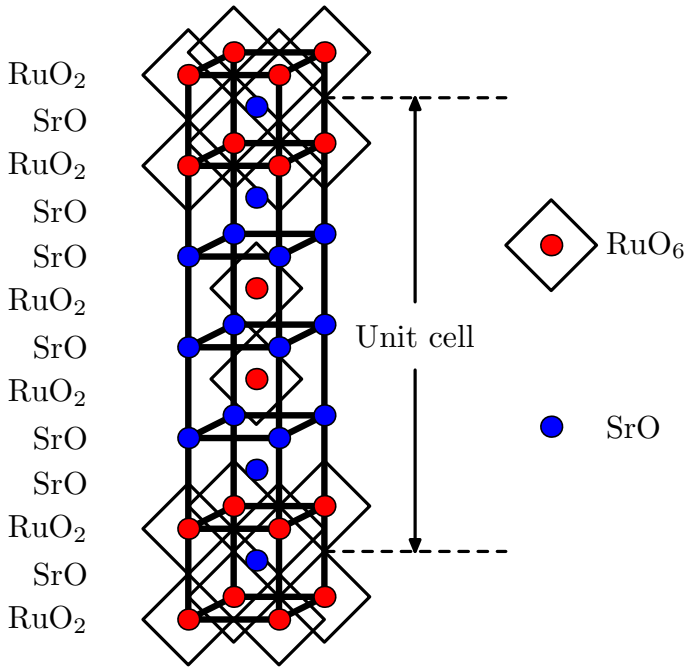

Fig. 4.9: The crystal structure of the bi-layered ruthenate $Sr_3Ru_2O_7$. Shown here is a pseudo unit-cell extended vertically to make the bi-layers clear. The bi-layers are composed of ruthenium-oxide octahedra (RuO_6), which are arranged in a body-centred fashion with SrO spacer layers. Due to the rotation of the RuO_6 octahedra, the unit cell is actually face-centred orthorhombic with equal basal plane lattice parameters (see text and figure 4.10). In the body-centred tetragonal unit cell depicted here (and used throughout) the basal plane lattice parameters (*i.e.* Ru-O-Ru distance) are both 3.87 Å and the *c*-axis lattice parameter is 20.7 Å, which is the same as in the true orthorhombic lattice.

Although the distortion of the RuO_6 octahedra affects the electronic properties (for example, it ought to reduce the Ru-O-Ru hopping matrix element (Capogna, 2003 and Singh & Mazin, 2001)), the basal plane is still square and it is therefore more convenient to use the undistorted body-centred tetragonal cell when describing the INS data. It is also more appropriate from a physical perspective because it was shown by Capogna *et al.* (2003) that the basic fluctuating units are the bi-layers. Therefore, henceforth the reciprocal lattice of $Sr_3Ru_2O_7$ will be referred to with respect to the reciprocal lattice of the undistorted bi-layers. In this notation, Bragg peaks with $h + k$ odd are systematically absent due to the structure factor of the face-centred arrangement (see figure 4.11).

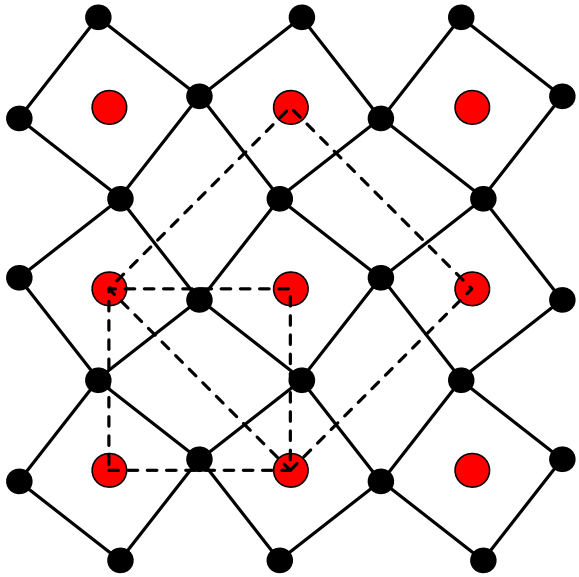

Fig. 4.10: Distortion of a ruthenium-oxide bi-layer shown from above due to the frozen rotational mode, which induces a 7° rotation of the octahedra alternating in sense between nearest-neighbours. (Ruthenium ions are denoted by ● and oxygen ions by ●.) This distortion makes the unit cell face-centred orthorhombic. The true unit cell is oriented at 45° relative to the undistorted unit cell used conventionally here and is $\sqrt{2} \times \sqrt{2}$ times larger (dashed squares). Note that the undistorted unit cell is still the basic unit of repetition of a single two-dimensional bi-layer.

The impetus to study $Sr_3Ru_2O_7$ has been provided by its interesting electronic and magnetic properties. Early work in this field was confused by various erroneous reports (*e.g.* low-temperature ferromagnetism) due to poor-quality samples often contaminated

with crucible elements or other strontium-ruthenate phases (*e.g.* $SrRuO_3$). The success of Ikeda *et al.* (1999) in growing sufficiently pure single-crystals (with in-plane residual resistivities of $3 - 4\,\mu\Omega$cm) has helped clear matters considerably. The work presented here and the references cited are all derived from samples of this purity or better.

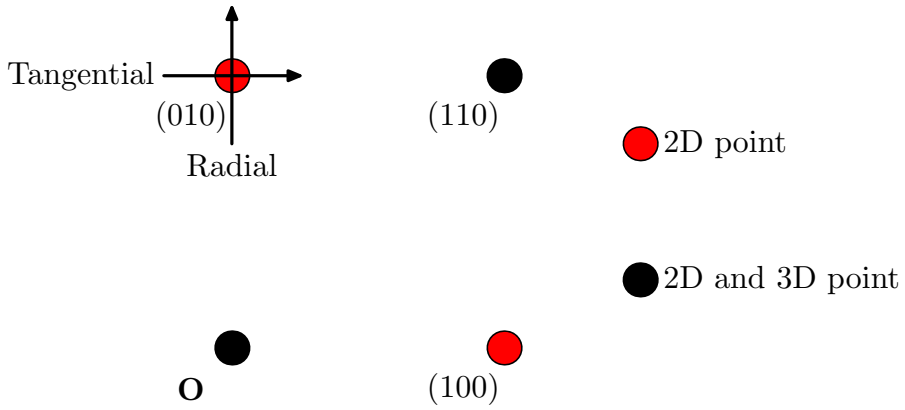

Fig. 4.11: A schematic of the $(hk0)$ slice through reciprocal space in $Sr_3Ru_2O_7$, drawn in terms of the reciprocal lattice vectors of the two-dimensional bi-layers. Only reciprocal space points with $h + k$ even are reciprocal lattice vectors of the distorted three-dimensional face-centred structure. The arrows around (010) define a naming convention for scan direction in terms of their direction relative to (010).

At high temperatures $Sr_3Ru_2O_7$ is an itinerant paramagnetic non-Fermi liquid, but rather than ordering magnetically at low temperatures, the low-field (0.3 T) susceptibility peaks at roughly 16 K (Ikeda *et al.*, 2000) then rapidly decreases at lower temperatures. Accompanying this is a gradual tendency towards Fermi liquid behaviour at low temperatures and zero field as measured by transport measurements (Grigera *et al.*, 2001). The previous zero-field INS measurements (Capogna, 2003) have provided insight into these observations. At high temperatures the spin fluctuations consist of a single broad ferromagnetic peak located at the (100) point (see figure 4.12). As the temperature is decreased the ferromagnetic peak evolves into two incommensurate peaks, which each disperse into a further two peaks at lower energy (figure 4.13). These were interpreted by Capogna *et al.* (2003) as arising from an enhanced susceptibility due to Fermi surface nesting at those wavevectors (see also Singh & Mazin, 2001).

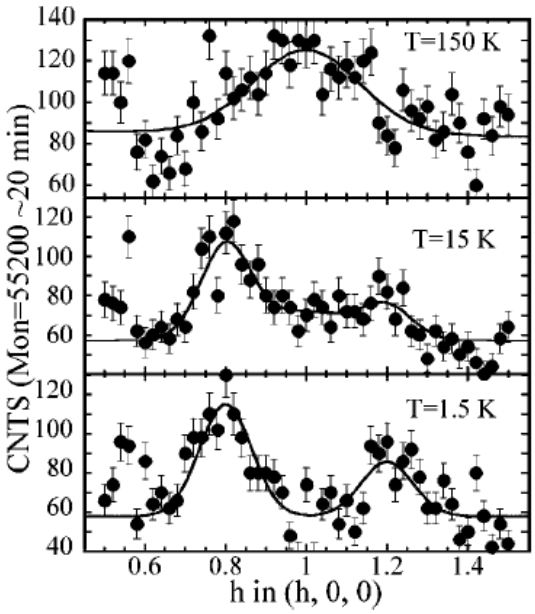

Fig. 4.12: (From Capogna *et al.*, 2003.) Spin fluctuations at 150 K, 15 K and 1.5 K in $Sr_3Ru_2O_7$ at zero field. The energy transfer was 3.1 meV and the scan was performed around the (100) position.

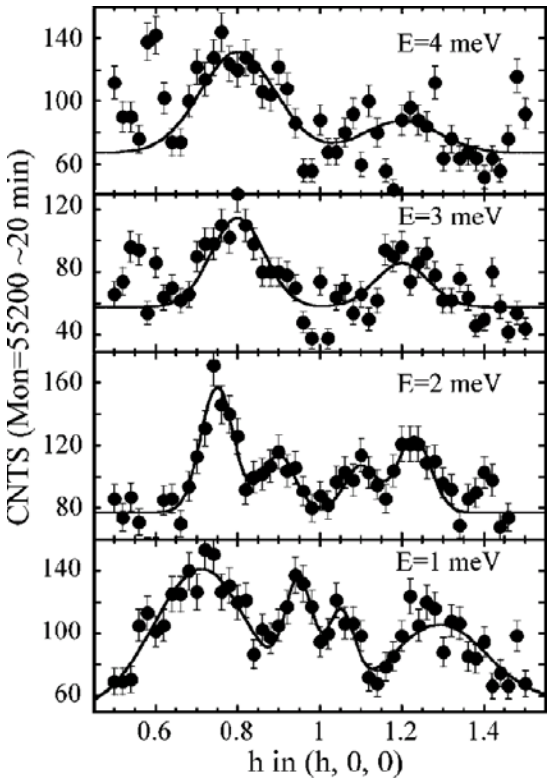

Fig. 4.13: (From Capogna *et al.*, 2003.) Dispersion at T =1.5 K of the two incommensurate peaks of figure 4.12.

Although interesting, the low field properties are not the motivation for studying $Sr_3Ru_2O_7$; instead, it is the high-field metamagnetic transition that provides the stimulus. The metamagnetic transition (a sudden super-linear rise in magnetisation) in $Sr_3Ru_2O_7$ occurs at low temperatures for applied fields ranging from 5.5 T (field applied in the basal plane) to 8 T (field applied parallel to the c-axis) (Perry *et al.*, 2001)*. A wholesale change in the electronic properties accompanies the metamagnetic transition. On approaching the metamagnetic transition from below, the resistivity changes from a T^2 dependence to a linear T dependence, signalling the departure from Fermi liquid behaviour (Perry *et al.*, 2001). At the same time, the electronic heat capacity divided by temperature (C_{el}/T), which is a measure of the quasi-particle mass, diverges. All of these signatures of metamagnetism become sharper at lower temperatures.

Perry *et al.* (2001) and Grigera *et al.* (2001) have intepreted these phenomena and their temperature dependence as resulting from the proximity of a quantum-critical end-point (QCEP — see figure 4.14). A QCEP may be created by depressing to zero using some physical parameter such as pressure (Chiao *et al.*, 2002) the temperature, $T^*(H)$, of a critical end-point of a line of first-order phase transitions, which in the case of $Sr_3Ru_2O_7$ is a line of Stoner-like instabilities in the Fermi surface. This process radically alters the nature of the transition because rather than being thermal, the critical fluctuations are now quantum in nature. Even when $Sr_3Ru_2O_7$ is tuned slightly away from a QCEP, the effects of quantum criticality may still be felt over a large region of phase space as is demonstrated by the "funnel" of non-Fermi-liquid behaviour emanating from the QCEP in the resistivity data of Perry *et al.* (2001). The observation by Borzi *et al.* (2004) of de Haas-van Alphen oscillations in ultra-pure crystals (less than 1 $\mu\Omega$cm) supports this view. They have observed clear quantum oscillations either side of the transition and noticed that the principal frequency peaks at low fields split and shift slightly when going through the metamagnetic transition, in agreement with a Stoner-like picture. One of the advantages of de Haas-van Alphen oscillations is that they provide a measurement of the quasi-particle mass associated with each piece of

* It should be noted that there is in fact a second metamagnetic field at around 13.5 T for **B** parallel to the crystal c-axis (Ohmichi *et al.*, 2003), but this has not been associated with any quantum-critical behaviour and so has attracted less attention.

Fermi surface. Rather large values of quasi-particle mass were calculated from the quantum oscillations and were seen to diverge in the vicinity of the non-Fermi-liquid region around the metamagnetic transition. This is consistent with a quantum critical interpretation in which the quasi-particle mass is strongly renormalised by quantum-critical fluctuations near to the metamagnetic field.

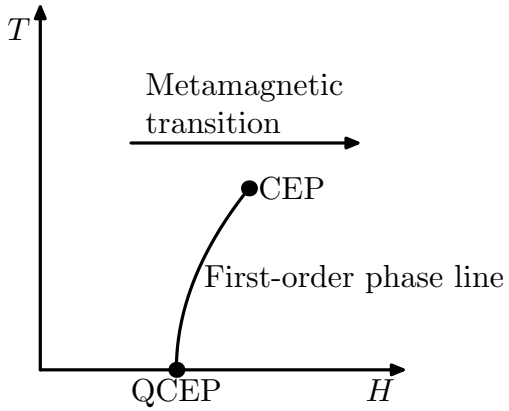

Fig. 4.14: The metamagnetic transition described in the text occurs above a line of first order phase transitions, which is terminated by a second-order critical end-point (CEP) at finite temperature. By tuning a physical parameter other than magnetic field (*e.g.* pressure) it may be possible to depress the temperature of the CEP to zero forming a quantum-critical end-point (QCEP).

More recent measurements (Perry *et al.*, 2004 and Grigera *et al.*, 2004) on the purest samples (at the time of writing) with residual resistivities below $1\,\mu\Omega$cm have revealed an even richer phase diagram near to the quantum critical point. Below 0.8 K, two first-order phase transitions are observed around the metamagnetic field, creating a region of a new type of ordered state. The nature of this state and why it forms are as yet not totally clear, but it is believed that a so-called Pomeranchuk distortion of the Fermi surface (Grigera *et al.*, 2004) is involved. The divergent susceptibility at the quantum-critical point is probably responsible for the phase transitions, which mask quantum-critical behaviour.

To complement the existing zero-field investigations of the spin fluctuations in $Sr_3Ru_2O_7$, similar measurements have been performed in applied fields in a range around the metamagnetic field (7.95 T when applied parallel to the *c*-axis in the samples used here). The measurements were performed on the cold-neutron triple-axis

spectrometer IN14 at ILL, Grenoble, France (see figure 4.15). Using a specially constructed cryomagnet, IN14 has the facility for high-field measurements up to 15 T, which easily encompasses the interesting range around the metamagnetic transition. Unfortunately, at the time of writing there did not exist a dilution refrigerator insert for the cryomagnet, which precluded measurements within the new phase found by Perry *et al.* (2004) and Grigera *et al.* (2004). However, the measurements presented here are still of great interest because they constitute the first investigation of the change in spin fluctuations in going through the metamagnetic transition.

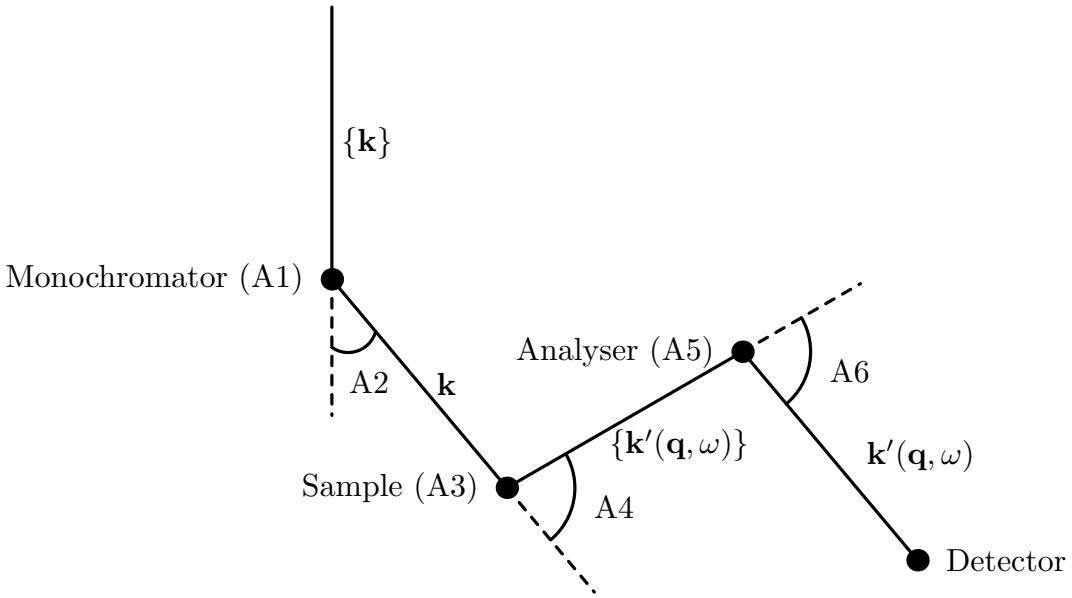

Fig. 4.15: Schematic of the triple-axis spectrometer IN14 showing the path of the neutrons of interest through the instrument (solid line). The principal degrees of freedom are the six angles, three of which are "take-off" angles (A2, A4 and A6) and the others are the orientations of the monochromator, sample and analyser crystal (A1, A3 and A5 respectively). The cold-neutron source produces a distribution of wavevectors denoted $\{\mathbf{k}\}$. A single wavevector, $\mathbf{k}$, is selected by Bragg diffraction off the crystal monochromator (for the appropriate value of A1 = $\frac{1}{2}$A2). The wavevector is then scattered off the sample giving a distribution of outgoing wavevectors $\{\mathbf{k}'(\mathbf{q},\omega)\}$ according to the sample's response and its orientation (angle A3). The intensity of each of the outgoing wavevectors may be deduced by analysing the outgoing beam by Bragg diffraction off the analyser crystal. This requires the appropriate setting of A4, and A5 = $\frac{1}{2}$A6. The detector functions in the same way as the neutron multi-detectors described in section 12, but it consists of only a single element.

The sample used in these experiments is a mosaic of single crystals grown by R. Perry at Kyoto University. Each element of the mosaic had a flat facet nearly perpendicular to the c-axis and was mounted on a pure aluminium plate (two or three samples per plate). The basal plane axes of the samples were aligned with respect to each other using a neutron diffractometer and the orientation of each sample was fixed with a *very* small amount of glue between the facet and plate. Most of the mechanical strength was provided by an aluminium brace across all the samples on a single plate (the brace was held in position by small brass bolts). Four plates containing ten samples in total were stacked up vertically and held together with three threaded pure aluminium rods screwed into an aluminium block, which could be affixed to the end of a sample stick. The sample stick was inserted into the variable-temperature insert of the cryostat with the c-axis of the mosaic vertical and the basal plane in the scattering plane (see figure 4.15).

In figure 4.16 are shown a series of radial scans through (010) (see figure 4.11) taken at low temperatures with the metamagnetic field applied. These plots show a marked departure from the behaviour of the spin fluctuations at zero field. Compare the data of figure 4.16 at 2 meV energy transfer with the equivalent zero-field data shown in figure 4.13. In the latter data, the spin fluctuations consist of two types of incommensurate response, but in the data taken at the metamagnetic field only a single type antiferromagnetic peak is observed (at roughly 0.25 reciprocal lattice units). The biggest change between the two data sets is the emergence of a ferromagnetic response at the metamagnetic field, which is confined to low energies (≤ 2 meV). The appearance of a peak at finite energy transfer at the commensurate position is interesting because the excitement of these fluctuations does not conserve spin, which could imply significant spin-orbit coupling or leakage from the bi-layers. At higher energies (≈ 4 meV) two incommensurate peaks dominate the response, but it is not clear whether these are resurgent antiferromagnetic peaks or whether the ferromagnetic response has spread out from the commensurate position. If the latter is true then the dispersion of the peaks (about 2 km·s^{-1}) is unusual because it is far smaller than the Fermi velocity.

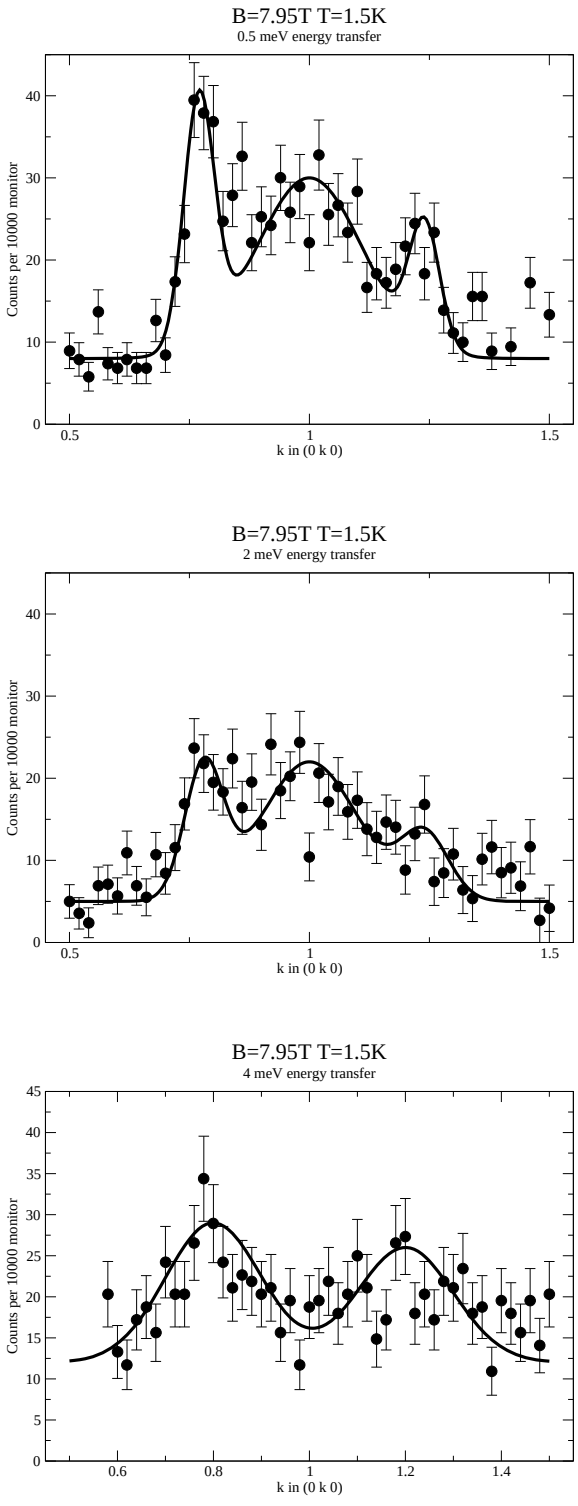

Fig. 4.16: Radial scans taken at 2 K with the metamagnetic field (7.95 T) applied. Scans at 0.5 meV (top), 2 meV (middle) and 4 meV (bottom) are shown. The lines drawn through the data are guides to the eye.

Scans transverse to the (010) reciprocal lattice vector have also been undertaken. Although this direction in reciprocal space is related by the tetragonal symmetry of the bi-layers to the radial scan direction, the mechanics of inelastic neutron scattering mean that doing both sets of scans is not necessarily redundant. Figure 4.17 shows a set of transverse scans at more-or-less equal energies to those of the radial scans shown in figure 4.13. It can be seen that the strong antiferromagnetic signal observed in the radial scan at 0.5 meV is completely absent in the 0.5 meV transverse scan. This anisotropy is due to a moment orientation effect. To illustrate the moment orientation effect, consider the two sets of static spins in figure 4.18. Each of these spin systems, whose basic repeat distances are equal, is being probed by the scattering triangle given by $\mathbf{k}_{\text{in}}$, $\mathbf{k}_{\text{out}}$ and $\mathbf{q}$, which corresponds to scattering from horizontally oriented planes spaced by the inter-spin distance. Naïvely, it might be thought that both situations would give rise to magnetic Bragg diffraction from the Fourier coefficients shown due to the visually "obvious" vertical periodicity. However, only the diagram on the right of figure 4.18 gives rise to scattering. Maxwell's second equation (the magnetic flux law) for a periodic system of spins may be written in terms of reciprocal space quantities as:

$$\mathbf{G} \cdot \mathbf{B}_{\mathbf{G}} = 0. \tag{31.3}$$

This expression prohibits any Fourier coefficient, $\mathbf{B}_{\mathbf{G}}$, from having a component parallel to the reciprocal lattice vector $\mathbf{G}$. Therefore no scattering arises from the scenario depicted in the left-hand of the figure.

Although the explanation of the moment orientation given above is confined to the static case, the same effect applies to inelastic scattering from fluctuating moments because equation 31.3 is time independent. In the scattering matrix element there is a term proportional to $\mathbf{q} \times (\hat{\mathbf{s}}_i \times \mathbf{q})$, where $\hat{\mathbf{s}}_i$ is the spin operator of an electron indexed by i, that is responsible for the moment-orientation effect (Lovesey, 1987). Since this term is proportional to $\sin\theta$, where θ is the angle between the scattering vector and the spin orientation, the partial differential cross-section for spin only scattering depends upon $\sin^2\theta$, which gives the expected moment orientation effect for dynamic moments.

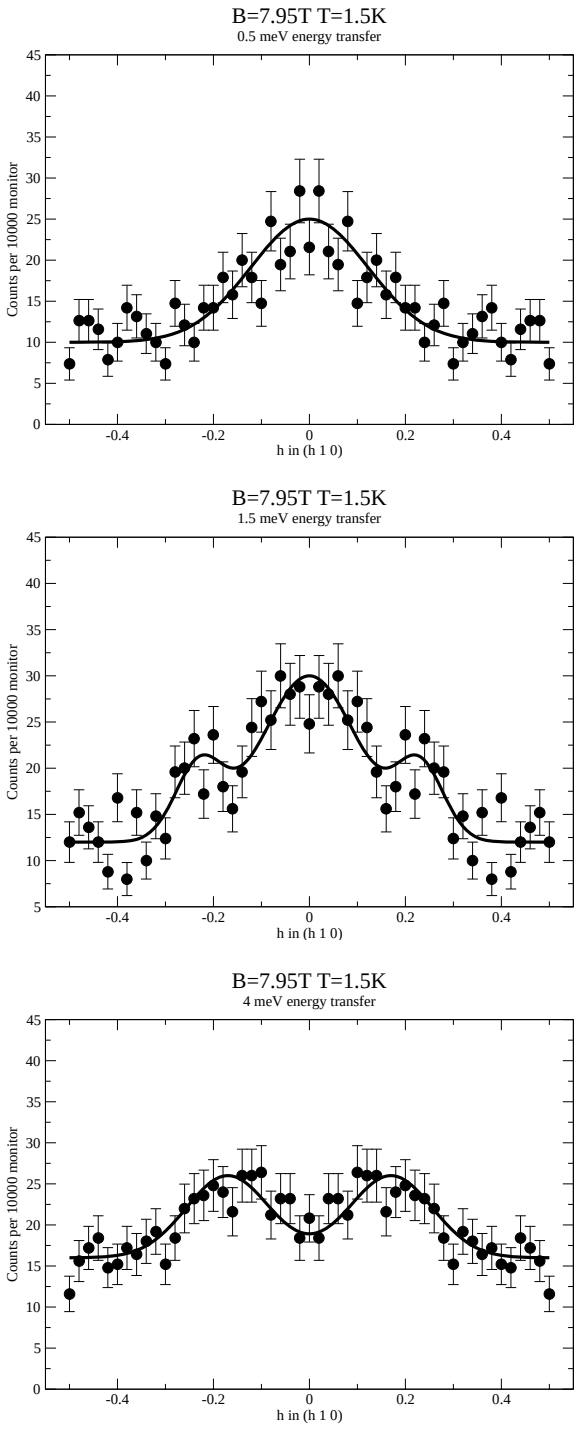

Fig. 4.17: Tangential scans taken at 2 K with the metamagnetic field (7.95 T) applied. Scans at 0.5 meV (top), 1.5 meV (middle) and 4 meV (bottom) are shown. The lines drawn through the data are guides to the eye. Note the symmetry about (010) in each of the scans: these graphs are formed from data taken for $0 < h < 0.5$, which was symmetrised to generate the data for $-0.5 < h < 0$.

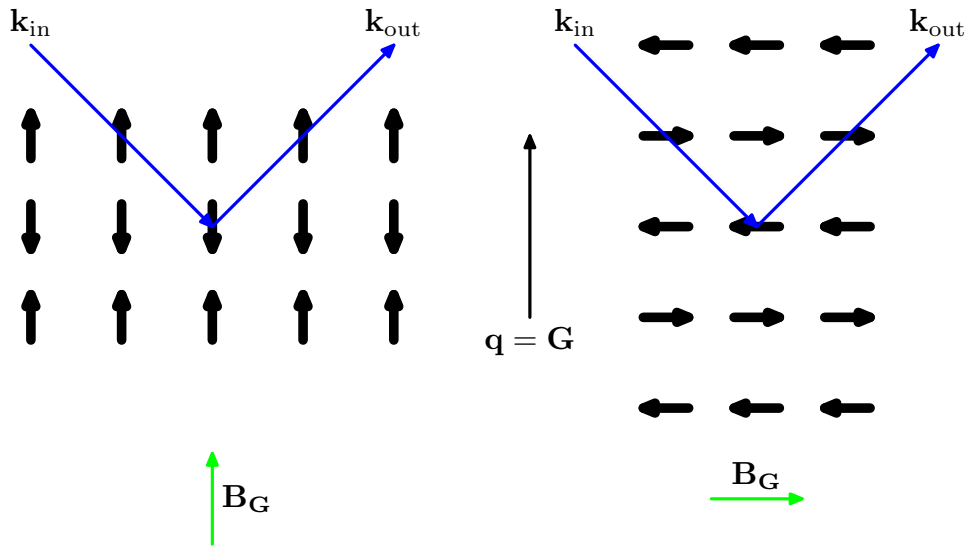

Fig. 4.18: The static moment-orientation effect. Two hypothetical static spin systems are shown, which are being investigated by scattering by the same **q**-vector. In reciprocal space Maxwell's magnetic flux equation, $\mathbf{G} \cdot \mathbf{B_G} = 0$, implies that the Fourier coefficient, $\mathbf{B_G}$, corresponding to $\mathbf{q} = \mathbf{G}$ must be identically zero for the spin system on the left, but is allowed to be non-zero for the right-hand system. This may appear counter-intuitive, but in the left diagram the contribution of the dipole fields over an infinite lattice will lead to no variation of **B** (anti)-parallel to the local spin direction.

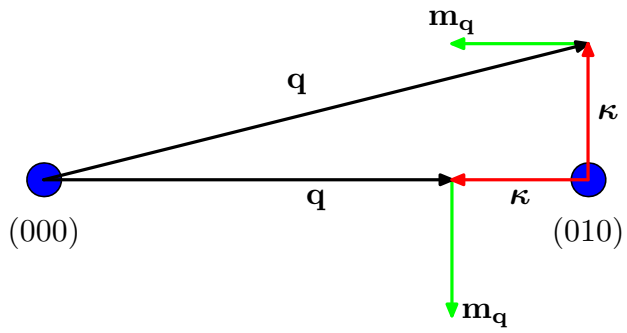

Fig. 4.19: Schematic explanation of the moment orientation effect observed in figures 4.16 and 4.17. To explain the effect, the spin fluctuations must firstly be perpendicular to the reciprocal lattice vector, $\boldsymbol{\kappa}$, (taking (010) as the origin) and secondly, must also lie in-plane. In this scenario, the scattering vector, **q**, for the transverse scan is nearly parallel to the orientation of the magnetisation vector, $\mathbf{m_q}$, of the fluctuation and so gives very little scattering, but in the radial scan the **q**-vector is always perpendicular to the magnetisation.

The moment orientation effect provides a convincing explanation of the anisotropy in scattering observed between the radial and transverse scans. Figure 4.19 demonstrates that if the fluctuating moments lie within the basal plane and are oriented perpendicular to the reciprocal lattice vector $\boldsymbol{\kappa}$, then the resulting anisotropy of scattering is consistent with the observations of figures 4.13 and 4.17. It can be seen that the fluctuating moments are perpendicular to the $\mathbf{q}$-vector for the radial scans, but nearly parallel for the tangential ones. Furthermore, none of the other possible orientations of fluctuations — either out-of-plane or parallel to $\boldsymbol{\kappa}$ — gives the observed anisotropy.

Measurements were also taken well beyond the metamagnetic field at 11 T (but well below the second metamagnetic transition). In figure 4.20 are shown some representative scans at this field. It seems that the qualitative behaviour at 11 T is the same as that at the metamagnetic field. The ferromagnetic response seen at the metamagnetic field (figure 4.13) at 1 meV energy transfer is also present at 11 T and at higher energy transfers disperses similarly. A moment orientation effect is observed too (compare the radial scan at 1 meV transfer with the transverse scan at 1.5 meV in figure 4.20).

In conclusion, measurements of the spin fluctuations at the metamagnetic field in $Sr_3Ru_2O_7$ reveal a striking change from the zero-field behaviour observed by Capogna *et al.* (2003). The principal result is the appearance at the (010) position of a ferromagnetic peak that seems to disperse very slowly ($2\,\mathrm{km{\cdot}s^{-1}} \ll v_\mathrm{F}$). At low energy there is also a single type of anti-ferromagnetic peak located at roughly $(0.25, 1, 0)$, compared with two types of peak at zero field. Given the association of the latter with Fermi surface nesting vectors, the difference may be a result of the change in Fermi surface topology at the metamagnetic field (Borzi *et al.*, 2004). Another effect of the application of the metamagnetic field along the c-axis is that it inhibits anti-ferromagnetic fluctuations out of the basal plane, which is manifested in the observation of a moment orientation effect.

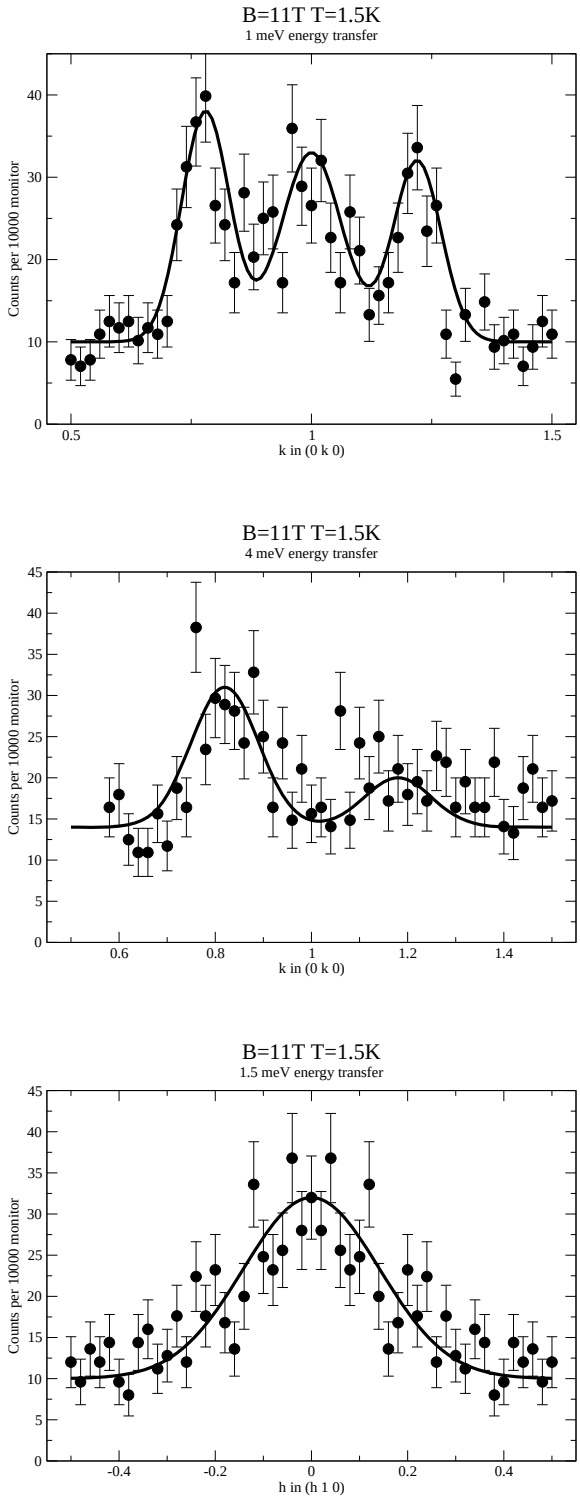

Fig. 4.20: A selection of scans taken at 11 T: radial scans at 1 meV and 4 meV energy transfer (top and middle respectively) and a tangential scan at 1.5 meV energy transfer (bottom).

Conclusion

In this thesis convincing evidence has been provided for the existence of unconventional square and rectangular vortex lattice structures in *d*-wave superconductors. Two families of superconductors were investigated (YBCO and NCCO) and the results have been published or are pending publication (Brown *et al.*, 2004; Gilardi *et al.*, 2004; Brown *et al.*, 2005 and Hinkov *et al.*, 2006). In each case, SANS was employed to determine the configuration of the vortex lattice. During the course of these investigations, SANS has demonstrated itself to be a unique and indispensible tool for determining the vortex lattice structure over a wide range of temperatures (2.5–90 K) and with fields up to 11 T applied along various crystal directions. This flexibility has yielded a wealth of information from the systems studied.

The principal results of this thesis were obtained using a twinned sample of stoichiometric $YBa_2Cu_3O_7$ in which a field-cooled vortex lattice was formed by applying a magnetic field parallel to the crystal *c*-axis. At low fields (<1 T), the anisotropic London model serves well in describing the distorted triangular vortex lattice structure, but as the field is increased, a continuous distortion of the vortex lattice occurs and it becomes rectangular at high fields (11 T). It was found that the rectangular vortex lattice domain was suppressed by increasing temperature or applying the field at an angle to the crystal *c*-axis.

That the transition to square is an intrinsic effect is beyond reasonable doubt since it was shown in section 30 that detwinned samples of $YBa_2Cu_3O_7$ exhibit similar phenomena, but exactly what mechanism causes it is not certain. It is definitely unconventional in nature and cannot be accounted for by anisotropic London theory for at least two inextricably related reasons: firstly, the observed square vortex lattice does not minimise the London free energy; secondly, an anisotropy of the second-rank tensor type can be built into London theory, but this ought to be static with field and only a field-dependent higher-rank anisotropy could cause the observed transition to square. Two possible origins of higher-rank field-dependent anisotropy were

discussed (see section 24): Fermi surface anisotropy in non-local London theory and the anisotropy due to the d-wave symmetry of the superconducting order parameter. Unlike other high-T_c superconductors (*e.g.* $La_{2-x}Sr_xCuO_4$), it is not possible to distinguish immediately between the two proposed effects because both predict within the experimentally observed field range the formation of a high-field square vortex lattice with the nearest-neighbour direction along {110}. (In some sense it is meaningless to decouple completely the two effects since the symmetries of the superconductivity and band structure are intimately related.) Although the temperature dependence of the vortex lattice structure, and the field dependence of the structure and ratio of form-factors were determined, none gave a definitive answer as to which anisotropy is responsible for the high-field square lattice. There is a lot of scope for further work here: better measurements of the form-factors than those presented here will be needed and a detailed theoretical study (within the experimentally accessible part of the phase diagram) of the type performed by Nakai *et al.* (2002) will be required for comparison. In pursuance of the former requirement, a new generation of detwinned samples are available (in addition to the old twinned one), which already have shown some promise. On the theoretical side, naïve expectation would favour d-wave effects as the principal source of unconventional anisotropy because the order parameter anisotropy is "100%" (*i.e.* the order parameter is zero along the nodal directions) whereas the Fermi surface in $YBa_2Cu_3O_7$ is less anisotropic (the Fermi surface of $YBa_2Cu_3O_7$ is considerably less anisotropic than that of $La_{2-x}Sr_xCuO_4$, for example). A proper calculation to verify (or otherwise) this hypothesis would require detailed information on the superconducting gap and the moments of the Fermi surface velocity, some of which are not as yet available.

Although there is more work to do, $YBa_2Cu_3O_7$ fits nicely with the emerging consensual picture of unconventional vortex lattices, which sees transitions to unconventional structures in terms of the increased effects of the finite core-size or, in other words, increasing non-locality due to core overlap. Part of the reason that it is difficult to differentiate between Fermi surface and order parameter anisotropies is that they are both non-local effects and therefore exhibit qualitatively similar field dependence for a given superconductor (as defined by κ). The measurements on $Nd_{1.85}Ce_{0.15}CuO_4$

disagree completely with this picture (see section 29). $Nd_{1.85}Ce_{0.15}CuO_4$ is an electron-doped high-T_c superconductor with an upper critical field of 8 T. Non-locality should become important at around 1 T in this material, but astonishingly a square vortex lattice is observed at inductions as low as 20 mT. Moreover, at 20 mT the vortex lattice appears to have very poor orientational order, which is hard to reconcile with the intrinsic aligning effects of the higher-order anisotropy usually associated with unconventional vortex lattices. Clearly, more work is needed to resolve this issue. However, the present samples of $Nd_{1.85}Ce_{0.15}CuO_4$ suffer from a far greater degree of point disorder than any of the YBCO samples, thus restricting the accessible field range to below about 0.5 T. Therefore, the next break-through in understanding the intrinsic behaviour of the vortex lattice in NCCO is likely to come only after significant improvements in crystal quality. If better crystals were available, the benefits to the study of unconventional vortex lattices in the cuprates would be immense. NCCO has a number of advantages over other systems such as YBCO: it is tetragonal (and thus twin free) and perhaps most importantly, has a sufficiently low value of H_{c2} to make the *entire* vortex lattice phase diagram accessible with the present apparatus.

In the near term, before much improved samples of NCCO are produced, most developments in the field will probably come from cleaner tried-and-tested materials such as YBCO. Some early progress in a new research programme utilising detwinned crystals was shown in section 30. The objective of the new programme is to expand on the measurements performed on the twinned $YBa_2Cu_3O_7$ samples. In the first instance, more data on the effects of angle of applied field would be useful to complement the vortex "zoo" found in the twinned sample. A very rich variety of angle-dependent vortex lattice structures was observed in the twinned sample and it would be of interest to investigate these further. There are various holes in the present data, particularly at low fields. It would be of great interest to see from what type of low-field structure the hexagonal domains seen at low temperatures with 5 T applied at 10° to the crystal *c*-axis evolve. Additionally, it remains to be seen how the high-field form-factors are affected by the field rotation.

Further angle dependent studies could be performed using either the twinned sample or the new detwinned ones, but the detwinned samples are unique in that they are

available with various different dopings. In section 30, data taken using a calcium-doped sample was presented. The familiar triangular to square transition was observed, but it occured at lower fields (it appears complete at 7 T). Although it is not yet clear what relation this has to the underlying physics, it is obvious that the electronic properties are affected by doping and it may be possible to tune the anisotropy of the Fermi surface and study its effect relative to the order parameter anisotropy. Therefore, charge-carrier concentration is set to become the next dimension of the unconventional vortex lattice phase diagram.

The measurements of the spin fluctuations in $Sr_3Ru_2O_7$ are not so well related to the main topic of this thesis, but they do illustrate another successful exploitation of the sensitivity of low-energy neutrons to magnetic scattering. These measurements show for the first time the effect of the metamagnetic field on the spin correlations in this itinerant system. At the metamagnetic field, other measurements (see section 31 and references therein) have determined that the enhancement in susceptibility is accompanied by a strong deviation from Fermi liquid theory as the Fermi surface undergoes an apparent instability. The spin fluctuations seem to concur. A strong ferromagnetic response was observed that was absent at zero field. In addition, the incommensurate fluctuations, which were attributed by Capogna *et al.* (2003) to Fermi surface nesting, change in nature. Another result of the application of the metamangetic field is the manifestation of a moment orientation effect in the incommensurate fluctuations, which are found to be in-plane and perpendicular to the reciprocal lattice vector at low energies. So far, measurements have been restricted to relatively high temperatures (>1.5 K). In the future, it would be interesting to repeat the measurements at lower temperature using a dilution refrigerator. Until recently, it was assumed that $Sr_3Ru_2O_7$ was close to a quantum-critical end-point. This in itself would provide motivation for a low-temperature study, but Grigera *et al.* (2004) have published evidence in favour of an unusual electronic phase (involving a so-called Pomerunchuk instability of the Fermi surface) replacing the quantum-critical end-point and bounded by lines of first-order phase transitions. An inelastic neutron study of the spin fluctuations in this region would bring considerable insight into the behaviour inferred from thermodynamic and transport measurements.

APPENDIX A

SANS RESOLUTION FUNCTION

In this appendix is calculated the resolution function for SANS. The resolution function describes the projection onto the detector of a single point in reciprocal space and specifies the distribution of scattering angles, $2\theta_x$ and $2\theta_y$, relative to the nominal beam direction. The instrumental factors relevant to this calculation are wavelength spread and beam divergence; they are assumed to be Gaussian-distributed quantities:

$$P(\lambda) \propto \exp\left(-\frac{(\lambda-\lambda_{\mathrm{n}})^2}{2\sigma_\lambda^2}\right),\ P(\alpha) \propto \exp\left(-\frac{\alpha^2}{2\sigma_\alpha^2}\right),\ P(\beta) \propto \exp\left(-\frac{\beta^2}{2\sigma_\beta^2}\right). \quad (31.1)$$

For a full explanation of the concepts underpinning this derivation the reader is referred to the section on resolution in the main text (section 14).

Consider some wavevector with wavelength λ present in the beam distribution that is parallel to the nominal beam direction. In general the Ewald circle corresponding to this wavelength for the rocking angles ω and ϕ will not be rocked onto the **q**-vector of interest (see the dashed line of figure A.1) and hence will not give rise to scattering. However, at this wavelength there will be present in the beam a wavevector at $(\hat{\alpha}(\lambda), \hat{\beta}(\lambda))$ relative to the nominal beam that is "perfectly" rocked on, *i.e.* not only does it satisfy the Bragg condition, but it is rocked on such that the **q**-vector spans the diameter of the Ewald circle (solid line of figure A.1). The perfect wavevector will be scattered by the Bragg angles $(2\theta_{\mathrm{B},x}(\lambda), 2\theta_{\mathrm{B},x}(\lambda))$ defined in equation 13.3, but these are measured relative to the wavevector at $(\hat{\alpha}(\lambda), \hat{\beta}(\lambda))$, not the nominal beam direction. Therefore to get the absolute scattering angles, the angle between the wavevector and the nominal beam must be subtracted:

$$\begin{aligned} 2\theta_x &= 2\theta_{\mathrm{B},x}(\lambda) - \hat{\alpha}(\lambda) = \theta_{\mathrm{B},x}(\lambda) + \omega = \frac{\lambda q_x}{4\pi} + \omega, \\ 2\theta_y &= 2\theta_{\mathrm{B},y}(\lambda) - \hat{\beta}(\lambda) = \theta_{\mathrm{B},y}(\lambda) + \phi = \frac{\lambda q_y}{4\pi} + \phi, \end{aligned} \quad (31.2)$$

where use has been made of the definitions $\hat{\alpha}(\lambda) \equiv \theta_{\mathrm{B},x}(\lambda) - \omega$ and $\hat{\beta}(\lambda) \equiv \theta_{\mathrm{B},y}(\lambda) - \phi$. To allow for the case where the beam divergence angles α and β are non-zero, the beam divergence angles must be added to $2\theta_x$ and $2\theta_y$ respectively:

$$\begin{aligned} 2\theta_x &= 2\theta_{\mathrm{B},x}(\lambda) - \hat{\alpha}(\lambda) + \alpha, \\ 2\theta_y &= 2\theta_{\mathrm{B},y}(\lambda) - \hat{\beta}(\lambda) + \beta, \end{aligned} \tag{31.3}$$

This follows from the geometry shown in figure 2.10 in section 14. (Essentially, adding α to the rocking angle increases the scattering angle by 2α in the frame of the wavevector, but relative to the nominal beam (at an angle α to the wavevector) the scattering angle is only increased by α.) Note that due to the Bragg condition only particular combinations of α and β will give rise to scattering — this will be built into the model presently.

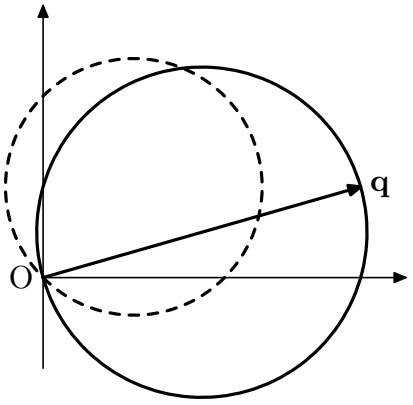

Fig. A.1: Scattering geometry in reciprocal space. The dashed line corresponds to the Ewald sphere for some wavevector with wavelength λ rocked by the angles ω and ϕ. This does not give rise to scattering, in general, but the Bragg condition may be satisfied by another wavevector of the same wavelength at $(\hat{\alpha}(\lambda), \hat{\beta}(\lambda))$ to the nominal beam (solid line).

It is convenient to redefine the beam divergence coordinate system relative to the paradigm wavevector $(\hat{\alpha}(\lambda), \hat{\beta}(\lambda))$:

$$\begin{aligned} \alpha \to \alpha' = \alpha + \hat{\alpha}(\lambda) \quad &\Longrightarrow \quad \exp\left(-\frac{\alpha^2}{2\sigma_\alpha^2}\right) \to \exp\left(-\frac{(\alpha' - \hat{\alpha}(\lambda))^2}{2\sigma_\alpha^2}\right), \\ \beta \to \beta' = \beta + \hat{\beta}(\lambda) \quad &\Longrightarrow \quad \exp\left(-\frac{\beta^2}{2\sigma_\beta^2}\right) \to \exp\left(-\frac{(\beta' - \hat{\beta}(\lambda))^2}{2\sigma_\beta^2}\right). \end{aligned} \tag{31.4}$$

Henceforth, the primes on α' and β' will be dropped. Matters are simplified even further if another coordinate transformation is made to the "diagonal" system in which beam

divergence and scattering angles are measured parallel to the **q**-vector and at a tangent to it. Denoting the radial component of beam divergence as δ and the tangential component as γ the transformation is given by:

$$\begin{cases} \alpha = \delta \cos q_\theta - \gamma \sin q_\theta \\ \beta = \delta \sin q_\theta + \gamma \cos q_\theta, \end{cases} \tag{31.5}$$

where q_θ is the polar angle of the **q**-vector $\mathbf{q}(q_r, q_\theta)$. An equivalent relationship holds between the scattering vector (θ_x, θ_y) in the old frame and $(\theta_\delta, \theta_\gamma)$ in the diagonal system.

Examining the form of the Bragg condition and the scattering angles demonstrates the benefit of the diagonal reference system. The scattering angles are given by:

$$\begin{aligned} 2\theta_\delta &= \omega \cos q_\theta + \phi \sin q_\theta + \frac{\lambda q_r}{4\pi} + \delta, \\ 2\theta_\gamma &= \phi \cos q_\theta - \omega \sin q_\theta + \gamma. \end{aligned} \tag{31.6}$$

As might be anticipated $2\theta_\gamma$ is λ-independent and the tangential smear is determined entirely by the beam divergence. The Bragg condition is even simpler:

$$\delta = 0 \tag{31.7}$$

Therefore, for a given λ the radial angle is fixed to the "perfectly"-rocked value, but the value of the tangential angle is unconstrained. This is a natural result of the two-dimensional Bragg condition (equation 13.3). As a concrete example, consider a **q**-vector with $q_\theta = 0$. The Bragg condition will be satisfied for some value of ω *independent* of the value of ϕ.

The resolution function may be written in terms of delta functions constructed from equation 31.6:

$$\begin{aligned} R(2\theta_\delta, 2\theta_\gamma) \propto & \int_0^\infty \int_{-\infty}^\infty \exp\left(-\frac{(\lambda - \lambda_\mathrm{n})^2}{2\sigma_\lambda^2}\right) \exp\left(-\frac{1}{2\sigma_\alpha^2}\left[-\gamma \sin q_\theta - \frac{\lambda q_r \cos q_\theta}{4\pi} + \omega\right]^2\right) \\ & \times \exp\left(-\frac{1}{2\sigma_\beta^2}\left[\gamma \cos q_\theta - \frac{\lambda q_r \sin q_\theta}{4\pi} + \phi\right]^2\right) \delta\left(2\theta_\gamma - [\gamma + \phi \cos q_\theta - \omega \sin q_\theta]\right) \mathrm{d}\gamma \\ & \times \delta\left(2\theta_\delta - \left[\omega \cos q_\theta + \phi \sin q_\theta + \frac{\lambda q_r}{4\pi}\right]\right) \mathrm{d}\lambda \end{aligned} \tag{31.8}$$

Performing this intergration gives:

$$
\begin{aligned}
R(2\theta_\delta, 2\theta_\gamma) \propto & \exp\left(-\frac{1}{2\sigma^2}\left[\frac{4\pi}{q_r}(2\theta_\delta - \omega\cos q_\theta - \phi\sin q_\theta - \lambda_\mathrm{n})\right]^2\right) \\
& \times \exp\left(-\frac{1}{2\sigma_\alpha^2}\left[-2\theta_\delta\cos q_\theta - 2\theta_\gamma\sin q_\theta + 2\omega\cos^2 q_\theta + 2\phi\cos q_\theta\sin q_\theta\right]^2\right) \\
& \times \exp\left(-\frac{1}{2\sigma_\beta^2}\left[-2\theta_\delta\sin q_\theta + 2\theta_\gamma\cos q_\theta + 2\phi\sin^2 q_\theta + 2\omega\cos q_\theta\sin q_\theta\right]^2\right).
\end{aligned}
\tag{31.9}
$$

Given the Cartesian geometry of SANS multi-detectors it is more useful to express equation 31.9 in Cartesian coordinates using the inverse of equation 31.4:

$$
\begin{aligned}
R(2\theta_x, 2\theta_y) \propto & \exp\left(-\frac{1}{2\sigma_\lambda^2}\left[\frac{4\pi}{q_r}(2\theta_x\cos q_\theta + 2\theta_y\sin q_\theta - \omega\cos q\theta - \phi\sin q_\theta) - \lambda_\mathrm{n}\right]^2\right) \\
& \times \exp\left(-\frac{1}{\sigma_\alpha^2}\left[\theta_x(\sin^2 q_\theta - \cos^2 q_\theta) - 2\theta_y\cos q_\theta\sin q_\theta + \omega\cos^2 q_\theta + \phi\cos q_\theta\sin q_\theta\right]^2\right) \\
& \times \exp\left(-\frac{1}{\sigma_\beta^2}\left[\theta_y(\cos^2 q_\theta - \sin^2 q_\theta) - 2\theta_x\cos q_\theta\sin q_\theta + \phi\sin^2 q_\theta + \omega\cos q_\theta\sin q_\theta\right]^2\right).
\end{aligned}
\tag{31.10}
$$

Converting from $(2\theta_x, 2\theta_y)$ to a coordinate on the detector is achieved (in the small-angle limit) by multiplying by the sample-detector distance, s_det.

APPENDIX B

Reciprocal-space sampling function

In appendix A the principal resolution function for SANS (equation 31.10) was calculated. This function maps a point in reciprocal space to a set of points on the detector and is sometimes called the point-spread function. In this appendix, a different type of resolution function $S_{\lambda_{\rm n}\omega\phi}(q_x, q_y)$ is calculated: for a given set of instrument parameters — *i.e.* wavelength, rocking angles, and distributions of wavelength, beam divergence and mosaic spread — this resolution function is a measure of the amount by which a given point in reciprocal space is sampled (hence its name). Put differently, such a resolution function describes how sensitive the instrument is to each part of the two-dimensional reciprocal space, which is useful information even only in the qualitative sense because it enables the experimentalist to visualise what the experiment is measuring.

The model of $S_{\lambda_{\rm n}\omega\phi}(q_x, q_y)$ is based on the following assumtions, which are explained more fully and justified in sections 14 and 15: firstly, the vortex lattice is assumed to be a pseudo two-dimensional structure consisting of two-dimensional crystallites with a distribution in orientation; and secondly, the instrument parameters are also distributed about their nominal values. For concreteness, all of these distributions are assumed to be Gaussian in each of the five variables λ (wavelength), α (horizontal beam-divergence), β (vertical beam-divergence), δ (horizontal mosaic-spread) and ϵ (vertical mosaic-spread):

$$P(j) \propto \exp\left(-\frac{(j-m_j)^2}{2\sigma_j^2}\right), \tag{31.1}$$

where $j = \{\lambda, \alpha, \beta, \delta, \epsilon\}$, σ_j are the widths of the distributions and m_j are the mean values, all of which are zero expect where $j = \lambda$ in which case $m_\lambda = \lambda_{\rm n}$. These five distributions may be reduced to three effective distributions because mosaic spread

has the same effect in reciprocal space as beam divergence, *i.e.* an effective rotation of the beam relative to the sample*. The effective beam divergence/mosaic spread distributions are obtained by the following convolutions:

$$P(\zeta) = P(\alpha) \otimes P(\delta) \quad \text{and} \quad P(\eta) = P(\beta) \otimes P(\epsilon), \tag{31.2}$$

where ζ and η are the effective angles of rotation in the horizontal and vertical planes respectively. The widths σ_ζ and σ_η are formed by adding in quadrature σ_α and σ_δ, and σ_β and σ_ϵ respectively.

The strategy to calculate $S_{\lambda_n \omega \phi}(q_x, q_y)$ from the assumptions above is depicted in figure B.1. As demonstrated in section 13, the intersection of the Ewald sphere with the vortex lattice plane is a circle, defined by λ, ω, ϕ, ζ and η:

$$(x - x_0)^2 + (y - y_0)^2 = r_0^2 \quad \text{where} \quad \mathbf{r}_0 = \begin{pmatrix} x_0 \\ y_0 \end{pmatrix} = \frac{2\pi}{\lambda} \begin{pmatrix} \omega + \zeta \\ \phi + \eta \end{pmatrix}. \tag{31.3}$$

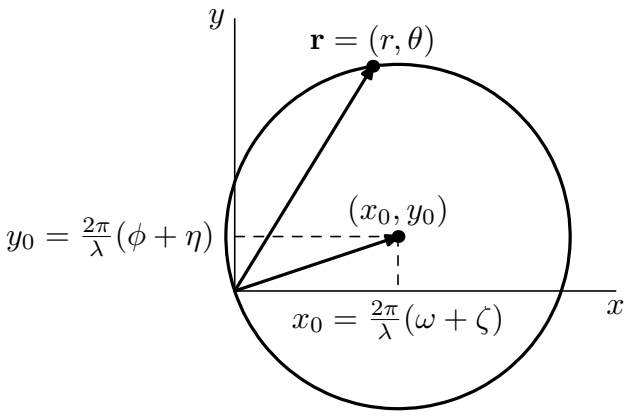

Fig. B.1: Geometry in reciprocal space for calculating $S_{\lambda_n \omega \phi}(q_x, q_y)$. For a given set of rocking angles, (ω, ϕ), and distribution variables (λ, ζ, η) the intersection of the Ewald sphere with the vortex lattice plane is a circle centred on $\mathbf{r}_0 = (x_0, y_0) = \frac{2\pi}{\lambda}(\omega + \zeta, \phi + \eta)$ with a radius $|\mathbf{r}_0|$.

Evaluating the sampled weight of a point $\mathbf{r}$ involves integrating over the distributions in λ, ζ and η, which is most easily performed in polar coordinates. In this coordinate system, the Bragg condition (equation 31.3) can be recast as:

$$r = \frac{4\pi}{\lambda} \left[(\omega + \zeta) \cos\theta + (\phi + \eta) \sin\theta \right]. \tag{31.4}$$

* This is not true in the detector space, which of course can distinguish between mosaic spread and beam divergence because the detector knows the nominal (undiffracted) beam direction.

The resolution function $S_{\lambda_n\omega\phi}(q_x, q_y)$ may be written as an integral over the three distributions with a delta function whose argument is equation 31.4:

$$S_{\lambda_n\omega\phi}(r,\theta) \propto \int_{-\infty}^{+\infty}\int_{-\infty}^{+\infty}\int_{0}^{\infty} \lambda^2 \exp\left(-\frac{(\lambda-\lambda_n)^2}{2\sigma_\lambda^2}\right)\exp\left(-\frac{\zeta^2}{2\sigma_\zeta^2}\right)\exp\left(-\frac{\eta^2}{2\sigma_\eta^2}\right) \times \delta\left(r - \frac{4\pi}{\lambda}\left[(\omega+\zeta)\cos\theta + (\phi+\eta)\sin\theta\right]\right) \mathrm{d}\lambda\mathrm{d}\zeta\mathrm{d}\eta \tag{31.5}$$

Note the factor of λ^2 in this integral: this is inserted to account for the small correction due to the density of states on the surface of the Ewald sphere. The delta function in $S_{\lambda_n\omega\phi}(r,\theta)$ is a one-dimensional delta function in r with θ as a parameter. The conversion to a two-dimensional distribution is described at the end of calculation.

Integrating equation 31.5 involves copious amounts of tedious algebra; below are listed some intermediate stages.

1. The integral in ζ is done trivially via the delta function, which for this purpose may be rewritten $\delta(\frac{4\pi\cos\theta}{\lambda}[R-\omega-\zeta-(\phi+\eta)t])$, where $R = \frac{r\lambda}{4\pi\cos\theta}$ and $t = \tan\theta$. This results in the expression:

$$S_{\lambda_n\omega\phi}(r,\theta) \propto \frac{1}{|\cos\theta|}\int_{-\infty}^{+\infty}\int_{0}^{\infty} \lambda^3 \exp\left(-\frac{(\lambda-\lambda_n)^2}{2\sigma_\lambda^2}\right) \times \exp\left(-\frac{\left[R-\omega-(\phi+\eta)t^2\right]^2}{2\sigma_\zeta^2}\right)\exp\left(-\frac{\eta^2}{2\sigma_\eta^2}\right)\mathrm{d}\lambda\mathrm{d}\eta$$

2. To perform the integral in η, terms containing η in the arguments of the exponentials are factorised into the form $-A(\eta+\frac{B}{2A})^2 + \frac{B^2}{4A}$, where $A = \frac{1}{2\sigma_\eta^2} + \frac{t^2}{2\sigma_\zeta^2}$ and $B = \frac{1}{\sigma_\zeta^2}(\phi t^2 + \omega t - Rt)$. The term $\frac{B^2}{4A}$ is η-independent and may be removed from the integral leaving just a Gaussian integral, which just gives an ignorable constant of proportionality ($\sqrt{\pi}$). This leaves only the λ integral:

$$S_{\lambda_n\omega\phi}(r,\theta) \propto \frac{1}{|\cos\theta|\sqrt{A}}\exp\left(-\frac{1}{2\sigma_\zeta^2}(\omega^2 + 2\phi\omega t + \phi^2 t^2)\right) \times \int_0^\infty \lambda^3 \exp\left(-\frac{(\lambda-\lambda_n)^2}{2\sigma_\lambda^2}\right)\exp\left(-\frac{1}{2\sigma_\zeta^2}(R^2 - 2R\omega - 2R\phi t)\right)\exp\left(\frac{B^2}{4A}\right)\mathrm{d}\lambda$$

3. The last integral in λ is done in the same manner as the one above. First some factorisation is needed, resulting in an integral of a Gaussian multiplied by a polynomial:

$$S_{\lambda_{\mathrm{n}}\omega\phi}(r,\theta) \propto \frac{1}{|\cos\theta|\sqrt{A}} \exp\left(-\frac{1}{2\sigma_\zeta^2}(\omega^2 + 2\phi\omega t + \phi^2 t^2)\right) \exp\left(-\frac{\lambda_{\mathrm{n}}^2}{2\sigma\lambda}\right)$$

$$\times \exp\left(\frac{1}{4A\sigma_\zeta^2}(\phi^2 t^4 + 2\phi\omega t^3 + \omega^2 t^2)\right) \exp\left(\frac{D^2}{4C}\right) \int_0^\infty \lambda^3 \exp\left(-C\left[R - \frac{D}{2C}\right]^2\right) \mathrm{d}\lambda,$$

where the constants D and C are defined in equation 31.6 below.

4. Recalling that $\lambda = \frac{4\pi\cos\theta}{r}R$, the last intergral may be performed using the substitution $x = \sqrt{C}(R - \frac{D}{2C})$. Note that converting the range of integration from $\lambda \in [0, \infty)$ gives either $x \in [-\frac{D}{2C\sqrt{C}}, \infty)$ or $x \in (-\infty, -\frac{D}{2C\sqrt{C}}]$ because $\cos\theta$ can assume both positive and negative values. These cases have to be considered separately, as does the case $\cos\theta = 0$, which needs to be handled by taking the appropriate limit.

5. The last step is to convert $S_{\lambda_{\mathrm{n}}\omega\phi}(r,\theta)$ to Cartesian form. Strictly speaking, the delta function in equation 31.5 gives a one-dimensional distribution in r with θ as a parameter. To use it as a two-dimensional distribution, $S'_{\lambda_{\mathrm{n}}\omega\phi}(r,\theta)$, requires correct handling of the differential area element at (r,θ). Let $S'_{\lambda_{\mathrm{n}}\omega\phi}(r,\theta)$ be the two-dimensional reciprocal-space sampling function in polar coordinates such that $S'_{\lambda_{\mathrm{n}}\omega\phi}(r,\theta)\mathrm{d}r\mathrm{d}\theta$ is the sampled weight of the region of reciprocal space near (r,θ). To convert $S_{\lambda_{\mathrm{n}}\omega\phi}(r,\theta)$, which is a one-dimensional slice, into $S'_{\lambda_{\mathrm{n}}\omega\phi}(r,\theta)\mathrm{d}r\mathrm{d}\theta$ requires taking into account the scale factor for θ when converting the linear differential element into an areal one:

$$S'_{\lambda_{\mathrm{n}}\omega\phi}(r,\theta)\mathrm{d}r\mathrm{d}\theta = S_{\lambda_{\mathrm{n}}\omega\phi}(r,\theta)r\mathrm{d}\theta\mathrm{d}r.$$

(Put more intuitively, the one-dimensional slice of linear elements $\mathrm{d}r$ needs to be converted into a wedge of area elements $r\mathrm{d}\theta\mathrm{d}r$.) To convert $S'_{\lambda_{\mathrm{n}}\omega\phi}(r,\theta)$ into a Cartesian distribution it should be divided by the Jacobian $J = r$, thus the factor r gained above is lost and the Cartesian distribution is obtained simply by substituting (x,y) for (r,θ) in $S_{\lambda_{\mathrm{n}}\omega\phi}(r,\theta)$.

The final result of this analysis is shown in equation 31.6. Note that no effort has been made to find the correct limit for $\theta = \pm\pi/2$. That labour has been avoided because all that is required of this calculation is a plot and this pathalogical case can be avoided by sensible choice of grid when evaluating $S_{\lambda_n \omega \phi}(x, y)$. The grid chosen is such that the origin lies at the corner of a pixel and therefore there is no pixel whose centre is at $\theta = \pm\pi/2$. No useful information is lost by this cheat because the correct limit will be visually obvious.

A plot of equation 31.6 for a set of reasonable parameters is shown in figure B.2. In accordance with expectation (see discussion in sections 14 and 15) the region of reciprocal space that is sampled is crescent-shaped. The apparent absence of sampling weight near the origin is an artefact of plotting: at the origin the Ewald spheres all coincide causing $S_{\lambda_n \omega \phi}(x, y)$ to vary very rapidly there. A cut of these data is shown in figure B.3. This shows that the cross-section of the crescent has a roughly Gaussian shape as would be expected from the Gaussian nature of the distributions from which it is derived. Owing to the λ^2 density-of-states factor in equation 31.5 this curve peaks slightly lower than the $19.7\,\mathrm{m\AA}^{-1}$ expected from Bragg's law for $\omega = 0.9°$ and $\lambda_n = 10\,\text{Å}$. However, the corresponding curve with $\sigma_\lambda = 0$ (dashed curve in figure B.3) does peak at the Bragg q.

$$
\begin{aligned}
S_{\lambda_{\mathrm{n}}\omega\phi}(x,y) \propto & \frac{k^4}{\sqrt{A}C^2|\cos\theta|}\left\{G_3(z)+\frac{5D}{\sqrt{C}}G_2(z)+\frac{3D^2}{4C}G_1(z)+\frac{D^3}{8C\sqrt{C}}G_0(z)\right\} \\
& \times\exp\left[-\frac{1}{2\sigma_\zeta^2}(\omega^2+2\omega\phi t+\phi^2t^2)+\frac{1}{4A\sigma_\zeta^2}(\phi^2t^4+2\phi\omega t^3+\omega^2t^2)-\frac{\lambda_{\mathrm{n}}^2}{2\sigma_\lambda^2}+\frac{D^2}{4C}\right] \\
\text{where} \quad & r=\sqrt{x^2+y^2} \\
& \theta=\operatorname{atan}\frac{y}{x} \\
& t=\tan\theta \\
& A=\frac{1}{2\sigma_\eta^2}+\frac{t^2}{2\sigma_\zeta^2} \\
& B=\frac{1}{\sigma_\zeta^2}(\phi t^2+\omega t-Rt) \\
& k=\frac{4\pi\cos\theta}{r} \\
& C=\frac{k^2}{2\sigma_\lambda^2}-\frac{t^2}{4A\sigma_\zeta^4}+\frac{1}{2\sigma_\zeta^2} \\
& D=\frac{k\lambda_{\mathrm{n}}}{\sigma_\lambda^2}-\frac{\phi t^3+\omega t^2}{2A\sigma_\zeta^4}+\frac{\omega+\phi t}{\sigma_\zeta^2} \\
& z=-\frac{D}{2\sqrt{C}} \\
& G_0(z)=\begin{cases}\frac{\sqrt{\pi}}{2}\mathrm{erfc}(z), & \theta\in[-\pi/2,\pi/2] \\ \frac{\sqrt{\pi}}{2}(\mathrm{erfc}(z)-2), & \text{otherwise}\end{cases} \\
& G_1(z)=\frac{1}{2}\exp(-z^2) \\
& G_2(z)=\begin{cases}\frac{1}{2}\left[z\exp(-z^2)+\frac{\sqrt{\pi}}{2}\mathrm{erfc}(z)\right], & \theta\in[-\pi/2,\pi/2] \\ \frac{1}{2}\left[z\exp(-z^2)+\frac{\sqrt{\pi}}{2}\mathrm{erfc}(z)-\sqrt{\pi}\right], & \text{otherwise}\end{cases} \\
& G_3(z)=\frac{1}{2}\exp(-z^2)\left[z^2+\frac{1}{2}\right] \\
& \mathrm{erfc}(z)=\frac{2}{\sqrt{\pi}}\int_z^\infty\exp(-t^2)\mathrm{d}t
\end{aligned}
\tag{31.6}
$$

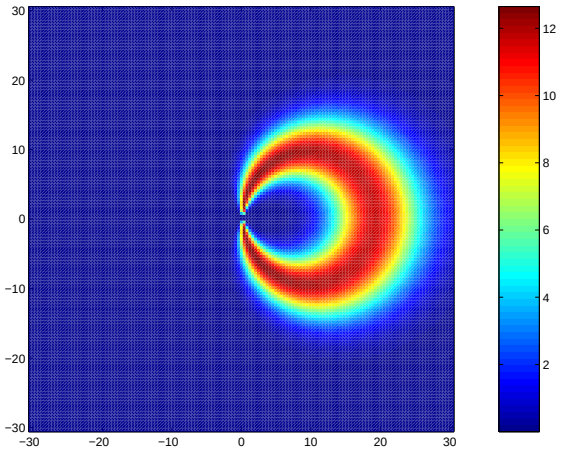

Fig. B.2: A colour plot (arbitrary units) of equation 31.6 for the following parameters: $\omega = 0.9°$, $\phi = 0°$, $\lambda = 10\,\text{Å}$, $\sigma_\lambda = 1\,\text{Å}$ and $\sigma_\zeta = 0.2° = \sigma_\eta$. The function was evaluated over a 150×150 grid. The grid axes are in mÅ^{-1}. (Note that $q = 19.7\,\text{mÅ}^{-1}$ for $\theta = 0.9°$ and $\lambda = 10\,\text{Å}$.)

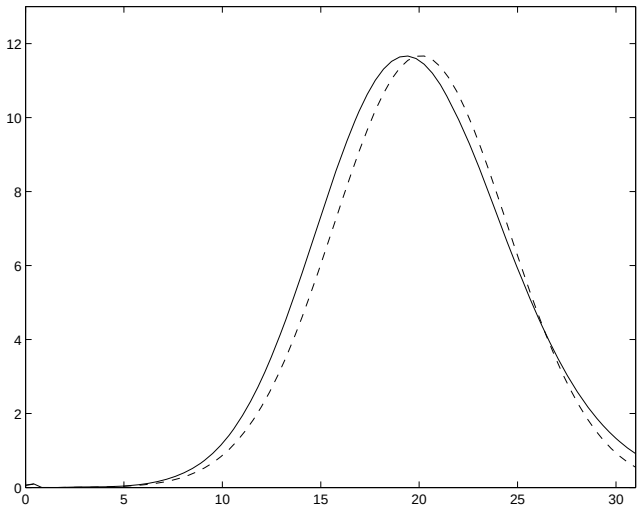

Fig. B.3: A graph showing the cut through $\theta = 0$ of the data presented in figure B.2 (continuous line). The dashed curve shows the same cut, but for data computed with $\sigma_\lambda = 0$. (Note that for presentation purposes the peak of the dashed line has been normalised to the peak of the continuous line.)

APPENDIX C

Numerical evaluation of the London free energy

In this appendix is listed the code used to evaluate the London free energy for an anisotropic vortex lattice. This is achieved by calculating the free energy (equation 3.6) over a set of test parameters and locating the minimum. There are three parameters required to define uniquely the vortex lattice structure given the vortex direction: the ratio of the reciprocal lattice vectors, the angle between the reciprocal lattice vectors and the orientation of the vortex lattice about the induction (relative to the crystal axes or their projection onto the plane perpendicular to the vortex lattice). However, the single crystal used in these investigations contained twin planes, which are known to enforce the orientation of the vortex lattice along the {110} direction. Therefore in the code presented below the loop over vortex lattice orientations has been disabled and the orientation fixed appropriately. (It would be easy to modify the programme to handle crystals without twin planes.)

As explained in section 2, the divergent nature of the London free energy necessitates a cut-off at wavevectors larger than roughly ξ^{-1}. This was performed using a Gaussian as suggested in the text. Hence, although the induction is normally not needed to calculate the London free energy (it simply scales with it) it has been included in order to fix the inter-vortex distance, which becomes relevant if finite-core effects are to be taken into account. The London penetration depth also needs to be specified since although it is a degenerate parameter in the bare London free energy, once the free energy is dressed with the Gaussian cut-off it serves to set the value of κ. (Mathematically, it is important because there are two dimensionless length-scales in the free energy sum: a magnetic one, $\lambda_{\mathrm{L}}G$, and one associated with the cores, ξG.)

The final ingredient is the mass tensor. In this implementation an orthorhombic crystal is assumed and in the programme the diagonal elements are entered. Since the coordinates are measured in the frame of the vortices, the mass tensor is rotated first

about the z-axis (the variable `alpha` in the programme) and then about the new y-axis (the variable `beta`); the rotation is calculated automatically by the programme just after the declaration of the mass tensor and the transformation to the vortex frame.

The programme to evaluate the free energy minimum is shown below. By and large it is rather *ad hoc* and all the necessary parameters are hard-wired, hence the programme requires recompiling before each new calculation. This lack of ease of use is justified by the numerical efficiency of the programme. Since Fourier sums can, depending on the conditions, take some time, the programme was written in ANSI C++, rather than an interpreted language like Matlab. The choice of C++ over plain C (and indeed Matlab) enables the benefits of object-oriented programming to be reaped. Since the free energy equation is a messy expression involving vector products and the contraction of tensors with vectors, a straightforward translation of the expression into a computer language would be a tedious and error-prone affair. Therefore classes implementing vectors and tensors have been provided. These classes are deliberately limited in function. The vector class provides a container for an ordinary three-vector (with an obvious constructor) and the simple operations associated with these, namely addition, subtraction, negation, multiplication by a scalar (both integer and floating point), the vector (outer) product and the scalar (inner) product. The tensor class is an extremely limited helper class that supports only second rank tensors in three dimensions (stored as three column vectors); the only operation supported for the tensor class is contraction with a vector to the tensor's right. All of these operations have been declared as inline to suggest to the compiler to insert a copy of the function whereever it is used in the hope that this will avoid an expensive function call. (In ANSI C++ compilers this is at the compiler's discretion, but since these are all simple arithmetical operations requiring presumably few registers most compilers should be able to follow the suggestion.) The function to evaluate a term in the free energy has also been declared inline and is only separated for ease of reading. In this function, use has been made of auxilliary variables to avoid uselessly repeating sub-calculations and the constants have been declared static to prevent the compiler generating instructions to define them in the innermost loop.

The ANSI C++ code to the programme described is listed on the following pages.

There are two files: the main programme file, `london.C`, and a header file that defines the vector and tensor classes, `london_maths.h`. These programmes should compile on a standard ANSI C++ compiler. For example, it will compile on the GNU C++ compiler, `g++ (GCC)`, which is available on many platforms. Here the programme was compiled using version 3.3.3 of this compiler. The target platform was GNU/Linux (SuSE 9.1, kernel version 2.6) running on a 32-bit 2.8 GHz Intel Pentium-4 processor. Compilation and linking was achieved by running the command:

```
g++ -O2 -o london london.C.
```

This invokes the project GNU C++ compiler and compiles the programme with full time optimisation.

```
/*============================================================
    london.C - Minimises london free energy
    Compilation:
        g++ -O2 -o london london.C
    Comments:
        london.C: calculates the london free energy for the
        fully anisotropic case using the equation in
        Burlachkov, Euro. Phys. Lett., 8 (7), 1989. Uses a
        Gaussian cutoff to force convergence.
============================================================*/

#include <iostream>
#include <math.h>
#include <stdlib.h>
#include "london_maths.h"

using namespace std;

// ******* GLOBAL VARIABLES ******************************
// mass tensor:  set in main(), used in F.
tensor m;
// 2*(cutoff-length)^2 in denominator of Gaussian.
double cutoffsq;
// penetration depth squared
double lambdasq;

//*********************************************************
// Calculates a term in the Fourier sum of the London free
// energy
static inline double F(vctr k)
{
    static const vctr l(0,0,1); // direction of vortices
// Constant auxilliaries for efficiency
// contraction of mass tensor (twice) with vortex unit vector
    static const double pre_lmlpart = lambdasq*(l*(m*l));
// contraction of mass tensor with vortex unit vec.
    static const vctr ml = m*l;
// auxilliaries (used more than once).
    double modksq = k.x*k.x + k.y*k.y + k.z*k.z; // k^2
    double lmlpart = 1+modksq*pre_lmlpart;
    vctr kcrossl = k^l;
// free energy expression of Burlachkov with gaussian cutoff
    return exp(-modksq/cutoffsq) * lmlpart / ( lmlpart*(1+lambdasq*(kcrossl*(m*kcrossl)))
       - lambdasq*lambdasq*modksq*( (kcrossl*ml) * (kcrossl*ml) ));
}

// ****************** MAIN ******************************
int main (int argc, char* argv[])
{
// ===== Maths/physics constants
    const double pi = 3.141592654;
    const double phi0 = 2067.83461; // flux quantum in (T.nm^2)
```

```
// ===== Size of lattice to sum over
    const int lsize=100;

// ===== Unit cell parameters
// direction of pinning
    const double theta=45.0*pi/180.0;
// parameters to vary: length of one of the
// basis vectors and angle between them
    double modg2, phi;
    double phi_start = 40.0*pi/180.0, phi_end=80.0*pi/180.0;
    double modg2_start = 0.8, modg2_end = 1.2;
    double modg2_step = 0.025, phi_step = 1.0*pi/180.0;
// Magnetic induction (Tesla)
    double B=1;
    double cellA = 4*pi*pi*B/phi0; // Unit cell area (nm^-2)
// measure vector lengths relative to undisorted lattice
    double ktri = sqrt(2*cellA/(sqrt(3.0)));
// normalise vector-length range to reciprocal unit cell area
    modg2_start *= ktri, modg2_end *= ktri, modg2_step *= ktri;

// ===== Physical paramters: B, mass tensor etc.
// coherence length and penetration depth
    double xi=3,lambda=150;
// auxilliaries of above, used in F(k).
    cutoffsq = 8*pi*pi/(xi*xi), lambdasq = lambda*lambda;
// Effective masses (=gamma^2)
    double ma=1.0,mb=1.64,mc=20.0, mGeoMean=ma*mb*mc;
// normalise to geometric mean.
    ma /= mGeoMean, mb /= mGeoMean, mc /= mGeoMean;
// angles of rotation of mass tensor: alpha is about z-axis,
// beta is about y' axis (new y-axis obtained from alpha rotation.
    double alpha=0.0*pi/180.0,beta=0.0*pi/180.0;
// Elements of the (symmetric) mass tensor as rotated by alpha
// and beta (global variable used in F(k)).
    m.x.x = cos(beta)*cos(beta)*( cos(alpha)*cos(alpha)*ma
        + sin(alpha)*sin(alpha)*mb ) + sin(beta)*sin(beta)*mc;
    m.x.y = m.y.x = cos(beta)*sin(alpha)*cos(alpha)*(ma-mb);
    m.x.z = m.z.x = (mc - cos(alpha)*cos(alpha)*ma + sin(alpha)*sin(alpha)*mb)
        * sin(beta)*cos(beta);
    m.y.y = sin(alpha)*sin(alpha)*ma + cos(alpha)*cos(alpha)*mb;
    m.y.z = m.z.y = sin(beta)*sin(alpha)*cos(alpha)*(mb-ma);
    m.z.z = sin(beta)*sin(beta)*( cos(alpha)*cos(alpha)*ma+sin(alpha)*sin(alpha)*mb )
        + cos(beta)*cos(beta)*mc;

    vctr g1, g2;// (avoid constructor call in loop)
    double phimin=-666.0,modg2min=-666.0,modg1min=-666.0,Fmin=6e66;

// Loop over shape of reciprocal lattice: vary length of one vector and angle
// between them. (Lenght of other determined by flux quantisation).
    for (phi=phi_start; phi<=phi_end; phi+=phi_step)
    {
```

```
        for (modg2=modg2_start; modg2<modg2_end; modg2+=modg2_step)
        {
// Work out basis vectors
            g2.x = modg2*cos(theta), g2.y = modg2*sin(theta);
// (flux quantisation)
            double modg1 = cellA/(sin(phi)*modg2);
            g1.x = modg1*cos(theta+phi), g1.y = modg1*sin(theta+phi);

            double Fsum=0;
// lattice sum
            for (int h=-lsize; h<=lsize; h++)
                for (int k=-lsize; k<=lsize; k++)
                    Fsum += F(h*g1+k*g2);

            cout << Fsum << " ";
            if (Fmin > Fsum) // find minimum for info at end
                Fmin=Fsum, phimin=phi, modg2min=modg2, modg1min=modg1;
        }
        cout << endl;
    }
    cerr.precision(10);
    cerr << "Minimum F=" << Fmin << " at phi=" << phimin*180.0/pi << ", g1="
        << modg1min/ktri << ", g2=" << modg2min/ktri << endl;
    return 0;
}
```

```
/*============================================================
    london_maths.h: defines some simple classes to make
    maths more readable
============================================================*/

// ****** vector class with simple operations ************
class vctr {
// All members public for ease
public:
    double x,y,z;
// constructors
    vctr() {x=0,y=0,z=0; }
    vctr(double _x, double _y, double _z) {x=_x,y=_y,z=_z; }
// operations
    inline vctr operator^ (const vctr& s)
        {return vctr(y*s.z-z*s.y,z*s.x-x*s.z,x*s.y-y*s.x); }
    inline vctr operator+ (const vctr& s)
        {return vctr(x+s.x, y+s.y, z+s.z); }
    inline vctr operator- (const vctr& s)
        {return vctr(x-s.x, y-s.y, z-s.z); }
    inline vctr operator- () {return vctr(-x,-y,-z); }
};

// declared outside class
inline double operator* (const vctr& f, const vctr& s)
    {return f.x*s.x+f.y*s.y+f.z*s.z; }
inline vctr operator* (int f, const vctr& s)
    {return vctr(f*s.x,f*s.y,f*s.z); }
inline vctr operator* (double f, const vctr& s)
    {return vctr(f*s.x,f*s.y,f*s.z); }

// *** 2nd rank tensor class ****************************
class tensor {
public:
// treat elements a 3 row vectors.
    vctr x, y, z;
// tensor contraction to the right with a vector
// (contraction to the left numerically awkward with
// this class, but only right is needed.)
    inline vctr operator* (const vctr& s) {return vctr(x*s,y*s,z*s);}
};
```

APPENDIX D

PUBLICATIONS

The following are papers arising from work carried out during this thesis that have been published, or submitted to be published:

Capogna, L., Forgan, E.M., Hayden, S.M., Wildes, A., Duffy, J.A., Mackenzie, A.P., Perry, R.S., Ikeda, S., Maeno, Y. and Brown, S.P., *Observation of two-dimensional spin fluctuations in the bilayer ruthenate* $Sr_3Ru_2O_7$ by inelastic neutron scattering, Phys. Rev. B **67**, 012504 (2003).

Gilard, R., Streule, S., Mesot, J., Drew, A., Divakar, U., Lee, S.L., Brown, S.P., Forgan, E.M., Momono, M. and Oda, N., *A small angle neutron scattering istudy of the vortex matter in* $La_{2-x}Sr_xCuO_4$ ($x = 0.17$), Int. J. Mod. Phys. B **17**, 3411 (2003).

Brown, S.P., Charalambous, D., Jones, E.C., Forgan, E.M., Kealey, P.G., Erb, A. and Kohlbrecher, J., *Triangular to square flux lattice phase transition in* $YBa_2Cu_3O_7$, Phys. Rev. Lett. **92**, 067004 (2004).

Gilardi, R., Mesot, J., Brown, S.P., Forgan, E.M., Drew, A.J., Lee, S.L., Cubitt, R., Dewhurst, C.D., Uefuji, T. and Yamada, K., *Square vortex lattice at anomalously low magnetic fields in electron-doped* $Nd_{1.85}Ce_{0.15}CuO_4$, Phys. Rev. Lett. **93**, 217001 (2004).

Charalambous, D., Forgan, E.M., Ramos, S., Brown, S.P., Lycett, R.J., Ucko, D.H., Drew, A.J., Lee, S.L., Fort, D., Amato, A. and Zimmerman, U., *Driven vortices in type-II superconductors: a muon spin rotation study*, Phys. Rev. B, submitted for publication (2005).

A copy of these papers (where an electronic version was available) can be found in the following pages.

The list below shows work associated with this thesis that are in preparation for publication:

Brown, S.P., Forgan, E.M., Charalambous, D., Jones, E.C., Kealey, P.G., Erb, A. and Laver, M., *Dependence upon temperature and angle of applied field of the configuration of the high-field vortex lattice in* $YBa_2Cu_3O_7$, Phys. Rev. B, to be published (2005).

Ramos, S., Brown, S.P., Forgan, E.M., Hayden, S., Wildes, A., Perry, R.S and Maeno, Y., *Observation of spin fluctuations at and beyond the metamagnetic field in* $Sr_3Ru_2O_7$, Phys. Rev. Lett., to be published (2006).

Hinkov, V., Keimer, B., Brown, S.P., Forgan, E.M., data to be published in Phys. Rev. Lett. (2006).

Observation of two-dimensional spin fluctuations in the bilayer ruthenate $Sr_3Ru_2O_7$ by inelastic neutron scattering

L. Capogna,[1,*] E. M. Forgan,[1,†] S. M. Hayden,[2] A. Wildes,[3] J. A. Duffy,[2,4] A. P. Mackenzie,[1,5] R. S. Perry,[1,6] S. Ikeda,[6,‡] Y. Maeno,[6,7] and S. P. Brown[1]

[1]*School of Physics and Astronomy, University of Birmingham, Birmingham B15 2TT, United Kingdom*
[2]*H.H. Wills Physics Laboratory, University of Bristol, Bristol BS8 1TL, United Kingdom*
[3]*Institut Laue-Langevin, 6 Rue Jules Horowitz, F38042 Grenoble Cedex, France*
[4]*Department of Physics, University of Warwick, Coventry CV4 7AL, United Kingdom*
[5]*School of Physics and Astronomy, University of St. Andrews, St. Andrews KY16 9SS, United Kingdom*
[6]*Department of Physics, Kyoto University, Kyoto 606-8502, Japan*
[7]*CREST, Japan Science and Technology Corporation, Kawaguki, Saitama 332-0012, Japan*

(Received 14 November 2002; published 31 January 2003)

We report an observation of two-dimensional incommensurate magnetic fluctuations in the layered metallic perovskite $Sr_3Ru_2O_7$. The wave vectors where the magnetic fluctuations are strongest are different from those observed in the superconducting single layer ruthenate Sr_2RuO_4 and appear to be determined by Fermi surface nesting. No antiferromagnetic ordering is observed for temperatures down to 1.5 K. For temperatures $T \gtrsim 20$ K, the fluctuations become predominately ferromagnetic. Our inelastic neutron scattering measurements provide concrete evidence of the coexistence of competing interactions in $Sr_3Ru_2O_7$ and of the low-energy scale of the fluctuations.

DOI: 10.1103/PhysRevB.67.012504 PACS number(s): 74.20.Mn, 78.70.Nx, 75.30.Kz, 75.40.Gb

The nature of magnetic correlations in layered oxide perovskites such as cuprates, manganites, and ruthenates is at the heart of theoretical and experimental challenges in contemporary solid state physics. In recent years, the discovery of unconventional superconductivity in the single-layer ruthenate Sr_2RuO_4 (Ref. 1) has generated great interest in this and related ruthenates. The observation of low energy incommensurate two-dimensional (2D) spin fluctuations in Sr_2RuO_4 (Refs. 2–4) has raised the question of the relevance of spin fluctuations to *p*-wave pairing in this material. The closest relative of Sr_2RuO_4, the bilayer $Sr_3Ru_2O_7$, is a paramagnet where ferromagnetic and antiferromagnetic correlations may be in competition, and ferromagnetism can be induced by pressure or impurities.[5–10] At low temperatures, high-quality single crystals of $Sr_3Ru_2O_7$ exhibit Fermi liquid behavior, such as a T^2 temperature dependence of the resistivity[6,11] and a linear electronic heat capacity with $\gamma = 110$ mJ/(K^2 mol Ru).[8] However, a moderate magnetic field (5.5–7.7 T, depending on field direction) induces a metamagnetic transition, which is accompanied by a striking deviation from Fermi liquid behavior.[8,12] $Sr_3Ru_2O_7$ appears to be a strong candidate to exhibit a metamagnetic quantum critical end-point, driven by the magnetic field and characterized by the absence of spontaneous symmetry breaking.[12] In this paper we report observations in zero field of low-energy spin fluctuations in $Sr_3Ru_2O_7$ as measured by inelastic neutron scattering.

With respect to the conducting and magnetic properties of $Sr_3Ru_2O_7$, the fundamental building blocks of its crystal structure are the RuO_2 bilayers joined by an SrO layer. These slabs are separated along the crystal $\boldsymbol{c}$ direction by two rock salt-type layers of SrO which decouple the slabs electronically and magnetically. In contrast to the single layer compound Sr_2RuO_4, the RuO_6 octahedra in $Sr_3Ru_2O_7$ are rotated around the $\boldsymbol{c}$ axis, by $\sim 7°$. This changes the unit cell from body-centered tetragonal to a $\sqrt{2}\times\sqrt{2}$ larger face-centered cell which is orthorhombic but has a and b equal within experimental error.[13] The rotation is expected to reduce the in-plane Ru-Ru hopping, and hence increase the density of states at the Fermi level,[14] which may enhance the magnetic fluctuations.

Single crystals of $Sr_3Ru_2O_7$ were grown in a mirror furnace, and were checked for homogeneity and purity by magnetic, resistive, and crystallographic measurements. All crystals used in this study showed the characteristic peak in susceptibility at $T \sim 17$ K and no ferromagnetism. For the inelastic neutron scattering experiments, three crystals were mounted so that their axes coincided to form a mosaic sample with total mass 0.9 g. This was mounted in a cryostat on the cold neutron three-axis spectrometer IN14 at the ILL. For simplicity, we describe our results using the tetragonal cell of the compound, which has the a and b lattice parameters equal to the in-plane Ru-O-Ru distance 3.87 Å. The $\boldsymbol{c}$ axis is perpendicular to the RuO_2 planes and has the magnitude 20.7 Å, which is twice the spacing of the RuO_2 bilayers, reflecting the body-centred stacking of bilayers.[13] Using this unit cell, the main nuclear Bragg peaks of the 3D structure occur at points (h,k,l) in reciprocal space with integer h, k, and l and $(h+k+l)$ even. The less intense ones, arising from the rotations of the octahedra, occur at some of the points where h and k are half-integral and l is an integer.

We performed extensive measurements with $(h,k,0)$ as the scattering plane and further measurements in the $(h,0,l)$ plane. Unlike Sr_2RuO_4, magnetic fluctuations at our base temperature of 1.5 K were *not* observed to peak along the $(h,h,0)$ direction from a reciprocal lattice point; instead they were detected along $(h,0,0)$. Figure 1 shows representative scans along major symmetry directions at a constant energy

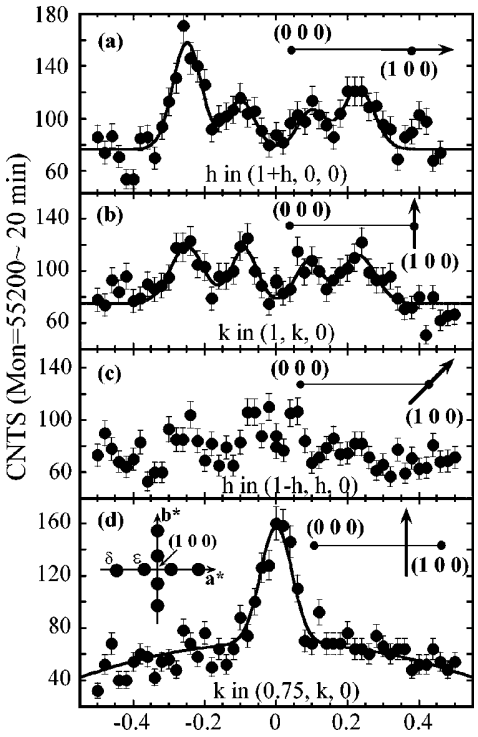

FIG. 1. Inelastic neutron scattering at 1.5 K: intensity versus wavevector along lines in the $(h,k,0)$ plane, at a constant energy transfer of 2 meV. Solid lines are a sum of Gaussians as a guide to the eye. The fwhm Q resolution, calculated for the relaxed collimation of our setup, is comparable to the width of the symbols. The inset to (d) indicates schematically the $\boldsymbol{Q}$ positions where peaks are observed. All measurements in this Letter, except those in Fig. 2, were taken with a varying incident energy and constant final energy of 4.97 meV, using PG (002) monochromator and analyser and a cooled beryllium filter before the analyser to remove higher order contamination.

transfer (from neutrons to the sample) of 2 meV. Figure 1(a) shows a double set of peaks along the $(h,0,0)$ direction at the positions $\boldsymbol{Q}\approx(1\pm0.25,0,0)$ and $(1\pm0.09,0,0)$. The intrinsic nature of such peaks was demonstrated by the observation of a signal of similar intensity around the symmetry-related (0,1,0) point and the presence of four peaks in the ''perpendicular'' scan through (1,0,0) shown in Fig. 1(b). The variation of intensity within each set of peaks is quantitatively consistent with the rapid falloff of the Ru magnetic form factor with the magnitude of $\boldsymbol{Q}$,[15] providing strong evidence for the magnetic nature of the excitations. Furthermore, as shown later, the intensity does not increase with temperature as would be expected if the scattering were due to lattice vibrations. The extent of the magnetic fluctuations in the $(h,k,0)$ plane of reciprocal space was established by the scans shown in Figs. 1(c) and 1(d). These show that the excitations give a broad peak centred on the $(h,0,0)$ axis. The results are summarized in the inset: the excitation intensity peaks at two incommensurate wave vectors of the form $\boldsymbol{q}_\delta\approx\{0.25,0,0\}$ and $\boldsymbol{q}_\epsilon\approx\{0.09,0,0\}$, distributed symmetrically about (1,0,0). It is natural to assume that these arise from peaks in the wave vector–dependent susceptibility at nesting

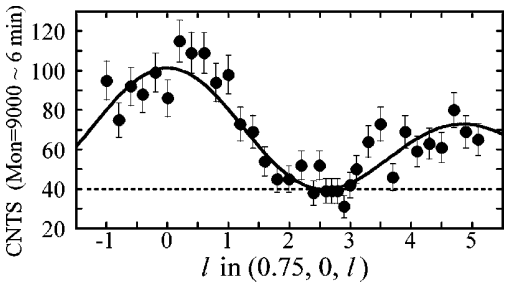

FIG. 2. l dependence of inelastic scattering at 2 meV and $h=0.75$, showing the effects of the bilayers. The solid line is the fit described in the text, plus a constant background. These measurements were performed at a constant incident energy of 14.67 meV, with a PG higher order filter in the incident beam.

vectors of the $Sr_3Ru_2O_7$ Fermi surface. This is not yet known experimentally, although it has been calculated.[14,16] The coupling between the two halves of a bilayer splits each of the three sheets observed in Sr_2RuO_4. This, and the rotation of the octahedra cause hybridization between the bands. It appears from the calculations,[14] that compared with Sr_2RuO_4, much of the nesting at the Fermi level is removed, except between parts of the α sheets (Ru d_{xz} and d_{yz} orbitals). The calculated sheets have nesting vectors along the (tetragonal) $\{1,0,0\}$ directions with values which are comparable with (although not equal to) those we observe. It seems reasonable to conclude that the differences of our results from those on single-layer Sr_2RuO_4 (Refs. 3,4) arise from the effects of bilayers and octahedral rotation on the Fermi surface in our system.

Measurements as a function of l allow us to determine the fundamental fluctuating unit in $Sr_3Ru_2O_7$ in this energy range. Figure 2 shows the variation along $\boldsymbol{c}^*$ of the intensity of the signal at $\boldsymbol{q}_\delta$. The experimental data are well represented by $I\propto f(\boldsymbol{Q})^2\cos^2(2\pi lz/c)$, where $f(\boldsymbol{Q})$ is the Ru form factor and $2z=0.194c$ is the distance between the RuO_2 planes in a bilayer. This function corresponds to the two halves of a bilayer fluctuating *in phase* with each other, but with *no* correlation between bilayers, so that the fluctuations are effectively two dimensional. A similar argument[17] was used to demonstrate 2D fluctuations in YBCO, but with the two halves of the bilayer in *antiphase*. We point out an important consequence of our results: since (1,0,0) *is* a reciprocal lattice point of a RuO_2 bilayer, the values of the $\boldsymbol{q}$ vectors of excitations should be measured from this point, rather than (0,0,0) or (1,0,1), which are the closest reciprocal lattice points of the 3D crystal structure.

We now consider the energy dependence of these excitations. Figure 3 shows four representative $\boldsymbol{Q}$ scans with energy transfers of 1, 2, 3, and 4 meV at $T=1.5$ K. The peaks appear to disperse slightly, and merge at higher energies. We have also performed a $\boldsymbol{Q}$ scan over this region at zero energy transfer, which showed no evidence for static magnetic ordering near $\boldsymbol{q}_\delta$ or $\boldsymbol{q}_\epsilon$. This result is in agreement with those of Refs. 18,19. We conclude that at finite temperature only finite frequency, short-range magnetic correlations exist.

Figure 4 shows the energy dependence of the signal at $\boldsymbol{q}_\delta$. To obtain a measure of the characteristic energy of these

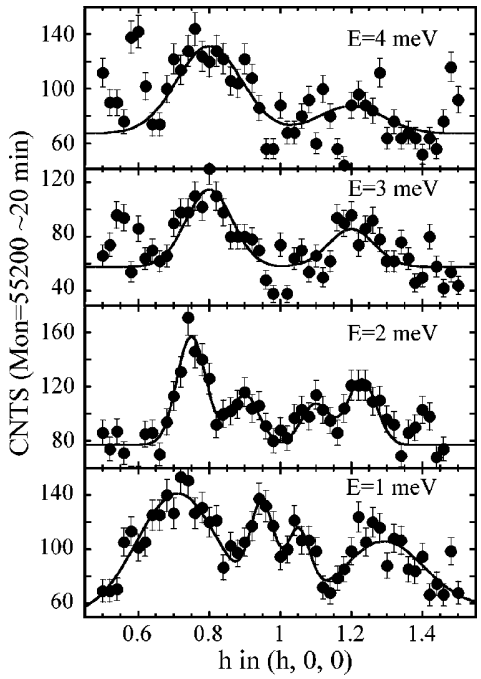

FIG. 3. Energy and $\boldsymbol{Q}$ dependence of scattering at 1.5 K. Scans along $(h,0,0)$ with energy transfers of 1, 2, 3, and 4 meV. We believe that the sharp features at the ends of the scan at 4 meV are due to optic phonons excited by second order contamination of the incoming beam.

excitations, we have fitted the response to a simple Lorentzian model for the susceptibility $\chi''(\boldsymbol{Q},\omega)=\chi'(\boldsymbol{Q})\times\omega\Gamma(\boldsymbol{Q})/[\Gamma^2(\boldsymbol{Q})+\omega^2]$. From the fit we obtain a value for the energy width $\hbar\Gamma=2.3\pm0.3$ meV. This is much less than 9 meV obtained by similar methods in the single layer compound Sr_2RuO_4.[3] The presence of dispersion on an energy scale much smaller than ϵ_F and the small energy scale of the fluctuations indicates the strong renormalising effects of electron correlations in our compound. A rough estimate[20] based on our data indicates that the very large observed specific heat γ may be understood in terms of the spin degrees of freedom.

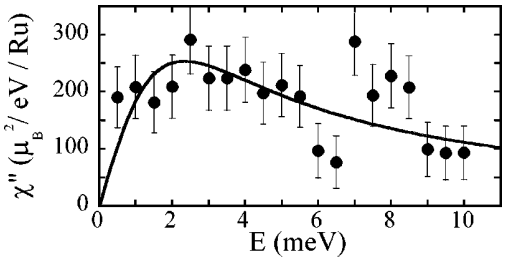

FIG. 4. Energy dependence of magnetic scattering at $\boldsymbol{Q}=(0.75,0,0)$, minus backgrounds taken at (1.48,0,0). The line represents a Lorentzian as described in the text. The ordinate has been corrected by the Bose factor $[n(\omega)+1]$ and the Ru form factor and converted to absolute units (with an accuracy $\sim$20%) by normalization to the intensity of a transverse acoustic phonon, measured at 3.1 meV around (1,1,0) at 100 K.

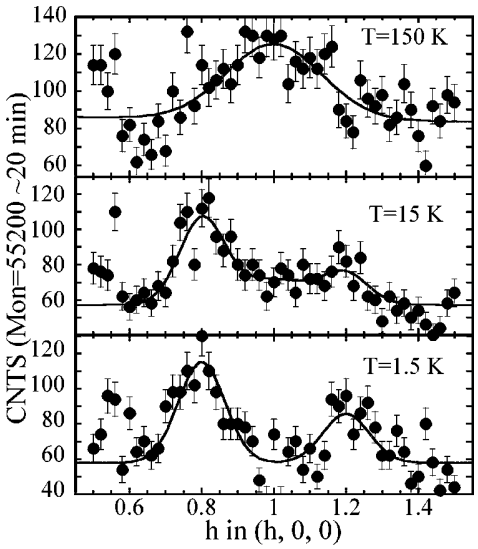

FIG. 5. $\boldsymbol{Q}$ dependence of scattering along $(h,0,0)$ for an energy transfer of 3.1 meV at three different temperatures, 1.5, 15, and 150 K. The peak near $h=0.6$ is believed to be spurious scattering.

We also note that the susceptibility is large, translating to $\chi'(\boldsymbol{Q}_\delta)$ of 1.6×10^{-2} emu/mol Ru. This indicates that $Sr_3Ru_2O_7$ is much closer to magnetic order than its sister compound.

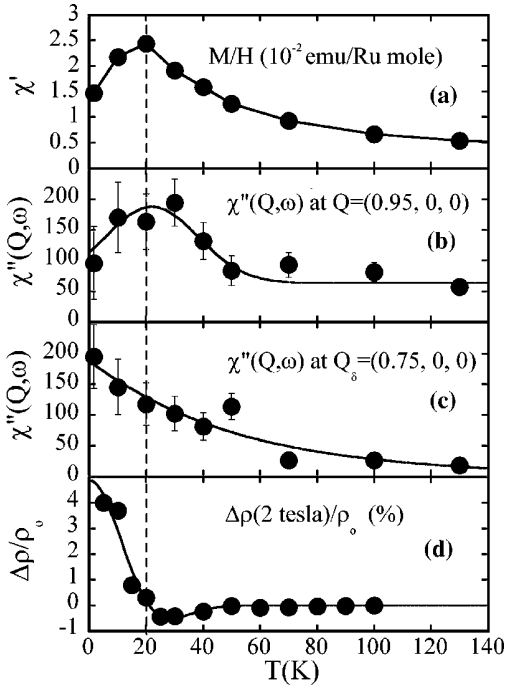

FIG. 6. Temperature-dependence of magnetic response from macroscopic and microscopic measurements (a) Static susceptibility from Ref. 6. (b) Susceptibility, $\chi''(\boldsymbol{Q},\omega)$ (units: μ_B^2/eV/Ru) from neutron scattering at $\boldsymbol{Q}=(0.95,0,0)$ and an energy transfer of 2 meV, minus a background at (0.55,0,0). (c) As for (b) at $\boldsymbol{Q}_\delta=(0.75,0,0)$. (d) Fractional magnetoresistance $[\rho(2T)-\rho(0)]/\rho(0)$ measured with current parallel to the magnetic field in the basal plane (Refs. 8,21). The lines serve as guides to the eye.

We have also followed the fluctuations as a function of temperature at an energy transfer of 3.1 meV around $\boldsymbol{Q}_\delta = (0.75,0,0)$ (Fig. 5). At base temperature, the two peaks associated with the incommensurate spin fluctuations are well defined and intense. However, as the temperature is increased, the intensity of the incommensurate peaks falls off, and is replaced by a broad peak of similar intensity around the 2D reciprocal lattice point (1,0,0). This position is not a Bragg peak of either the tetragonal or the orthorhombic cell, so does not give rise to a low-energy acoustic phonon. Hence the peak at (1,0,0) is most likely of magnetic origin. We have confirmed by measurements along $\boldsymbol{c}^*$ that this signal also arises from fluctuations of a bilayer unit. Our findings point to a crossover in the nature of the low-energy magnetic correlations in this material. At high temperatures, 2D ferromagnetic fluctuations dominate the correlations; as the temperature is lowered, instead of converging to a long-lived ferromagnetic state, the system is sidetracked to a different behavior with antiferromagnetic finite frequency 2D excitations.

In Fig. 6, we show that the change with temperature in the nature of magnetic fluctuations is reflected in macroscopic properties. At a temperature ≈ 20 K, there is a peak in the magnetic susceptibility (a), and also in the susceptibility close to a ferromagnetic position measured by neutron scattering (b). The antiferromagnetic fluctuations (c) fall away rapidly with increasing temperature and this is reflected in the change in sign of the longitudinal magnetoresistance (d).[7] It is not clear what causes this dramatic change in magnetic correlations, but it may be related to a loss in *c*-axis electronic coherence, which reveals itself as a steep rise in the c-axis resistivity in this temperature region.[6] It is of interest that in the compound $Ca_{2-x}Sr_xRuO_4$,[22,23] doping with Sr drives the system from an insulating antiferromagnetic state, through a phase with a ferromagnetic instability to a metallic superconducting one. In contrast, in $Sr_3Ru_2O_7$ the competing interactions coexist in the same high-quality stoichiometric samples. In manganite materials the nature of the magnetic fluctuations can also change with temperature;[24] however, the cause in this case is a structural/magnetic transition.

In conclusion, we have observed strong 2D spin fluctuations of the bilayers in $Sr_3Ru_2O_7$ in zero field. At high temperatures these fluctuations are predominantly ferromagnetic in nature, and cross over to incommensurate ones at low temperatures, with wavevectors close to those expected for nesting vectors of the Fermi surface. The characteristic energy of these fluctuations is small (compared with the sister compound Sr_2RuO_4), and their ambivalent nature suggests that they are implicated in and related to the metamagnetic transition observed at low temperatures. We note that a strong temperature dependence of the electronic properties and magnetic excitations is also observed in high-T_c superconductors[25] and heavy fermion systems.[26] Thus the behavior of $Sr_3Ru_2O_7$ may ultimately be related to its proximity to a quantum critical point.[12]

*Present address: FKF, Max Planck Institute, Stuttgart, D-70569, Germany; Email address: l.capogna@fkf.mpg.de
†Email address: e.m.forgan@bham.ac.uk
‡Present address: Electrotechnical Laboratory, Tsukuba, Ibara 305-8568, Japan.

[1] Y. Maeno *et al.*, Nature (London) **372**, 532 (1994).
[2] R. J. Cava *et al.*, J. Solid State Chem. **116**, 141 (1995).
[3] Y. Sidis *et al.*, Phys. Rev. Lett. **83**, 3320 (1999).
[4] F. Servant *et al.*, Solid State Commun. **116**, 489 (2000).
[5] S. Ikeda *et al.*, Phys. Rev. B **57**, 978 (1998).
[6] S. Ikeda *et al.*, Phys. Rev. B **62**, 6089 (2000).
[7] Y. Liu *et al.*, Phys. Rev. B **63**, 174435 (2001).
[8] R. S. Perry *et al.*, Phys. Rev. Lett. **86**, 2661 (2001).
[9] C. May *et al.* (unpublished).
[10] G. Cao *et al.*, Phys. Rev. B **55**, R672 (1997).
[11] L. Capogna *et al.*, Phys. Rev. Lett. **88**, 076602 (2002).
[12] S. Grigera *et al.*, Science **294**, 329 (2001).
[13] H. Shaked *et al.*, J. Solid State Chem. **154**, 361 (2000).
[14] D. J. Singh and I. I. Mazin, Phys. Rev. B **63**, 165101 (2001).
[15] *International Tables for Crystallography*, edited by A. J. C. Wilson and E. Prince (Kluwer, Dordrecht, 1999), Vol. C, p. 455.
[16] I. Hase and Y. Nishihara, J. Phys. Soc. Jpn. **66**, 3517 (1997).
[17] M. Sato *et al.*, Phys. Rev. Lett. **61**, 1317 (1988).
[18] L. Capogna *et al.*, Appl. Phys. A, ICNS supplement (Munich 2001).
[19] Q. Huang *et al.*, Phys. Rev. B **58**, 8515 (1998).
[20] S.M. Hayden *et al.*, Phys. Rev. Lett. **84**, 999 (2000).
[21] R. S. Perry, Ph.D thesis, University of Birmingham, 2001.
[22] S. Nakatsuji and Y. Maeno, Phys. Rev. Lett. **84**, 2666 (2000).
[23] O. Friedt *et al.*, Phys. Rev. B **63**, 174432 (2001).
[24] W. Bao *et al.*, Phys. Rev. Lett. **78**, 543 (1997).
[25] G. Aeppli *et al.*, Science **278**, 1432 (1997).
[26] G. Aeppli *et al.*, Phys. Rev. Lett. **60**, 615 (1988).

Triangular to Square Flux Lattice Phase Transition in $YBa_2Cu_3O_7$

S. P. Brown,[1,*] D. Charalambous,[1] E. C. Jones,[1] E. M. Forgan,[1] P. G. Kealey,[1] A. Erb,[2] and J. Kohlbrecher[3]

[1]*School of Physics and Astronomy, University of Birmingham, Birmingham B15 2TT, United Kingdom*

[2]*Walther-Meissner Institut, Garching D-85748, Germany*

[3]*Paul Scherrer Institut, Villigen PSI, CH 5232, Switzerland*

(Received 21 August 2003; published 10 February 2004)

We have used the technique of small-angle neutron scattering to observe magnetic flux lines directly in a $YBa_2Cu_3O_7$ single crystal at fields higher than previously reported. For field directions close to perpendicular to the CuO_2 planes, we find that the flux lattice structure changes smoothly from a distorted triangular coordination to nearly perfectly square as the magnetic induction approaches 11 T. The orientation of the square flux lattice is as expected from recent *d*-wave theories but is 45° from that recently observed in $La_{1.83}Sr_{0.17}CuO_{4+\delta}$.

DOI: 10.1103/PhysRevLett.92.067004 PACS numbers: 74.25.Qt, 61.12.Ex, 74.20.Rp, 74.72.Bk

The technique of small-angle neutron scattering (SANS) from flux lines has a long and honorable record in measuring the properties of flux lines in superconductors. However, it continues to bring new dividends, especially in unconventional superconductors, since important information about the nature of the superconducting state is often revealed by the flux line lattice (FLL) structure, for example [1–4]. The diffraction pattern not only reveals the coordination and perfection of the FLL, and its correlation with the crystal lattice, but also the absolute intensity may be used to determine the actual spatial variation of the magnetic field within the mixed state and the values of the coherence length and penetration depth [1,5,6]. In the simplest approximation, flux lines would order in a regular triangular FLL; however, anisotropy of the Fermi surface or of the superconducting order parameter can cause distortions of the triangular lattice or transitions to other structures. The simplest situation in a high-κ material is anisotropy of the magnetic penetration depth associated with effective mass anisotropy [7]; for example, the anisotropy in the *ab* plane of $YBa_2Cu_3O_{7-\delta}$ (YBCO) leads at low values of field to a corresponding distortion of triangular FLLs [8]. At lower values of κ, "nonlocal" effects are expected [9] and observed to give a variety of FLL distortions and transitions in, e.g., the borocarbides [4,10] and V_3Si [11,12]. If the superconducting order parameter has a different symmetry from that of the crystal, this can again be revealed via its effects on the FLL structure, for instance, in the *p*-wave superconductor Sr_2RuO_4 [6,13]. In general in *d*-wave superconductors [14–16], there is expected to be a tendency towards a square FLL as the field is increased and the anisotropic flux line cores overlap. This may be the cause of the FLL phase transition recently observed in overdoped $La_{1.83}Sr_{0.17}CuO_{4+\delta}$ (LSCO) at the comparatively low field of 0.4 T [2]. According to [14,15], the FLL nearest-neighbor directions should lie along the directions of the nodes of the order parameter, which would be at 45° to the Cu-O bonds in the superconducting layers. This is not, however, the orientation of the square FLL observed in LSCO [2]. The *orientation* may instead be controlled by band structure effects [17], even if the *symmetry* of the FLL is controlled by *d*-wave effects. It has been suggested that a peak effect in magnetization measurements on overdoped YBCO may be a signature of a continuous triangular-to-square FLL transition in this material at high fields [18]. However, others have suggested that there is a glass transition in this region [19]. Only by *direct* measurements may such suggestions be tested and the correlation between FLL and crystal lattice (or superconducting order parameter) be determined.

Our experiments were performed on the SANS-I instrument at SINQ, Paul Scherrer Institut, Switzerland. Cold neutrons (8 to 14 Å, with a FWHM wavelength spread of 10%) were collimated over distances from 4.5 to 15 m, depending on the field and hence q range required. The diffracted neutrons were registered on a $128 \times 128 \times 7.5$ mm^2 multidetector, which was similarly adjustable in distance from the sample. The undiffracted main beam was intercepted by a cadmium beamstop. A magnetic field of up to 11 T applied approximately parallel to the neutron beam, was provided by a cryomagnet with a field uniformity of 0.2% over a 1 cm sphere. A variable temperature insert containing He heat exchange gas allowed sample temperatures from 1.5 to 300 K. The sample was a 40 mg low–twin-density (a fully detwinned crystal of this size was not available) high-purity single crystal of YBCO grown in a $BaZrO_3$ crucible [20] and oxygenated close to O_7 by high-pressure oxygen treatment in order to reduce pinning by oxygen vacancies in the Cu-O chains [21]. It was therefore overdoped and had a T_c of 86 K. It was initially mounted with its **c** axis parallel to the field direction. In order to satisfy the Bragg condition for each diffraction spot in turn and hence establish the FLL structure, the cryomagnet and sample together

could be rotated or tilted to bring the FLL Bragg planes to the appropriate small angles ($\sim 1°$) to the incident neutron beam.

In Fig. 1 is shown the FLL diffraction pattern obtained at the low field of 1 T. The most obvious feature of this pattern is its fourfold symmetry which reflects the average fourfold symmetry of the twinned orthorhombic structure of our YBCO sample. However, the FLL structure itself has *triangular* coordination, and the symmetry of Fig. 1 arises from four orientations of distorted triangular FLLs, present in different domains in the sample, as was first observed by Keimer *et al.* [22]. The diffraction spots arising from these four triangular lattices are represented in Fig. 2. It appears that the *distortion* of the individual lattices arises mainly from the a/b anisotropy present in each orthorhombic domain in the crystal [23,24]. This interpretation was confirmed by measurements on an untwinned sample [8] which show diffraction spots distributed around an *ellipse* aligned with the **a** and **b** axes. The ratio of the principal axes of the ellipse should represent the anisotropy of the London penetration depth for $B_{c1} \ll B \ll B_{c2}$ [7]. The value we observe for the anisotropy ratio, γ_{ab}, in our sample is 1.28(1), whereas many estimates of this quantity are rather larger [25]. However, comparable values to ours were obtained by measurements on a separate untwinned sample using neutrons [8] and muons and torque magnetometry [26]. Our results are also corroborated by recent surface-sensitive measurements using a novel atomic-beam magnetic-resonance technique [27]. It seems likely that the precise value of γ_{ab} depends on the degree of perfection of the Cu-O chains along the **b** direction [28]. The *orientation* of the triangular FLLs has been ascribed to pinning of a pair of spots, and hence planes of flux lines, to the twin planes [23,24]. However, results reported later in this Letter also support the existence of a correlation between the nearest-neighbor FLL directions and the directions of zeros of the *d*-wave order parameter.

In Fig. 3, we show diffraction patterns taken at higher fields. The data taken at 7 T show a distortion of the triangular FLLs so that some of the weaker spots are closer to the strong spots, and others have moved towards the diagonals. There is clearly another source of distortion than pure a/b anisotropy. Finally at 11 T, the FLL has become almost exactly square, with the weak corner spots now playing the role of second order $\{1, 1\}$ spots of a square FLL instead of first order spots from a distorted triangular FLL. In order to investigate this steady change in the FLL structure with field, we rotated the crystal about the vertical axis in Fig. 3, so that the field was 5° from the **c** axis. This was done in order to break the degeneracy between those FLL structures giving strong vertical diffraction spots [Figs. 2(a) and 2(c)], and those giving strong horizontal spots [Figs. 2(b) and 2(d)]. Within anisotropic London theory, this small angle of rotation should make a negligible change to the FLL distortion. As shown in Fig. 4, we found that at high fields the FLL structures giving horizontal spots were suppressed and instead only the structures depicted in Figs. 2(a) and 2(c) were observed. The advantage of this

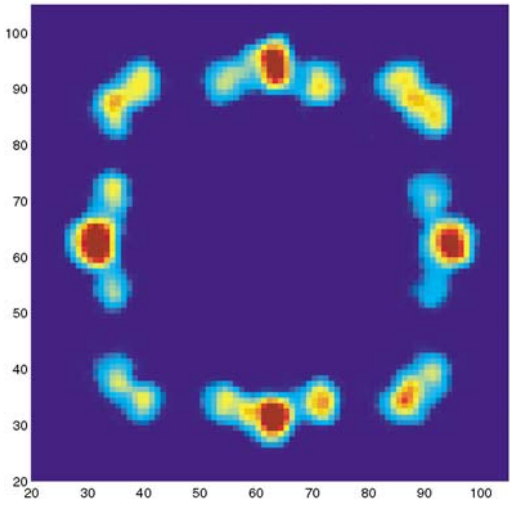

FIG. 1 (color). FLL diffraction pattern at 1 T. The figure shows the counts on the SANS multidetector at 4 K (minus backgrounds obtained above T_c) summed over a range of angles between the field direction and the neutron beam. Noise at the center of the picture has been masked. The cryostat was rocked by $\pm 1°$ about horizontal and vertical axes, ensuring that all spots in the diffraction pattern from the sample are detected. The {110} directions, corresponding to twin plane directions, are vertical and horizontal in this picture. In all cases, the FLL was formed by applying the field above T_c and cooling.

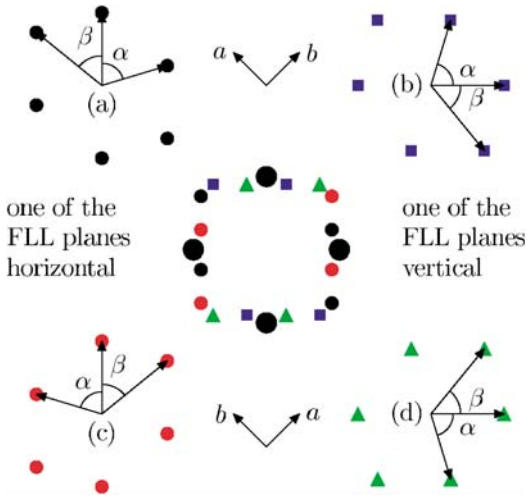

FIG. 2 (color). Schematic of diffraction patterns from four distorted triangular FLLs that together account for the pattern in Fig. 1. In each orthorhombic domain in the twinned crystal, there are two orientations of FLL [e.g., (a) and (b)], derived by taking a regular hexagonal pattern and distorting it by the a/b anisotropy [7]. The more intense pair of spots in each pattern is aligned with one of the {110} directions. The center figure is the superposition of the four FLL domains (a), (b), (c), and (d), which gives rise to the pattern in Fig. 1. The angles between reciprocal lattice vectors, α and β, are defined for use in Fig. 5.

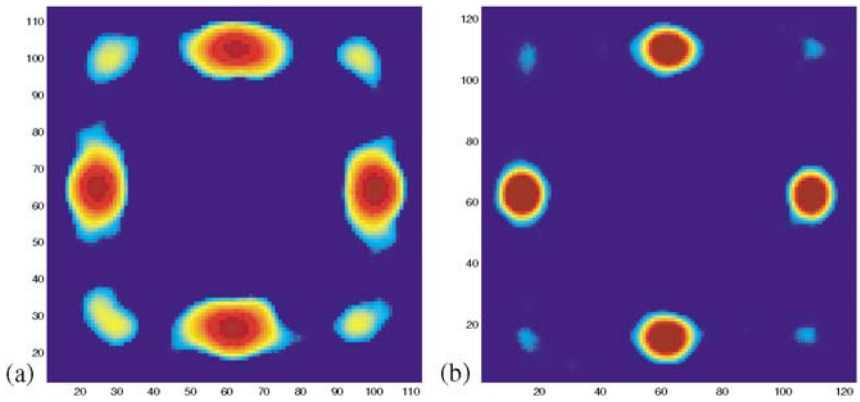

FIG. 3 (color). FLL diffraction patterns, as in Fig. 1 (but with a logarithmic intensity scale and smoothed to make the weaker spots more clearly visible), (a) at $B = 7$ T, (b) at $B = 11$ T, showing the change in position of the weaker spots as the field is increased.

arrangement is that the pairs of spots *near* the horizontal axis in Fig. 4 could be observed easily, without being overlaid by the strong ones *on* the axis. This allowed us to measure accurately the spot positions and hence the FLL distortion. Nevertheless, at high field, this pair of spots overlaps, but by assuming that the spot size is independent of field, we may estimate the angle between them even when they overlap. Further measurements of spot positions allow us to give a complete description of the FLL distortions versus field in terms of the angles between the FLL reciprocal lattice vectors. The results of this analysis are shown in Fig. 5. It is clear that the low field structure progressively changes with increase of field, although in our available field range the FLL never exactly reaches a perfectly square shape. This may partly be because the phase transition is at the extreme of our available field range, but it is also clearly a result of the orthorhombic structure of YBCO. As depicted in the inset to Fig. 5, the a/b anisotropy of each domain must, on symmetry grounds, distort a square lattice to a rectangular one, causing a slight splitting of the "square" spots from a twinned crystal such as ours.

We have further investigated [29] the temperature dependence of the FLL distortion shown in Fig. 5. We find that with increasing temperature, the FLL structure changes more towards triangular. Thus the boundary between square and triangular phases must curve up in field as temperature is increased. We would expect this if the triangular to square transition is due to d-wave effects, as the nature of the pairing becomes less important as $k_B T$ becomes comparable with the magnitude of the gap. The shape of the phase boundary is similar to that seen in an overdoped sample by macroscopic measurements [19], but not the same as that proposed in Ref. [18]. Unlike LSCO [2], the *orientation* of the FLL that we observe is aligned as expected from d-wave theories [15,16]. It may be argued that twin planes, which are present in LSCO and YBCO are controlling the FLL orientation. To rule this out, measurements were also taken with the field at an angle to both sets of twin planes in our sample and the shape and orientation of the FLL was essentially unchanged. One should also note that the predicted difference in free energy between the two orientations of a square FLL is much larger than that between any triangular and the lower energy square orientation [15]. We also note that a similar correlation between FLL orientation and probable direction of d-wave nodes has recently also been observed in $CeCoIn_5$ [30]. Further

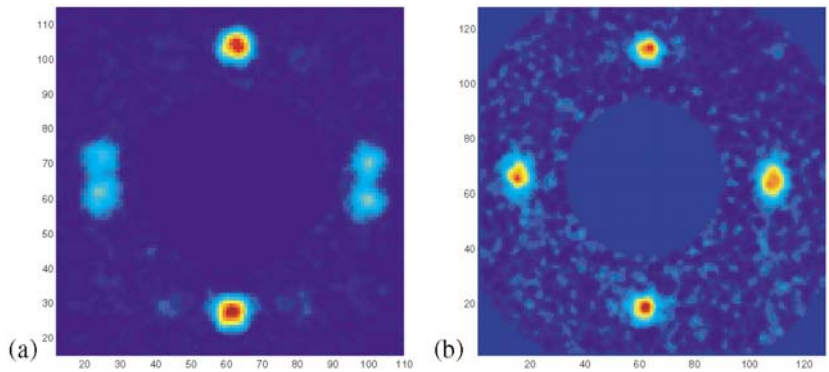

FIG. 4 (color). FLL diffraction patterns with the field rotated 5° from the **c** axis, to give only two FLL domains: (a) at $B = 7$ T and (b) at $B = 10.8$ T.

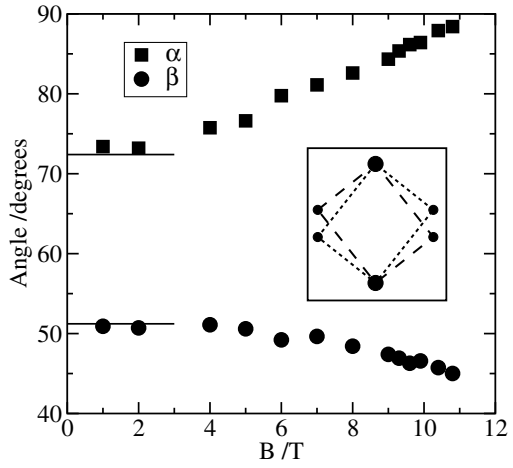

FIG. 5. Field variation at 5 K of two of the angles between reciprocal lattice vectors, α and β, depicted in Fig. 2. (Errors are comparable with the marker size.) All data were obtained with **B** parallel to the crystal **c** axis except the data for α at fields greater than 6 T, which were taken with **B** at 5° to **c** in order to resolve this angle more clearly (see text). A *regular* hexagonal lattice would have $\alpha = \beta = 60°$, and an exactly square one $\alpha = 90°$ and $\beta = 45°$. Also marked by horizontal lines are predictions of anisotropic London theory [7] for α and β, using a basal plane anisotropy, $\gamma_{ab} = 1.28$, and assuming that one pair of spots is tied to the {110} directions. In the inset is shown the orthorhombic distortion from an exactly square pattern (exaggerated for clarity), expected in the two orthorhombic domains present in our crystal.

support of the *d*-wave origin of the triangular-square transition in YBCO is the value of the transition field, which is a similar order of magnitude to the predicted $0.15B_{c2}$ [15]. It should also be noted that a triangular to square transition in the FLL is predicted by the nonlocal London theory of Kogan *et al.* [9], in which an isotropic *s*-wave gap is assumed and is therefore not directly applicable to the FLL in YBCO. Furthermore, in a *d*-wave superconductor *s*-wave components of the order parameter are induced near the vortex core, resulting in a four-lobe structure [31] that cannot be predicted from Fermi surface anisotropy alone. Nevertheless, nonlocal and *d*-wave origins of the triangular to square transition are clearly related, since both result in core anisotropy, which becomes more important for intervortex interactions with increasing field. Finally, we note that our *bulk* observations of FLL structure are not in complete agreement with surface measurements by STM techniques [32,33].

In conclusion, using small-angle neutron scattering, we have directly observed a change from triangular to square coordination of the flux line lattice as a function of magnetic field in fully oxygenated $YBa_2Cu_3O_7$. This phase transition is most naturally interpreted as a consequence of the *d*-wave character of the order parameter, which is expected to be more prominent at high magnetic fields, where the flux line cores begin to overlap. The *orientation* of the FLL, with nearest neighbors along nodal directions is as expected from *d*-wave theory [15,16], unlike that in LSCO [2]. It appears that further investigation of these phenomena will allow stringent tests of theories of the order parameter in the mixed state of high-T_c materials as a function of angle of field and doping.

This work was performed at the Swiss Spallation Neutron-Source SINQ, Paul Scherrer Institut (PSI), Villigen, Switzerland. We acknowledge financial support from the UK EPSRC, from H. Keller (University of Zürich), from PSI, from the University of Birmingham, and from the University of Warwick.

*Electronic address: sp.brown@physics.org

[1] P. G. Kealey *et al.*, Phys. Rev. Lett. **84**, 6094 (2000).
[2] R. Gilardi *et al.*, Phys. Rev. Lett. **88**, 217003 (2002).
[3] A. Huxley *et al.*, Nature (London) **406**, 6792 (2000).
[4] D. McK. Paul *et al.*, Phys. Rev. Lett. **80**, 1517 (1998).
[5] E. M. Forgan *et al.*, Phys. Rev. Lett. **88**, 167003 (2002).
[6] T. M. Riseman *et al.*, Nature (London) **404**, 6778 (2000).
[7] S. L. Thiemann *et al.*, Phys. Rev. B **39**, 11 406 (1989).
[8] S. T. Johnson *et al.*, Phys. Rev. Lett. **82**, 2792 (1999).
[9] V. G. Kogan *et al.*, Phys. Rev. B **55**, R8693 (1997).
[10] Y. DeWilde *et al.*, Phys. Rev. Lett. **78**, 4273 (1997).
[11] M. Yethiraj *et al.*, Phys. Rev. Lett. **82**, 5112 (1999).
[12] C. E. Sosolik *et al.*, Phys. Rev. B **68**, 140503(R) (2003).
[13] D. F. Agterberg, Phys. Rev. Lett. **80**, 5184 (1998).
[14] I. Affleck *et al.*, Phys. Rev. B **55**, R704 (1997).
[15] M. Ichioka *et al.*, J. Phys. Soc. Jpn. **66**, 3928 (1997); M. Ichioka *et al.*, Phys. Rev. B **59**, 8902 (1999).
[16] J. Shiraishi *et al.*, Phys. Rev. B **59**, 4497 (1999).
[17] N. Nakai *et al.*, Phys. Rev. Lett. **89**, 237004 (2002).
[18] B. Rosenstein *et al.*, Phys. Rev. Lett. **83**, 844 (1999).
[19] K. Shibata *et al.*, Phys. Rev. B **66**, 214518 (2002).
[20] A. Erb *et al.*, Physica (Amsterdam) **258C**, 9 (1996).
[21] A. Erb *et al.*, Solid State Commun. **112**, 245 (1999).
[22] B. Keimer *et al.*, Phys. Rev. Lett. **73**, 3459 (1994).
[23] E. M. Forgan *et al.*, Phys. Rev. Lett. **75**, 1422 (1995).
[24] M. B. Walker *et al.*, Phys. Rev. B **52**, 97 (1995).
[25] N. L. Wang *et al.*, Phys. Rev. B **57**, R11 081 (1998); D. N. Basov *et al.*, Phys. Rev. Lett. **74**, 598 (1995); A. G. Sun *et al.*, Phys. Rev. B **52**, R15 731 (1995).
[26] C. Ager *et al.*, Phys. Rev. B **62**, 3528 (2000).
[27] H. Hauglin *et al.*, Phys. Rev. B **67**, 014507 (2003).
[28] J. L. Tallon *et al.*, Phys. Rev. Lett. **74**, 1008 (1995).
[29] S. P. Brown *et al.* (to be published).
[30] M. R. Eskildsen *et al.*, Phys. Rev. Lett. **90**, 187001 (2003).
[31] A. J. Berlinksy *et al.*, Phys. Rev. Lett. **75**, 2200 (1995).
[32] Ø. Fischer *et al.*, Physica (Amsterdam) **282C**, 315 (1997).
[33] K. Shibata *et al.*, Physica (Amsterdam) **388**C, 277 (2003).

Square Vortex Lattice at Anomalously Low Magnetic Fields in Electron-Doped $Nd_{1.85}Ce_{0.15}CuO_4$

R. Gilardi,[1] J. Mesot,[1] S. P. Brown,[2] E. M. Forgan,[2] A. Drew,[3] S. L. Lee,[3] R. Cubitt,[4] C. D. Dewhurst,[4] T. Uefuji,[5] and K. Yamada[5]

[1]*Laboratory for Neutron Scattering, ETH Zurich and PSI Villigen, CH-5232 Villigen PSI, Switzerland*
[2]*School of Physics and Astronomy, University of Birmingham, Birmingham B15 2TT, United Kingdom*
[3]*School of Physics and Astronomy, University of St. Andrews, Fife KY16 9SS, United Kingdom*
[4]*Institut Laue-Langevin, BP 156, F-38042 Grenoble, France*
[5]*Institute for Materials Research, Tohoku University, Sendai 980-8577, Japan*

(Received 18 June 2004; published 15 November 2004)

We report here on the first direct observations of the vortex lattice in the bulk of electron-doped $Nd_{1.85}Ce_{0.15}CuO_4$ single crystals. Using small-angle neutron scattering, we have observed a square vortex lattice with the nearest neighbors oriented at 45° from the Cu-O bond direction, which is consistent with theories based on the *d*-wave superconducting gap. However, the square symmetry persists down to unusually low magnetic fields. Moreover, the diffracted intensity from the vortex lattice is found to decrease rapidly with increasing magnetic field.

DOI: 10.1103/PhysRevLett.93.217001 PACS numbers: 74.25.Qt, 61.12.Ex, 74.20.Rp, 74.72.Jt

It is a matter for debate whether hole-doped and electron-doped high-T_c cuprate superconductors (HTSC) can be described within a unified physical picture [1,2]. Indeed, electron-doped HTSC have markedly different properties from hole-doped HTSC. For example, electron-doped materials have comparatively low values of the superconducting transition temperature, T_c, and much lower values of the upper critical field, B_{c2}. Furthermore, their normal-state resistivity varies as T^2 as expected for a Fermi liquid [3,4], and the presence of a pseudogap is still under discussion [5]. Electron-doped HTSC also appear much closer to long-range antiferromagnetic (AF) order, which can in fact coexist with superconductivity [6–9]. In hole-doped HTSC, the *d*-wave nature of the order parameter is well established [10]. However, the evidence for the symmetry of the superconducting gap in electron-doped materials (which has important implications for the pairing mechanism [2]) is somewhat contradictory. Earlier measurements of the penetration depth [11] and tunneling experiments [12] supported *s*-wave symmetry, whereas a *d*-wave superconducting order parameter is indicated by more recent phase-sensitive [13] and angle resolved photoemission spectroscopy (ARPES) experiments [14,15]. The electron-doped superconductors are of particular interest in this respect, since they have a tetragonal structure (rather than orthorhombic) and therefore should show pure *d*-wave behavior, unaffected by admixture of an *s*-wave component associated with the orthorhombicity [10].

Recently, there has been considerable interest in the nature of the vortex lattice (VL) in unconventional superconductors. For instance, vortex cores in *d*-wave superconductors are predicted to have a distinctive fourfold structure [16–20]. This leads to the expectation that a square VL is formed at high magnetic field, with the nearest-neighbor directions aligned with the nodes of the order parameter. These theoretical predictions are consistent with the small-angle neutron scattering (SANS) observation of a transition from an Abrikosov-like hexagonal VL to a square VL in the hole-doped HTSC $YBa_2Cu_3O_7$ (YBCO) [21]. However, similar measurements on overdoped $La_{2-x}Sr_xCuO_4$ (LSCO) [22] show a square lattice with nearest neighbors oriented at 45° to the nodes of the superconducting order parameter. The orientation of the nodal directions in the heavy-fermion superconductor $CeCoIn_5$ is at present uncertain [23], so it is unclear if the recent SANS observations of the VL in this material [24] confirm theoretical expectations. It is therefore of great interest to gain further information from another class of superconductors, such as the electron-doped HTSC. Moreover, these compounds do not have twin planes present in orthorhombic systems such as YBCO and LSCO. These planar defects with a suppressed order parameter are capable of pinning the VL [25]. Finally, the low values of the upper critical field ($B_{c2} \sim 10$ T compared to $B_{c2} \sim 100$ T in hole-doped HTSC) allow the investigation of the whole magnetic phase diagram.

Only recently could large enough electron-doped crystals be produced, and to our knowledge, a SANS investigation of their VL has not yet been published. We report here the first direct observation of a VL in $Nd_{1.85}Ce_{0.15}CuO_4$ (NCCO). Our SANS experiments (see Ref. [26] for a description of the technique) were performed on the instrument D22 at the Institut Laue-Langevin, France, using neutrons with a wavelength $\lambda_n = 6$–20 Å. Crystals of NCCO were grown in a mirror furnace and annealed as described in Ref. [27] to give an onset $T_c \approx 25$ K ($\Delta T_c \approx 3$ K, 10%–90% criterion). Samples with two shapes were investigated in applied magnetic fields up to 0.4 T. In high fields, a cylinder of 5 mm diameter, consisting of two nearly aligned crystals,

was mounted in a cryostat with the magnetic field direction bisecting the two **c** directions and at 7° to each of them. Single crystal plates of ~1.5 mm thickness were used at low fields: this required a long neutron wavelength and the smaller thickness reduced the effects of neutron absorption in the sample. They were mounted so that the **c** direction was within ~2° of the applied field, which was approximately parallel to the incident beam. There were no significant differences in the VL diffraction patterns obtained from different samples in measurements at the same field.

In Fig. 1 we show the VL diffraction patterns obtained at various magnetic fields. A background measured above T_c has been subtracted because the VL signal is extremely weak (~0.013% of the total detector counts at 50 mT). For magnetic fields larger than 50 mT, the VL clearly has square coordination. The nearest-neighbor directions are parallel to the {110} crystal directions, which correspond to the nodes of the superconducting order parameter, in agreement with predictions for *d*-wave HTSC [16–20]. Further evidence for a square VL is given by the positions of the Bragg spots in reciprocal space. For first-order diffraction, the relationship between the magnitude q of the wave vector and the magnetic field B is given by flux quantization:

$$q = 2\pi\sqrt{\frac{B}{\sigma\Phi_0}}, \tag{1}$$

where σ is equal to 1 or $\sqrt{3}/2$ for square and hexagonal lattices, respectively, and Φ_0 is the flux quantum. q can be obtained by fitting the tangential sum of the neutron signal with a Gaussian, as shown in Fig. 2. As expected, the position of the peak shifts to higher q with increasing magnetic field (confirming the VL origin of the neutron signal), and the extracted values of σ are consistent with a square VL at *all* fields measured (see the inset to Fig. 2 for the lower fields). We have confirmed by magnetization measurements that the value of the trapped flux at low fields is within ~1% of the applied field. Hence, flux expulsion has an insignificant effect on the value of the q vector.

As shown in Fig. 1, the VL orientation is not perfect at any field. However, the orientation becomes rather more disordered as the field is decreased below 50 mT and at 20 mT the intensity distribution becomes ringlike. A similar distribution of intensity at low magnetic fields has been observed in LSCO [22] and was attributed to the superposition of diffraction patterns from various domain orientations of *hexagonal* coordination, since the value of σ at low fields was consistent with that of a hexagonal VL. Moreover, by rotating the **c** axis 10° away from the field direction, the degeneracy of the VL system could be reduced, and the hexagonal coordination of the VL in LSCO was confirmed. In NCCO, on the contrary, the values of σ at low magnetic fields are still consistent with that of a square VL, and measurements at 20 mT with the **c** axis rotated away from the field direction caused little change in the pattern. The effects of rotating of the field away from the **c** axis at 50 mT are shown in Fig. 3. At 20° little change is observed, whereas at 30° the pattern becomes rather disordered and the scattered intensity lies on an ellipse as expected from the uniaxial anisotropy of the crystal. However, the average value of σ is unchanged. It is surprising that the vortex lattice maintains square coordination without being aligned to the crystal lattice.

In addition to the *d*-wave scenario for square VL coordination, one should also consider the effects of Fermi surface anisotropy. An appropriate theory for large-κ materials well below B_{c2} is London theory with nonlocal corrections [28], which has been extensively used to account for VL phase transitions in the borocarbides

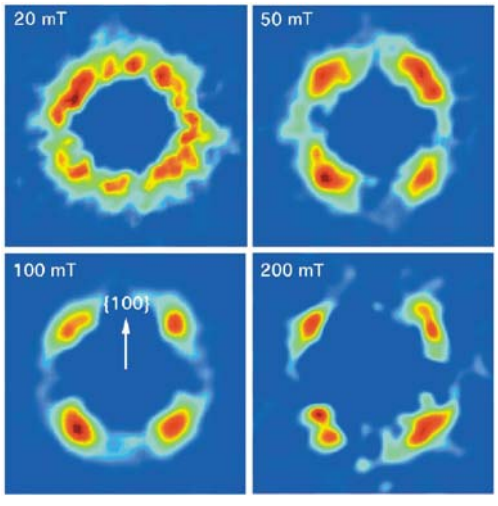

FIG. 1 (color). SANS diffraction patterns measured at $T \approx 2.5$ K, after field cooling from 30 K in $B = 20$, 50, 100, and 200 mT. A background taken at $T = 30$ K has been subtracted. The {100} directions, corresponding to the Cu-O bond directions in the CuO_2 planes, are oriented vertically or horizontally in the pictures.

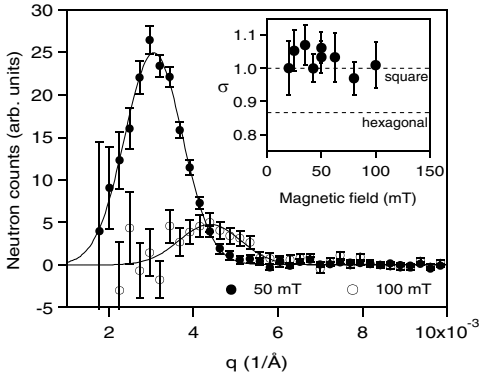

FIG. 2. Tangential sum of the neutron signal vs wave vector q for $B = 50$ and 100 mT at $T \approx 2.5$ K. Inset: field dependence of the coordination-dependent quantity σ [see Eq. (1)] at low fields; the horizontal lines indicate the expected values for hexagonal and square VL.

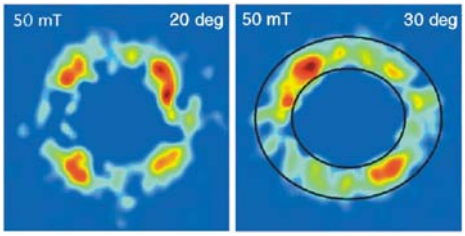

FIG. 3 (color). SANS diffraction patterns at $B = 50$ mT taken as in Fig. 1 but with the **c** direction rotated about the vertical axis by 20° and 30° to the field direction. The growth direction and long axis of the sample lay 15° counterclockwise to the vertical and may be associated with the stronger intensity in these quadrants. The ellipses drawn have an axial ratio of cos(30°).

[29,30]. If both these effects are present [31], we would expect the strong angular variation of the d-wave gap to dominate over the usually smaller variation of the Fermi velocity. ARPES experiments together with band structure calculations [32] indicate that NCCO and YBCO both have nearly isotropic holelike Fermi surfaces with a slight fourfold distortion oriented so as to favor the observed square VL orientation. In overdoped LSCO, on the other hand, the Fermi surface is electronlike [33,34] with a square shape oriented at 45° to that of the other two compounds. Moreover LSCO exhibits a pronounced anisotropy in the Fermi velocity. Both the shape of the Fermi surface and the Fermi velocity anisotropy would indicate (via nonlocal effects) the VL orientation actually observed in LSCO [22].

However, both d-wave and nonlocal effects should be important only at fields which are a substantial fraction of B_{c2}, when the intervortex spacing is comparable to the coherence length. For instance, d-wave calculations indicate that the square symmetry has lower free energy than the hexagonal one at applied fields greater than $0.15B_{c2} \approx 1.2$ T [19], or than $B_{c2}/\kappa \approx 0.4$ T [20] (taking the values of $B_{c2} \approx 8$ T [35], penetration depth $\lambda_L \approx 1250$ Å [36], and coherence length $\xi \approx 60$ Å [35], therefore $\kappa = \lambda_L/\xi \approx 20$). Although the characteristic fields in electron-doped HTSC are generally lower than in the hole-doped materials, these estimates are too large to explain our results. Hence, our observation of a square VL in NCCO down to very low magnetic fields is rather surprising, unless another source of anisotropy in the CuO_2 planes is present. One candidate for this is the Cu antiferromagnetic correlations, whose characteristic wave vector [7] coincides in direction with the VL reciprocal lattice wave vector.

Another matter of great interest is the variation of the diffracted intensity with field. The intensity I_{hk} of a single (h, k) reflection (integrated over the rocking curve of the VL) is given by [37]

$$I_{hk} = 2\pi\phi\left(\frac{\mu}{4}\right)^2 \frac{V\lambda_n^2}{\Phi_0^2 q_{hk}} |F_{hk}|^2 \propto \frac{|F_{hk}|^2}{q_{hk}}, \qquad (2)$$

where ϕ is the incident neutron flux, μ is the neutron magnetic moment, V is the sample volume, and q_{hk} is the (h, k) reciprocal lattice vector. F_{hk} is the "form factor" of the (h, k) reflection. It is a Fourier component of the spatial variation of the magnetic field, and in the London limit is related to the penetration length λ_L by

$$F_{hk} = \frac{B}{1 + (q_{hk}\lambda_L)^2}. \qquad (3)$$

For $B_{c1} \ll B \ll B_{c2}$, the second term in the denominator is dominant and this gives $I_{hk} \propto q_{hk}^{-1} \propto B^{-1/2}$. In our NCCO samples, the rocking curves of the VL diffracted intensity were found to be flat, over a range of ±4°, within experimental error. The expected width of the rocking curves can be estimated using Eqs. (2) and (3) and the value of λ_L quoted in Ref. [36]. At 50 mT we obtain a width larger than 10°, consistent with our experimental observations. We therefore measured the intensity as a function of field at a fixed sample angle. Assuming that the rocking curve width remains constant with field, the measured intensity is proportional to the integrated intensity. In contrast with the London prediction, we observe a strong field dependence of the scattered intensity (see Figs. 2 and 4), which becomes immeasurably small above $B \approx 0.4$ T, which is well below B_{c2}. If represented by a power law, this variation has an exponent of about −2. (If the rocking curve becomes narrower with increasing field, then the field dependence of the VL intensity becomes even more rapid and more difficult to interpret. A broadening of the rocking curve as a function of increasing field would be consistent with increasing disorder as discussed below.)

We consider two possible intrinsic reasons for the fast decrease of the VL intensity with field. One is the effect of the finite size of the vortex core, which will lead to deviations from the London predictions at large values of the wave vector q. This effect can be modeled by a calculation using Ginzburg-Landau theory [38], giving an algebraic expression for the correction to the

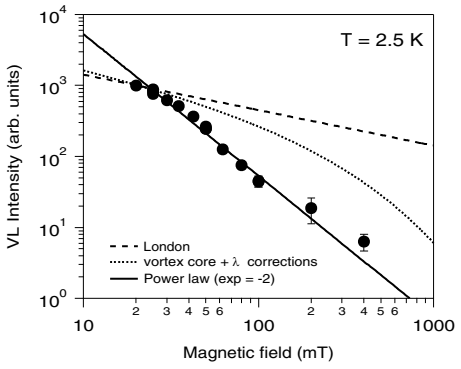

FIG. 4. VL intensity measured at $T \approx 2.5$ K as a function of magnetic field. The dotted line is the expected field dependence taking into account core effects and field dependence of the penetration depth (see the text).

form factor: $\exp(-\sqrt{2}q\xi)$, which may also be written as $\exp[-2(\pi B/B_{c2})^{1/2}]$. In addition, there is expected to be a specifically d-wave effect—an increase of the penetration depth with field [39]. Muon spin rotation (μSR) measurements in YBCO indicate that the variation of λ with B is linear at low fields ($B < 2$ T) [40]:

$$\frac{\lambda(B)}{\lambda(0)} = 1 + \beta\frac{B}{B_0}, \tag{4}$$

where β is a temperature-dependent coefficient that remains finite at $T = 0$ K, and B_0 is a characteristic field on the order of the thermodynamic critical field B_c. If we assume that a similar linear dependence of $\lambda(B)$ is valid for NCCO, and include the core-size effects as well, we can model the variation of the VL intensity with field:

$$I_{hk} \sim B^{-1/2}\left(1 + \beta\frac{B}{B_0}\right)^{-4}\exp[-4(\pi B/B_{c2})^{1/2}]. \tag{5}$$

For NCCO we used $\beta = 7 \times 10^{-2}$ (as for YBCO) and $B_0 \sim B_{c2}/\sqrt{2}\kappa = 0.28$ T. As can be seen in Fig. 4, we cannot represent the strong field dependence of our experimental data by these intrinsic effects. It may be that an enhancement of AF correlations by the applied field [6] is reducing the superfluid density. However, we find that even doubling β and the exponential prefactor does not reproduce our results. The rapid decrease of the VL intensity is more likely to be due to a transition to a more disordered vortex system, as has been predicted theoretically [41] and associated with a second peak in magnetization measurements [42]. SANS experiments in the isotropic (K, Ba)BiO_3 system [43] revealed a similar rapid loss of diffracted intensity near the second peak. In hole-doped $Bi_{2.15}Sr_{1.95}CaCu_2O_{8+x}$, a strong decrease of the VL intensity with increasing field was attributed to a crossover from a 3D to a 2D vortex system [44]. In NCCO, however, such a dimensional crossover is expected to occur at a much higher magnetic field $B_{2D} = \Phi_0/(\gamma s)^2 \sim 13$ T ($> B_{c2}$), where $s \sim 6$ Å is the distance between CuO_2 planes and $\gamma \sim 21$ [3] is the anisotropy. In this respect, NCCO seems to be similar to underdoped LSCO [45], in which μSR measurements have given clear evidence of a field-induced crossover to a more disordered, but still three-dimensional VL.

In conclusion, we have made the first direct observation of the VL in the electron-doped NCCO, which is the first tetragonal HTSC to be investigated by SANS. Contrary to theoretical expectations, the VL remains square down to very small fractions of B_{c2}. In addition, we have observed an unusually fast decrease of the VL intensity with increasing magnetic field, which is probably due to a crossover to a more disordered vortex state.

This work was supported by the Swiss National Science Foundation, by the Engineering and Physical Sciences Research Council of the U.K., and by the Ministry of Education and Science of Japan.

[1] N.-C. Yeh and C.-T. Chen, Int. J. Mod. Phys. B **17**, 3575 (2003).
[2] D. Manske *et al.*, Phys. Rev. B **62**, 13 922 (2000).
[3] Y. Hidaka and M. Suzuki, Nature (London) **338**, 635 (1989).
[4] C. C. Tsuei *et al.*, Physica (Amsterdam) **161C**, 415 (1989).
[5] L. Alff *et al.*, Nature (London) **422**, 698 (2003).
[6] H. J. Kang *et al.*, Nature (London) **423**, 522 (2003).
[7] K. Yamada *et al.*, Phys. Rev. Lett. **90**, 137004 (2003).
[8] M. Fujita *et al.*, Phys. Rev. B **67**, 014514 (2003).
[9] T. Uefuji *et al.*, Physica (Amsterdam) **357C–360C**, 208 (2001).
[10] C. C. Tsuei and J. R. Kirtley, Rev. Mod. Phys. **72**, 969 (2000), and references therein.
[11] D. H. Wu *et al.*, Phys. Rev. Lett. **70**, 85 (1993).
[12] S. Kashiwaya *et al.*, Phys. Rev. B **57**, 8680 (1998).
[13] C. C. Tsuei and J. R. Kirtley, Phys. Rev. Lett. **85**, 182 (2000).
[14] T. Sato *et al.*, Science **291**, 1517 (2001).
[15] N. P. Armitage *et al.*, Phys. Rev. Lett. **86**, 1126 (2001).
[16] A. J. Berlinsky *et al.*, Phys. Rev. Lett. **75**, 2200 (1995).
[17] M. Franz *et al.*, Phys. Rev. Lett. **79**, 1555 (1997).
[18] I. Affleck *et al.*, Phys. Rev. B **55**, R704 (1997).
[19] M. Ichioka *et al.*, Phys. Rev. B **59**, 8902 (1999).
[20] J. Shiraishi *et al.*, Phys. Rev. B **59**, 4497 (1999).
[21] S. P. Brown *et al.*, Phys. Rev. Lett. **92**, 067004 (2004).
[22] R. Gilardi *et al.*, Phys. Rev. Lett. **88**, 217003 (2002); Int. J. Mod. Phys. B **17**, 3411 (2003); Physica (Amsterdam) **408C–410C**, 491 (2004).
[23] H. Aoki *et al.*, J. Phys. Condens. Matter **16**, L13 (2004).
[24] M. R. Eskildsen *et al.*, Phys. Rev. Lett. **90**, 187001 (2003).
[25] M. Yethiraj *et al.*, Phys. Rev. Lett. **70**, 857 (1993).
[26] E.M. Forgan, in *Neutron Scattering in Layered Copper-Oxide Superconductors*, edited by A. Furrer (Kluwer, Dordrecht, 1998), p. 375.
[27] K. Kurahashi *et al.*, J. Phys. Soc. Jpn. **71**, 910 (2002).
[28] V. G. Kogan *et al.*, Phys. Rev. B **55**, R8693 (1997).
[29] M. R. Eskildsen *et al.*, Phys. Rev. Lett. **86**, 5148 (2001).
[30] S. J. Levett, C. D. Dewhurst, and D. McK. Paul, Phys. Rev. B **66**, 014515 (2002).
[31] N. Nakai *et al.*, Phys. Rev. Lett. **89**, 237004 (2002).
[32] A. Damascelli, Z. Hussain, and Z.-X. Shen, Rev. Mod. Phys. **75**, 473 (2003), and references therein.
[33] T. Yoshida *et al.*, Phys. Rev. B **63**, 220501(R) (2001).
[34] A. Ino *et al.*, Phys. Rev. B **65**, 094504 (2002).
[35] J. Herrmann *et al.*, Phys. Rev. B **54**, 3610 (1996).
[36] S. M. Anlage *et al.*, Phys. Rev. B **50**, 523 (1994).
[37] D. K. Christen *et al.*, Phys. Rev. B **15**, 4506 (1977).
[38] A. Yaouanc, P. Dalmas de Reotier, and E. H. Brandt, Phys. Rev. B **55**, 11 107 (1997).
[39] M. H. S. Amin, I. Affleck, and M. Franz, Phys. Rev. B **58**, 5848 (1998); Phys. Rev. Lett. **84**, 5864 (2000).
[40] J. E. Sonier *et al.*, Phys. Rev. B **55**, 11 789 (1997).
[41] T. Giamarchi and P. Le Doussal, Phys. Rev. B **55**, 6577 (1997).
[42] D. Giller *et al.*, Phys. Rev. Lett. **79**, 2542 (1997).
[43] I. Joumard *et al.*, Phys. Rev. Lett. **82**, 4930 (1999).
[44] R. Cubitt *et al.*, Nature (London) **365**, 407 (1993).
[45] U. K. Divakar *et al.*, Phys. Rev. Lett. **92**, 237004 (2004).

Driven vortices in type-II superconductors: a muon spin rotation study

D. Charalambous,* E.M. Forgan, S. Ramos, S.P. Brown, R.J. Lycett, and D.H. Ucko†
School of Physics & Astronomy, University of Birmingham, Birmingham B15 2TT, United Kingdom

A.J. Drew and S.L. Lee
School of Physics & Astronomy, University of St. Andrews, St. Andrews, Fife, KY16 9SS, United Kingdom

D. Fort
School of Metallurgy & Materials, University of Birmingham, Birmingham B15 2TT, United Kingdom

A. Amato and U. Zimmerman
Paul Scherrer Institut, CH-5232 Villigen PSI, Switzerland
(Dated: September 8, 2005)

We present a detailed study of vortex motion in a type-II superconductor using the muon spin rotation (μSR) technique. The vortices were set in motion by an alternating transport current. By adjusting the frequency and amplitude of the driving force so that vortices 'visible' to the implanted muons did not cross the sample boundaries, a μSR lineshape was obtained corresponding to almost perfectly-ordered vortex motion. We also observed sidebands to the μSR lineshape which correspond to the frequency at which vortices pass the implanted muon, and allow a direct measurement of the vortex velocity. Both these features of the lineshape confirm numerical predictions reported in a previous study (see Charalambous *et al.*, Phys. Rev. B **66** (2002), art. no. 054506).

PACS numbers: 74.25.Qt, 74.25.Fy, 74.70.Ad, 76.75.+i

I. INTRODUCTION

It is well known that when a transport current is applied to a type-II superconductor in the mixed state, individual vortex lines experience a Lorentz force $\boldsymbol{F}_{\rm L}$ per unit volume given by [1]

$$\boldsymbol{F}_{\rm L} = \boldsymbol{J} \wedge \boldsymbol{B}, \tag{1}$$

where $\boldsymbol{J}$ is the applied current density and $\boldsymbol{B}$ is the magnetic induction in the superconductor. The vortices are normally pinned by quenched disorder (*e.g.* material defects such as grain boundaries, dislocations, second phase particles, roughness of the sample surfaces, *etc*) but when $\boldsymbol{F}_{\rm L}$ exceeds the pinning force, the vortex lines are set in motion with an average velocity $\boldsymbol{v}$. Moving vortices give rise to an electric field [2]

$$\boldsymbol{E} = \boldsymbol{v} \wedge \boldsymbol{B}, \tag{2}$$

and hence energy dissipation occurs. This is due to the relaxation of the order parameter as well as due to normal currents in the vortex core [3–5].

As an intriguing example of non-equilibrium physics, systems of moving vortices have attracted much attention from both experimentalists and theorists [6–13] . Their dynamic properties are governed by an interplay between disorder, thermal fluctuations and driving force, as well as applied magnetic field, temperature and dimensionality. Furthermore, from a technological point of view, a detailed understanding of vortex motion is crucial for the design and manufacture of superconductors to be used in various applications, since vortex motion-induced energy dissipation is one of the main factors which limit the range of applicability of these materials [14].

It is now well established that the moving vortex system is more ordered than it is in the pinned state: theoretical and computational investigations predicted a variety of dynamic phases [6–9, 15] all of which are consistent with the moving vortex system exhibiting orientational ordering compared to the static, pinned case. Recent small-angle neutron scattering (SANS) experiments on low-temperature Pb-alloy superconductors [10–12, 16] show the ordering of the vortex system in the flux flow state, which manifests itself as six Bragg peaks in the structure factor, arranged in a hexagonal pattern. The vortex nearest-neighbor direction tends to lie parallel to the direction of vortex motion; however, the moving vortex system does not form a perfect crystal, as can be seen by careful measurement of the transverse width of the Bragg peaks.

In this paper is presented a detailed experimental and theoretical investigation of vortex motion in type-II superconductors using muon spin rotation (μSR). In a previous study [17], vortex motion was induced by the application of a pulsed, unidirectional driving force and it was found that the moving vortex system exhibited a significant amount of disorder. In the present work, we have studied the effects of an alternating driving force,

*Present address: Department of Physics, Lancaster University, Lancaster LA1 4YB, U.K.; Electronic address: demetris.c@physics.org
†Present address: PR/PRL Editorial Offices, One Research Road, Box 9000, Ridge, NY 11961-9000, USA

and we find that this tends to cause a greater degree of dynamic ordering of the vortex lines. The ordering shows a dependence on the frequency and amplitude of the alternating force, which suggests that a significant part of the disordering observed in our previous unidirectional study resulted from vortex lines crossing the sample boundaries, and the disorder is therefore not an intrinsic property of the moving vortex system. It is also possible that the earlier results partly reflect the very high frequencies represented by the pulsed driving force.

The experimental method and results are presented in section II, followed by a detailed discussion in section III. The conclusions from this work are presented in section IV.

II. EXPERIMENTAL

A. Experimental method

The μSR experiments were carried out using the General Purpose Surface muon facility (GPS) at the Paul Scherrer Institut (PSI), Switzerland. The GPS spectrometer has available a muon spin rotator which allows the muon spin polarization to be rotated to about 60° from the momentum direction [18]. The muons are implanted individually in a sample placed in a magnetic field parallel to their incoming momentum. The perpendicular component of the spin of each muon precesses about the field axis (which will be referred to as the z-direction). The frequency of precession is given by $\gamma_\mu B_z$, where B_z is the *local* value of the magnetic field at the muon implantation site, and γ_μ is the gyromagnetic ratio of the muon ($\gamma_\mu/2\pi \approx 135.54\,\mathrm{MHz\ T^{-1}}$). When a muon decays (with a lifetime τ_μ of 2.197 μs) the decay positron is emitted preferentially along the muon spin direction. Scintillators around the sample detect the positrons; the counts from typically 10^7 muons are recorded in histograms as a function of time after muon implantation. From such data, the time-evolution of the average muon polarization can be deduced, and hence the distribution of local values of magnetic field.

In our experiments, the complex muon polarization $P^+(t) = P_x + \mathrm{i}P_y$ was obtained by utilizing a set of positron detectors around the sample in the region of the xy plane, with the magnetic field applied in the z direction. The magnetic field probability density function $p(B)$, which gives rise to the precession signal in the xy plane, was obtained from the μSR data by employing a maximum-entropy–based inversion algorithm [19–22]. $p(B)$ is related to $P^+(t)$ according to the equations [17].

$$p(B) = \mathrm{Re}\left\{ \frac{\gamma_\mu}{\pi P^+(0)} \int_0^\infty P^+(t)\, \mathrm{e}^{-\mathrm{i}\gamma_\mu B t} \mathrm{d}t \right\}, \qquad (3)$$

$$P^+(t) = P^+(0) \left\langle \exp\left(\mathrm{i}\gamma_\mu \int_0^t B(\boldsymbol{r} - \boldsymbol{v}\tau)\, \mathrm{d}\tau \right) \right\rangle_{\boldsymbol{r}}. \qquad (4)$$

The brackets $\langle \cdots \rangle_{\boldsymbol{r}}$ denote an average over all muon implantation sites with position vector $\boldsymbol{r}$, and $\boldsymbol{v}$ is the velocity of the vortex lattice.

The sample used in the measurements was a platelet-shaped, polycrystalline Pb-In alloy, measuring $15 \times 15 \times 0.5\,\mathrm{mm}^3$ and prepared in the same way as in our previous study [17]. It was placed with its flat surface perpendicular to the applied magnetic field and the incoming muon beam (z-direction). The current leads consisted of copper strips coated with Pb-Sn solder. At the temperatures and magnetic fields used in our experiments, the solder was superconducting and the leads had a critical current much larger than that of the sample. The current leads were soldered along two opposite edges of the sample, providing a transport current in the horizontal (y) direction (that is, perpendicular to the incoming muons and applied field). This geometry gives rise to vortex motion in the vertical (x) direction. A mylar shield, coated with ~ 1 mm thick layer of antiferromagnetic Fe_2O_3 was placed symmetrically in front of the sample, exposing the central area ($10 \times 10\,\mathrm{mm}^2$) to the incoming muons. The strong atomic magnetic fields in Fe_2O_3 ensure that any muons stopping outside the central region of the specimen do not contribute to the precession signal.

The superconducting specimen was placed inside a continuous flow cryostat, which provided efficient helium gas flow cooling of both the sample and the superconducting transport current leads connected to it. The sample was cooled in an applied magnetic field to establish the equilibrium density of vortex lines in the specimen before each series of measurements.

Initially, a unidirectional pulsed transport current was applied to the sample. As illustrated schematically in Fig. 1, two routing signals (labeled "Data A" and "Data B") were also created. They were used to gate the data acquisition electronics so that measurements could be taken both with and without a current flowing through the sample and stored in separate histograms. The current pulse sequence had 1:1 mark-space ratio, with data acquisition gated to the central 90% of each half-period.

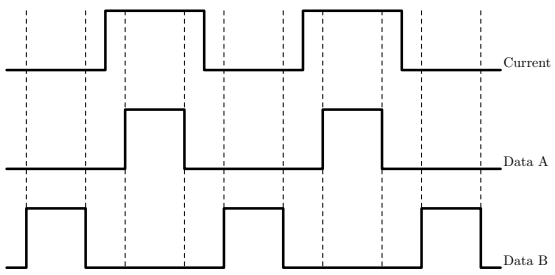

FIG. 1: The current pulse sequence applied to the sample relative to the data acquisition routing signals.

This gating allows any transients in the current pulse to die away, and for vortex motion to reach steady state, well before data-taking begins and also ensures that data-taking ends well before the current changes again. The current was provided by a superconducting magnet DC power supply, the output of which was passed either through the sample, or through a dummy load, using a simple FET switching circuit, which in turn was driven by a programmable function generator. The current was switched typically at 10's of Hz, so that if heating by the current were important, the sample would remain warm during the current-off period. Data taken during the current-off period were used to confirm that the observed effects on the μSR lineshape were due to vortex motion and not due to heating.

A different FET switching circuit was subsequently used to supply a square-wave alternating current to the sample. The "Data A" (B) signals of Fig. 1 gated the acquisition electronics to collect data during positive (negative) current flowing through the superconductor.

B. Experimental results

In Fig. 2 are shown the μSR spectra obtained at a temperature of 2 K and an applied field $\mu_0 H_a = 0.14$ T, for a range of unidirectional pulsed transport currents.

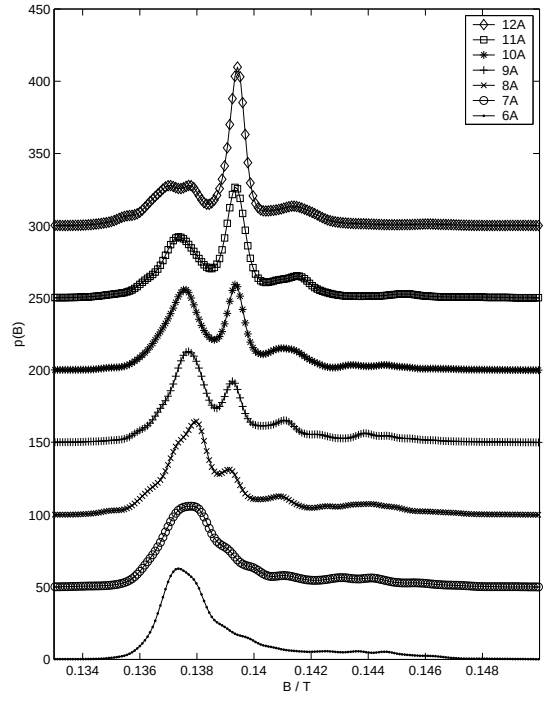

FIG. 2: μSR lineshapes obtained at 2 K and $\mu_0 H_a = 0.14$ T, for a range of unidirectional transport currents applied at 10 Hz. For clarity, each curve is shifted vertically by 50 units relative to the previous one.

It can be seen that $p(B)$ is strongly modified from the characteristic form for a static triangular vortex lattice. As the current is increased, a peak develops at approximately 0.139 T, which corresponds to the average magnetic induction in the sample; for very large currents, $p(B)$ is said to be *motionally narrowed*, similar to the results in [17].

The effect of current flow on $p(B)$ cannot be due to heating of the sample, since the $p(B)$ obtained between the current pulses, shown in Fig. 3, is almost identical to that shown in Fig. 2 for a very small (below critical) applied current. The dramatic difference between 'current on' and 'current off' results in Fig. 3 must therefore be due to vortex motion.

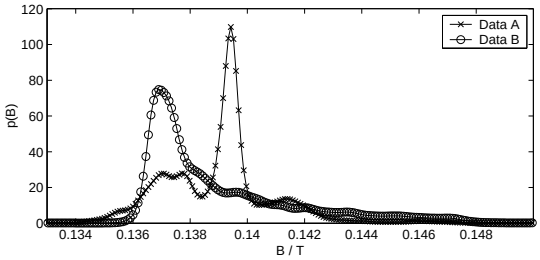

FIG. 3: The 12 A lineshape shown in Fig. 2 (labelled Data A) plotted along with the lineshape corresponding to data collected between the current pulses (Data B).

The μSR spectra obtained when an *alternating* square-wave current was applied to the sample are shown in Fig. 4. These were obtained at 4.2 K, with $\mu_0 H_a = 0.1$ T and with current applied at a frequency of 25.9 Hz. (The data for both current flow directions were identical within experimental error, so they were analyzed together to give these results.) For low driving current amplitude, these lineshapes are significantly different from those in Fig. 2: full motional narrowing is not observed for currents up to 15 A. Instead, the lineshapes exhibit a characteristic double-peak structure, similar to that predicted theoretically in [17] for the case of ordered vortex motion along a principal vortex lattice direction.

An important feature of the spectra in Fig. 4 is the existence of small sidebands on either side of the main $p(B)$ distribution (see also Fig. 5). These sidebands also exist in the lineshapes of Fig. 2 but they are broader and less pronounced. In order to make the sidebands more visible, the lineshapes of Fig. 4 are also plotted individually with the vertical scale increased, in Fig. 5.

It should finally be noted that all these measurements were taken at much higher fields than those presented in [17]. This is mainly due to the finite time-width of the muon pulses used in [17]; this reduces the amplitude of the precession signal at high frequencies, and hence limits the field value that can be used to observe muon spin rotation. In the present work, the higher applied magnetic field has the advantage that the flux flow state can be attained at relatively low transport currents.

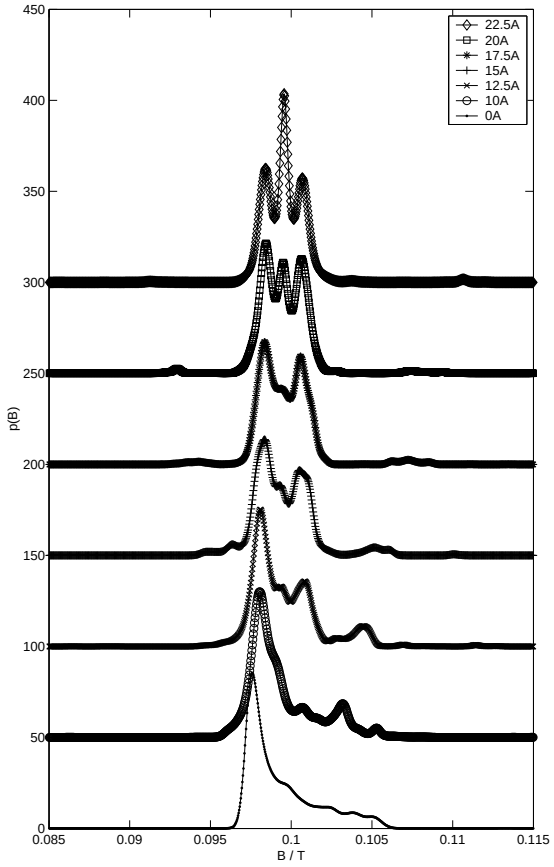

FIG. 4: μSR lineshapes for a range of alternating transport current amplitudes, obtained for $\mu_0 H_a = 0.1\,\mathrm{T}$ at 4.2 K. The frequency of the current pulses was 25.9 Hz.

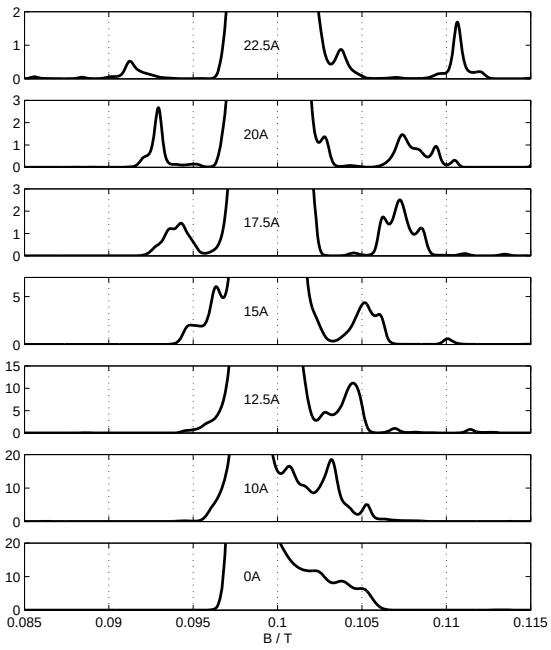

FIG. 5: The μSR lineshapes of fig. 4, with the vertical scale altered in order to make small sidebands more visible.

III. DISCUSSION

A. Unidirectional driving force

The lineshapes obtained for unidirectional pulsed current (see Fig. 2) are consistent with those obtained by [17]. However, the present results refer to a much higher applied field and simpler sample/field geometry. (That is, the sample was placed at right angles to the applied field as opposed to the 45° geometry, which was necessarily employed in [17].)

It is clear that when the vortex lattice moves, the time-averaged magnetic field at any point is more spatially uniform than that for a static vortex lattice. Hence motional narrowing of the field distribution $p(B)$ is to be expected at large driving currents. However, the numerical calculations presented in [17] demonstrate that *aligned* motion of the vortex lattice does not cause *complete* motional narrowing; however, when the vortex lattice moves with a range of orientations, the field at the muons motionally averages to a single peak at large velocities. The field distributions plotted in Fig. 2 are in good agreement with the non-ordered simulations in [17], implying that there is a significant amount of disorder in the orientation of the moving vortex system. It is important to note that the moving vortex system is not completely disordered. As shown in [17], the vortex system exhibits some degree of orientational order and moves, on average, along a principal vortex lattice direction. This was confirmed by small-angle neutron scattering (SANS) measurements, where the structure factor $S(\boldsymbol{q})$ was found to be anisotropic, consisting of six Bragg peaks arranged in a hexagonal pattern. The transverse width of these peaks was much larger than the radial width, implying a range of vortex lattice orientations.

B. Spectral Shapes

A detailed analytical discussion of the expected lineshapes is given in the Appendix. The first case considered is when the vortex velocity is not parallel to a Bragg plane of the vortex lattice. For this case, we demonstrate explicitly a complete motional narrowing of the lineshape at large vortex velocities. Conversely, if the vortex lattice moves in a direction exactly parallel to a Bragg plane, then at large vortex velocities a characteristic two-peaked lineshape is seen, with a shape described by Eq. (14) which is plotted in Fig. 6. As discussed in [17], this lineshape arises because the *time averaged* field due to a rapidly moving orientationally-ordered vortex lattice varies only in the direction perpendicular to the vortex velocity. The field variation in this direction is

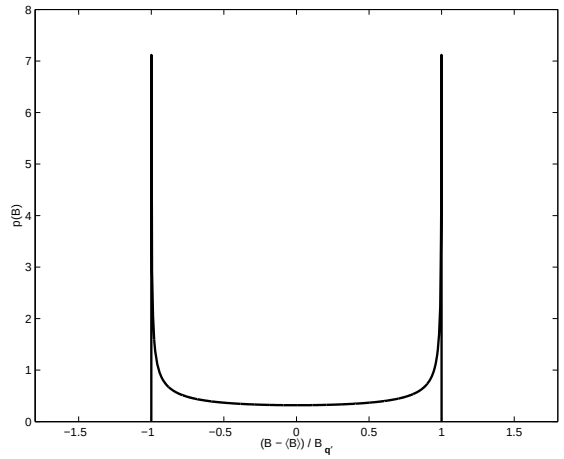

FIG. 6: Magnetic field probability distribution corresponding to vortex motion along a Bragg plane, for $|\boldsymbol{v}| \to \infty$.

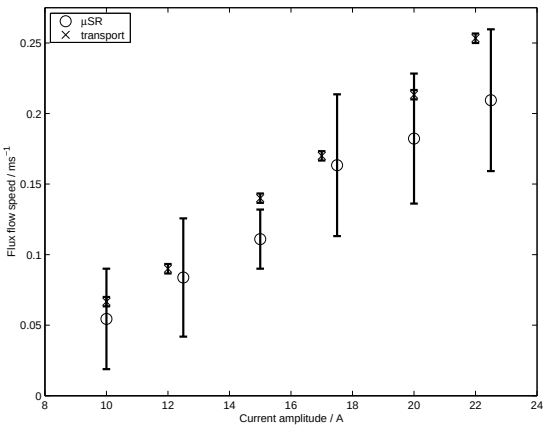

FIG. 7: Flux flow - current characteristics, obtained from μSR and transport measurements for $\mu_0 H_a = 0.1$ T and temperature of $4.2\,K$. These both extrapolate to a zero flux flow velocity at a critical current $\sim 6A$.

approximately sinusoidal, with a maximum value along the lines traversed by the vortices and a minimum value between these lines. The two peaks in $p(B)$ at large velocities are at the values of the maximum and minimum time-averaged fields. At *finite* vortex lattice velocities, our analytical calculations predict the appearance of small 'sideband' peaks, which are separated from the main peaks by multiples of the vortex lattice 'washboard frequency' $\nu_{\rm wb}$, which is the frequency at which vortex lattice unit cells move past an implanted muon. Such sidebands are visible in the experimental data shown in Figs. 2, 4 and 5 and the numerical simulations in [17]. The existence of such features may be understood as arising from a modulation of the muon precession frequency as the field maxima and minima of the vortex lattice sweep past the implanted muon. As is well known in telecommunications theory, such frequency modulation gives rise to sidebands spaced from the carrier frequency by multiples of the modulation frequency. The strength of the sidebands increases with the amplitude of modulation, which will be largest for those muons implanted near the lines where the vortex centers pass. These regions give rise to the higher-field peak of the pair seen at large velocities. Thus the stronger sidebands will be satellites of the higher-field peak.

These sidebands are of interest because they are a *direct* consequence and measure of the local vortex lattice velocity. Let $B_{\rm wb}$ be the distance of the first sideband peak from the rightmost satellite peak of the $p(B)$ spectrum. The vortex lattice velocity v is related to the washboard frequency by

$$\frac{v}{a_0} = \nu_{\rm wb} = \frac{\gamma_\mu}{2\pi} B_{\rm wb}, \tag{5}$$

where a_0 is the equilibrium vortex line spacing. However, from Eq. (2), the flux flow velocity v can also be expressed in terms of the value of the voltage, $V_{\rm ff}$, across the sample due to flux flow:

$$v = \frac{V_{\rm ff}/\ell}{B}, \tag{6}$$

where ℓ is the separation of the voltage contacts (equal to 15 mm in these measurements) and B is the average magnetic induction. This allows a direct comparison of microscopic and macroscopic measurements of this velocity.

$B_{\rm wb}$ was estimated from the lineshapes of Fig. 5 and converted to a flux flow velocity according to Eq. (5). This μSR-determined flux flow velocity is plotted in Fig. 7 along with that determined using a conventional voltmeter connected across the sample. (The voltage measurements were carried out at a factor ~ 100 lower frequency to allow for the DC voltmeter settling time).

Fig. 7 indicates that there is reasonable agreement between transport current - voltage measurements and μSR, bearing in mind that, for a given applied current, there exists a range of values of v as well as a range of vortex lattice orientations. Both of these departures from ideal behavior will broaden the sidebands and make the calculation of v/a_0 difficult and relatively inaccurate. Nevertheless, the agreement between transport and μSR measurements further confirms the validity of the model used to account for our results.

Analogous measurements were carried out on sliding charge-density waves (CDWs) by Jánossy *et al* [23]. They induced a drift velocity of the CDW in $Rb_{0.3}MoO_3$ by passing a current, and measured the voltage and voltage noise and NMR spectrum as a function of the CDW current. Weak sidebands were observed in the NMR spectra, indicating a periodic temporal modulation of the local field at a nucleus, due to the moving CDW. The position of these sidebands was consistent with that expected from other expressions for the CDW drift velocity.

C. Alternating driving force

If a square wave alternating transport current I of frequency f is applied to the sample, the vortex lines will experience an alternating force, causing them to move forwards and backwards at a frequency f, provided that the amplitude of the current exceeds the critical current, I_c. Assuming, for simplicity, that the mark-space ratio of the current pulses is 1:1, then it is easy to see that the vortex lines located more than a distance d from the edges of the sample, where

$$d = \frac{v}{2f}, \tag{7}$$

will not cross the sample boundaries during a current cycle. Since the Fe_2O_3-coated mylar window symmetrically covers a 'strip' of width 2.5 mm around the sample, then if $v/(2f) < 2.5\,\mathrm{mm}$ the vortex lines 'visible' to the implanted muons will not have passed through the sample boundaries. For $f = 25.9\,\mathrm{Hz}$, $B = 0.1\,\mathrm{T}$, $\ell = 15\,\mathrm{mm}$ and $d = 2.5\,\mathrm{mm}$, inequality (7) is satisfied provided that $V_{\mathrm{ff}} \lesssim 2 \times 10^{-4}\,\mathrm{V}$. This corresponds to a transport current amplitude of approximately 15 A, as can be calculated from Fig. 7. For higher applied current amplitudes, a certain fraction of the vortex lines 'visible' to the implanted muons will have passed through the sample edges. For instance, for a current of 17 A, $V_{\mathrm{ff}} \approx 2.5 \times 10^{-4}\,\mathrm{V}$. Hence, vortex lines move, on average, a distance of 3.2 mm during a current cycle, corresponding to 0.7 mm inside the mylar window. The visible fraction is thus $2 \times 0.7 \times 10/(10^2) = 0.14$. In other words, 14% of the vortex lines within the mylar window have interacted with the sample boundaries. For a current of 20 A, this fraction is 32% and 46% for 22.5 A. These results are consistent with the lineshapes of Fig. 4: when the fraction of vortex lines interacting with the sample edges (and visible to the implanted muons) is small (less than about 15%), the $p(B)$ has a characteristic double-peak structure, which corresponds to well-ordered vortex motion along a principal vortex lattice direction [17]. When a larger fraction of vortex lines within the mylar window interact with the sample boundaries, motional narrowing is clearly observed.

Our observations are consistent with those of Xiao *et al* [13]: by carrying out careful current-voltage (IV) measurements on 2H-$NbSe_2$ crystals, they found that the non-linear features in the measured IV characteristics are due to edge currents which in turn depend on vortices crossing the sample boundaries through a current-dependent surface barrier. On the other hand, the bulk IV characteristics were found to be linear, corresponding to vortex motion in the bulk of the sample.

We now make a more detailed comparison between a particular example of our results and a simulation of the same situation. To discuss the latter, Charalambous *et al.* [17] introduced a dimensionless measure of vortex velocity, R, given by

$$R = \frac{2\pi|\boldsymbol{v}|}{\gamma_\mu a_0 \Delta B}, \tag{8}$$

where $\Delta B = \max\{B\} - \min\{B\}$ is the width of $p(B)$ corresponding to a stationary vortex system (a similar dimensionless quantity was also introduced by Delrieu [24]). For an applied current of 15 A, $V_{\mathrm{ff}} = 0.17\,\mathrm{mV}$ which corresponds to a vortex velocity of $v = 0.11\,\mathrm{ms}^{-1}$. From the 0 A lineshape of Fig. 4, $\Delta B \approx 0.01\,\mathrm{T}$. The equilibrium vortex line spacing corresponding to $B = 0.1\,\mathrm{T}$ is $a_0 = 1.5 \times 10^{-7}\,\mathrm{m}$. Hence, $R \approx 0.54$.

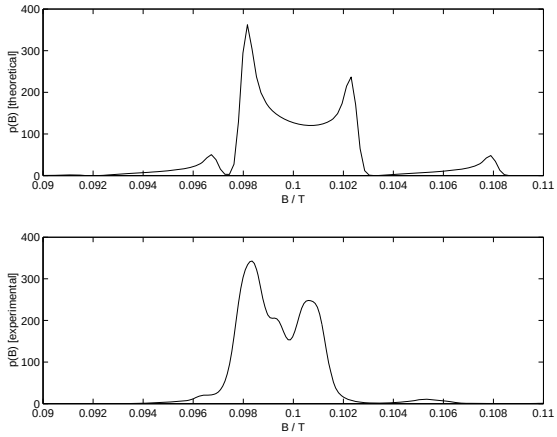

FIG. 8: The top $p(B)$ plot was calculated using the method developed by [17] for $B = 0.1\,\mathrm{T}$, $R = 0.54$ and $\sigma_\phi = 0$. The experimentally-determined $p(B)$ (bottom) is identical to that shown in fig. 4 for 15 A.

Using this value of R, and representing the static vortex lattice by a solution to the Ginzburg-Landau equations with a GL parameter of 5.2 (see [17] for more details), a theoretical $p(B)$ was calculated. This is shown in Fig. 8(top) along with the corresponding experimentally-determined $p(B)$ (bottom graph). It is important to note that the calculated spectrum was obtained by assuming that the vortex lattice has the spatial variation of field given by a solution to the GL equations, and that it moves with a single orientation along a vortex lattice principal direction. Clearly, the lineshapes shown in Fig. 8 are in very good agreement. There are, however, slight discrepancies which could be attributed to pinning (disorder tends to smear the van Hove singularities: see [25]), the existence of a small range of orientations of the flowing vortex lattice and possibly a range of vortex velocities.

IV. CONCLUSIONS

Our experimental results and calculations suggest that the interaction of vortex lines with the sample boundaries is the main factor determining the amount of disor-

der present in the moving vortex phase: for vortex lines which are not allowed to interact with the sample edges, the μSR spectrum exhibits a characteristic double-peak structure, indicative of highly-ordered motion along a principal vortex lattice vector. The speed of this motion is directly indicated by the position of 'washboard frequency' sidebands in the spectrum. When vortices do cross the sample edges, motional narrowing of the μSR lineshape is observed, which is characteristic of motion in which the vortex lattice is misaligned and probably disordered.

Acknowledgments

The experimental work was carried out at the Swiss Muon Source, Paul Scherrer Institut, Switzerland. We would like to thank E.H. Brandt for providing a copy of his code for solving the Ginzburg-Landau equations, and G.R. Walsh, D. Brewster, M. Parkes, J. Sutton and A. Bradshaw for technical assistance. Fruitful discussions with M.W. Long, W.F. Vinen, R. Cywinski, C.E. Gough and A.I.M. Rae are also acknowledged. DC was financially supported by the School of Physics & Astronomy of the University of Birmingham, the A.G. Leventis Foundation and the Committee of Vice-Chancellors and Principals through an ORS award.

V. APPENDIX: ANALYTICAL DISCUSSION OF LINESHAPES

An analytical expression for the muon precession frequency distribution due to a moving vortex lattice may be obtained as follows. We express the magnetic field distribution in the sample as the Fourier series [24]

$$B(\boldsymbol{r}) = \sum_{\boldsymbol{q}\in\mathcal{A}} B_{\boldsymbol{q}}\, \mathrm{e}^{\mathrm{i}\boldsymbol{q}\cdot\boldsymbol{r}}, \tag{9}$$

where $\mathcal{A}$ denotes the set of reciprocal lattice vectors $\boldsymbol{q}$ of the vortex lattice, and $B_{\boldsymbol{q}}$ is the corresponding Fourier coefficient of the magnetic field distribution. Substitution of Eq. (9) into Eq. (4) gives $P^+(t)$, which can be used to calculate $p(B)$ by employing Eq. (3). We distinguish between two cases; firstly, when vortex motion does not occur along a Bragg plane, *i.e.* when $\boldsymbol{q}\cdot\boldsymbol{v} \neq 0$ for all $\boldsymbol{q} \in \mathcal{A}$, it can be shown that

$$p(B) = \left(\sum_{\{n_{\boldsymbol{q}}\}} \prod_{\boldsymbol{q}\in\mathcal{A}^*} \left[J_{n_{\boldsymbol{q}}}\!\left(\frac{\gamma_\mu B_{\boldsymbol{q}}}{\boldsymbol{q}\cdot\boldsymbol{v}} \right) \right] \right)^2, \tag{10}$$

where $\{n_{\boldsymbol{q}}\}$ is a set of integers defined by

$$\{n_{\boldsymbol{q}}\} \equiv \left\{ n_{\boldsymbol{q}} : B = \langle B\rangle - \frac{1}{\gamma_\mu} \sum_{\boldsymbol{q}\in\mathcal{A}^*} n_{\boldsymbol{q}} \boldsymbol{q}\cdot\boldsymbol{v} \right\} \tag{11}$$

and $\mathcal{A}^* \equiv \{\boldsymbol{q} : \boldsymbol{q} \in \mathcal{A}, \boldsymbol{q}\cdot\boldsymbol{v} \neq 0, \boldsymbol{q} \neq \boldsymbol{0}\}$. The function $J_p(z)$ denotes a Bessel function of the first kind of order p and argument z.

Delrieu [24] obtained a similar expression for the expected NMR lineshape when the vortex velocity $\boldsymbol{v}$ satisfies $\boldsymbol{q}\cdot\boldsymbol{v} \neq 0$ for all $\boldsymbol{q} \in \mathcal{A}$. However, his calculation relates to the square of the magnitude of the NMR lineshape, even though the final result is similar to the one given above.

Alternatively, when vortex motion takes place along a Bragg plane, then there exists a reciprocal lattice vector $\boldsymbol{q}' \in \mathcal{A}$ such that $\boldsymbol{q}'\cdot\boldsymbol{v} = 0$. In fact there are infinitely many such vectors of the form $n\boldsymbol{q}'$ (for integer n) which are orthogonal to $\boldsymbol{v}$ but we will only consider a first order ($n = 1$) reciprocal lattice vector for simplicity. In the limit $T \to T_{\mathrm{c}}$ and $\langle B\rangle \gtrsim 0.5B_{\mathrm{c2}}$ this approximation is very good since $B_{\boldsymbol{q}'} \gg B_{n\boldsymbol{q}'}$. (This approximation becomes less good as $T \to 0$; in this case, the Fourier coefficients of the magnetic field decay much more slowly with q.) Assuming a single reciprocal lattice vector $\boldsymbol{q}'$ satisfying $\boldsymbol{q}'\cdot\boldsymbol{v} = 0$, it can be shown that

$$p(B) = \sum_{\{m_{\boldsymbol{k}}\}} \left\{ \prod_{\boldsymbol{k}\in\mathcal{A}^*} \left[J_{m_{\boldsymbol{k}}}\!\left(\frac{\gamma_\mu B_{\boldsymbol{k}}}{\boldsymbol{k}\cdot\boldsymbol{v}} \right) \right] \right\} \sum_{\{n_{\boldsymbol{q}}\}} \left\{ \prod_{\boldsymbol{q}\in\mathcal{A}^*} \left[J_{n_{\boldsymbol{q}}}\!\left(\frac{\gamma_\mu B_{\boldsymbol{q}}}{\boldsymbol{q}\cdot\boldsymbol{v}} \right) \right] \frac{1}{\pi|B_{\boldsymbol{q}'}|} \frac{1}{\sqrt{1 - A_{\boldsymbol{q}'}^2}} \right\}, \tag{12}$$

where

$$A_{\boldsymbol{q}'} \equiv \frac{1}{B_{\boldsymbol{q}'}} \left(B - \langle B\rangle - \frac{1}{\gamma_\mu} \sum_{\boldsymbol{q}\in\mathcal{A}^*} n_{\boldsymbol{q}}\, \boldsymbol{q}\cdot\boldsymbol{v} \right) \tag{13}$$

and $m_{\boldsymbol{k}}$ are integers defined exactly as in Eq. (11). In the limit $|\boldsymbol{v}| \to \infty$, $p(B)$ from Eq. (10) tends to a delta function centered on the average field, $\langle B\rangle$. In the same limit for Eq. (12), only terms with $n_{\boldsymbol{q}} = 0$ and $m_{\boldsymbol{k}} = 0$ contribute and $p(B)$ tends to the function

$$p(B) = \frac{1}{\pi|B_{\boldsymbol{q}'}|} \frac{1}{\sqrt{1 - \left(\frac{B - \langle B\rangle}{B_{\boldsymbol{q}'}} \right)^2}}. \tag{14}$$

Eq. (14) gives a characteristic double-peak lineshape, as shown in Fig. 6.

In the more general case of finite velocity described by Eq. (12), the lineshape $p(B)$ consists of a rather complicated combination of lineshapes of similar mathematical

form to that of Eq. (14). This combination of lineshapes gives rise to the spectral sidebands, which look similar to the main $p(B)$ distribution but their shape appears to be more strongly affected by the high-field end of the main spectrum. This is due to the fact that the magnetic field varies more strongly around the vortex core. The position of the sidebands relative to the average field depends, in general, on the velocity of the vortex lines as well as on the direction of vortex motion relative to the vortex lattice unit cell. However, the first side-band will appear, to a good approximation, at a magnetic field spacing from a main peak corresponding to the vortex lattice 'washboard frequency'.

[1] P. G. de Gennes, *Superconductivity of Metals and Alloys* (Addison-Wesley Publishing Co., Reading, Massachusetts, 1989).
[2] B. Josephson, Phys. Lett. **16**, 242 (1965).
[3] P. Nozières and W. Vinen, Philos. Mag. **14**, 667 (1966).
[4] J. Bardeen and M. Stephen, Phys. Rev. **140A**, 1197 (1965).
[5] M. Tinkham, *Introduction to Superconductivity* (McGraw-Hill Inc., New York, 1996), 2nd ed.
[6] P. le Doussal and T. Giamarchi, Phys. Rev. B **57**, 11356 (1998).
[7] S. Spencer and H. J. Jensen, Phys. Rev. B **55**, 8473 (1997).
[8] T. Natterman and S. Scheidl, Adv. Phys. **49**, 607 (2000).
[9] A. E. Koshelev and V. M. Vinokur, Phys. Rev. Lett. **74**, 3580 (1994).
[10] C. Goupil, A. Pautrat, C. Simon, P. G. Kealey, E. M. Forgan, S. L. Lee, S. T. Johnson, G. Lazard, B. Placais, Y. Simon, et al., Physica C **341**, 999 (2000).
[11] A. Pautrat, C. Goupil, C. Simon, D. Charalambous, E. M. Forgan, G. Lazard, P. Mathieu, and A. Brûlet, Phys. Rev. Lett. **90**, 087002 (2003).
[12] E. M. Forgan, D. Charalambous, P. G. Kealey, P. J. C. King, R. Khasanov, and A. Amato, Physica B **326**, 342 (2003).
[13] Z. Xiao, E. Andrei, Y. Paltiel, E. Zeldov, P. Shuk, and M. Greenblatt, Phys. Rev. B **65**, 094511 (2002).
[14] A. Campbell and J. Evetts, Adv. Phys. **21**, 199 (1972).
[15] C. R. C.J. Olson and F. Nori, Phys. Rev. Lett. **81**, 3757 (1998).
[16] E. M. Forgan, D. Charalambous, D. Fort, R. Cubitt, C. Simon, S. L. Lee, and A. Amato, J. Phys. IV France **12**, 155 (2002).
[17] D. Charalambous, P. G. Kealey, E. M. Forgan, T. M. Riseman, M. W. Long, C. Goupil, R. Khasanov, D. Fort, P. J. C. King, S. L. Lee, et al., Phys. Rev. B **66**, 054506 (2002).
[18] A. Amato, *GPS Users' Guide* (Paul Scherrer Institut, Villigen, Switzerland, 2002), see also `http://lmu.web.psi.ch`.
[19] B. Rainford and G. Daniell, Hyperfine Interactions **87**, 1129 (1994).
[20] T. M. Riseman and E. M. Forgan, Physica B **326**, 226 (2003).
[21] T. M. Riseman and E. M. Forgan, Physica B **326**, 230 (2003).
[22] T. M. Riseman and E. M. Forgan, Physica B **326**, 234 (2003).
[23] A. Jánossy, C. Berthier, P. Ségransan, and P. Butaud, Phys. Rev. Lett. **59**, 2348 (1987).
[24] J. M. Delrieu, J. Phys. F: Metal Phys. **3**, 893 (1973).
[25] E. H. Brandt, J. Low Temp. Phys. **73**, 355 (1988).

References

Abrikosov, A., *On the magnetic properties of superconductors of the second group*, Sov. Phys. JETP **5**, 1174 (1957).

Affleck, I., Franz, M., Sharifzadeh Amin, M.H, *Generalized London free energy for high-T_c vortex lattices*, Phys. Rev. B **55**, R704 (1997).

Amin, M.H.S., Affleck, I. and Franz, M., *Low-temperature behavior of the vortex lattice in unconventional superconductors.*, Phys. Rev. B **58**, 5848 (1998).

Bardeen, J., Cooper, L.N. and Schrieffer, J.R., *Theory of superconductivity*, Phys. Rev. **108**, 1175 (1957).

Bean, C.P., *Magnetization of high-field superconductors*, Rev. Mod. Phys. **36**, 31 (1964).

J.G. Bednorz and K.A. Müller, *Possible superconductivity in the La-Ba-Cu-O system*, Z. Phys. **64**, 189 (1986).

Bending, S.J., *Local magnetic probes of superconductors*, Adv. Phys. **48**, 449 (1999).

Berlinsky, A.J., Fetter, A.L., Franz, M., Kallin, C. and Soninen, P.I., *Ginzburg-Landau theory of vortices in d-wave superconductors*, Phys. Rev. Lett. **75**, 2200 (1995).

Borzi, R.A., Grigera, S.A., Perry, R.S., Kikugawa, N., Kitigawa, K., Maeno, Y. and Mackenzie, A.P., *de Haas-van Alphen effect across the metamagnetic transition in* $Sr_3Ru_2O_7$, Phys. Rev. Lett. **92**, 216403 (2004).

Brandt, E.H., *The flux line lattice in superconductors*, Rep. Prog. Phys. **58**, 1465 (1995).

Brown, S.P., *Small-angle neutron scattering from flux-lines in type-II superconductors* (dissertation submitted for assessment towards M.Sci. degree programme), The University of Birmingham (2001).

Brown, S.P., Charalambous, D., Jones, E.C., Forgan, E.M., Kealey, P.G., Erb, A. and Kohlbrecher, J., *Triangular to square flux lattice phase transition in* $YBa_2Cu_3O_7$, Phys. Rev. Lett. **92**, 067004 (2004).

Brown, S.P., Forgan, E.M., Charalambous, D., Jones, E.C., Kealey, P.G., Erb, A. and Laver, M., *Dependence upon temperature and angle of applied field of the configuration of the high-field vortex lattice in* $YBa_2Cu_3O_7$, Phys. Rev. B, to be published (2005).

Burlachkov, L., *Structure of the vortex lattice in biaxial superconductors*, Eur. Phys. Lett. **8**, 673 (1989).

Burns, G., *High-temperature superconductivity, an introduction*, Acamdemic Press, New York (1991).

Campbell, L.J., Doria, M.M. and Kogan, V.G., *Vortex lattice structures in uniaxial superconductors*, Phys. Rev. B **38**, 2439 (1988).

Capogna, L., Forgan, E.M., Hayden, S.M., Wildes, A., Duffy, J.A., Mackenzie, A.P., Perry, R.S., Ikeda, S., Maeno, Y. and Brown, S.P., *Observation of two-dimensional spin fluctuations in the bilayer ruthenate* $Sr_3Ru_2O_7$ by inelastic neutron scattering, Phys. Rev. B **67**, 012504 (2003).

Chiao, M., Pfleiderer, C., Julian, S.R., Lonzarich, G.G., Perry, R.S., Mackenzie, A.P. and Maeno, Y., *Effect of pressure on metamagnetic* $Sr_3Ru_2O_7$, Physica B **312**, 698 (2002).

Cribier, D., Jacrot, B., Madhav, Rao, L. and Farnoux, B., *Mise en evidence par diffraction de neutrons d'une structure periodique du champ magnetique dans le niobium supraconducteur*, Phys. Lett. **9**, 106 (1964).

Cubitt, R., Forgan, E.M., McK. Paul, D., Lee, S.L., Abell, J.S., Mook, H. and Timmins, P.A., *Neutron diffraction by the flux lattice in high-T_c superconductors*, Physica B **180**, 377 (1992).

Cubitt R., Forgan E.M., Yang G., Lee S.L., Paul D.M., Mook H.A., Yethiraj M., Kes P.H., Li T.W., Menovsky A.A., Tarnawski Z., Mortensen K.,*Direct observation of magnetic-flux lattice melting and decomposition in the high-T_c superconductor* $Bi_{2.15}Sr_{1.95}CaCu_2O_{8+x}$, Nature **365**, 407 (1993).

Darmascelli, A., Hussain, Z. and Shen Z.-X., *Angle-resolved photemission studies of the cuprate superconductors*, Rev. Mod. Phys. **75**, 473 (2003).

Deligiannis, K., de Groot, P.A.J., Oussena, M., Pinfold, S., Langan, R., Gagnon, R. and Taillefer, L., *New features in the vortex phase diagram of* $YBa_2Cu_3O_{7-\delta}$, Phys. Rev. Lett. **79**, 2121, (1997).

Dewhurst, C.D., Levett, S.J. and Paul, D.McK., *Small-angle neutron scattering studies of vortex lattice morphology in* YNi_2B_2C, Physica C **388**, 189 (2003).

Divakar, U., Drew, A.J., Lee, S.L., Gilardi, R., Mesot, J., Ogrin, F.Y., Charalambous, D., Forgan, E.M., Menon, G.I., Monomo, N., Oda, M., Dewhurst, C.D. and Baines, C., *Direct observation of the flux-line vortex glass phase in a type II superconductor*, Phys. Rev. Lett. **92**, 237004 (2004).

Dolan, G.J, Holtzberg, F., Feild, C. and Dinger, T.R., *Anisotropic vortex structure in* $YBa_2Cu_3O_7$, Phys. Rev. Lett. **62**, 2184 (1989).

Eilenberger, G., *Transformation of Gorkov's equation for type II superconductors into transport-like equations*, Z. Phys. **214**, 195 (1968).

Erb, A., Walker, E. and Flükiger, R., *The use of* $BaZrO_3$ *crucibles in crystal growth of the high-*T_c *superconductors. Progress in crystal growth as well as in sample quality.*, Physica C **258**, 9 (1996).

Eskildsen, M.R., Abrahamsen, A.B., Kogan, V.G., Gammel, P.L., Mortensen, K., Andersen, N.H. and Canfield P.C. , *Temperature dependence of the flux line lattice transition into square symmetry in superconducting LuNi2B2C*, Phys. Rev. Lett. **86**, 5148 (2001).

Eskildsen, M.R., Dewhurst, C.D., Hoogenboom, B.W., Petrovic, C. and Canfield, P.C., *Hexagonal and square flux lattices in* $CeCoIn_5$, Phys. Rev. Lett. **90**, 187001 (2003).

Essman, U. and Traüble, H., *The direct observation of individual flux lines in type-II superconductors*, Phys. Lett. **24A**, 526 (1967).

Fischer, Ø., Renner, Ch., Maggio-Aprile, I., Erb, A., Walker, E., Revaz, B. and Genoud, J.-Y., *Tunneling spectroscopy and STS obseravtion of vortices on high temperature superconductors*, Physica C **282**, 315 (1997).

Forgan, E.M., Paul, Mck.D., Mook, H.A., Timmins, P.A., Keller, H., Sutton S. and Abell, J.S., *Observation by neutron-diffraction of the magnetic-flux lattice in single crystal* $YBa_2Cu_3O_{7-\delta}$, Nature **343**, 735 (1990).

Forgan, E.M. and Lee, S.L., *Comment on "Vortex lattice symmetry and electronic structure in* $YBa_2Cu_3O_7$*"*, Phys. Rev. Lett. **75**, 1422 (1995).

Forgan, E.M., *Small angle neutron scattering experiments of vortices in copper oxide superconductors*, pp. 375 in *Neutron scattering in layered copper-oxide superconductors* (Ed. Furrer, A.), Kluwer Academic Publishers (1998a).

Forgan, E.M., Lloyd, S.H., Rykov, A., Tajima, S., Kealey, P. and Lee, S.L., *Characterisation of untwinned YBCO crystals*, ILL experimental report for instrument D10, expt. no. 5-16-250 (1998b).

Franz, M., Kallin, C., Soninen, P.I., Berlinsky, A.J., Fetter, A.L., *Vortex state in a d-wave superconductor*, Phys. Rev. B **53**, 5795 (1996).

Gammel, P.L., Bishop, D.J., Dolan, G.J, Kwo, J.R., Murray, C.A. and Schneemeyer, L.F., *Observation of hexagonally correlated flux quanta in* $YBa_2Cu_3O_7$, Phys. Rev. Lett. **59**, 2592 (1987).

Giamarchi, T. and Le Doussal, P., *Phase diagrams of flux lattices with disorder*, Phys. Rev. B **55**, 6577 (1997).

Giamarchi, T. and Bhattacharya, S., *Vortex phases*, Cond. Mat., 0111052 (2001).

Gilardi, R., Mesot, J., Drew, A., Divakar, U., Lee, S.L., Forgan, E.M., Zaharko, O., Conder, K., Aswal, V.K., Dewhurst, C.D., Cubitt, R., Momono, N., and Oda, M., *Direct evidence for an intrinsic square vortex lattice in the overdoped high-*T_c *superconductor* $La_{1.83}Sr_{0.17}CuO_{4+\delta}$, Phys. Rev. Lett. **88**, 217003 (2002).

Gilardi, R., Mesot, J., Brown, S.P., Forgan, E.M., Drew, A., Lee, S.L., Cubitt, R., Dewhurst, C.D., Uefuji, T. and Yamada, K., *Square vortex lattice at anomalously low magnetic fields in electron-doped* $Nd_{1.85}Ce_{0.15}CuO_4$, Phys. Rev. Lett. **93**, 217001 (2004).

Ginzburg, V.L. and Landau, L.D., *On the theory of superconductivity*, Zh. Eksperim. i. Teor. Fiz. **20**, 1064 (1950).

Gor'kov, L.P., *On the energy spectrum of superconductors*, Sov. Phys. JEPT **7**, 505 (1958).

Grigera, S.A., Perry, R.S., Schofield, A.J., Chiao, M., Julian, S.R., Lonzarich, G.G., Ikeda, S.I., Maeno, Y., Millis, A.J. and Mackenzie, A.P., *Magnetic field-tuned quantum criticailty in the metallic ruthenate* $Sr_3Ru_2O_7$, Science **294**, 329 (2001).

Grigera, S.A., Gegenwart, P., Borzi, R.A., Weickert, F., Schofield, A.J., Perry, R.S., Tayama, T., Sakakibara, T., Maeno, Y., Green, A.G. and Mackenzie, A.P., *Disorder-sensitive phase formation linked to metamagnetic quantum criticality*, Science **306**, 1154 (2004).

Harshman, D.R., Kossler, W.J., Wan, X., Fiory, A.T., Greer, A.J., Noakes, D.R., Stronach, C.E., Koster, E. and Dow, J.D., *Nodeless pairing state in single crystal* $YBa_2Cu_3O_7$,Phys. Rev. B **69**, 174505 (2004).

Hauglin, H., Woodard, N.G., Dapore-Schwartz, S. and Lafyatis, G. P., *Low-field vortex matter in* $YBa_2Cu_3O_{7-\delta}$*: an atomic-beam resonance study.*, Phys. Rev. B **67**, 014507 (2003).

Hess, H.F., Robinson, R.B. and Waszczak, J.V., *Vortex-core structure observed with a scanning tunneling microscope*, Phys. Rev. Lett. **64**, 2711 (1990).

Hinkov, V., Keimer, B., Brown, S.P., Forgan, E.M., data to be published in Phys. Rev. Lett. (2006).

Hinkov, V., Ph.D thesis to be submitted to Max-Planck-Institut für Festkörperforschung, Stuttgart (2006).

Ichioka, M., Enomoto, N., Hayachi, N. and Machida, K., *s- and* d_{xy}*-wave components induced around a vortex in* $d_{x^2-y^2}$*-wave superconductors*, Phys. Rev. B **53**, 2233 (1996a).

Ichioka, M., Hayashi, N., Enomoto, N., Machida, K., *Vortex structure in d-wave superconductors*, Phys. Rev. B **53**, 15316 (1996b).

Ichioka, M., Hasegawa, A., Machida, K., *Field dependece of the vortex structure in d-wave and s-wave superconductors*, Phys. Rev. B **59**, 8902 (1999).

Ikeda, S.-I. and Maeno, Y., *Magnetic properties of bilayered* $Sr_3Ru_2O_7$, Physica B **261**, 947 (1999).

Ikeda, S.-I., Maeno, Y., Nakatsuji, S., Kosaka, M. and Uwatoko, Y., *Ground state in* $Sr_3Ru_2O_7$: Fermi liquid close to a ferromagnetic instability, Phys. Rev. B **62**, R6089 (2000).

Jackson, T.J., Riseman, T.M., Forgan, E.M., Gluckler, H., Prokscha, T., Morenzoni, E., Pleines, M., Niedermayer, C., Schatz, G., Luetkens, H. and Litterst, J, *Depth-resolved profile of the magnetic field beneath the surface of a superconductor with a few nm resolution*, Phys. Rev. Lett. **84**, 4958 (2000).

Johnson, S.T., Forgan, E.M., Lloyd, S.H, Aegerter, C.M., Lee, S.L., Cubitt, R., Kealey, P.G., Ager, C., Tajima, S., Rykov, A. and Mck.Paul, D., *Flux-line lattice structures in untwinned* $YBa_2Cu_3O_{7-\delta}$, Phys. Rev. Lett. **82**, 2792 (1999).

Joumard, I., Marcus, J., Klein T. and Cubitt, R., *Small angle neutron scattering and magnetization measurements in the cubic* (K,Ba)BiO_3 superconductor, Phys. Rev. Lett. **82**, 4930 (1999).

Kealey, P.G., Riseman, T.M., Forgan, E.M., Galvin, L.M., Mackenzie, A.P., Lee, S.L., Mck.Paul, D., Cubitt, R., Agterberg, D.F., Heeb, R., Mao, Z.Q. and Maeno, Y., *Reconstruction from small-angle neutron scattering measurements of the real space magnetic field distribution in the mixed state of* Sr_2RuO_4, Phys. Rev. Lett. **84**, 6094 (2000).

Kealey, P.G., Charalambous, D., Forgan, E.M., Lee, S.L., Johnson, S.T., Schleger, P., Cubitt, R., McK. Paul, D., Aegerter, C.M., Tajima and S., Rykov, A., *Transverse-field components of the flux-line lattice in the anisotropic superconductor* $YBa_2Cu_3O_{7-\delta}$, Phys. Rev. B **64**, 174501 (2001).

Keimer, B., Shih, W.Y., Erwin, R.W., Lynn, J.W., Dogan, F. and Aksay, I.A., *Vortex lattice symmetry and electronic structure in* $YBa_2Cu_3O_7$, Phys. Rev. Lett. **73**, 3459 (1994).

Keterson, J.B. and Song, S.N., *Superconductivity*, Cambridge University Press, Cambridge (1999).

Khaykovich, B., Zeldov, E., Majer, D., Li, T.W., Kes, P.H. and Konczykowski, M., Phys. Rev. Lett. **76**, 2555 (1996).

Klein, T., Joumard, I., Blanchard, S., Marcus, J., Cubitt, R., Giamarchi, T. and Le Doussal, P., A Bragg glass phase in the vortex lattice of a type II superconductor, Nature **413**, 404 (2001).

Kogan, V.G., *London approach to anisotropic type-II superconductors*, Phys. Rev. B **24**, 1572 (1981).

Kogan, V.G., Gurevich, A., Cho, J.H., Johnston, D.C., Ming, X., Thompson, J.R. and Martynovich, A., *Nonlocal electrodynamics and low-temperature magnetization of clean high-κ superconductors*, Phys. Rev. B **54**, 12386 (1996).

Kogan, V.G, Bullock, M., Harmon, B., Miranović, P., Dobrosavljević, Lj., Gammel, P.L. and Bishop, D.J., *Vortex lattice transitions in borocarbides*, Phys. Rev. B **55**, R8693 (1997).

Kopnin, N., *Theory of nonequilibrium superconductivity*, Oxford University Press, Oxford (2001).

Kurahashi, K., Matsushita, H., Fujita, M. and Yamada, K., *Heat treatment effects on the superconductivity and crystal structure of* $Nd_{1.85}Cei_{0.15}CuO_4$*studied using a single crystal*, J. Phys. Soc. Jpn. **71**, 910 (2002).

Larkin, A.I., *Effect of inhomogeneities on structure of mixed state of superconductors*, Sov. Phys. JETP **31**, 784 (1970).

Lawrence, W.E. and Doniach, S., Proc. 12th Int. Conf. Low Temperature Physics (ed. E Kanda), Academic Press of Japan (1971).

Liu, R., Veal, B.W., Paulikas, A.P., Downey, J.W., Kostić, P.J., Fleshler, S., Welp, U., Olson, C.G., Wu, X., Arko A.J. and Joyce, J.J., *Fermi-surface topology of* $YBa_2Cu_3O_x$ with varied oxygen stoichiometry: a photoemission study, Phys. Rev. B **46**, 11056 (1992).

London, F. and London, H., *The electromagnetic equations of the supraconductor*, Proc. Roy. Soc. (London) **A149**, 71 (1935).

Lovesey, S.W., *Theory of neutron scattering from condensed matter*, Oxford University Press, Oxford (1987).

Mackenzie, A.P. and Maeno, Y., *The superconductivity of* Sr_2RuO_4 and the physics of spin-triplet pairing, Rev. Mod. Phys. **75**, 657 (2003).

Maggio-Aprile, I., Renner, Ch., Erb, A., Walker, E. and Fischer, Ø, *Direct vortex lattice imaging and tunneling spectroscopy of flux lines on* $YBa_2Cu_3O_{7-\delta}$, Phys. Rev. Lett. **75**, 2754 (1995).

Merzbacher, E., *Quantum mechanics* (Third ed.), John Wiley & Sons, Inc., New York (1998).

Müller, K.A., *On the macroscopic s- and d-wave symmetry in cuprate superconductors*, J. Superconductivity **15**, 319 (2002).

Nakai, N., Miranović, P., Ichioka, M. and Machida, K., *Reentrant vortex lattice transformation in fourfold symmetric superconductors*, Phys. Rev. Lett. **89**, 237004 (2002).

Ohmichi, E., Yoshida, Y., Ikeda, S.I., Mushunikov, N.V., Goto, T. and Osada, T., *Double metamagnetic transition in the bilayer ruthenate* $Sr_3Ru_2O_7$, Phys. Rev. B **67**, 024432 (2003).

Pan, S.H., Hudson, E.W., Gupta, A.K., Ng, K.-W., Eisaki, H., Uchida, S. and Davis, J.C., *STM studies of the electronic structure of vortex cores in* $Bi_2Sr_2CaCu_2O_{8+\delta}$, Phys. Rev. Lett. **85**, 1536 (2000).

Park, T., Malinowski, A., Hundley, M.F., Thompson, J.D., Sun, Y., Salamon, A.B., Choi, E.M., Kim, H.J., Lee, S.I., Canfield, P.C. and Kogan, V.G., *Anomalous paramagnetic effects in the mixed state of* $LuNi_2B_2C$, Phys. Rev. B **71**, 054511 (2005).

Perry, R.S., Galvin, L.M., Grigera, S.A., Capogna, L., Schofield, A.J. and Mackenzie, A.P., *Metamagnetism and critical fluctuations in high quality single crystals of the bilayer ruthenate* $Sr_3Ru_2O_7$, Phys. Rev. Lett. **86**, 2661 (2001).

Perry, R.S., Kitigawa, K., Grigera, S.A., Borzi, R.A., Mackenzie, A.P., Ishida, K. and Maeno, Y., *Multiple first-order metamagnetic transitions and quantum oscillations in ultrapure* $Sr_3Ru_2O_7$, Phys. Rev. Lett. **92**, 166602 (2004).

Ramos, S., Brown, S.P., Forgan, E.M., Hayden, S., Wildes, A., Perry, R.S and Maeno, Y., *Observation of spin fluctuations at and beyond the metamagnetic field in* $Sr_3Ru_2O_7$, Phys. Rev. Lett., to be published (2006).

Ren, Y., Xu, J.-H. and Ting, C.S., *Ginzburg-Landau equations and vortex structure of a* $d_{x^2-y^2}$ *superconductor*, Phys. Rev. Lett. **74**, 3680 (1995).

Rosenstein, B. and Knigavko, A., *Anisotropic peak effect to to structural phase transition in the vortex lattice*, Phys. Rev. Lett. **83**, 844 (1999).

Sardella, E. and Moore, M.A., *Tilt-wave instabilities of the flux-line lattice in anisotropic superconductors*, Phys. Rev. B **48**, 9664 (1993).

Schabel, M.C., Park, C.H., Matsuura, A., Shen, Z.X., Bonn, D.A., Liang R. and Hardy, W.N., *Angle-resolved photoemission on untwinned* $YBa_2Cu_3O_{6.95}$*. I. Electronic structure and dispersion relations of surface and bulk bands*, Phys. Rev. B **57**, 6090 (1998a).

Schabel, M.C., Park, C.H., Matsuura, A., Shen, Z.X., Bonn, D.A., Liang R. and Hardy, W.N., *Angle-resolved photoemission on untwinned* $YBa_2Cu_3O_{6.95}$*. II. Determination of Fermi surfaces*, Phys. Rev. B **57**, 6107 (1998b).

Schilling, A., Fisher, R.A., Phillips, N.E., Welp, U., Kwok, W.K. and Crabtree, G.W., *Calorimetric evidence for the occurence of a first-order transition in the mixed state of untwinned* $YBa_2Cu_3O_{7-\delta}$, Physica C **282**, 327 (1997).

Schofield, A.J., *Non Fermi-liquids*, Contemporary Physics **40**, 95 (1999).

Schrieffer, J.R. and Tinkham, M., *Superconductivity*, Rev. Mod. Phys. **71**, S313 (1999).

Shaked, H., Jorgensen, J.D., Chmaissem, O., Ikeda, S. and Maeno, Y., *Neutron diffraction study of the structural distortions in* $Sr_3Ru_2O_7$, J. Solid State Chem. **154**, 361 (2000).

Shibata, K., Nishizaki, T., Sasaki, T. and Kobayashi, N., *Phase transition in the vortex liquid and the critical endpoint in* $YBa_2Cu_3O_y$, Phys. Rev. B **66**, 214518 (2002).

Shibata, K., Maki, M., Nishizaki, T. and Kobayashi, N., *Quasiparticle spectra and their spatial variation on* $YBa_2Cu_3O_y$ *by scanning tunneling spectroscopy*, Physica C **388**, 277 (2003a).

Shibata, K., Maki, M., Nishizaki, T. and Kobayashi, N., *Scanning tunneling spectroscopy studies on vortices in* $YBa_2Cu_3O_y$ *single crystals*, Physica C **392**, 323 (2003b).

Simon, Ch., Pautrat, A., Poullain, G., Goupil, C., Leblond-Harnois, C., Chaud, X and Brûlet, A., *Influence of twin boundaries on the flux-line-lattice strcture in* $YBa_2Cu_3O_{7-\delta}$*: a small-angle study*, Phys. Rev. B **70**, 024502 (2004).

Singh, D.J. and Mazin, I.I., Electronic structure and magnetism of $Sr_3Ru_2O_7$, Phys. Rev. B **63**, 165101 (2001).

Sonier, J.E., Kiefl, R.F., Brewer, J.H., Bonn, D.A., Dunsiger, S.R., Hardy, W.N., Liang, R., MacFarlane, W.A. and Riseman, T.M., *Magnetic field dependence of the London penetration depth in the vortex state of* $YBa_2Cu_3O_{6.95}$, Phys. Rev. B **55**, 11789 (1997).

Sonier, J.E., Brewer, J.H and Kiefl, R.F., *μSR studies of the vortex state in type-II superconductors*, Rev. Mod. Phys. **72**, 769 (2000).

Soninen, P.I., Kallin, C. and Berlinsky, A.J., *Structure of a vortex line in a $d_{x^2-y^2}$ superconductor*, Phys. Rev. B **50**, 13883 (1994).

Sun, A.G., Han, S.H., Katz, A.S., Gajewski, D.A., Maple, M.B. and Dynes, R.C., *Anisotropy of the penetration depth in* $YBa_2Cu_3O_{7-\delta}$*: Josephson-tunneling studies*, Phys. Rev. B **52**, R15731 (1995).

Takagi, H., Uchida, S and Tokura, Y., *Superconductivity produced by electron doping in* CuO_2*-layered compounds*, Phys. Rev. Lett. **62**, 1197 (1989).

Thiemann, S.L., Radovič, Z. and Kogan, V.G., *Field structure of vortex lattices in uniaxial superconductors*, Phys. Rev. B **39**, 11406 (1989).

Tinkham, M., *Introduction to superconductivity* (2nd Ed.), McGraw Hill, New York (1996).

Tsuei, C., Kirtley, J.R., Chi, C.C., Yu-Jahnes, L.S., Gupta, A., Shaw, T., Sun, J.Z. and Ketchen, M.B., *Pairing symmetry and flux quantization in a tricrystal superconducting ring of* $YBa_2Cu_3O_{7-\delta}$, Phys. Rev. Lett. **73**, 593 (1994).

Tsuei, C. C. and Kirtley, J.R., *Pairing symmetry in cuprate superconductors*, Rev. Mod. Phys. **72**, 969 (2000a).

Tsuei, C.C. and Kirtley, J.R., *Phase-sensitive evidence for d-wave pairing symmetry in electron-doped cuprate superconductors*, Phys. Rev. Lett. **85**, 182 (2000b).

J.R. Waldram, *Superconductivity of metals and cuprates*, IOP Publishing Ltd., Bristol (1996).

Walker, M.B. and Timusk. T., *Interpretation of the oblique Abrikosov flux lattice in* $YBa_2Cu_3O_7$, Phys. Rev. B **52**, 97 (1995).

Wang, N.L., Tajima, S., Rykov, A.I. and Tomimoto, K., *Zn-substitution effects on the optical conductivity in* $YBa_2Cu_3O_{7-\delta}$ *crystals: strong pair breaking and reduction of in-plane anisotropy*, Phys. Rev. B **57**, R11081 (1998).

Wu, M.K., Ashburn, J.R., Torng, C.J., Hor, P.H., Meng, R.L., Gao, L., Huang, Z.J., Wang Y.Q. and Chu, C.W., *Superconductivity at 93 K in a new mixed-phase Yb-Ba-Cu-O compound system at ambient pressure*, Phys. Rev. Lett. **58**, 908 (1987).

Yamada, K., Kurahashi, K., Uefuji, T., Fujita, M., Park, S., Lee, S.-H. and Endoh, Y., *Commensurate spin dynamics in the superconducting state of an electron-doped cuprate superconductor*, Phys. Rev. Lett. **90**, 137004 (2003).

Yaouanc, A., Dalmas de Réotier, P. and Brandt, E.H., *Effect of the vortex core on the magnetic field in hard superconductors*, Phys. Rev. B **55**, 11107 (1997).

Yethiraj, M., Mook, H.A., Wignall, G.D., Cubitt, R., Forgan, E.M., Paul, D.M. and Armstrong, T., *Small-angle neutron scattering study of flux line lattices in twinned* $YBa_2Cu_3O_7$, Phys. Rev. Lett. **70**, 857 (1993a).

Yethiraj, M., Mook, H.A., Wignall, G.D., Cubitt, R., Forgan, E.M., Lee, S.L., Paul, D.M. and Armstrong, T., *Anisotropic vortex lattice in* $YBa_2Cu_3O_7$, Phys. Rev. Lett. **71**, 3019 (1993b).

Yip, S.K. and Sauls, J.A., *Nonlinear Meissner effect in CuO superconductors*, Phys. Rev. Lett. **69**, 2264 (1992).

Zeldov, E., Majer D., Konczykowski, M., Geshkebein, V.B., Vinokur, V.M. and Shtrikman, H., *Thermodynamic observation of first-order vortex-lattice melting transition in* $Bi_2Sr_2CaCu_2O_8$, Nature **375**, 373 (1995).